Solar Water Oxidation by Composite Cobalt-Based Catalyst/Oxide Semiconductor Photoanodes

Diane Kai Ning Zhong

A dissertation submitted in partial fulfillment of the requirements for the degree of

Doctor of Philosophy

University of Washington
2012

Reading Committee:
Daniel R. Gamelin, Chair
James M. Mayer
David S. Ginger

Program Authorized to Offer Degree:
Department of Chemistry

University of Washington

Abstract

Solar Water Oxidation by Composite
Cobalt-Based Catalyst/Oxide Semiconductor Photoanodes

Diane Kai Ning Zhong

Chair of the Supervisory Committee:
Professor Daniel R. Gamelin
Department of Chemistry

Photoelectrochemical (PEC) water splitting is an attractive approach to capturing and storing the earth's abundant solar energy influx. The challenging four-electron water-oxidation half-cell reaction has hindered this technology, giving rise to slow water oxidation kinetics at the photoanode surfaces relative to competitive loss processes. Inspired by nature's photosynthesis, where the tasks of photon absorption, charge separation, and water-oxidation catalysis are performed by separate protein components, division-of-labor strategies for solar water splitting in PEC cells are explored in this thesis. Prototypical α-Fe_2O_3 nanostructured photoanodes are interfaced with cobalt-phosphate water oxidation catalysts (Co-Pi) that can operate at low overpotentials. The resulting composite photoanodes exhibit onset potentials over one hundred millivolts lower than the semiconductor alone, indicating a reduced external bias would be needed to drive overall water splitting. A kinetic bottleneck limiting the performance of such photoanodes was identified to be related to the deposition of thick catalyst layers. This bottleneck was then circumvented by employing a photo-assisted electrodeposition technique to deposit the catalyst, which allows deposition only where visible light generates oxidizing equivalents, and provides a more uniform distribution of catalyst onto semiconductor surfaces. In order to achieve even lower photocurrent onset potentials, the influence of Co-Pi on W:$BiVO_4$ photoanode surfaces was also investigated. Using peroxide as a surrogate substrate revealed that interfacing Co-Pi with W:$BiVO_4$ photoanodes almost completely eliminates losses due to surface electron-hole recombination. The low absolute onset potential achieved with Co-Pi/W:$BiVO_4$ is promising for overall solar water splitting in low-cost tandem PEC cells, and is encouraging for application of this surface modification strategy to other candidate photoanodes. Finally the role of Co-Pi in enhancing the photocatalytic activity of various oxide semiconductors towards water oxidation is examined by a series of PEC, impedance spectroscopy, photoconductive microscopy, and PEC kinetic experiments. All evidence strongly suggests the superior PEC performance of Co-Pi/ semiconductor composite photoanodes is a direct result of efficient water oxidation catalysis by the Co-Pi surface electrocatalyst competing with surface electron-hole recombination in the semiconductor.

TABLE OF CONTENTS

List of Figures iv

List of Abbreviations ix

Introduction 1

Chapter 1: The Photoelectrochemical Cell 10

1.1 Solar Water Splitting with Semiconductors 10

1.2 Semiconductor Photoelectrochemistry 12

1.3 PEC Measurements 14

1.4 Solar-to-Hydrogen Conversion Efficiency 18

1.5 Efficiency Losses 19

1.6 The Catalyst/Semiconductor Photoanode 20

1.7 Practical Applications 21

1.8 Notes to Chapter 1 22

Chapter 2: Composite Photoanodes for Photoelectrochemical Solar Water Splitting 24

2.1 Introduction 24

2.2 Direct Photocatalytic Water Splitting 24

2.3 Separation of Photon absorption, Charge Separation, and Redox Chemistries 26

2.4 Mesostructured α-Fe_2O_3 Photoanodes for Solar Water Oxidation 28

2.5 A Family of Cobalt-Based Electrocatalysts for Water Oxidation 31

2.6 Composite Co-Pi/Semiconductor Photoanodes for PEC Solar Water Oxidation 32

2.7 Composite Catalyst/Dye/Semiconductor Photoanodes for PEC Solar Water Splitting 35

2.8 Summary and Perspective 37

2.9 Notes to Chapter 2 38

Chapter 3: Solar Water Oxidation by Composite Catalyst/α-Fe_2O_3 Photoanodes 42

3.1 Introduction 42

3.2 Experimental Details 43

3.3 Results and Discussion 44

3.4. Summary 46

3.5 Notes to Chapter 3 46

Chapter 4: Photoelectrochemical Water Oxidation by Cobalt Catalyst ("Co-Pi")/α-Fe_2O_3 Composite Photoanodes: Oxygen Evolution and Resolution of a Kinetic Bottleneck 48

4.1 Introduction 48

4.2 Experimental Details 49

4.3 Results and Analysis 50

4.4. Summary 58

4.5 Notes to Chapter 4 59

Chapter 5: Photo-Assisted Electrodeposition of Cobalt-Phosphate (Co-Pi) Catalyst on Hematite Photoanodes for Solar Water Oxidation 61

5.1 Introduction 61

5.2 Experimental Section 63

5.3 Results & Discussion 64

5.4 Summary 70

5.5 Notes to Chapter 5 70

Chapter 6: Near-Complete Suppression of Surface Recombination in Solar Photoelectrolysis by "Co-Pi" Catalyst-Modified W:$BiVO_4$ 72

6.1 Introduction 72

6.2 Experimental Section 73

6.3 Results 75

6.4 Analysis and Discussion 82

6.5 Conclusion 86

6.6 Notes on Chapter 6 87

Chapter 7: Understanding the Cobalt-Catalyst/Semiconductor Interface: Conclusions and Outlook 89

7.1 The Catalyst/Semiconductor Relationship 89

7.2 Origin of the Kinetic Bottleneck 91

7.3 Other Composite Catalyst/Semiconductor Photoanodes 93

7.4 Impedance Spectroscopy and Mott-Schottky Analyses 96

7.5 Photoconductive Microscopy on Cobalt Catalyst/α-Fe_2O_3 Photoanodes 99

7.6 Photoelectrochemical Kinetics Analyses 100

7.7 Conclusions and Outlook 104

7.8 Notes to Chapter 7 106

Bibliography 108

Appendix A. Supplementary Information for Chapter 3 115

Appendix B. Supplementary Information for Chapter 4 117

Appendix C. Supplementary Information for Chapter 5 119

Appendix D. Supplementary Information for Chapter 6 121

List of Figures

Figure Number Page

0.1. The Solar Spectrum 2

1.1. Basic Principles of Solar Water Splitting 10

1.2. Diagram of Semiconductor Band Edge Potentials 11

1.3. The Photoelectrochemical Cell....12

1.4. Energy Diagram of the Semiconductor-Electrolyte Interface 13

1.5. Charge Distribution and Capacitance of the Semiconductor-Electrolyte Contact 15

1.6. Band Energetics of an n-type Semiconductor Under an Applied Bias....16

1.7. Current-Voltage Characteristics of a Semiconductor Photoanode 17

1.8. Productive and Nonproductive Pathways for Water Oxidation 20

1.9. Separation of Photon Absorption, Charge Separation, and Water Oxidation Catalysis 20

1.10. PEC Cell with a Catalyst/Semiconductor Composite Photoanode....21

2.1. Three Approaches to PEC Solar Water Splitting....27

2.2 The Solar Spectrum with Band Gap Positions of Metal Oxide Semiconductors 28

2.3 Si-doped Dendritic α-Fe_2O_3 Photoanodes 30

2.4 α-Fe_2O_3 Nanotube Arrays....31

2.5 Co-Pi Water-Oxidation Electrocatalyst 32

2.6. SEM Images and J-V Curves of Co-Pi/α-Fe_2O_3....33

2.7. SEM Images and PEC Measurements of Co-Pi/ZnO Nanorods 35

2.8. Schematic and PEC Measurements of a TiO_2/Dye/IrO_2 Photoanode....36

3.1. SEM Images of α-Fe_2O_3 and Co-Pi/α-Fe_2O_3 Photoanodes 44

3.2. PEC and Spectroscopic Measurements of a Co-Pi/α-Fe_2O_3 Photoanode....45

3.3. Scheme for PEC Water Oxidation with Co-Pi/α-Fe_2O_3 46

4.1. J-V Curves of Thick Co-Pi/α-Fe_2O_3 Photoanodes in NaOH and KPi....51

4.2. Scan Rate and Power Dependence of a Co-Pi/α-Fe_2O_3 Photoanode....53

4.3. Scan Rate Dependence of Co-Pi on FTO....54

4.4 Scanning Electron Micrographs of Co-Pi/α-Fe_2O_3 Composite Photoanodes 55

4.5. J-V Curves of Thin Co-Pi/α-Fe_2O_3 Photoanodes in NaOH and KPi....56

4.6. Photocurrent Transients of Co-Pi/α-Fe_2O_3 in Various Electrolytes....57

4.7. PEC and Oxygen Detection Measurements on a Co-Pi/α-Fe_2O_3 Photoanode....58

4.8. Scheme of O_2 Evolution with Co-Pi/α-Fe_2O_3 Composite Photoanodes....59

5.1. Scheme of Co-Pi PEC Deposition, Electrodeposition, and Co^{2+} Wet Impregnation....63

5.2 SEM Images of α-Fe_2O_3 and Cobalt-Catalyst Modified α-Fe_2O_3 Photoanodes....65

5.3. EDX of α-Fe_2O_3 and Co-Pi/α-Fe_2O_3....66

5.4. PEC Measurements on Various Cobalt Catalyst/α-Fe_2O_3 Photoanodes....67

5.5. PEC and IPCE Data on the Best Co-Pi/α-Fe_2O_3 Photoanodes....68

5.6. Comparison of Various Cobalt-Based Catalysts on α-Fe_2O_3....69

6.1. SEM Images of $BiVO_4$ and W:$BiVO_4$ Photoanodes....75

6.2. XRD of $BiVO_4$ and W:$BiVO_4$....76

6.3. IPCE and J-V Curves of $BiVO_4$ and W:$BiVO_4$....77

6.4. PEC and IPCE Measurements of a Co-Pi/W:$BiVO_4$ Photoanode....79

6.5. Oxygen Detection of a Co-Pi/W:$BiVO_4$ Photoanode....80

6.6. PEC Measurements of W:$BiVO_4$ Photoanodes in H_2O_2....81

6.7. Energy Diagram of PEC Water Oxidation by W:$BiVO_4$ with and without Co-Pi....83

6.8. Water Oxidation and Charge Separation Efficiencies of W:$BiVO_4$....84

7.1. Scheme for Mechanism of Water Oxidation by Co-Pi....90

7.2. Dependence of the Water Oxidation Current with Co-Pi Thickness....91

7.3. Dependence of Co-Pi/α-Fe_2O_3 Performance on the Co-Pi Thickness....92

7.4. SEM and J-V Curves of a TiO_2 Nanowire Photoanode and Co-Pi-modified TiO_2 Photoanode....93

7.5. J-V Curves of a Co-MePi/α-Fe_2O_3 Composite Photoanode....94

7.6. J-V Curves of a CoO_x/α-Fe_2O_3 Composite Photoanode....95

7.7. CV of Fe-Pi and J-V Curves of Fe-Pi/α-Fe_2O_3 and the Parent α-Fe_2O_3 Photoanode....96

7.8. Nyquist Plots of Co-Pi/α-Fe_2O_3 and Unmodified α-Fe_2O_3 Photoanodes....97

7.9. Resistance and Mott-Schottky Plot of Co-Pi/α-Fe_2O_3 and α-Fe_2O_3....98

7.10. AFM, cAFM, and pcAFM Images of a Co-Pi/α-Fe_2O_3 Composite Photoanode....100

7.11. PEC Kinetic Measurements on Co-Pi/α-Fe_2O_3.....102

7.12. Electrochemical Kinetics on Ni-B_i and N_i-Bi/α-Fe_2O_3 Composite Electrodes.....103

Acknowledgments

The author would like to express her deepest gratitude towards those who have supported her pursuit of a PhD. I would like to especially thank Professor Daniel Gamelin for his excellent mentorship. His patience, positive thinking, and scholarly guidance has been most inspirational throughout my studies. I would also like to thank former and current members of the Gamelin group and a few collaborators for sharing their knowledge and friendship (*vide infra*). In addition, I would like to thank the faculty and staff at the Department of Chemistry. I give many thanks to my family and friends, as well, for their endless support. I am also grateful for the financial support provided by the Department of Chemistry, the National Science Foundation Integrative Graduate Education and Research Traineeship (NSF-IGERT), and Sun Catalytix.

The Gamelin Group:

Prof. Daniel R. Gamelin
Prof. G. Mackay Salley
Prof. Victor Polinger
Prof. Rémi Beaulac
Prof. Kevin R. Kittilstved
Dr. Stefan Ochsenbein
Dr. Jianwei Sun
Dr. Nils Janßen
Dr. William K. Liu
Dr. Paul Archer
Dr. Claire Johnson
Dr. Kelly Whitaker
Dr. Michael White
Dr. Jillian Dempsey
Dr. Emily McLaurin
Dr. Jeffrey Rinehart
Curtis Deer
Vladimir Vlaskin
Alicia Cohn
Amanda Weaver
Alina Schimpf
Liam Bradshaw
Bo (Peter) Zhao
G. Z. (Mike) Carroll
Patrick Whitham
Hiroki Inumaru
Josh Graves
Tom Draskovic
Troy Kilburn
Sujung Choi
Rob Johns
Shirley Leu

Collaborators:

Prof. Michel Grätzel (EPFL)
Dr. Kevin Sivula (EPFL)
Dr. Thomas Moehl (EPFL)
Dr. S. David Tilley (EPFL)
Dr. Elijah Thimsen (EPFL)
Dr. Scott C. Warren (EPFL)
Dr. Florian LeFormal (EPFL)
Dr. Sophie Wenger (EPFL)
Maurin Cornuz (EPFL)
Jérémie Brillet (EPFL)
Arianna Marchioro (EPFL)
Prof. David S. Ginger (UW)
Dr. Raj Giridharagopal (UW)
Steve Reece (Sun Catalytix)

Dedication

To my father for his continuous sacrifice and inspiration,
and to my bunnies, Pepper and Vanilla, for their perpetual cuteness.

List of Abbreviations

AACVD	aerosol-assisted chemical vapor deposition
AFM	atomic force microscopy
AM	air mass
APCE	absorbed photon-to-current conversion efficiency
APCVD	atmospheric pressure chemical vapor deposition
cAFM	conductive atomic force microscopy
CBM	conduction band minimum
CE	counter electrode
CIGS	$Cu(In,Ga)Se_2$
Co-Bi	cobalt-borate
Co-MePi	cobalt-methyl phosphonate
Co-O_x	cobalt-oxide
Co-Pi	cobalt-phosphate
DSSC	dye-sensitized solar cell
e^-	electron
e-h	electron-hole
EDX	energy dispersive X-ray analysis
EQE	external quantum efficiency
EXAFS	extended X-ray absorption fine structure
Fe-Pi	iron-phosphate
FTO	fluorine doped tin oxide
h^+	hole
IPCE	incident photon-to-current conversion efficiency
IQE	internal quantum efficiency
IR	infrared
J-V	current density-voltage
KB_i	potassium borate
KPi	potassium phosphate
kWh	kilowatt-hour
MnOEC	Mn_4O_4Ca oxygen-evolving cluster of PS-II
MOD	metal-organic decomposition
$NADP^+$	nicotinamide adenine dinucleotide phosphate
NHE	normal hydrogen electrode
Ni-B_i	nickel-borate
pcAFM	photoconductive atomic force microscopy
PEC	photoelectrochemical
PS-I	photosystem I
PS-II	photosystem II
PV	photovoltaic
RE	reference electrode
RHE	reversible hydrogen electrode
SEM	scanning electron microscopy
SP	spray pyrolysis
STH	solar-to-hydrogen
TW	terawatt = 10^{12} watts
USP	ultrasonic spray pyrolysis
UV	ultraviolet
VBM	valence band maximum
WE	working electrode
XRD	X-ray diffraction

Introduction

Photosynthesis is Nature's way of absorbing sunlight, water, and carbon dioxide and converting these raw materials into oxygen and reduced carbohydrates that serve as fuel.[1,2] In 1995, artificial photosynthesis, the conversion of sunlight into chemical fuels, was identified as one of the Holy Grails of Chemistry.[1] Based on Nature's motif, artificial photosynthesis would allow us to bottle and store the abundant energy of sunlight for use as an alternative to fossil fuels. One of the most attractive approaches to solar energy storage is solar water splitting, whereby solar photons are used to drive the uphill conversion of water into its elemental components, H_2 and O_2.[2,3] The reverse reaction, combustion of H_2 fuel liberates the energy stored and leaves H_2O as the only byproduct, making the entire process clean, renewable and carbon-free. Thin film semiconductor materials have been shown to absorb photons and produce charges to drive uphill redox reactions.[2,4-6] However, no single material has been shown to perform solar water splitting in an efficient and practical manner, partially due to the difficulty in driving the four-electron multinuclear water oxidation reaction.[6,7] This thesis will focus on photoelectrochemical (PEC) water splitting using thin film semiconductor photoanodes interfaced with proficient water oxidation electrocatalysts for enhanced solar water oxidation.

The Global Energy Demand

Humanity is one of the largest energy consumers on Earth. From powering light bulbs to motor vehicles, in 2001, our global energy consumption rate was 13.5 terawatts (TW = 10^{12} W), an average of 2.2 kW per capita.[3] This value is moderately projected to double by 2050 with the growth in world population and the rapid economic growth of countries like China and India.[3,8] Currently the demand is 85% supplied by fossil fuels consisting of oil, coal, and natural gas.[9] Only 10% of the energy is supplied by renewables, including wind, hydro, biomass, solar and geothermal power, and 5% by nuclear.[9] If the world energy supply distribution remains unchanged, the consumption rate of fossil fuels will be expected to double in 2050 to a considerable 23 TW.[3,8] Although extracting more fuel from the ground is possible, over time the practice is unsustainable. Because of its regional abundance, serious economic and political security concerns arise, and this combined with the environmental consequences of greenhouse gas emissions make fossil fuels a poor long term energy resource.[8,10,11]

Few alternative energy resources can replace fossil fuels and simultaneously meet the projected energy consumption increase by 2050. Nuclear energy requires an additional 10,000 power plants be constructed, equating to a rate of one power plant being built every other day for the next 50 years in order to meet the energy demand.[3,8] Neither hydroelectric, geothermal, wind and biomass energy alone will feasibly meet the projected energy consumption rate.[8] The energy provided by sunlight is by far the only renewable energy resource that can compete with our rapidly expanding global energy use. Sunlight strikes the Earth at a rate of 120,000 TW/year, almost three orders of magnitude larger than what we use today.[2,8]

Solar Energy

More energy from the sun strikes the Earth in 1 hour than all the energy consumed by the world in a year.[10] Yet, solar energy is quite diffuse compared to fossil fuels, making it economically difficult to capture and harness. With an irradiance of 1367 W/m^2, the solar spectrum is close to that of 5800 K blackbody irradiation at

the top of the Earth's atmosphere, denoted as air mass 0 (AM 0) in Figure 0.1.[2] When sunlight hits the Earth some of it is filtered by the Earth's atmosphere and the resulting spectrum is no longer blackbody. At sea level with the sun directly overhead (solar zenith angle = 0°), a good approximation for equatorial regions, the spectrum is referred to as AM 1. However, at mid-lattitudes where sunlight is received at a tilt, the AM 1.5 spectrum is more appropriate to describe the average sunlight experienced by most regions of the world, including the United States, Europe, China, and Japan.[2] The AM 1.5 spectrum in Figure 0.1 corresponds to a solar zenith angle of 48.19°. It is defined as the solar spectrum with the Earth's surface facing the sun at an inclined plane of 37° tilt toward the equator. The total output irradiance is then reduced to 964 W/m^2.[2] Consequently, for standardized solar cell testing the solar industry uses AM 1.5 simulated sunlight at 1000 W/m^2, also referred to as 1 sun.

To effectively harness solar energy, photoactive materials should absorb a significant fraction of the solar spectrum. Figure 0.1 shows that the solar spectrum consists of 5% ultraviolet (UV), 43% visible, and 52% infrared (IR) light. Most of the light is concentrated in the visible region. Therefore, ideal materials for solar energy conversion would be visible light absorbing compounds that can convert photons to electricity or fuel.

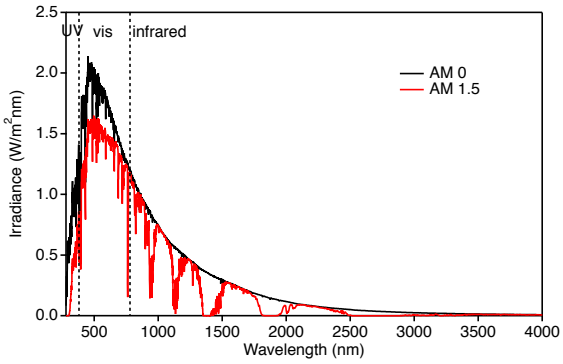

Figure 0.1. The Solar Spectrum
Spectral solar irradiance on Earth before passing through the atmosphere, AM 0 (black curve), and at sea level with a solar zenith angle of 48.19°, AM 1.5 (red curve). The data is obtained from NREL.[12]

Unlike other renewables, solar energy does not need to be implemented at an unreasonably large scale to supply all of the world's energy needs. In the United States, for a mediocre 10% efficient solar cell system, a square area of 400 km wide (<2% of the United States) is all that is required to power the entire country.[8] A fairly unpopulated area of this size already exists covering part of Kansas and very small parts of Texas, Oklahoma, and Colorado. Although solar energy is technologically feasible, cost remains a major disadvantage when competing with fossil fuels.[3,10] Combined with the diurnal cycle of the sun, widespread implementation of solar energy would require low cost conversion, distribution, and storage.

Solar Cells Today

Today, the solar cell market is dominated mainly by silicon photovoltaic (PV) devices.[2,10] The solar cell is based on a p-n junction type system where light is absorbed by positively and negatively doped Si, and photo-generated electron-hole (e-h) pairs are separated at the interface to generate electricity. The first Si PV was discovered in Bell Laboratories in 1954 with a 6% efficiency,[13] making it a promising device for solar

electricity. After almost 5 decades of research, today Si PVs are now ~10-20% efficient and still dominate the solar cell industry.[8]

The most efficient Si solar cells today are 27.6% efficient,[14] which actually approaches the maximum efficiency for a single band gap PV. The ideal PV device maximizes the electrical power generated with the power of the incident photon flux. In 1961, Shockley and Queisser reported that the maximum efficiency obtained from a single band gap PV cell is approximately 33%.[15] The losses considered were *i*) only energy greater than the band gap is absorbed and the rest is forfeited, *ii*) the excess energy of absorbed photons with energy larger than the band gap is lost as heat, and *iii*) only a fraction of the energy in the excited state can be converted into work. Hence, wide band gap materials that absorb only shorter wavelengths of light produce larger voltages but forego more of the solar spectrum, leading to lower photocurrent densities. Small band gap materials, on the other hand, can output larger current densities but at lower voltages. The maximum theoretical efficiency of a single band gap PV corresponds to a band gap of 1.3 eV or ~900 nm.[15] Silicon is very close to that value with a band gap of 1.1 eV, or 1100 nm, making it a good candidate for PVs.[2]

Sadly, the largest drawback of Si PVs is that they are relatively expensive. The price of electricity generated from commercial solar cells (10-20% efficiency) is 25-50 cents per kilowatt-hour (kWh), with the majority of these costs stemming from the raw materials, manufacturing, and installation of solar panels.[8,10] When fossil fuels cost ten times less at <5 cents per kWh, it is difficult for solar energy to compete.[3,8,10] The high cost of silicon arises from the intensive purification process needed to obtain high quality silicon from SiO_2. Single crystalline silicon has the highest cost, but also the highest efficiency approaching the Shockley-Queisser limit.[10] Lower quality polycrystalline silicon is less efficient, but is also less expensive, making it a promising alternative. Amorphous silicon is the least expensive, but low efficiency limits its use to handheld calculators.

Solar cells using other materials are emerging as low cost alternatives to silicon. PVs based on thin film semiconductors, such as CdTe and $Cu(In,Ga)Se_2$ (CIGS), are gaining attention with efficiencies of up to 20.3% reported.[14] These materials can be deposited onto a variety of materials, including flexible substrates.[16] This will decrease the cost associated with the installation of heavy rigid solar panels and allows for more possibilities in where PVs can be implemented.

PV devices convert solar energy to electricity, but electricity is difficult to store. When the sun sets, electricity is no longer generated from PVs at a time when it is needed most. Moreover, electricity makes up only ~10-20% of the world's total energy demand,[9] and current grid-based distribution technologies lead to substantial losses. The rest of the world's energy consumption is in the form of chemical fuels, which are used predominately for heat and transportation. Therefore, in order to meet the global energy demand with solar power, it is imperative to establish a dependable technology for the conversion of solar energy into fuel.

Solar Water Splitting

Nature long ago established a way to harness the abundant energy of sunlight through photosynthesis, a process where sunlight, water, and carbon dioxide is absorbed and converted into oxygen and reduced carbohydrates for food and fuel in plants and cyanobacteria.[1,2,17] For humans, however, borrowing this concept of storing solar energy in the form of chemical energy has been a long-standing challenge. One attractive

approach, solar water splitting, is a photosynthetic analog where sunlight is used to drive the thermodynamic uphill reaction of splitting water into oxygen and hydrogen energy (Equation 0.1).[1,2,6,18] The reverse reaction, combustion of H_2 (Equation 0.2) liberates the energy stored in hydrogen and leaves H_2O as the only byproduct, making the entire process clean, renewable and carbon-free.

$$H_2O(l) + h\nu \rightarrow H_2(g) + O_2(g) \qquad E° = -1.23V \qquad \text{(Equation 0.1)}$$

$$H_2(g) + O_2(g) \rightarrow H_2O(l) \qquad \Delta H° = -572.5\ \text{kJ/mol} \qquad \text{(Equation 0.2)}$$

The splitting of water requires 237.2 kJ/mol of free energy under standard room temperature conditions, or 1.23 eV to occur.[2,18,19] Hence, photons higher in energy than 1.23 eV or ~1000 nm are necessary for photolysis, which are easily provided by sunlight considering most of the photons in the solar spectrum are in this region (Figure 0.1). Since water does not absorb a significant fraction of solar photons, a light harvesting substrate is necessary for efficient decomposition of water using sunlight. Consequently, solar water splitting would involve *i*) light absorption by a photoconverter, *ii*) the conversion of light energy into electron-hole pairs, and *iii*) the use of these charges to drive the water oxidation and reduction half reactions (Equations 0.3 and 0.4, respectively).[1,2,18]

$$2H_2O(l) \rightarrow O_2(g) + 4H^+(aq) + 4e^- \qquad E_{red}° = 1.23V \text{ vs NHE} \qquad \text{(Equation 0.3)}$$

$$4H^+(aq) + 4e^- \rightarrow 2H_2(g) \qquad E_{red}° = 0V \text{ vs NHE} \qquad \text{(Equation 0.4)}$$

Theoretically one can drive water splitting with electricity from a PV device to a water electrolyzer. Commercial electrolyzers usually have efficiencies of about 85%.[1,2,8] Combined with a typical Si solar cell with efficiency of 15%, the maximum efficiency of a PV-electrolyzer system is ~10%.[1,8] The major disadvantage of this configuration is the high cost associated with the components and fabrication of such a system. Commercial electrolyzers also typically operate using nickel under hot alkaline conditions which makes them non-ideal for widespread use.[1,2] In contrast, a direct solar water splitting system, primarily consisting of a photocatalyst submerged in water would avoid high system costs, energy loss between the PV and electrolyzer, and the harsh operating conditions of a PV-electrolyzer system.

The feasibility of photocatalytic water splitting was first demonstrated in 1972 by Fujishima and Honda.[20] With UV light excitation the semiconductor TiO_2 was used to absorb photons, separate charges, and catalyze water oxidation to O_2, while electrons were directed to a Pt counter electrode for water reduction to H_2.[20] Since this seminal report, enormous effort has been made towards the development of photoactive materials for efficient solar water splitting.[1,5,7,19,21-25]

Solar Water Splitting Using Metal Oxide Semiconductors

Metal oxide nanostructures are among the most attractive candidates for solar water splitting because they envelop many of the properties for solar water splitting.[4,7,19,23,26-28] In general, they exhibit long term

stability under photolysis conditions, are inexpensive, easily processable, abundant, and environmentally benign. Many of them also have thermodynamically favorable band edge potentials for water splitting. In addition, nanostructuring can overcome the usually low carrier mobilities of metal oxide semiconductors.[5,6,26,28] The high surface area and porosity in nanostructures allow for an increased interface versus bulk materials where photogenerated carriers are produced and photo-electrolysis occurs. Also, their small grain sizes can be within the minority carrier diffusion lengths.

At present, very few materials actually split water both reliably and efficiently under solar irradiation. There have been many studies centered on nanostructured metal oxides, due to their morphology and excellent stability under oxidizing conditions.[6,7,19,27,28] $SrTiO_3$, $BaTiO_3$, and various perovskite structures have been extensively studied for overall water splitting without an external bias.[19,27,29,30] However, these are wide band gap materials that only absorb UV light. In recent years, there has been some progress in oxide materials that can split water under visible light excitation. A GaN/ZnO solid solution modified with a mixed oxide of rhodium and chromium nanoparticles gives an efficiency of 2.5% under visible light irradiation.[24,31] Also, Ni^{2+} doped $InTaO_4$ loaded with NiO gives a quantum yield of 0.66%.[32,33] Although these materials are inexpensive and robust, their efficiencies are too low for practical purposes. The development of new photoactive materials for photocatalysis is challenged by the need to find a single material that is both sufficiently active in the visible region of the solar spectrum, and has enough potential to both oxidize and reduce water.

Overcoming the Challenges of Solar Water Splitting

For practical solar water splitting, a material must be low cost, abundant, and stable under photolysis conditions.[6,7,26,34] In addition, for high efficiencies, the material must also absorb a significant portion of the solar spectrum, efficiently separate charges, and catalyze the water splitting half reactions.[2,3,6,7] One major hurdle of solar water splitting is the kinetically challenging water oxidation reaction (Equation 0.3).[2,3,30] Two water molecules are required to produce one molecule of O_2 coupled to the release of four electrons and four protons from water. Often high overpotentials are needed for sufficient reaction rates. Although a semiconductor may possess enough energy to overcome the thermodynamic potential for water oxidation, the reaction may not proceed efficiently without a large driving force. Consequently, few materials can split water with little or no applied bias. Semiconductor photoanodes that do so are generally wide band gap materials that only absorb UV light, such as $SrTiO_3$ and TiO_2.[2,6,19,23,27,29] Small band gap semiconductor materials, such as CdS and GaInP, are typically unstable because photogenerated holes prefer to oxidize the semiconductor rather than the surrounding water molecules.[6,22,30] A few stable visible light absorbing materials, such as Fe_2O_3 and WO_3, can oxidize water but do not have sufficient energy to undergo water reduction.[5-7,25] Furthermore, large external applied voltages are necessary for water oxidation to proceed appreciably in these materials.

To date, no single material has been able to simultaneously meet all of the requirements for solar water splitting. Almost four decades since the Fujishima-Honda effect,[20] finding one material that can absorb visible photons, separate charges, and catalyze the uphill reactions of water oxidation and reduction seems highly unlikely. Drawing on Nature's photosynthesis, a division-of-labor approach seems imperative. In photosynthesis, water splitting occurs through a Z-scheme-like mechanism where water is oxidized into oxygen and the resulting electrons are used in the reduction of $NADP^+$ (nicotinamide adenine dinucleotide phosphate)

to NADPH.[2,17,35,36] Water oxidation and reduction are performed by separate protein components, denoted photosystem II and I (PS-II and PS-I), respectively. In PS-II, the P_{680} chromophore absorbs photons, which triggers a series of electron transfer steps that funnel out reducing equivalents, and water oxidation is performed at the embedded Mn-based water oxidizing complex.[2,17,35-37] The electrons are shuttled to PSI, where additional photons help them reduce $NADP^+$ to NADPH, which is ultimately is used for carbon fixation. Not only is water oxidation separate from $NADP^+$ reduction, but the tasks of photon absorption, charge separation, and water oxidation catalysis are also separated in a chromophore-catalyst arrangement.

Similarly, a division-of-labor approach can be implemented in an artificial photosynthetic system. Tandem solar cell configurations, where water oxidation and reduction are performed by separate photoactive materials, have been envisioned to overcome the limitation of one single material.[4,5,22,30,38] Each material can absorb complementary parts of the solar spectrum and be separately optimized for water oxidation and reduction. Since water oxidation is the more challenging of the two water splitting half reactions, this thesis will focus on developing materials for the water oxidation half of a tandem cell. Materials for water oxidation will be studied independently in a PEC cell. Low water splitting efficiencies often result from using a single photoanode material that poorly balances all of the criteria for PEC water oxidation. In a heterogeneous catalyst/semiconductor photoanode, however, photon absorption, charge separation, and water oxidation catalysis can be performed separately in a division-of-labor approach.[39] This approach also allows each component to be optimized individually, ultimately resulting in a more efficient water splitting configuration.

Catalyst/Semiconductor Photoanodes

For a practical and efficient PEC water oxidation system, catalyst-semiconductor photoanodes composed of low cost, Earth-abundant materials are attractive. For light harvesting, oxide semiconductors that absorb visible light, such as Fe_2O_3, WO_3, and $BiVO_4$ are preferred.[2,6,7] Although such materials often do not exhibit the appropriate conduction band potentials for water reduction, in a tandem PEC/PV cell the additional bias for water reduction can be provided by the second electrode.

α-Fe_2O_3, with an indirect bandgap of 2.1 eV, has been extensively studied as a photoanode for PEC water oxidation due to its low cost, robustness, visible light absorption, and ease of preparation.[40-49] Until recently, photocurrent efficiencies for α-Fe_2O_3 have been low due to its short hole-diffusion length (~2-4 nm),[50] low electron mobility (~10^{-1} cm^2 V^{-1} s^{-1}),[44,51] and efficient charge carrier recombination characteristics of bulk α-Fe_2O_3.[48,52] With controlled growth and doping of α-Fe_2O_3, nanostructures of iron oxide have been shown to reach photocurrents up to several mA/cm^2.[41,53-55] Unfortunately, α-Fe_2O_3 is still a poor catalyst and requires a large external bias for PEC water oxidation. Consequently, in tandem PEC/PV configurations, two PV cells, each providing >1 V, are required to generate enough bias for overall water splitting.[38] These factors make α-Fe_2O_3 an excellent prototypical candidate for integration with a proficient water oxidation catalyst.

The application of catalysts onto semiconductor surfaces in order to enhance their water splitting efficiency is a well-known practice. Typically, Pt, NiO, or RuO_2 co-catalysts are deposited onto oxide semiconductor powders and an increase in oxygen evolution is observed.[25,27,56] It has been hypothesized that these catalysts may inhibit surface recombination or certain back reactions at the semiconductor surface.[7,27] However, there are few studies devoted to the integration of water oxidation catalysts onto semiconductor

photoanodes and their effects on the photoelectrochemistry. A comprehensive review[39] on heterogeneous catalyst/semiconductor photoanodes, including work on α-Fe_2O_3, is given in Chapter 2.

For practical purposes, an inexpensive, earth-abundant water oxidation catalyst that can be easily applied onto photoanode surfaces is of interest. Recently, Nocera and coworkers have discovered a family of cobalt-containing catalysts that can oxidize water electrochemically at relatively low overpotentials under neutral pH conditions.[57-59] Of particular interest is an amorphous cobalt-phosphate (Co-Pi) water oxidation electrocatalyst composed of Co:K:P in a 2:1:1 ratio.[57] From EXAFS studies, it is believed that the active site is a cobalt oxo-cubane cluster resembling that of the Mn oxygen evolving complex in PS-II.[60,61] Water oxidation is proposed to occur through a Co-Pi self-healing mechanism involving multiple cobalt oxidation states.[58,62,63] Co-Pi is easily synthesized by electrodeposition from a solution of Co^{2+} in a potassium phosphate (KPi) buffer,[57,59] making it compatible for application onto conductive photoanode surfaces. Additional details on Co-Pi are given in Chapters 2 and 7.

This thesis will focus on the integration of oxide semiconductors with cobalt-containing water oxidation catalysts, with emphasis on improving PEC performance and optimization. A majority of the studies will be on Co-Pi/α-Fe_2O_3 composite photoanodes, presented in Chapters 3-5. Chapter 6 will focus on the effects of Co-Pi on $BiVO_4$, a 2.4-2.5 eV band gap semiconductor that possesses significantly lower onset potentials than α-Fe_2O_3 and has been of recent interest for solar water oxidation.[64-70] Finally, Chapter 7 will address the possible role of Co-Pi in the PEC enhancement of α-Fe_2O_3 and other metal oxide materials within the catalyst/ semiconductor assembly.

Notes to the Introduction

1. Bard, A. J.; Fox, M. A., *Acc. Chem. Res.* **1995,** *28*, 141-145.
2. Grimes, C. A.; Varghese, O. K.; Ranjan, S., *Light, Water, Hydrogen*. Springer: New York, 2007.
3. Lewis, N. S.; Nocera, D. G., *Proc. Nat. Acad. Sci.* **2006,** *103*, 15729-15735.
4. Alexander, B. D.; Kulesza, P. J.; Rutkowska, I.; Solarska, R.; Augustynski, J., *J. Mater. Chem.* **2008,** *18*, 2298-2303.
5. Grätzel, M., *Nature* **2001,** *414*, 338-344.
6. Navarro Yerga, R. M.; Álvarez Galván, M. C.; del Valle, F.; Villoria de la Mano, J. A.; Fierro, J. L. G., *ChemSusChem* **2007,** *2*, 471-485.
7. Kudo, A.; Miseki, Y., *Chem. Soc. Rev.* **2009,** *38*, 253-278.
8. Lewis, N. S., *MRS Bulletin* **2007,** *32*, 808-820.
9. Internation Energy Outlook 2010. U. S. Department of Energy: Energy Information Administration: Washington, DC, 2010; Vol. DOE/EIA-0484.
10. Lewis, N. S., *Science* **2007,** *315*, 798-801.
11. Hoffert, M. I.; Caldeira, K.; Benford, G.; Criswell, D. R.; Green, C.; Herzog, H.; Jain, A. K.; Kheshgi, H. S.; Lackner, K. S.; Lewis, J. S.; Lightfoot, H. D.; Manheimer, W.; Mankins, J. C.; Mauel, M. E.; Perkins, L. J.; Schlesinger, M. E.; Volk, T.; Wigley, T. M. L., *Science* **2002,** *298*, 981-987.
12. Solar Spectra. http://rredc.nrel.gov/solar/spectra/ (accessed 10/16/11).
13. Chapin, D. M.; Fuller, C. S.; Pearson, G. L., *J. Appl. Phys.* **1954,** *26*, 676-677.

14. Kazmerski, L. Best Research Cell Efficiencies. http://www.nrel.gov/ncpv/images/efficiency_chart.jpg (accessed 10/26/2011).
15. Shockley, W.; Queisser, H. J., *J. Appl. Phys.* **1961,** *32*, 510-519.
16. Chirilă, A.; Buecheler, S.; Pianezzi, F.; Bloesch, P.; Christina Gretener, C.; Uhl, A. R.; Fella, C.; Kranz, L.; Perrenoud, J.; Seyrling, S.; Verma, R.; Nishiwaki, S.; Romanyuk, Y. E.; Bilger, G.; Tiwari, A. N., *Nat. Mater.* **2011,** *10*, 857-861.
17. McEvoy, J. P.; Brudvig, G. W., *Chem. Rev.* **2006,** *106*, 4455-4483.
18. Kato, H.; Kudo, A., *J. Phys. Chem. B.* **2001,** *105*, 4285-4292.
19. Rajeshwar, K., *J. Appl. Electrochem.* **2007,** *37*, 765-787.
20. Fujishima, A.; Honda, K., *Nature* **1972,** *238*, 37-8.
21. Nozik, A. J., *Annu. Rev. Phys. Chem.* **1978,** *29*, 189-222.
22. Khaselev, O.; Turner, J. A., *Science* **1998,** *280*, 425-427.
23. Aroutiounian, V. M.; Arakelyan, V. M.; Shahnazaryan, G. E., *Sol. Energy* **2005,** *78*, 581-592.
24. Maeda, K.; Domen, K., *J. Phys. Chem. C* **2007,** *111*, 7851-7861.
25. Hoffmann, M. R.; Martin, S. T.; Choi, W.; Bahnemann, D. W., *Chem. Rev.* **1995,** *95*, 69-96.
26. Woodhouse, M.; Parkinson, B. A., *Chem. Mater.* **2008,** *20*, 2495-2502.
27. Osterloh, F. E., *Chem. Mater.* **2008,** *20*, 35-54.
28. van de Krol, R.; Liang, Y.; Schoonman, J., *J. Mater. Chem.* **2008,** *18*, 2311-2320.
29. Kato, H.; Kudo, A., *J. Phys. Chem. B* **2002,** *106*, 5029-5034.
30. Walter, M. G.; Warren, E. L.; McKone, J. R.; Boettcher, S. W.; Mi, Q.; Santori, E. A.; Lewis, N. S., *Chem. Rev.* **2010,** *110*, 6446-6473.
31. Maeda, K.; Teramura, K.; Takata, T.; Hara, M.; Saito, N.; Toda, K.; Inoue, Y.; Kobayashi, H.; Domen, K., *J. Phys. Chem. B* **2005,** *109*, 20504-20510.
32. Zou, Z.; Arakawa, H., *J. Photochem. Photobiol., A* **2003,** *158*, 145-162.
33. Zou, Z.; Ye, J.; Sayama, K.; Arakawa, H., *Nature* **2001,** *414*, 625-627.
34. Gray, H. B., *Nat. Chem.* **2009,** *1*, 7-7.
35. Rupprecht, J.; Hankamer, B.; Mussgnug, J. H.; Ananyev, G.; Dismukes, G. C.; Kruse, O., *Appl. Microbiol. Biotechnol.* **2006,** *72*, 422-449.
36. McEvoy, J. P.; Gascon, J. A.; Batista, V. S.; Brudvig, G. W., *Photochem. Photobiol. Sci.* **2005,** *4*, 940-949.
37. Yano, J.; Kern, J.; Sauer, K.; Latimer, M. J.; Pushkar, Y.; Biesiadka, J.; Loll, B.; Saenger, W.; Messinger, J.; Zouni, A.; Yachandra, V. K., *Science* **2006,** *314*, 821-825.
38. Brillet, J.; Cornuz, M.; Le Formal, F.; Yum, J.-H.; Grätzel, M.; Sivula, K., *J. Mater. Res.* **2010,** *25*, 17-24.
39. Sun, J.; Zhong, D. K.; Gamelin, D. R., *Energy Environ. Sci.* **2010,** *3*, 1252-1261.
40. Bjoerksten, U.; Moser, J.; Grätzel, M., *Chem. Mater.* **1994,** *6*, 858-863.
41. Cesar, I.; Kay, A.; Gonzalez Martinez, J. A.; Grätzel, M., *J. Am. Chem. Soc.* **2006,** *128*, 4582-4583.
42. Duret, A.; Grätzel, M., *J. Phys. Chem. B* **2005,** *109*, 17184-17191.
43. Jorand Sartoretti, C.; Ulmann, M.; Alexander, B. D.; Augustynski, J.; Weidenkaff, A., *Chem. Phys. Lett.* **2003,** *376*, 194-200.
44. Kennedy, J. H.; Frese, K. W., Jr., *J. Electrochem. Soc.* **1978,** *125*, 709-14.

45. LaTempa, T. J.; Feng, X.; Paulose, M.; Grimes, C. A., *J. Phys. Chem. C* **2009,** *113*, 16293-16298.
46. Lindgren, T.; Wang, H.; Beermann, N.; Vayssieres, L.; Hagfeldt, A.; Lindquist, S.-E., *Sol. Energy Mater.* **2002,** *71*, 231-243.
47. Majumder, S. A.; Khan, S. U. M., *Int. J. Hydrogen Energy* **1994,** *19*, 881-887.
48. Sivula, K.; Le Formal, F.; Grätzel, M., *ChemSusChem* **2011,** *4*, 432-449.
49. Ingler, W. B., Jr.; Khan, S. U. M., *Electrochem. Solid-State Lett.* **2006,** *9*, G144-G146.
50. Gardner, R. F. G.; Sweett, F.; Tanner, D. W., *J. Phys. Chem. Solids* **1963,** *24*, 1183-1186.
51. Dare-Edwards, M. P.; Goodenough, J. B.; Hamnett, A.; Trevellick, P. R., *J. Chem. Soc., Faraday Trans.* **1983,** *79*, 2027-2041.
52. Dotan, H.; Sivula, K.; Grätzel, M.; Rothschild, A.; Warren, S., *Energy Environ. Sci.* **2011,** *4*, 958-964.
53. Cesar, I.; Sivula, K.; Kay, A.; Zboril, R.; Grätzel, M., *J. Phys. Chem. C* **2009,** *113*, 772-782.
54. Kay, A.; Cesar, I.; Grätzel, M., *J. Am. Chem. Soc.* **2006,** *128*, 15714-15721.
55. Tilley, S. D.; Cornuz, M.; Sivula, K.; Grätzel, M., *Angew. Chem. Int. Ed.* **2010,** *49*, 6405-6408.
56. Inoue, Y., *Energy Environ. Sci.* **2009,** *2*, 364-386.
57. Kanan, M. W.; Nocera, D. G., *Science* **2008,** *321*, 1072-1075.
58. Kanan, M. W.; Surendranath, Y.; Nocera, D. G., *Chem. Soc. Rev.* **2009,** *38*, 109-114.
59. Surendranath, Y.; Dincă, M.; Nocera, D. G., *J. Am. Chem. Soc.* **2009,** *131*, 2615-2620.
60. Kanan, M. W.; Yano, J.; Surendranath, Y.; Dincă, M.; Yachandra, V. K.; Nocera, D. G., *J. Am. Chem. Soc.* **2010,** *132*, 13692-13701.
61. Risch, M.; Khare, V.; Zaharieva, I.; Gerencser, L.; Chernev, P.; Dau, H., *J. Am. Chem. Soc.* **2009,** *131*, 6936-6937.
62. Lutterman, D. A.; Surendranath, Y.; Nocera, D. G., *J. Am. Chem. Soc.* **2009,** *131*, 3838-3839.
63. Surendranath, Y.; Kanan, M. W.; Nocera, D. G., *J. Am. Chem. Soc.* **2010,** *132*, 16501-16509.
64. Sayama, K.; Nomura, A.; Arai, T.; Sugita, T.; Abe, R.; Yanagida, S.; Oi, T.; Iwasaki, Y.; Abe, Y.; Sugihara, H., *J. Phys. Chem. B* **2006,** *110*, 11352-11360.
65. Sayama, K.; Wang, N.; Miseki, Y.; Kusama, H.; Onozawa-Komatsuzaki, N.; Sugihara, H., *Chem. Lett.* **2010,** *39*, 17-19.
66. Ye, H.; Lee, J.; Jang, J. S.; Bard, A. J., *J. Phys. Chem.* **2010,** *114*, 13322-13328.
67. Berglund, S. P.; Flaherty, D. W.; Hahn, N. T.; Bard, A. J.; Mullins, C. B., *J. Phys. Chem. C* **2011,** *115*, 3794-3802.
68. Yin, W.-J.; Wei, S.-H.; Al-Jassim, M. M.; Turner, J.; Yan, Y., *Phys. Rev. B* **2011,** *83*, 155102.
69. Ng, Y. H.; Iwase, A.; Kudo, A.; Amal, R., *J. Phys. Chem. Lett.* **2010,** *1*, 2607-2612.
70. Hong, S. J.; Lee, S.; Jang, J. S.; Lee, J. S., *Energy Environ. Sci.* **2011,** *4*, 1781-1787.

Chapter 1: The Photoelectrochemical Cell

1.1 Solar Water Splitting with Semiconductors

Semiconductors are ideal photoconverters for solar water splitting because many absorb visible light leading to electron-hole (e-h) pairs that can serve as charges for water oxidation and reduction.[1,2] The basic principles of solar water splitting by a semiconductor material are outlined in Figure 1.1. When photons of energy greater than the semiconductor band gap irradiate the semiconductor, electrons in the valence band are excited to the conduction band, leaving a hole behind. A fraction of the e-h pairs will separate and migrate out to react at the surface, the rest will ultimately recombine. The holes (h^+) at the valence band edge, if they possess enough driving force, can then oxidize water to form oxygen gas. Similarly, electrons (e^-) at the conduction band minimum can reduce water to hydrogen gas.[2-6]

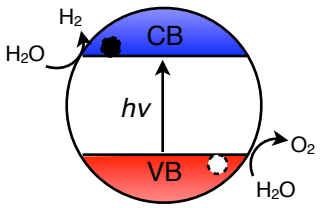

Figure 1.1. Basic Principles of Solar Water Splitting

To drive overall water splitting using sunlight, the material must simultaneously satisfy the following criteria: *i*) Be stable under operating conditions of photo-electrolysis, *ii*) absorb a significant portion of the solar spectrum, mainly visible light, *iii*) possess a conduction-band edge potential more negative than the reduction potential of H^+/H_2 (Equation 0.4), and *iv*) possess a valence-band edge potential more positive than the reduction potential of O_2/H_2O (Equation 0.3).[2-5,7] For practical solar water splitting, the material should also be inexpensive, and comprise of Earth-abundant elements. In addition to these minimum requirements, the semiconductor should also possess good charge separation efficiency, high mobility, comparatively long electron and hole lifetimes relative to the reaction kinetics, and good surface catalysis for the water reduction and oxidation half reactions.[2,3,8]

Figure 1.2 shows the band gap energies and band edge positions of common semiconductor materials that have been explored for solar water splitting, along with the standard reduction potentials for water reduction and oxidation vs NHE at pH 0.[3,5,9] In general, small band gap materials that absorb plenty of light, such as CdS, CdSe, GaP, and Si, are unstable under water oxidation conditions because valence band holes preferably oxidize the semiconductor itself rather than water.[2,3] Moreover, some do not have band edge potentials that straddle water oxidation and reduction potentials. On the other hand, materials that are stable under photolysis conditions are generally metal oxide semiconductors which usually have wide band gaps, such as SnO_2, $SrTiO_3$, and TiO_2.[2,7,10,11] These semiconductors only absorb UV light which encompasses only 5% of the solar spectrum. There are however, some oxide materials that have smaller band gaps in the visible region, such as WO_3, Fe_2O_3, and $BiVO_4$, but their conduction band potentials do not have sufficient energy to reduce water to hydrogen.[3,5,8,9] Band gap engineering by cation or anion doping has been extensively explored as a

strategy to increase visible light absorption via new energy levels, however, the result is often little or no increase in overall photocatalytic activity due to new recombination loss channels from impurity centers.[3]

Metal oxide semiconductors are the most well studied photoanodes for solar water oxidation due to their long-term stability under photo-oxidation conditions.[2,5,7,8,10-13] They also embody many of the requirements for solar water oxidation, they are inexpensive, abundant, and have a valence band maximum more positive than the thermodynamic potential for water oxidation.[2,10,13,14] Unlike non-oxide materials, many metal oxide semiconductors exhibit Nernstian behavior.[2,8,14] The conduction and valence band edge potentials shift -59 mV/pH in the same direction as the water oxidation and reduction potentials, due to the interaction of H^+ or OH^- ions at the semiconductor surface.[2,14] As a result, the thermodynamic overpotentials for water splitting are pH independent, allowing for versatile operating conditions.

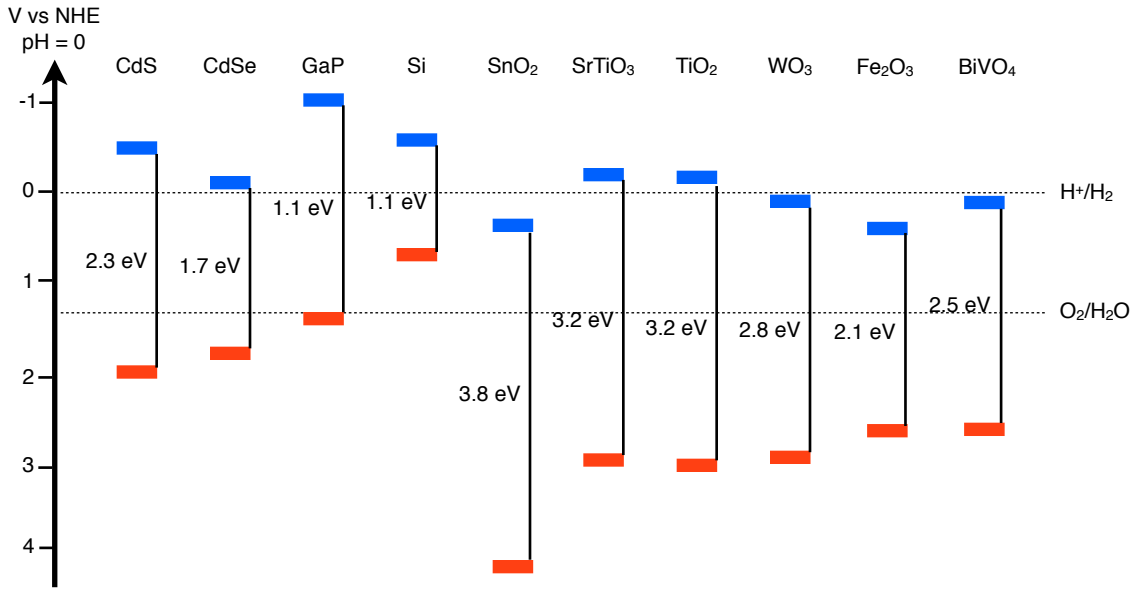

Figure 1.2. Diagram of Semiconductor Band Edge Potentials
Band gap energies along with the conduction (blue) and valence (red) band edge potentials of common semiconductors. The standard reduction potentials of water reduction to H_2 and and oxidation to O_2 vs. NHE at pH 0 are shown with a dotted line.

A functional setup for solar water splitting can be as simple as irradiating semiconductor particles suspended in water and collecting the evolved hydrogen and oxygen gases.[5,7,10] Indeed, this configuration is often used to characterize the water splitting activity of many semiconductor photocatalysts, especially those that are mainly synthesized as powders.[5-7,10] To separately probe the water reduction or oxidation half reactions, a sacrificial donor or acceptor is usually employed in an aqueous electrolyte. A number of metal oxide materials, including many perovskite or layered structures and oxynitrides,[5,7,10] are commonly evaluated for water splitting in this way. One major drawback of using semiconductor powders is that they are difficult to compare across research labs. Differences in illumination, particle size, and concentration make it a challenge to standardize measurements. It is also difficult to characterize the materials by optical spectroscopy and photoelectrochemistry, which can provide valuable information on the band gap energy, band edge positions, current-voltage behavior, and reaction kinetics of the semiconductor.

A photoelectrochemical (PEC) cell allows for additional flexibility in the study of photoelectrodes. In a three-electrode PEC configuration, the water oxidation and reduction half reactions can be individually examined and optimized. Instead of measuring the evolved gases from water splitting, which is relatively difficult and time consuming especially at low reaction rates, water splitting can be measured by counting the electrons associated with oxidation or reduction. In a PEC cell, shown in Figure 1.3, semiconductor thin films coated on a conductive substrate are typically used. Current is measured between the semiconductor working electrode (WE) and the counter electrode (CE) with an applied potential in reference to a stable reference electrode (RE). The current and voltage of a PEC cell is controlled by a potentiostat. If an n-type photoanode is used as the WE and an anodic bias is applied, then water oxidation occurs at the WE and electrons flow from the WE to the CE, where they reduce water to H_2. Hence, the amount of water oxidation can be quantified by measuring current flow, assuming water oxidation to O_2 is the only reaction occurring at the anode. Caution must be taken to ensure that no side reactions occur by avoiding other reductants species in the electrolyte, such as halides, alcohols, and peroxides. For stable operation, the CE is usually Pt and the RE is an electrode of known potential, such as Ag/AgCl, that does not affect or is affected by the photochemical reactions in the cell. The actual PEC cell used in these studies is shown in Figure 1.3b. In this setup, water oxidation is easily quantified in terms of current density, along with the current-voltage characteristics of the semiconductor.

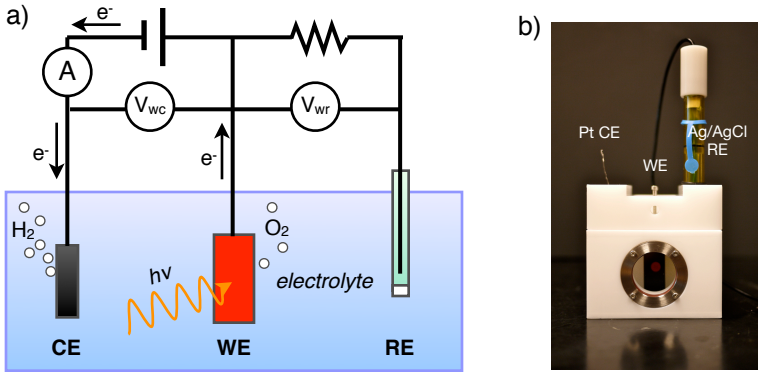

Figure 1.3. The Photoelectrochemical Cell
a) Schematic representation of a conventional three-electrode PEC cell showing a working electrode (WE), counter electrode (CE), and reference electrode (RE). For an n-type photoanodes as the WE, and a metal cathode as the CE, with an anodic bias oxygen evolution occurs at the WE and hydrogen evolution occurs at the CE. **b**) The home-built PEC cell used to characterize the semiconductor photoanodes in this study.

1.2 Semiconductor Photoelectrochemistry

To understand semiconductor photoelectrochemistry, one should first understand what occurs at the semiconductor-electrolyte interface. An idealized semiconductor-electrolyte interface is best described as a Schottky barrier, or a junction between a semiconductor and a metal.[2,14-17] Figure 1.4 presents the energy levels of an n-type semiconductor/electrolyte interface before equilibrium, after equilibrium, and under illumination. For the n-type semiconductor, its conduction band minimum (E_{CB}), valence band maximum (E_{VB}), and Fermi energy level (E_F) are shown. The Fermi level is defined as the energy where the probability of the electron population is exactly one-half. It can be calculated from Equation 1.1, where E_{VB} and E_{CB} are, respectively, the

valence and conduction band edge energies, k is the Boltzmann constant, T is the temperature, and N^*_{VB} and N^*_{CB} are the effective density of states function in valence and conduction bands, respectively.

$$E_F = \frac{1}{2}\left(E_{VB} + E_{CB}\right) + \frac{1}{2}\left(kT \ln \frac{N^*_{VB}}{N^*_{CB}}\right) \qquad \text{(Equation 1.1)}$$

For an n-type semiconductor, where electrons are the majority charge carriers, the Fermi energy lies just below the conduction band edge due to increased donor density. Hence, before equilibrium, in Figure 1.4a, the Fermi energy of the semiconductor, E_F, lies above the Fermi energy of the redox couple, $E_{F,\,redox}$. When the semiconductor comes into contact with the liquid electrolyte, their electrochemical potentials equilibrate resulting in a flow of negative charges from the semiconductor to the liquid as E_F of the semiconductor decreases.[2,14-17] The semiconductor then becomes positively charged at the surface and a space charge region or depletion region, W, is generated, where the net charge is non-neutral. Analogously, a thin Helmholtz layer exists at the electrolyte side. This region is generated by adsorption of ions on the semiconductor surface, orientation of dipoles, or formation of surface bonds between the semiconductor and electrolyte.[2,15] As a result, an upwards band-bending, ϕ_{sc}, of the semiconductor occurs, as depicted in Figure 1.4b. For p-type materials, E_F is below $E_{F,\,redox}$ and a downwards band-bending occurs.

N-type semiconductors function as photoanodes because their upwards band-bending provides a driving force for e-h separation. Under light excitation, photo-generated electrons are generally swept away from the semiconductor/liquid junction, and photo-generated holes rise to the surface of the semiconductor where they drive uphill oxidation reactions.[2,14,15] Figure 1.4c depicts the energy levels of the semiconductor-electrolyte contact under illumination. With photo-generated e-h pairs, electron and hole populations cause the Fermi level to split into electron and hole quasi-Fermi levels, $E_{F,\,n}$ and $E_{F,\,p}$, respectively.[2,14,15]

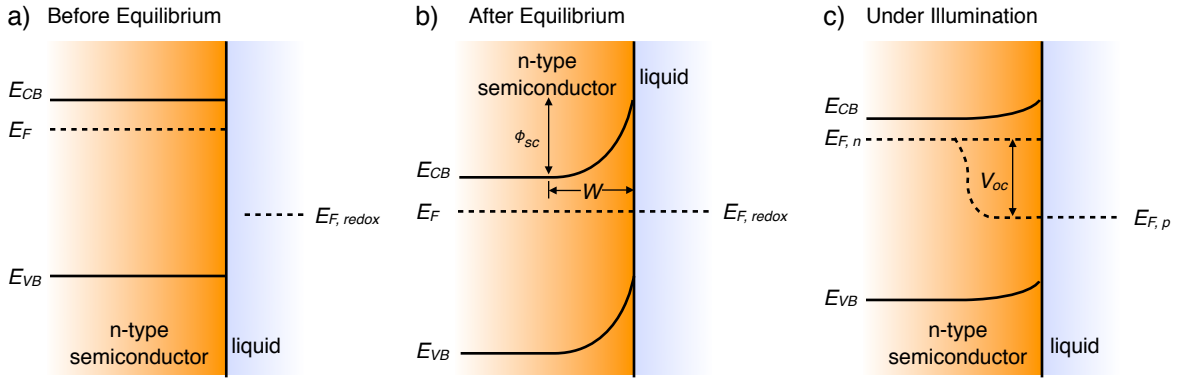

Figure 1.4. Energy Diagram of the Semiconductor-Electrolyte Interface
Energy levels of an n-type semiconductor-electrolyte junction **a)** before equilibrium, **b)** after equilibrium of the Fermi levels showing band-bending, ϕ_{sc}, in the space charge region, W, at the semiconductor surface, and **c)** under illumination where the resulting electron and hole populations give quasi-Fermi levels of the electron, $E_{F,n}$, and hole, $E_{F,p}$, respectively.

Using an applied bias, the energy levels, and hence band-bending, of the semiconductor can be altered. This changes the driving force towards water oxidation reactions for n-type materials and allows us to analyze

the water oxidation efficiency and band potentials of a semiconductor through current-voltage measurements. Typical PEC measurements for semiconductor water splitting include Mott-Schottky analysis, current density-voltage (*J-V*) curves, and wavelength dependent incident photon-to-current conversion efficiency (IPCE) measurements, all of which are described in detail below.

1.3 PEC Measurements

Conduction and valence band edge positions of a semiconductor, such as the ones shown in Figure 1.2, can be determined from the degree of band bending at the semiconductor-electrolyte interface as an external bias is applied. Band bending increases with applied bias and the relationship between the depletion layer width, W, and the potential applied, V_{app}, is given by Equation 1.2 where ε_0 is the permittivity of free space, ε_r is the dielectric constant of the semiconductor, V_{FB} is the flatband potential also known as E_F, and N_d is the donor density for an n-type material.[2,15]

$$W = \left(\frac{2\varepsilon_0 \varepsilon_r \left(V_{app} - V_F \right)}{eN_d} \right)^{1/2} \qquad \text{(Equation 1.2)}$$

As discussed above, when an n-type semiconductor comes into contact with an electrolyte, their electrochemical potentials equilibrate and negative charges flow from the semiconductor to the electrolyte. The charge distribution of this semiconductor-electrolyte contact is represented in Figure 1.5. In the space charge region, positive charges reside near the semiconductor surface and negative charges accumulate as the distance increases away from the surface due to coulombic interactions.[2,14,15] Hence, the area within W can be approximated as a parallel plate capacitor, with capacitance C_{sc}. Likewise, the Helmholtz layer also exhibits a capacitance, C_H, although it does not change significantly with applied potential in very conductive electrolytes. The diffuse Gouy layer, an outer diffuse layer in the electrolyte, is neglected due to its small potential drop. In consequence, the depletion layer capacitance, C_{sc}, can then be described by Equation 1.3,[2,15] where e is the elementary charge, ε is the dielectric constant of the material, ε_0 is the permittivity of free space, N_D is the donor density, V_{app} is the PEC applied potential, V_{FB} is the flatband potential (E_F), k is the Boltzmann distribution, and T is the temperature. Equation 1.3 is known as the Mott-Schottky equation and a Mott-Schottky plot graphs the relationship of $1/C_{sc}^2$ vs V_{app}.

$$\frac{1}{C_{sc}^2} = \left(\frac{2}{e\varepsilon\varepsilon_0 N_D} \right) \left(\left(V_{app} - V_{FB} \right) - \frac{kT}{e} \right) \qquad \text{(Equation 1.3)}$$

As with a parallel plate capacitor, as W decreases, C_{sc} increases such that when $W = 0$ at the flatband potential, C_{sc} approaches infinity and $1/C_{sc}^2 = 0$.[2,15,17,18] Hence, the flat band potential can be obtained from the x-intercept of a Mott-Schottky plot and the slope can be used to obtain N_D. If N_D is large, the flat band potential is approximately equal to the conduction band minimum and the valence band position can be determined from

the band gap of the semiconductor. These differential capacitance PEC measurements require a potentiostat equipped with an impedance analyzer, and can be used to determine the band potentials and donor density of a semiconductor.

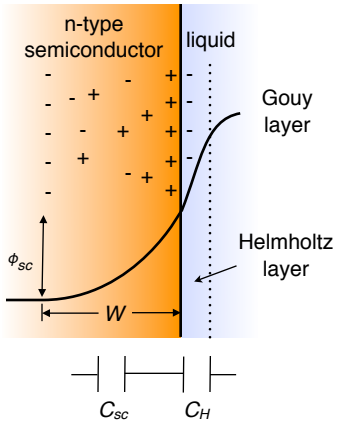

Figure 1.5. Charge Distribution and Capacitance of the Semiconductor-Electrolyte Contact
Schematic of the semiconductor-electrolyte contact showing the charge distribution and capacitance of the space charge region, C_{SC}, and of the Helmholtz layer, C_H. The band-bending, ϕ_{sc}, in the space charge region, W, is also shown.

To address water splitting with a semiconductor photoanode, one of the most routine PEC measurements is the current density-voltage (*J-V*) curve. The fundamental basis of a *J-V* curve can be explained in Figure 1.6, which depicts the band energetics of an n-type semiconductor under conditions of reverse (anodic) bias, flatband position, and forward (cathodic) bias. In a PEC cell, the applied potential, V_{app}, is equal to the flatband potential ($V_{FB} = E_F$) together with the band-bending potential (ϕ_{sc}), such that $V_{app} = V_{FB} + \phi_{sc}$.[2,15] Under reverse bias, where $V_{app} > V_{FB}$, the depletion layer width, W, increases and anodic current flows (panel a). As V_{app} increases, the greater the driving force for surface reactions and the larger the current density becomes. Conversely, as V_{app} becomes more negative, W decreases until the band potentials become flat (panel b), followed by an accumulation region where downwards band bending occurs and cathodic current flows (panel c).[2,15]

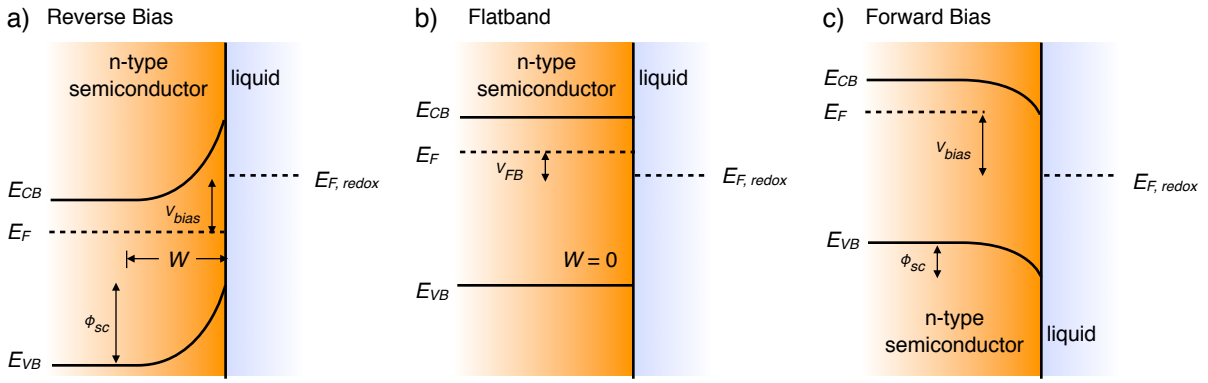

Figure 1.6. Band Energetics of an n-type Semiconductor Under an Applied Bias
Band energy levels of an n-type semiconductor-electrolyte junction under **a)** reverse bias, **b)** flatband potential, and **c)** forward bias, where V_{bias} is the difference between E_F and $E_{F, redox}$, V_{app}, is equal to the flatband potential ($V_{FB} = E_F$) together with the band-bending potential (ϕ_{sc}), such that $V_{app} = V_{FB} + \phi_{sc}$.

The current-potential relationship of a semiconductor photoanode is described by the Gärtner model[19] in Equation 1.4, where J_{PEC} is the measured photocurrent density, I_0 is the incident photon current density, α is the absorption coefficient of the material, W is the depletion layer width, and L_p is the diffusion length of minority carriers. The Gärtner model represents an idealized flat semiconductor/electrolyte Schottky junction, shown in Figure 1.5. Upon photoexcitation of the photoanode, the generation of e-h pairs is dependent on α, the absorption coefficient of the semiconductor. The charge separation efficiency is then based on the bulk properties of the material, where minority carriers in the bulk that are within the diffusion length, L_p, of the depletion width will move to the depletion layer.[19] In the depletion layer, it is approximated that no recombination occurs due to the driving force from band-bending. In the absence of surface recombination, all charges are collected and measured as photocurrent density J_{PEC}.

$$J_{PEC} = I_0\left(1 - \frac{e^{-\alpha W}}{1+\alpha L_p}\right) \qquad \text{(Equation 1.4)}$$

Equation 1.4 holds fairly well for planar semiconductor electrodes at large applied potentials where the depletion layer model is valid. At low applied potentials, band bending is small and the approximation that there is no e-h recombination within the depletion region fails. Surface recombination also becomes competitive at low applied biases where the overpotential is not sufficient for high water oxidation rates.

Typical *J-V* curves of a photoanode under dark and illumination conditions are shown in Figure 1.7. In the dark, almost no current flows below the thermodynamic potential for water oxidation, 1.23 V, although, due to the large overpotential usually required for water oxidation, dark current is negligible until closer to ~1.8 V.[2] Under light irradiation, photocurrent is produced as a result of the photovoltage generated. The potential where the current density crosses zero is defined as the open circuit voltage, V_{oc}. V_{oc} has been used as a rough estimate of the flatband potentials of semiconductors in the absence of Mott-Schottky data, and is a good approximation in the cases where band bending is minor.[2,20] The difference between the open circuit voltage and the potential

where electrolysis occurs, 1.23 V, is the open circuit photopotential, ΔV_{oc}. If ΔV_{oc} > 1.23 V, then water oxidation will proceed without the need for an external bias.

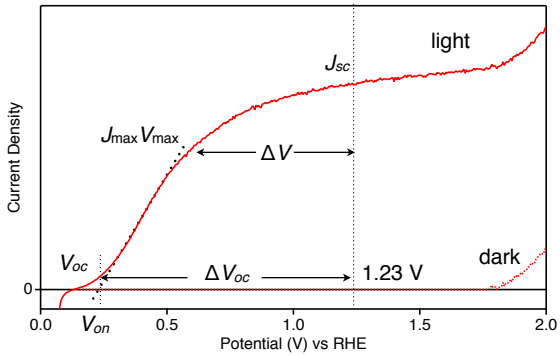

Figure 1.7. Current-Voltage Characteristics of a Semiconductor Photoanode
J-V curve of a typical semiconductor photoanode in the dark and under illumination, highlighting the open circuit voltage, V_{oc}, the short circuit current density, J_{sc}, the onset potential V_{on}, and the maximum power density, $J_{max}V_{max}$. See text for details.

As the applied voltage increases, the photoanode overcomes the threshold for water oxidation and the current density rapidly rises until a plateau region. The potential where the photocurrent rises is the known as the onset potential, V_{on}. There are several ways to define the onset potential. For consistency and simplicity, hereto the onset potential will be defined as the potential obtained by an extrapolation to zero current from the linear portion of the *J-V* curve. At large applied potentials, the photocurrent density reaches a plateau region where it does not change significantly over a large potential range. In this region, bulk recombination is usually the dominant limiting factor in the photocurrent generated. At 1.23 V, the thermodynamic potential for water splitting, photo-excitation is no longer assisting an uphill reaction (ΔV_{oc} = 0), and the corresponding current density is known as the short circuit current, J_{sc}. The "squareness" of the *J-V* curve is an indication of how efficient the photoanode is and can be measured by the fill factor, *FF*, a ratio of the maximum power, J_{max} ΔV_{max}, over the total power, J_{sc} ΔV_{oc} (Equation 1.5).[2,14]

$$FF = \frac{J_{max}\Delta V_{max}}{J_{sc}\Delta V_{oc}} \qquad \text{(Equation 1.5)}$$

For standardizing PEC measurements, photocurrents are generally reported per area of illumination under 1 sun AM 1.5 simulated solar irradiation. One sun is equivalent to 100 mW/cm^2, roughly the intensity of sunlight at the Earth's surface. For ease of comparison, applied potentials are converted to V vs NHE by adding the standard potential of the reference electrode, 0.1976 V for a saturated Ag/AgCl. Because the potential at which water splitting occurs is also pH dependent, sometimes it is more convenient to express potentials vs the reversible hydrogen electrode (RHE), where the thermodynamic potential for water splitting is at 1.23 V (pH = 0). According to the Nernst equation, $E_{NHE} = E_{RHE} - 0.0591\ V \times pH$. For most oxide semiconductors, the valance and conduction band potentials also follow Nernstian behavior, due to the absorption of protons and hydroxide ions on the surface.[2,8,14] Therefore, for ease of comparison among PEC measurements in different pH

environments, potentials are sometimes reported in V vs RHE using Equation 1.6, when using a saturated Ag/AgCl reference.

$$E_{RHE} = E_{Ag/AgCl} + 0.0591\text{pH} + 0.1976 \quad \text{(Equation 1.6)}$$

To evaluate the efficiency and wavelength response of a semiconductor photoanode, incident photon-to-current conversion efficiency (IPCE) spectra are often used. IPCE is calculated using Equation 1.7, where 1240 is the conversion to eV (*hc/e*), *J* is the current density in A/cm^2, λ is the excitation wavelength (nm), and *P* is the power density from the monochromatic light source in W/cm^2.

$$IPCE = 1240\frac{J}{\lambda P} \quad \text{(Equation 1.7)}$$

In general, integration of the IPCE spectra with respect to the solar spectrum should reproduce the current density obtained in a PEC measurement under 1 sun AM 1.5 illumination.[2,15,21] Therefore, in order to avoid impractical efficiencies due to a nonlinear dependence on photon density, it is important to collect IPCE spectra with light intensities approximately close to those of 1 sun AM 1.5 spectra.

IPCE is also known as external quantum efficiency (EQE) and is dependent on the light harvesting efficiency of the photoanode. IPCE may be low for thin photoanodes where more light is transmitted rather than absorbed. Therefore, sometimes it is useful to obtain the internal quantum efficiency (IQE), which reports the efficiency of a semiconductor at converting only the absorbed photons into current. IQE is calculated from Equation 1.8, where *T* is the transmittance and *R* is the reflectance, which is sometimes neglected.[2,15,22]

$$IQE = \frac{IPCE}{1 - T - R} \quad \text{(Equation 1.8)}$$

1.4 Solar-to-Hydrogen Conversion Efficiency

In solar water splitting, the maximum solar-to-hydrogen (STH) conversion efficiency is 30.7% for a single junction device at a band gap energy of 1.6 eV.[2,23] For a double-junction tandem cell the limit is 41%.[2] However, additional losses from electron transport, interfacial charge transfer, and heat put the practical limit closer to ~18% at ~2 eV for a single photosystem.[2,23] For practical purposes, STH conversion efficiencies of 10%, corresponding to a current density of 12.3 mA/cm^2 under 1 sun conditions, are desired.[1,2,10] High STH conversion efficiencies have been achieved mainly with expensive and unsustainable semiconductor devices, such as the p-n GaAs/$GaInP_2$ tandem cell with 12.4 % efficiency.[24] For stable oxide materials, STH conversion efficiencies are closer to 1% under 1 sun illumination.[2,14]

STH conversion efficiency is obtained from Equation 1.9, where $\Delta G°$ is the change in free energy of reaction, R_{H_2} is the rate of hydrogen generated, and P_t is the total power of the incident light.[2] If the generated

products are measured photoelectrochemically as current density, $\Delta G°R_{H_2}$ becomes $E°J$, the standard reaction potential (1.23 V) multiplied by the current density.

$$STH(\%) = \frac{\Delta G° R_{H_2}}{P_t} = \frac{E° J}{P_t} \qquad \text{(Equation 1.9)}$$

For a PEC cell where an external bias is applied, the actual thermodynamic STH efficiency is depicted by Equation 1.10 where V_{app} is the potential in V vs RHE.[2,14] Under 1 sun conditions, the equation becomes STH(%) = J(mA/cm^2) × (1.23V − V_{app}). However, when the photoanode is entirely powered in tandem by another PEC or PV cell, V_{app} equals zero and STH efficiency simplifies to J (mA/cm^2) × 1.23 V. Although high STH efficiency can be obtained when neglecting V_{app}, it may not be feasible to supply large voltages without connecting multiple PEC/PV devices in series, which increases materials and fabrication costs.

$$STH(\%) = \frac{\left(1.23V - V_{app}\right) J}{P_t} \qquad \text{(Equation 1.10)}$$

1.5 Efficiency Losses

Solar water oxidation is generally inefficient because it is challenging to simultaneously achieve photon absorption in the visible region, good charge separation and transport efficiency to the surface, and fast surface water oxidation catalysis in any one material.[2,3,5,25] In a PEC cell the current density collected (J_{PEC}) for water oxidation is typically low compared to the total current density (J_{abs}) achieved with 100% absorbed photon to current conversion efficiency (APCE = IQE). Figure 1.8 depicts the number of productive and nonproductive pathways for PEC water oxidation. When an n-type semiconductor is photoexcited, e-h pairs are generated (J_{abs}), which can recombine with radiative or non-radiative recombination in the bulk (J_{br}) depending on their conductivity and mobility.[2,14,15,26] In the limit where bulk recombination is the only photocurrent loss pathway, J_{PEC} is described by the Gärtner model.[15,19] In actuality, depletion layer, J_{dr}, and surface e-h recombination, J_{sr}, can be major loss pathways dependent upon surface reaction kinetics. Surface recombination at the semiconductor/liquid junction may be facilitated by surface traps or defects. Though, usually negligible, some degree of electron transfer by traversing the interfacial barrier, J_{et}, may also occur. Even though the band gap of a semiconductor is >1.23 V, if the total productive pathways towards water oxidation do not exceed the total nonproductive pathways, then no net photocurrent or water oxidation takes place. In other words, ultimately the reactive holes that reach the photoanode surface, J_{ox}, must be competitive with J_{sr}.

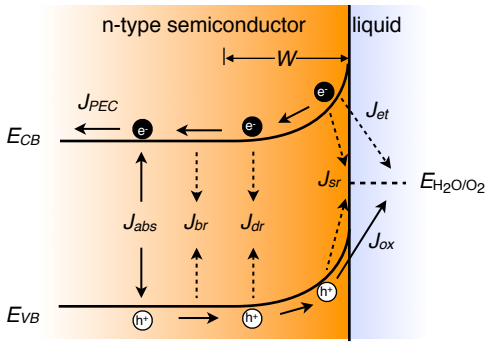

Figure 1.8. Productive and Nonproductive Pathways for Water Oxidation
Energy diagram showing the productive (solid lines) and nonproductive (dashed lines) pathways for PEC water oxidation by an n-type semiconductor photoanode. Electron-hole pairs are generated with photon absorption (J_{abs}) and can recombine nonproductively with radiative or non-radiative recombination in the bulk (J_{br}), depletion layer recombination (J_{dr}) surface recombination possibly due to defects (J_{sr}), and electron transfer current from semiconductor to electrolyte (J_{et}). Electron collection at the back contact (J_{PEC}) and hole transfer to water oxidation (J_{ox}) are productive processes contributing to PEC device efficiency.

Due to the challenging four-electron water oxidation process leading to poor reaction kinetics at many photoanode surfaces, surface e-h recombination is a predominate loss mechanism. As a result, large onset potentials for water oxidation are characteristic of photoanodes such as Fe_2O_3[21,27] and $BiVO_4$.[28-30] Application of surface water oxidation catalysts is commonly used to enhance water splitting rates, by decorating semiconductor powders with Pt, RuO_2, or IrO_2.[7,10,31] However, these contain expensive precious metals and some require extreme pH conditions for stable operation.[14] There are few reports of composite catalyst/ semiconductor photoanodes involving low cost, earth-abundant materials.

1.6 The Catalyst/Semiconductor Photoanode

Analogous to PS-II,[2,32] in a catalyst/semiconductor composite photoanode, photon absorption, charge separation, and water oxidation catalysis are performed by separate components as presented in Figure 1.9. In this division-of-labor approach, the light harvesting ability of an oxide semiconductor is combined with the water oxidation proficiency of a surface electrocatalyst to create a superior composite photoanode. Upon light absorption by the semiconductor, photogenerated holes in the valence band transfer to the water oxidation electrocatalyst where water oxidation proceeds at significantly lower overpotentials.

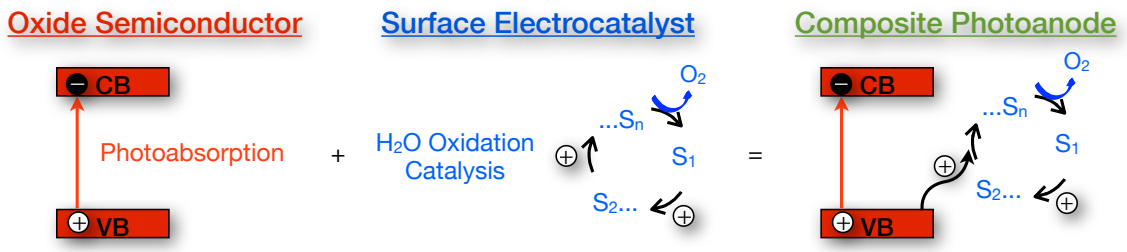

Figure 1.9. Separation of Photon Absorption, Charge Separation, and Water Oxidation Catalysis
Schematic of a division-of-labor approach where photon absorption by an oxide semiconductor is combined with the water oxidation capability of a proficient surface electrocatalyst to create a composite photoanode where photon absorption, charge separation, and water oxidation catalysis are performed by separate entities.

The integration of a surface electrocatalyst onto a semiconductor photoanode results in an improvement in the electrode kinetics for water oxidation. The PEC effects of a good catalyst deposited onto a semiconductor is reflected as an overall cathodic, or negative, shift in the *J-V* curve when compared to the unmodified semiconductor. However, the V_{oc} is unaffected because the catalyst improves reaction rates and not the thermodynamics of the system. The result is increased solar-to-chemical conversion efficiencies at reduced external bias with the composite photoanode.

1.7 Practical Applications

The device configuration for a catalyst/semiconductor photoanode is depicted in Figure 1.10. Similar to that of Figure 1.3, oxygen is produced at the photoanode while hydrogen is produced at the cathode. It is important to note that light absorption by the catalyst layer should be minimized, especially when illuminating from the frontside of the electrode, in order to avoid filtering effects. Ultimately, a photocathode material is envisioned to replace the dark cathode for overall water splitting in a tandem configuration.[9,12,14,25] The second PEC or PV cell will absorb light transmitted by the photoanode and provide any additional bias necessary to achieve overall water splitting. The bias provided by the additional electrode is limited by its V_{oc}, which is typically between 0.5-1.0 V for most materials. Therefore, reducing the additional bias necessary for water oxidation by applying a water oxidation catalyst onto a semiconductor photoanode will allow for tandem operation using one instead of multiple PEC/PV cells connected in series.

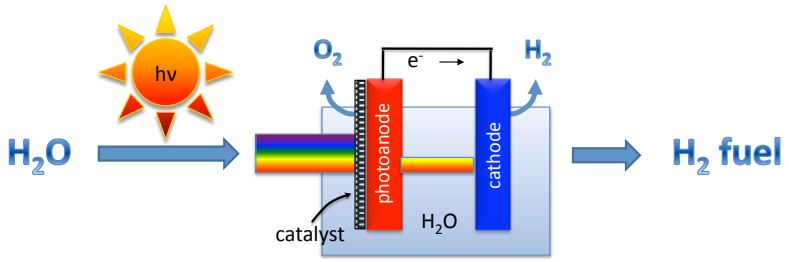

Figure 1.10. PEC Cell with a Catalyst/Semiconductor Composite Photoanode
Schematic of a PEC cell showing water oxidation by a catalyst/semiconductor composite photoanode and water reduction by a cathode. In a tandem configuration, the cathode can be a photocathode material that utilizes the lower energy portion of sunlight that is not absorbed by the photoanode.

Although the work in this thesis focuses on PEC cells, specifically water oxidation with catalyst/ semiconductor composite photoanodes, it is important to note that the presented results has implications in overall solar water splitting in general. Decreasing the onset potential for solar water oxidation will lessen the power demand supplied by a second electrode, PEC cell, PV device, or semiconductor photocatalyst. In practice, tandem water splitting can be implemented by a Z-scheme solar water splitting configuration with suspended catalyst-loaded semiconductor particles. Domen and coworkers have demonstrated nonsacrificial visible-light induced water splitting through a two-step photoexcitation process with $Pt/ZrO_2/TaON$ and Pt/WO_3 powders.[33] The use of catalysts was essential to obtain efficient water splitting and minimize surface e-h recombinations in the semiconductors. The development and understanding of catalyst/semiconductor composite photoanodes for separating photon absorption, charge separation, and water oxidation catalysis offers

promising prospects for improving solar hydrogen production, ultimately leading to sustainable, affordable, and distributed solar fuel technologies.

1.8 Notes to Chapter 1

1. Bard, A. J.; Fox, M. A., *Acc. Chem. Res.* **1995,** *28*, 141-145.
2. Grimes, C. A.; Varghese, O. K.; Ranjan, S., *Light, Water, Hydrogen*. Springer: New York, 2007.
3. Navarro Yerga, R. M.; Álvarez Galván, M. C.; del Valle, F.; Villoria de la Mano, J. A.; Fierro, J. L. G., *ChemSusChem* **2007,** *2*, 471-485.
4. Navarro, R. M.; Alvarez-Galvan, M. C.; Villoria de la Mano, J. A.; Al-Zahranib, S. M.; Fierroa, J. L. G., *Energy Environ. Sci.* **2010,** *3*, 1865-1882.
5. Kudo, A.; Miseki, Y., *Chem. Soc. Rev.* **2009,** *38*, 253-278.
6. Maeda, K.; Domen, K., *J. Phys. Chem. C* **2007,** *111*, 7851-7861.
7. Osterloh, F. E., *Chem. Mater.* **2008,** *20*, 35-54.
8. Hoffmann, M. R.; Martin, S. T.; Choi, W.; Bahnemann, D. W., *Chem. Rev.* **1995,** *95*, 69-96.
9. Grätzel, M., *Nature* **2001,** *414*, 338-344.
10. Rajeshwar, K., *J. Appl. Electrochem.* **2007,** *37*, 765-787.
11. Aroutiounian, V. M.; Arakelyan, V. M.; Shahnazaryan, G. E., *Sol. Energy* **2005,** *78*, 581-592.
12. Alexander, B. D.; Kulesza, P. J.; Rutkowska, I.; Solarska, R.; Augustynski, J., *J. Mater. Chem.* **2008,** *18*, 2298-2303.
13. Woodhouse, M.; Parkinson, B. A., *Chem. Mater.* **2008,** *20*, 2495-2502.
14. Walter, M. G.; Warren, E. L.; McKone, J. R.; Boettcher, S. W.; Mi, Q.; Santori, E. A.; Lewis, N. S., *Chem. Rev.* **2010,** *110*, 6446-6473.
15. Licht, S., *Encyclopedia of Electrochemistry: Semiconductor Electrodes and Photoelectrochemistry*. Wiley-VCH: Weinheim, 2002.
16. Gerischer, H., *J. Electrochem. Soc.* **1966,** *113*, 1174-81, discussion 1181-2.
17. Nozik, A.; Memming, R., *J. Phys. Chem.* **1996,** *100*, 13061-13078.
18. Gerischer, H., *J. Electrochem. Soc.* **1966,** *113*, 1174-1182.
19. Gärtner, W. W., *Phys. Rev.* **1959,** *116*, 84-87.
20. Butler, M. A., *J. Appl. Phys.* **1977,** *48*, 1914-1920.
21. Sivula, K.; Le Formal, F.; Grätzel, M., *ChemSusChem* **2011,** *4*, 432-449.
22. Liu, W. K.; Mackay Salley, G.; Gamelin, D. R., *J. Phys. Chem. B* **2005,** *109*, 14486-14495.
23. Bolton, J. R.; Strickler, S. J.; Connolly, J. S., *Nature* **1985,** *316*, 495-500.
24. Khaselev, O.; Turner, J. A., *Science* **1998,** *280*, 425-427.
25. Sun, J.; Zhong, D. K.; Gamelin, D. R., *Energy Environ. Sci.* **2010,** *3*, 1252-1261.
26. Lewis, N. S., *Acc. Chem. Res.* **1990,** *23*, 176-183.
27. Kay, A.; Cesar, I.; Grätzel, M., *J. Am. Chem. Soc.* **2006,** *128*, 15714-15721.
28. Sayama, K.; Nomura, A.; Arai, T.; Sugita, T.; Abe, R.; Yanagida, S.; Oi, T.; Iwasaki, Y.; Abe, Y.; Sugihara, H., *J. Phys. Chem. B* **2006,** *110*, 11352-11360.

29. Sayama, K.; Wang, N.; Miseki, Y.; Kusama, H.; Onozawa-Komatsuzaki, N.; Sugihara, H., *Chem. Lett.* **2010,** *39*, 17-19.
30. Berglund, S. P.; Flaherty, D. W.; Hahn, N. T.; Bard, A. J.; Mullins, C. B., *J. Phys. Chem. C* **2011,** *115*, 3794-3802.
31. Inoue, Y., *Energy Environ. Sci.* **2009,** *2*, 364-386.
32. McEvoy, J. P.; Brudvig, G. W., *Chem. Rev.* **2006,** *106*, 4455-4483.
33. Maeda, K.; Higashi, M.; Lu, D.; Abe, R.; Domen, K., *J. Am. Chem. Soc.* **2010,** *132*, 5858-5868.

Chapter 2: Composite Photoanodes for Photoelectrochemical Solar Water Splitting

This chapter is a review on recent efforts to improve PEC efficiencies by modification of semiconductor photoanode surfaces with water-oxidation catalysts that can operate at low overpotentials. A general overview of the challenges of solar water splitting is given, with emphasis on a need for the separation of photon absorption, charge separation, and water oxidation catalysts. This division-of-labor approach is designed to overcome the slow water oxidation kinetics at photoanode surfaces relative to competitive loss processes. Included in this review is work on Co-Pi/α-Fe_2O_3 composite photoanodes which will be presented in more detail in chapters 3-5. Around the same time, the emergence of additional water-oxidation electrocatalysts have led to the development of other composite catalyst/(dye)/semiconductor photoanode assemblies, which will also be discussed. The review is reproduced by permission of The Royal Society of Chemistry (RSC) from Sun, J., Zhong, D. K., Gamelin, D. R. *Energy. Environ. Sci.*, **2010**, *3*, 1252-1261 (http://pubs.rsc.org/en/content/articlelanding/2010/ee/c0ee00030b).

2.1 Introduction

The emergence of successful technologies for efficient solar energy conversion and storage would ameliorate concerns over rising global energy demand and environmental sustainability.[1,2] One very attractive potential technology involves using solar photons to drive the chemistry of splitting H_2O molecules to generate O_2 and H_2, tantamount to storing the photon energy in the chemical bond of H_2.[2-4] Hydrogen is an attractive energy carrier because of its high energy density (143 kJ/kg) and clean combustion (Equation 2.1).

$$2H_2(g) + O_2(g) \rightarrow 2H_2O(l) \qquad \Delta H° = 572 \text{ kJ/mol} \qquad \text{(Equation 2.1)}$$

Inspiration for this chemistry can be drawn from Nature, which already uses chlorophyll-containing proteins to harvest solar energy and drive the uphill chemistry of water oxidation. Rather than forming molecular hydrogen, Photosystem I and II store the solar energy in the initial form of trans-membrane proton gradients.[5-7] In 1972, Fujishima and Honda demonstrated the feasibility of an artificial analog to photosynthetic water splitting with UV light, using the semiconductor TiO_2 to absorb photons, separate charges, and catalyze water oxidation to generate O_2. Electrons were pumped to a Pt counter electrode, which reduced protons to generate H_2.[8] Since this seminal report, tremendous effort has been made to develop new materials and approaches showing improved solar water splitting efficiencies using visible light irradiation.[3,9-19] After nearly four decades of research, this fundamental objective remains a major challenge in chemistry.

2.2 Direct Photocatalytic Water Splitting

The cleavage of water molecules to form O_2 and H_2 involves the redox half-cell reactions shown in Equations 2.2 and 2.3.

$$2H_2O(l) \rightarrow O_2(g) + 4H^+(aq) + 4e^- \qquad E_{red}° = 1.23 \text{ V vs NHE} \qquad \text{(Equation 2.2)}$$

$$4H^+(aq) + 4e^- \rightarrow 2H_2(g) \qquad E_{red}° = 0 \text{ V vs NHE} \quad \text{(Equation 2.3)}$$

For one material to perform direct overall solar water splitting, it must be stable under photolysis conditions, have its valence band maximum (VBM) and conduction band minimum (CBM) potentials straddling those for water oxidation (Equation 2.2) and water reduction (Equation 2.3), respectively, and it should absorb a significant portion of the solar spectrum.[4,13,16,20] The minimum band gap of the semiconductor required by thermodynamics is only 1.23 eV, or ~1010 nm, but large overpotentials are typically required for water oxidation.

TiO_2 satisfies two of the above three conditions, failing only to absorb significant solar irradiation because of its very wide energy gap (~3.0 eV). Various approaches have been explored to increase the solar water splitting efficiency of this and many related wide-gap oxides such as $SrTiO_3$, SnO_2, and ZnO.[4,13,21,22] Cation or anion doping can be used to introduce new impurity energy levels within the semiconductor energy gap, and this strategy has been explored to engineer these materials to absorb more of the visible energy spectrum, with only partial success. Although visible light absorption can be enhanced by doping, this approach often results in little or no increase in overall photocatalytic activity because of new recombination loss channels or reduced conductivity also introduced upon doping.[21] Tantalates and niobates with layered or tunneling structures,[16,17] such as $MTaO_3$[23] (M = Li, Na, K) and $Sr_2Nb_2O_7$,[24] show high photocatalytic activity, but usually exhibit band gaps of ≥4.0 eV, making them only active under UV light irradiation. Nitrogen doping can increase the visible light response of these materials, but reactivity is demonstrated usually only in the presence of sacrificial agents such as methanol or $AgNO_3$. Although narrower gap semiconductors thus appear to be obvious candidates for absorption of more of the visible spectrum, common intermediate-gap semiconductors such as CdS and CdSe are unstable under water oxidation conditions because of the facile oxidation of sulfides or selenides.[25] Coating CdS or CdSe with conductive polymers, catalysts, or oxides can slow its degradation,[26-30] but to date a suitable solution to this challenge has not been established.

Control over semiconductor shapes and sizes on nanometer length scales can increase photocatalytic efficiencies by decreasing effective particle dimensions to within the carrier diffusion lengths, thereby allowing more effective minority carrier collection at the nanostructure surfaces.[31] However, not all semiconductor materials can be synthesized easily in such shape-controlled nanostructures, and thus this approach has not been explored thoroughly in conjunction with doping.

Despite many advances, the development of any single material that is photoactive in the visible region, stable under photolysis conditions, and can simultaneously oxidize and reduce water with high efficiency remains a daunting challenge. Frequently one criterion is met at the expense of another, limiting overall efficiency. Efforts in direct overall photocatalytic water splitting have been reviewed in several excellent comprehensive articles.[16,17,32] In order to achieve sufficient overall water splitting, photon absorption and charge separation must be balanced against the demands of stability and catalytic competence, and this may best be accomplished by separation of tasks. Co-catalysts such as RuO_2, NiO, or Pt can significantly enhance the photocatalytic activity of a photoactive semiconductor,[17] and dye molecules can substantially extend the light absorption of wide-gap oxides. Combining materials in a division-of-labor approach appears imperative.

This strategy has been employed in molecular chromophore/catalyst constructs designed to mimic PS-II. Such systems have been reviewed comprehensively elsewhere[33,34] and are beyond the scope of the present article, but they represent important homogeneous analogs of the heterogeneous composite photoelectrodes discussed here. In one set of studies, photoexcitation of ruthenium (II) *tris*-bipyridyl complexes covalently linked to MnOEC-like complexes was shown to successfully induce intramolecular electron transfer from the Mn catalyst to the photoexcited Ru chromophore. In the presence of external electron acceptors, oxidizing equivalents could be accumulated at the Mn and ultimately lead to irreversible substrate oxidation.[35-37] A variation on this approach was demonstrated using Cr^{VI} or $Ti^{IV}Cr^{III}$ charge transfer chromophores in mesoporous silica coupled to di-μ-oxo dinuclear Mn complexes[38] or Ir_xO_y water oxidation catalysts,[39] respectively, to generate accumulated oxidizing equivalents. Photosensitization of $Ru^{IV}_4O_4$–containing polyoxometallates with oxidatively resistant $[SiW_{10}O_{32}]^{8-}$ ancillary groups using ruthenium (II) *tris*-bipyridyl, has also yielded very interesting sensitized redox catalysis built on such a division-of-labor strategy.[40] Although molecular systems are sometimes challenged by stability issues, they represent extremely important well-defined model systems for advancing our fundamental understanding of solar photoredox processes in complex architectures.

2.3 Separation of Photon absorption, Charge Separation, and Redox Chemistries

In contrast with direct photoelectrolysis, photoelectrochemical (PEC) cells, such as that used by Fujishima and Honda,[8] separate the oxygen and hydrogen evolution half reactions physically, allowing each to be optimized independently. A semiconductor suited for photochemical water reduction may not be at all effective at water oxidation, and vice versa. Of these two half-cell reactions, water oxidation is more complex because it is a four-electron process, coupled to removal of four protons from two water molecules (Equation 2.2). In PEC cells, large overpotentials are therefore typically associated with the water oxidation half reaction. In principle, the necessary bias can be provided by an external photovoltaic (PV) cell as shown in Figure 2.1a, allowing completely solar powered PEC water splitting. Indeed, this configuration also no longer requires the CBM of the photoelectrode to be positioned above the water reduction potential, because the necessary additional bias can be provided by the PV cell. The PEC configuration thus affords more flexibility in materials choice than the direct photoelectrolysis approach. By the same token, optimization of the water-oxidation half reaction to minimize overpotential is essential for efficient solar hydrogen production.

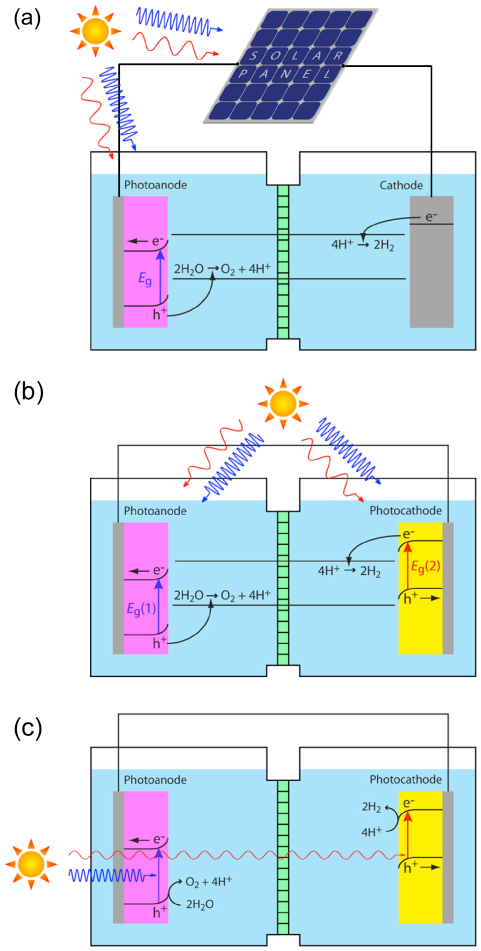

Figure 2.1. Three Approaches to PEC Solar Water Splitting
a) A single-photoelectrode PEC cell assisted by a photovoltaic (PV) cell. The photoanode here is an n-type semiconductor with a positive valance band edge relative to the water oxidation potential. The PV cell boosts the potential of the photogenerated electrons to allow water reduction at the cathode surface. **b)** A two-photoelectrode PEC cell in which the photoanode and photocathode are suitably matched n-type and p-type semiconductors, respectively, assembled in parallel. **c)** A tandem two-photoelectrode PEC cell assembled in series, such that low-energy photons that are not absorbed by the photoanode are absorbed by the photocathode.

A related device configuration employs two separate semiconductor photoelectrodes. As in Figure 2.1a, an n-type semiconductor is used as the photoanode. Instead of Pt as the cathode, a p-type semiconductor having a sufficiently high CBM is used as a photocathode, allowing sunlight to provide some or all of the additional bias needed to power the overall reaction (Figure 2.1b).

An attractive variation on both Figure 2.1a and Figure 2.1b is to align the two photoelectrodes in a serial tandem configuration (Figure 2.1c), with the wider-gap component first, such that photons transmitted by the top layer can be absorbed by the bottom layer.[3,41] This configuration parallels that of multijunction PVs, and in principle can improve overall solar-to-hydrogen conversion efficiencies. A variation on this cell design invoking direct connection of the two photoelectrodes, thereby obviating the need for wiring or even transparent conductive oxide substrates, has also been proposed.[2]

Properties of the ideal PEC photoanode include *i*) a relatively small band gap to absorb solar photons, *ii*) an appropriate VBM position relative to the water-oxidation potential, *iii*) effective separation and diffusion of photogenerated charge carriers, *iv*) efficient surface electrocatalysis, *v*) high chemical and photochemical

stability, and *vi*) low cost. Although extensive efforts have been made since 1970s, none of the semiconductors investigated so far meets all these requirements simultaneously. Moreover, it appears increasingly unlikely that any one material will ever be discovered that satisfies all of these demands simultaneously. As with direct photocatalytic water oxidation, modification of photoanodes in PEC cells with competent water-oxidation catalysts can be expected to yield marked improvements. Because of the rapid development of nanostructured semiconductor photoanodes and water oxidation electrocatalysts, several promising composite catalyst/ semiconductor photoanodes that show enhanced PEC solar water splitting relative to their individual components have been reported recently. In the following section, we highlight these recent advances.

2.4 Mesostructured α-Fe_2O_3 Photoanodes for Solar Water Oxidation

Metal oxides are attractive candidate photoanode materials for solar water oxidation. TiO_2 (rutile and anatase), Fe_2O_3 (α-form, hematite), and WO_3 are the mostly studied binary oxide photoanodes. If only considering the band gap, α-Fe_2O_3 is the most promising of these due to its relatively small band gap of ~2.1 eV (~590 nm), which can use ~18% of the solar photons in AM1.5 sunlight (Figure 2.2). Other advantages of α-Fe_2O_3 include its high chemical and photochemical stability in basic electrolytes, low cost, and environmental compatibility.

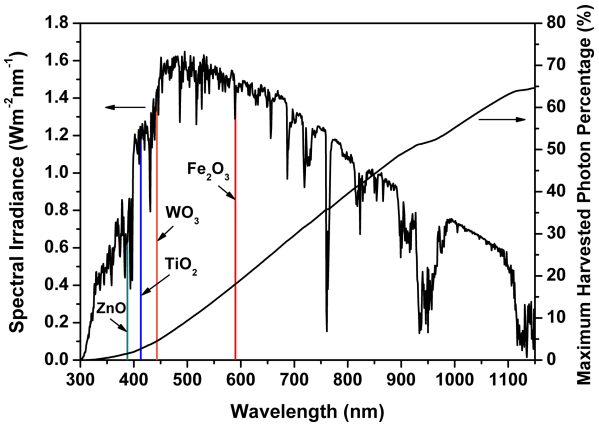

Figure 2.2 The Solar Spectrum with Band Gap Positions of Metal Oxide Semiconductors
Solar spectrum (AM 1.5) and the bulk band gap positions of various binary metal oxide semiconductors: α-Fe_2O_3, 2.1 eV (590 nm), WO_3, 2.8 eV (443 nm); rutile TiO_2, 3.0 eV (413 nm); ZnO, 3.2 eV (388 nm).

A variety of intrinsic problems impede the desired performance of α-Fe_2O_3 photoanodes for PEC solar water splitting. First, the band gap of α-Fe_2O_3 is indirect. Absorption of photons in the visible region is therefore limited by a low absorption coefficient, corresponding to a long light penetration depth (on the order of 100 nm).[42] Second, α-Fe_2O_3 has short hole diffusion length (~2-4 nm),[43] which is exacerbated by the long light penetration depth, meaning that for bulk α-Fe_2O_3 most of the photogenerated charge carriers recombine long before reaching the photoanode surface where they might catalyze the oxidation of water. Third, it has been demonstrated that the water-oxidation kinetics at the α-Fe_2O_3 surface by the valence band holes is slow,[44] making non-productive recombination processes more competitive. Fourth, α-Fe_2O_3 has poor conductivity. Overall, in its pure form, α-Fe_2O_3 is an inefficient photoanode material. It is not surprising that early studies of

α-Fe_2O_3 photoelectrodes typically yielded low photoresponses, with PEC current densities on the order of $\mu A/cm^2$.[43-47]

Morphological control and impurity doping have been successful in overcoming some of the above-mentioned problems. To counter the short hole diffusion length, several groups have prepared mesostructured α-Fe_2O_3 photoanodes such that holes have only short distances to travel before encountering surfaces. Compared to other methods, such as film preparation directly from colloidal nanoparticles,[48] nanocrystalline α-Fe_2O_3 photoanodes prepared by spray pyrolysis (SP) show improved photoresponse.[49-52] Recently, ultrasonic spray pyrolysis (USP) was used to prepare platelet-like α-Fe_2O_3 photoanodes, which showed significantly enhanced photoresponse compared to those prepared by the conventional SP method.[53] The photoresponse enhancement was attributed to the small thickness (<10 nm) of the platelets, which is commensurate with the hole diffusion length in α-Fe_2O_3. Incorporation of Si dopants further reduced the size of these α-Fe_2O_3 platelets and yielded even higher photocurrent densities.[54]

Si doping has also been shown to be beneficial in the performance of dendritic α-Fe_2O_3 nanostructured photoanodes grown by atmospheric pressure chemical vapor deposition (APCVD).[54-56] Si doping plays several roles in improving the performance of these photoanodes. The dopants appear to induce growth of smaller nanocrystals, or inhibit growth of larger nanocrystals, such that the outermost grains are < ~20 nm in diameter (Figure 2.3a, b), which is small enough for hole diffusion to the semiconductor surface, whereas they reached ~40 nm in the absence of Si doping. The introduction of Si also leads to preferential growth of the α-Fe_2O_3 along the [110] axis perpendicular to the substrate surface. α-Fe_2O_3 has higher conductivity along [110] direction,[57] and this oriented growth thus enhances carrier transport to the back contact. Finally, Si dopants likely serve as electron donors, thereby also improving the α-Fe_2O_3 conductivity. These α-Fe_2O_3 photoanodes grown by APCVD yielded high solar-to-hydrogen efficiencies in pH = 13.6 electrolyte under AM 1.5G simulated sunlight irradiation (100 mW/cm^2). The photocurrent density reached ~2.2 mA/cm^2 at 1.23 V vs RHE (the thermodynamic water-oxidation potential), which could be further increased to ~2.7 mA/cm^2 upon adsorption of Co^{2+} ions onto the surface by wet impregnation (Figure 2.3c, vide infra). α-Fe_2O_3 photoanodes prepared by the same method without Si showed dramatically reduced photoresponse.[56]

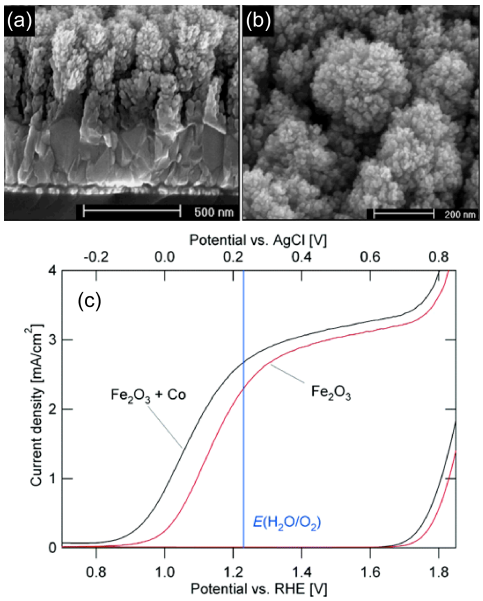

Figure 2.3 Si-doped Dendritic α-Fe_2O_3 Photoanodes
a) Cross-sectional SEM image. The bottom layer is the fluorine-doped tin oxide (FTO) substrate. **b)** Top-view SEM image showing the small surface nanocrystals (10-20 nm in diameter). **c)** Linear sweep voltammetry measurements in dark and in simulated AM 1.5 G sunlight at a scan rate of 50 mV/s. The red curves are the Si-doped α-Fe_2O_3. The black curves are the same anode after wet impregnation with a cobalt nitrate solution. (Adapted with permission from ref. 55. Copyright 2006 American Chemical Society.)

Electrochemical deposition,[58-60] chemical solution deposition,[61] and reactive magnetron sputtering[62] have also been used to synthesize undoped and doped α-Fe_2O_3 nanostructured photoanodes. Different from the one-step SP, USP, and APCVD methods that operate at high temperatures (> 400°C), these methods generally involve film deposition at relatively low temperatures, followed by annealing at high temperatures (> 500°C) to obtain nanocrystalline α-Fe_2O_3 photoanodes. Although the photoresponses of such photoanodes have been lower than those achieved using APCVD, these approaches appear to be amenable to incorporation of a wide variety of dopants such as Ti or Cr,[59,63] which could lead to improved light harvesting or electrical conductivity.

One-dimensional semiconductor nanostructures such as nanorods/nanowires and nanotubes are also attractive for PEC applications because their small radial dimensions should allow efficient hole capture at the photoelectrode surfaces while maintaining electron transport in the longitudinal dimension,[41,64] stimulating efforts to develop photoanodes involving highly anisotropic α-Fe_2O_3 nanostructures. Early studies on α-Fe_2O_3 nanorod photoanodes showed low photoresponses,[65,66] however, mainly attributed to fast carrier recombination and slow water oxidation kinetics at the anode surfaces. An aerosol-assisted chemical vapor deposition (AACVD) method was used to prepare rod-like α-Fe_2O_3 photoanodes that showed photocurrent densities ~0.6 mA/cm^2 at 1.23 V vs RHE in AM 1.5G simulated sunlight and basic electrolyte.[67]

Recently, the preparation of micron-long α-Fe_2O_3 nanotube arrays via electrochemical anodization of Fe foils has been reported.[68-70] The nanotube wall thicknesses were typically <~20 nm, and their pore diameters were <100 nm (Figure 2.4). Photocurrent densities of ~1 mA/cm^2 at 1.23 V vs RHE were achieved with these nanotube arrays using AM 1.5 simulated sunlight and basic electrolyte,[69,70] which is likely the highest reported value for undoped α-Fe_2O_3 photoanodes.

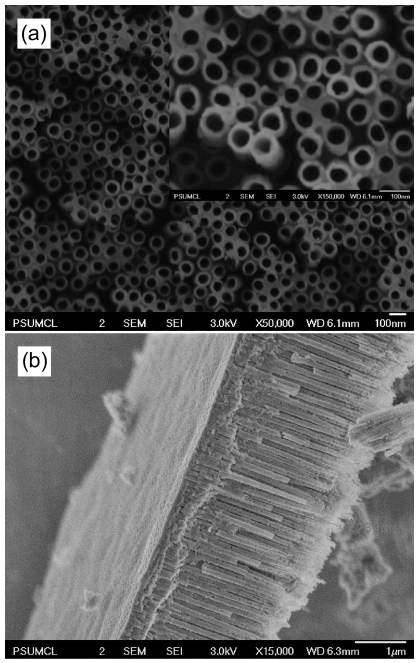

Figure 2.4 α-Fe_2O_3 Nanotube Arrays
a) Top-view and **b)** side-view SEM images of α-Fe_2O_3 nanotube arrays prepared by anodization of Fe foil at a potential of 50 V in ethylene glycol. (Adapted with permission from ref. 68. Copyright 2009 American Chemical Society.)

2.5 A Family of Cobalt-Based Electrocatalysts for Water Oxidation

In photosynthesis, water oxidation is performed by the Mn_4O_4Ca oxygen-evolving cluster of photosystem II (MnOEC of PS-II).[71] For artificial photosynthesis based on water splitting, a variety of homogeneous and heterogeneous water-oxidation catalysts have been developed.[72-78] Some of these catalysts contain precious metals or do not operate in neutral water under ambient conditions, factors that may ultimately limit their widespread applicability, but a great deal has nevertheless been learned about the criteria for active photoelectrolysis from broad investigation of such catalysts.

Recently, a new family of cobalt-based electrocatalysts was discovered that show electrochemical oxygen evolution at relatively low overpotentials under mild ambient conditions (pH = 7-9.2, 1 atm, and room temperature).[79-82] These catalysts, which include cobalt phosphate (Co-Pi), cobalt methylphosphonate (Co-MePi), and cobalt borate (Co-Bi) variations, can be electro- or photo-deposited onto various electrodes from the corresponding Co^{2+} solutions in anion buffer. Figure 2.5a shows an SEM image of one typical Co-Pi catalyst film. From EXAFS studies of this catalyst, the active centers are likely cobalt-oxo cubane-type clusters (Figure 2.5b).[83] The prominent Co-O and Co-Co distances in the Co-Pi catalyst EXAFS data indicate distances of 0.19 nm and 0.28 nm, respectively, which are remarkably close to the corresponding Mn-O and Mn-Mn distances found in the Mn_4O_4Ca clusters of PS-II.[71] Moreover, the Co-Pi water-oxidation catalyst has been noted to possess some of the attractive general characteristics of the MnOEC of PS-II, including a "self-healing" capacity under turnover conditions in phosphate buffer.[80] Like manganese, the relative abundance of cobalt makes this family of water-oxidation catalysts promising for low-cost artificial solar water splitting.

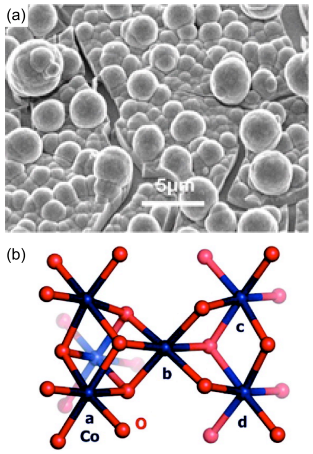

Figure 2.5 Co-Pi Water-Oxidation Electrocatalyst
a) SEM image of a Co-Pi catalyst layer prepared by electrodeposition onto ITO for ~7 hours at 1.3 V vs NHE from a 0.1 M potassium phosphate buffer solution (pH 7) containing 0.5 mM Co^{2+}. (Adapted from ref. 71. Reprinted with permission from AAAS) **b)** Proposed structure of the cobalt-oxo active core of the Co-Pi catalyst (cobalt in blue and oxygen in red), based on EXAFS data. (Adapted with permission from ref. 83. Copyright 2009 American Chemical Society.)

2.6 Composite Co-Pi/Semiconductor Photoanodes for PEC Solar Water Oxidation

As noted above, α-Fe_2O_3 has a relatively narrow band gap that can absorb a large portion of visible photons from sunlight (Figure 2.2). Although its valance band edge potential is ~1.2 V more positive than required for water oxidation thermodynamically (Equation 2.2), its performance is still hindered by slow water-oxidation kinetics. As such, α-Fe_2O_3 serves as a prototype photoanode material for testing strategies to overcome this challenging chemistry. Like in direct photoelectrolysis, modification of the α-Fe_2O_3 surfaces by cocatalysts offers an attractive route to improved performance. For example, cocatalysts such as RuO_2, NiO, or Pt can significantly enhance the photocatalytic activity of a photoactive semiconductor.[17] Deposition of RuO_2 nanocrystals onto α-Fe_2O_3 surfaces led to a ~120 mV cathodic shift of the photocurrent onset potential,[84] as did adsorption of Co^{2+} ions by wet impregnation[55] (~80 mV, Figure 2.3c). In the latter case, the proposed mechanism involved trapping of photogenerated holes by the surface cobalt ions to give stepwise oxidation of Co^{2+} to Co^{4+}, followed by water oxidation, in a fashion directly parallel to the mechanism of water oxidation in PS-II.

Surface adsorbed anions appear to play a different role. Modification of TiO_2 photoelectrode surfaces with F^- in acetonitrile[85,86] and in aqueous solution[87] was reported to result in a cathodic shift of the flat-band potential. A ~150 mV cathodic shift of the photocurrent onset potential in Ti-doped α-Fe_2O_3 photoanodes was observed after wet impregnation in aqueous CoF_3 solutions.[63] Control experiments excluded possible contributions from cobalt cations or other anions such as Cl^- in their measurements, and the observed performance enhancement was proposed to reflect a cathodic shift of the flat-band potential.

Recently, composite Co-Pi/α-Fe_2O_3 photoanodes were explored for PEC solar water splitting.[88,89] Co-Pi was electrodeposited onto the surfaces of APCVD-grown Si-doped α-Fe_2O_3 mesostructured thin films. SEM images of the parent α-Fe_2O_3 photoanode (Figure 2.6a) reveal highly structured electrode surfaces with dendritic features like in Figure 2.3. After Co-Pi deposition, a ~200 nm thick catalyst layer covered the α-Fe_2O_3 film (Figure 2.6b). Extensive cracking of the Co-Pi layer was observed, which is believed to be due to drying

prior to the SEM measurement. Figure 2.6c shows a portion of the catalyst layer that has curled off of the α-Fe_2O_3 film upon drying, allowing its underside to be seen. Interestingly, the inverse mesostructure from the α-Fe_2O_3 thin film can be seen in this underside, indicating that the catalyst deposits conformally onto the highly structured α-Fe_2O_3 surface. A high degree of interfacial contact between the α-Fe_2O_3 and the catalyst layer is essential for fast hole transfer from the oxide to the catalyst.

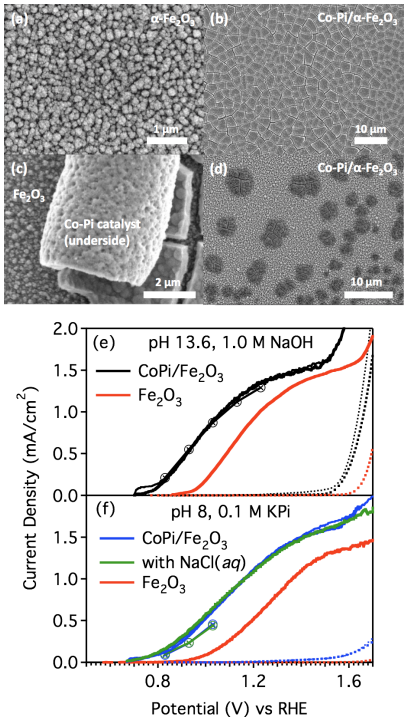

Figure 2.6. SEM Images and *J-V* Curves of Co-Pi/α-Fe_2O_3
a) SEM image of Si-doped α-Fe_2O_3 photoanode before electrodeposition of Co-Pi catalyst. SEM images of composite Co-Pi/α-Fe_2O_3 photoanodes collected following **b, c)** 1 hour and **d)** 15 min of Co-Pi electrodeposition. The catalyst layer cracking occurs upon drying for the SEM measurement and in some cases allows inspection of the catalyst underside (c), which shows that the Co-Pi layer conforms to the α-Fe_2O_3 mesostructure. The dark spots in panel (d) are the catalyst. **e)** and **f)** Linear sweep voltammetry measurements of Si-doped α-Fe_2O_3 (red) and composite Co-Pi/ α-Fe_2O_3 photoanodes in 1 M NaOH (black) and 0.1 M KPi electrolyte with (green) and without (blue) 0.1 M NaCl in the dark (dashed) and in simulated one-sun AM 1.5 sunlight (solid) with front-side illumination at a scan rate of 10 mV/s. (Adapted with permission from ref. 88 and 89. Copyright 2009 and 2010, respectively, American Chemical Society.)

Linear sweep voltammetry measurements of the parent α-Fe_2O_3 and composite Co-Pi/α-Fe_2O_3 photoanodes in 1 M NaOH under AM 1.5 simulated sunlight demonstrated that Co-Pi modification shifts the photocurrent onset potential for solar water oxidation by several hundred millivolts compared to that of α-Fe_2O_3 alone.[88] Current densities were low (~0.5 mA/cm^2), however, because of the need for backside illumination of the photoanode with such a thick, absorbent catalyst layer.

Optimization of the Co-Pi/α-Fe_2O_3 composite photoanode structure for frontside illumination gave ~200% enhancement of efficiency at +1.0 V vs RHE.[89] Non-productive photon absorption by the catalyst was reduced by decreasing the deposition time to yield a thinner Co-Pi layer. This thinner deposition also remediated an apparent kinetic bottleneck associated with the catalyst thickness.[89] SEM images show only Co-Pi islands on the α-Fe_2O_3 (Figure 2.6d), but a thin layer of Co-Pi over the entire surface was detected by energy dispersive

X-ray analysis (EDX). The Co-Pi islands were hypothesized to form over pinholes or scratches in the α-Fe_2O_3 film, where current could flow more freely during catalyst electrodeposition. Figure 2.6e shows the current–voltage characteristics of one such Co-Pi/α-Fe_2O_3 photoanode, compared to data from the parent α-Fe_2O_3 photoanode, both under frontside illumination in pH 13.6, 1 M NaOH. With Co-Pi, a ~180 mV cathodic shift in the PEC onset potential was observed. Modification of α-Fe_2O_3 surfaces with Co-Pi thus significantly reduces the external bias required for solar water splitting in a PEC cell configuration such as those shown in Figure 2.1, illustrating the advantage of separating photon harvesting from multi-electron redox catalysis.

Sustained solar water oxidation by Co-Pi/α-Fe_2O_3 composite photoanodes was also demonstrated at lower pH levels. Figure 6f shows the current–voltage curves of the same photoanodes from Figure 6e, measured instead in 0.1 M potassium phosphate (KPi) buffered at pH 8, which is the average pH of seawater. A similar cathodic shift is observed. Remarkably, J-V curves with 0.1 M NaCl added are essentially indistinguishable from those without NaCl (Figure 2.6f), demonstrating that PEC water oxidation with Co-Pi/α-Fe_2O_3 composite photoanodes can be performed equally well in the presence of chloride. Oxygen detection experiments show enhanced oxygen production even after several hours of illumination, with enhancement factors comparable to those of the photocurrent, confirming sustained solar water oxidation by Co-Pi/α-Fe_2O_3 composite photoanodes.

The IPCE measurements of the composite Co-Pi/α-Fe_2O_3 photoanode at 1.0 V vs RHE showed that the photoresponse comes exclusively from α-Fe_2O_3 photoexcitation, indicating that Co-Pi functions solely as a surface electrocatalyst.[88] The composite photoanode thus relies on efficient transfer of photogenerated holes from α-Fe_2O_3 to the Co-Pi catalyst layer. Appending Co-Pi to the α-Fe_2O_3 surface is thus akin to introducing well-defined surface hole traps in place of the poorly defined native surface states that catalyze water oxidation in the absence of catalyst. This modification should enhance irreversible electron-hole separation and reduce unwanted carrier recombination processes. Overall, the composite Co-Pi/semiconductor photoanodes allow photon absorption, carrier separation, and redox surface catalysis to be effectively decoupled, yielding improved performance.

Electrodeposition of a uniform Co-Pi surface catalyst layer requires small conductivity variations over the entire semiconductor electrode. For many attractive semiconductor photoanodes, such as nanorod arrays on conducting fluorine-doped tin oxide (FTO) substrates, this condition is difficult to achieve. Electrodeposition of Co-Pi onto semiconductor nanorod surfaces is hindered by the fact that the FTO substrate is substantially more conductive than the nanorods grown upon it, making the Co-Pi deposit preferentially on the bare FTO surface. This difficulty can be overcome by photochemical deposition. Co-Pi nanoparticles with ~10-30 nm diameters were recently deposited onto ZnO nanorods grown on FTO (Figure 2.7a, b) by UV light illumination in the absence of external bias.[90] The narrower band gap of ZnO than FTO allows selective excitation of the nanorods, directing catalyst deposition to only these surfaces. Formation of Co-Pi nanoparticles instead of a uniform surface layer suggests that the most readily available photogenerated holes are not uniformly distributed on the ZnO surfaces. Photodeposition thus places the Co-Pi catalyst precisely at those locations that have the highest photochemical activity.

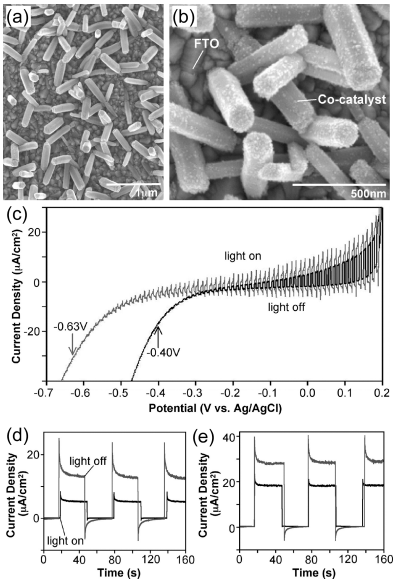

Figure 2.7. SEM Images and PEC Measurements of Co-Pi/ZnO Nanorods
SEM images of **a)** ZnO and **b)** composite Co-Pi/ZnO nanorod photoanodes, grown on fluorine-doped tin oxide (FTO) substrates. **c)** Linear sweep voltammetry measurements of ZnO (black) and Co-Pi/ZnO (gray) photoanodes using chopped light (100 mW/cm^2, 1Hz) at a scan rate of 10 mV/s. Arrows indicate the photocurrent onset potential. **d)** and **e)** Photocurrent of ZnO (black) and Co-Pi/ZnO (gray) photoanodes measured at 0.0 and 0.2 V vs Ag/AgCl, respectively. (Adapted from ref. 90. Copyright 2009 National Academy of Sciences, USA.)

Figure 2.7c shows linear sweep voltammetry measurements of such ZnO and Co-Pi/ZnO nanorod photoanodes measured using chopped photoexcitation. The photocurrent densities are substantially lower than for α-Fe_2O_3 because ZnO is a poor photon absorber (E_g = 3.2 eV, Figure 2.2). Upon Co-Pi deposition, the photocurrent onset potential was cathodically shifted by ~0.2 V relative to the parent ZnO, very similar to the results from the composite Co-Pi/α-Fe_2O_3 photoanodes. The photocurrent was also enhanced over the entire potential range investigated (Figure 2.7c), becoming less significant at more positive potentials. For example, under steady-state conditions, the composite Co-Pi/ZnO photoanode showed photocurrent enhancements of 2.6- and 1.5-fold at 0.0 V and 0.2 V vs Ag/AgCl (Figure 2.7d, e), respectively, relative to the parent ZnO anode. This result suggests that the increased band bending at high potentials already provides sufficient driving force for efficient electron-hole separation even in the absence of the Co-Pi surface catalyst. As with the Co-Pi/α-Fe_2O_3 composite photoanodes, the role of surface modification is thus most important at low applied potentials. For practical energy conversion applications, a reduction in applied potential translates into a lower overall cost of the solar-to-hydrogen conversion technology.

2.7 Composite Catalyst/Dye/Semiconductor Photoanodes for PEC Solar Water Splitting

TiO_2 was the first semiconductor photoanode material investigated for PEC water splitting.[8] It is cheap, environmentally benign, and highly stable over a broad pH range, making it attractive for such applications.[91,92] Unfortunately, its large band gap (> 3.0 eV, Figure 2.2) allows it to absorb only the UV portion of sunlight, leading to low solar-to-hydrogen conversion efficiency. One popular approach to extend absorption into the visible in TiO_2-based solar-energy-conversion devices is to anchor dye molecules to the TiO_2 surfaces, which can absorb visible light and transfer photoexcited carriers into the TiO_2. This approach is mainly employed in

dye-sensitized solar cells (DSSCs).[93,94] In DSSCs, TiO_2 acts as an acceptor of the photogenerated electrons, and the photogenerated holes in the dye molecules are quenched by redox mediators such as the I^-/I_3^- couple. Because the photogenerated holes are typically localized on the dye molecules without sufficient potential for water oxidation, and because dyes are typically only one-electron photoredox reagents, this approach has rarely been used for PEC solar water splitting.

Recently, Mallouk and coworkers[95,96] demonstrated the feasibility of attaching $IrO_2 \cdot nH_2O$ nanoparticles, which are well-known water-oxidation catalysts,[72] to a dye-sensitized TiO_2 photoanode. A tailor-made ruthenium dye acts not only as the visible-light absorber but also as a stabilizer of the $IrO_2 \cdot nH_2O$ nanoparticles (Figure 2.8a). In these initial experiments, electron transfer from the solid catalyst nanoparticles to the oxidized dye molecules was found to be slow and could not compete well with the faster back electron transfer from TiO_2 to the dye, yielding small photocurrents (Figure 2.8b). Nevertheless, this catalyst/dye/semiconductor approach provides an exciting proof-of-concept strategy for achieving efficient PEC solar water splitting based on stable large-band-gap semiconductors sensitized by surface dyes, in analogy to DSSCs.

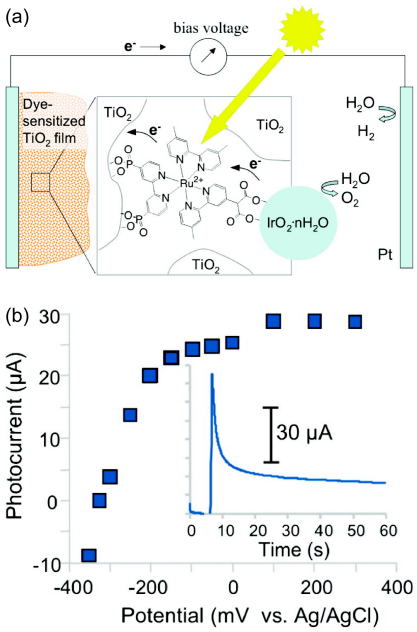

Figure 2.8. Schematic and PEC Measurements of a TiO_2/Dye/IrO_2 Photoanode
a) Schematic of a TiO_2/dye/IrO_2 photoanode for solar water splitting in a photoelectrochemical cell. **b)** Plot of steady-state photocurrent vs applied potential. The inset shows the photocurrent decay profile measured at 0 mV vs Ag/AgCl. (Adapted with permission from ref. 96. Copyright 2009 American Chemical Society.)

The problem of slow electron transfer from catalyst to dye molecules could potentially be alleviated by using a molecular water-oxidation catalyst, and recent efforts have helped make important steps toward application of molecular catalysts in PEC solar water splitting devices.[97] In one related molecular photoanode assembly that parallels the photon absorption, charge seperation, and MnOEC-catalyzed water oxidation of photosynthesis, attachment of a dinuclear di-μ-oxo Mn-based water-oxidation catalyst, $[H_2O(2,2'{:}6',2''\text{-terpy})Mn^{III}(\mu\text{-}O)_2Mn^{IV}(2,2'{:}6',2''\text{-terpy})H_2O](NO_3)_3$, onto TiO_2 nanoparticle surfaces using a robust dye linker capable of absorbing visible light was reported.[98] The $Mn^{III}(\mu\text{-}O)_2Mn^{IV}$ inorganic core could be oxidized to

$Mn^{IV}(\mu\text{-}O)_2Mn^{IV}$ upon visible-light absorption, indicating effective electron transfer from the manganese catalyst to the dye linker. The PEC solar water splitting performance of this assembly remains to be elucidated. Very recently, a photo-responsive tetranuclear Mn-oxo water-oxidation catalyst ($[Mn_4O_4((MeOPh)_2PO_2^-)_6]^+$) dispersed in a proton-conductive Nafion membrane was attached to $[Ru^{II}(bipy)_2(bipy(COO)_2)]$-sensitized TiO_2.[99] The PEC performance of this composite photoanode assembly measured in neutral electrolyte (0.1M Na_2SO_4) using a two-electrode system has established that water splitting could be achieved using visible light in the absence of external bias. The photocurrent density was rather low, which is likely due to the slow interfacial electron transfer. Additionally, significant photocurrent decay was observed, which could indicate photodegradation of some of the components of the assembly. In parallel, the catalytic water-oxidation properties of $[Ru(Mebimpy)(4,4'\text{-}((HO)_2OPCH_2)_2bpy)(OH_2)]^{2+}$ anchored onto metal-oxide electrode surfaces has been established,[100] providing further impetus for exploring this strategy thoroughly.

The successes in anchoring molecular water-oxidation catalysts to metal-oxide semiconductor surfaces may portend efficient composite photoanodes of this type that are competitive with the crystalline or amorphous composite photoelectrodes discussed above. Further improvement of catalyst/dye/semiconductor and related composite photoanodes involving molecular components will rely on controlling the semiconductor-catalyst, semiconductor-dye, and dye-catalyst interfaces for favorable electron transfer kinetics across these interfaces.[101] Whether with crystalline, amorphous, or molecular catalysts, photoanodes with greater absorption in the visible are needed, which should refocus efforts onto the development of composite structures designed to protect oxidatively less robust materials against degradation.[26-30] This general approach is modular and therefore conducive to stepwise evolution as photoanodes with greater light harvesting capabilities are developed, or better redox catalysts that can be interfaced with such anodes emerge.

2.8 Summary and Perspective

The development of practical technologies for the generation of H_2 fuel using sunlight is challenged by inefficiencies in the four-electron water oxidation chemistry. This chemistry is generally inefficient because it is challenging to achieve photon absorption in the visible region, efficient charge separation/transport to the surfaces, and fast surface redox catalysis simultaneously in any one material. Strategies that separate the above tasks allow optimization of each function independently, and offer the possibility of vast improvements in practical solar water splitting technologies.

Following recent improvements of promising metal-oxide mesostructured photoanodes, and the emergence of attractive water-oxidation electrocatalysts that can be interfaced with such photoanodes, composite catalyst/(dye)/semiconductor photoanode assemblies are now becoming more prominent research targets for addressing the challenges of solar water splitting via separation of tasks. This approach has already uncovered significant opportunities to reduce photocurrent onset potentials of well characterized photoanodes without hindering other performance characteristics such as photocurrent densities, stability, or tolerance to impurity ions. PEC performance at reduced external bias lessens the demand for external power, which ultimately reduces manufacturing expense and improves the overall competitiveness of solar hydrogen technologies.

2.9 Notes to Chapter 2

1. Hoffert, M. I.; Caldeira, K.; Benford, G.; Criswell, D. R.; Green, C.; Herzog, H.; Jain, A. K.; Kheshgi, H. S.; Lackner, K. S.; Lewis, J. S.; Lightfoot, H. D.; Manheimer, W.; Mankins, J. C.; Mauel, M. E.; Perkins, L. J.; Schlesinger, M. E.; Volk, T.; Wigley, T. M. L., *Science* **2002,** *298*, 981-987.
2. Lewis, N. S.; Nocera, D. G., *Proc. Nat. Acad. Sci.* **2006,** *103*, 15729-15735.
3. Grätzel, M., *Nature* **2001,** *414*, 338-344.
4. Grimes, C. A.; Varghese, O. K.; Ranjan, S., *Light, Water, Hydrogen*. Springer: New York, 2007.
5. McEvoy, J. P.; Brudvig, G. W., *Chem. Rev.* **2006,** *106*, 4455-4483.
6. Yachandra, V. K.; Sauer, K.; Klein, M. P., *Chem. Rev.* **1996,** *96*, 2927-2950.
7. McEvoy, J. P.; Gascon, J. A.; Batista, V. S.; Brudvig, G. W., *Photochem. Photobiol. Sci.* **2005,** *4*, 940-949.
8. Fujishima, A.; Honda, K., *Nature* **1972,** *238*, 37-8.
9. Nozik, A. J., *Annu. Rev. Phys. Chem.* **1978,** *29*, 189-222.
10. Bard, A. J.; Fox, M. A., *Acc. Chem. Res.* **1995,** *28*, 141-145.
11. Khaselev, O.; Turner, J. A., *Science* **1998,** *280*, 425-427.
12. Bak, T.; Nowotny, J.; Rekas, M.; Sorrell, C. C., *Int. J. Hydrogen Energy* **2002,** *27*, 991-1022.
13. Rajeshwar, K., *J. Appl. Electrochem.* **2007,** *37*, 765-787.
14. Alexander, B. D.; Kulesza, P. J.; Rutkowska, I.; Solarska, R.; Augustynski, J., *J. Mater. Chem.* **2008,** *18*, 2298-2303.
15. van de Krol, R.; Liang, Y.; Schoonman, J., *J. Mater. Chem.* **2008,** *18*, 2311-2320.
16. Kudo, A.; Miseki, Y., *Chem. Soc. Rev.* **2009,** *38*, 253-278.
17. Osterloh, F. E., *Chem. Mater.* **2008,** *20*, 35-54.
18. Boettcher, S. W.; Spurgeon, J. M.; Putnam, M. C.; Warren, E. L.; Turner-Evans, D. B.; Kelzenberg, M. D.; Maiolo, J. R.; Atwater, H. A.; Lewis, N. S., *Science* **2010,** *327*, 185-187.
19. Maeda, K.; Domen, K., *Chem. Mater.* **2010,** *22*, 612-623.
20. Woodhouse, M.; Parkinson, B. A., *Chem. Mater.* **2008,** *20*, 2495-2502.
21. Navarro Yerga, R. M.; Álvarez Galván, M. C.; del Valle, F.; Villoria de la Mano, J. A.; Fierro, J. L. G., *ChemSusChem* **2007,** *2*, 471-485.
22. Aroutiounian, V. M.; Arakelyan, V. M.; Shahnazaryan, G. E., *Sol. Energy* **2005,** *78*, 581-592.
23. Kato, H.; Kudo, A., *J. Phys. Chem. B.* **2001,** *105*, 4285-4292.
24. Kim, H. G.; Hwang, D. W.; Kim, J.; Kim, Y. G.; Lee, J. S., *Chem. Commun.* **1999,** *12*, 1077-1078.
25. Gerischer, H.; Mindt, W., *Electrochim. Acta* **1968,** *13*, 1329-1341.
26. Frank, A. J.; Honda, K., *J. Phys. Chem.* **1982,** *86*, 1933-1935.
27. Frank, A. J.; Honda, K., *J. Photochem.* **1985,** *29*, 195-204.
28. Suleymanov, A. S., *Int. J. Hydrogen Energy* **1991,** *16*, 741-743.
29. Kaneko, M.; Yao, G.-J.; Kira, A., *Chem. Commun.* **1989**, 1338-1939.
30. Yan, X.; Liu, G.; Wang, L.; Wang, Y.; Zhu, X.; Zou, J.; Lu, G. Q., *J. Mater. Res.* **2010,** *25*, 182-188.
31. Lewis, N. S., *Science* **2007,** *315*, 798-801.
32. Inoue, Y., *Energy Environ. Sci.* **2009,** *2*, 364-386.

33. Lomoth, R.; Magnuson, A.; Sjödin, M.; Huang, P.; Styring, S.; Hammarström, L., *Photosynth. Res.* **2005,** *87*, 25-40.
34. Magnuson, A.; Anderlund, O. J.; Lindblad, P.; Lomoth, R.; Polivka, T.; Ott, S.; Stensjö, K.; Styring, S.; Sundström, V.; Hammarström, L., *Acc. Chem. Res.* **2009,** *42*, 1899-1909.
35. Burdinski, D.; Wieghardt, K.; Steenken, S., *J. Am. Chem. Soc* **1999,** *121*, 10781-10787.
36. Sun, L.; Hammarström, L.; Akermark, B.; Styring, S., *Chem. Soc. Rev.* **2001,** *30*, 36-49.
37. Huang, P.; Magnuson, A.; Lomoth, R.; Abrahamsson, M.; Tamm, M.; Sun, L.; van Rotterdam, B.; Park, J.; Hammarström, L.; Åkermark, B.; Styring, S., *J. Inorg. Biochem.* **2002,** *91*, 159-172.
38. Weare, W. W.; Pushkar, Y.; Yachandra, V. K.; Frei, H., *J. Am. Chem. Soc* **2008,** *130*, 11355-11363.
39. Han, H.; Frei, H., *J. Phys. Chem. C* **2008,** *112*, 16156-16159.
40. Geletii, Y. V.; Huang, Z.; Hou, Y.; Musaev, D. G.; Lian, T.; Hill, C. L., *J. Am. Chem. Soc.* **2009,** *131*, 7522-7523.
41. Gray, H. B., *Nat. Chem.* **2009,** *1*, 7-7.
42. Gardner, R. F. G.; Sweett, F.; Tanner, D. W., *J. Phys. Chem. Solids* **1963,** *24*, 1183-1186.
43. Kennedy, J. H.; Frese, K. W., Jr., *J. Electrochem. Soc.* **1978,** *125*, 709-14.
44. Dare-Edwards, M. P.; Goodenough, J. B.; Hamnett, A.; Trevellick, P. R., *J. Chem. Soc., Faraday Trans.* **1983,** *79*, 2027-2041.
45. Hardee, K. L.; Bard, A. J., *J. Electrochem. Soc.* **1976,** *123*, 1024-1026.
46. Hardee, K. L.; Bard, A. J., *J. Electrochem. Soc.* **1977,** *124*, 215-224.
47. Yeh, L.-S. R.; Hackerman, N., *J. Electrochem. Soc.* **1977,** *124*, 833-836.
48. Bjoerksten, U.; Moser, J.; Grätzel, M., *Chem. Mater.* **1994,** *6*, 858-863.
49. Khan, S. U. M.; Akikusa, J., *J. Phys. Chem. B* **1999,** *103*, 7184-7189.
50. Sartoretti, C. J.; Alexander, B. D.; Solarska, R.; Rutkowska, I. A.; Augustynski, J.; Cerny, R., *J. Phys. Chem. B* **2005,** *109*, 13685-13692.
51. Sartoretti, C. J.; Ulmann, M.; Alexander, B. D.; Augustynski, J.; Weidenkaff, A., *Chem. Phys. Lett.* **2003,** *376*, 194-200.
52. Satsangi, V. R.; Kumari, S.; Singh, A. P.; Shrivastav, R.; Dass, S., *Int. J. Hydrogen Energy* **2008,** *33*, 312-318.
53. Duret, A.; Grätzel, M., *J. Phys. Chem. B* **2005,** *109*, 17184-17191.
54. Cesar, I.; Kay, A.; Gonzalez Martinez, J. A.; Grätzel, M., *J. Am. Chem. Soc.* **2006,** *128*, 4582-4583.
55. Kay, A.; Cesar, I.; Grätzel, M., *J. Am. Chem. Soc.* **2006,** *128*, 15714-15721.
56. Cesar, I.; Sivula, K.; Kay, A.; Zboril, R.; Grätzel, M., *J. Phys. Chem. C* **2009,** *113*, 772-782.
57. Iordanova, N.; Dupuis, M.; Rosso, K. M., *J. Chem. Phys.* **2005,** *122*, 144305-10.
58. Hu, Y.-S.; Kleiman-Shwarsctein, A.; Forman, A. J.; Hazen, D.; Park, J.-N.; McFarland, E. W., *Chem. Mater.* **2008,** *20*, 3803-3805.
59. Kleiman-Shwarsctein, A.; Hu, Y.-S.; Forman, A. J.; Stucky, G. D.; McFarland, E. W., *J. Phys. Chem. C* **2008,** *112*, 15900-15907.
60. Spray, R. L.; Choi, K.-S., *Chem. Mater.* **2009,** *21*, 3701-3709.
61. Souza, F. L.; Lopes, K. P.; Nascente, P. A. P.; Leite, E. R., *Sol. Energy Mater. Sol. Cells* **2009,** *93*, 362-368.

62. Glasscock, J. A.; Barnes, P. R. F.; Plumb, I. C.; Savvides, N., *J. Phys. Chem. C* **2007,** *111*, 16477-16488.
63. Hu, Y.-S.; Kleiman-Shwarsctein, A.; Stucky, G. D.; McFarland, E. W., *Chem. Comm.* **2009**, 2652-2654.
64. Spurgeon, J. M.; Atwater, H. A.; Lewis, N. S., *J. Phys. Chem. C* **2008,** *112*, 6186-6193.
65. Beermann, N.; Vayssieres, L.; Lindquist, S.-E.; Hagfeldt, A., *J. Electrochem. Soc.* **2000,** *147*, 2456-2461.
66. Lindgren, T.; Wang, H.; Beermann, N.; Vayssieres, L.; Hagfeldt, A.; Lindquist, S.-E., *Sol. Energy Mater.* **2002,** *71*, 231-243.
67. Tahir, A. A.; Wijayantha, K. G. U.; Saremi-Yarahmadi, S.; Mazhar, M.; McKee, V., *Chem. Mater.* **2009,** *21*, 3763-3772.
68. LaTempa, T. J.; Feng, X.; Paulose, M.; Grimes, C. A., *J. Phys. Chem. C* **2009,** *113*, 16293-16298.
69. Mohapatra, S. K.; John, S. E.; Banerjee, S.; Misra, M., *Chem. Mater.* **2009,** *21*, 3048-3055.
70. Rangaraju, R. R.; Panday, A.; Raja, K. S.; Misra, M., *J. Phys. D: Appl. Phys.* **2009,** *42*, 135303.
71. Yano, J.; Kern, J.; Sauer, K.; Latimer, M. J.; Pushkar, Y.; Biesiadka, J.; Loll, B.; Saenger, W.; Messinger, J.; Zouni, A.; Yachandra, V. K., *Science* **2006,** *314*, 821-825.
72. Harriman, A.; Pickering, I. J.; Thomas, J. M.; Christensen, P. A., *J. Chem. Soc., Faraday Trans. 1* **1988,** *84*, 2795 - 2806.
73. Mills, A., *Chem. Soc. Rev.* **1989,** *18*, 285 - 316.
74. Ruttinger, W.; Dismukes, G. C., *Chem. Rev.* **1997,** *97*, 1-24.
75. Yagi, M.; Kaneko, M., *Chem. Rev.* **2001,** *101*, 21-35.
76. Brimblecombe, R.; Dismukes, G. C.; Swiegers, G. F.; Spiccia, L., *Dalton Trans.* **2009**, 9374-9384.
77. Sala, X.; Romero, I.; Rodríguez, M.; Escriche, L.; Llobet, A., *Angew. Chem. Int. Ed.* **2009,** *48*, 2842-2852.
78. Concepcion, J. J.; Jurss, J. W.; Brennaman, M. K.; Hoertz, P. G.; Patrocinio, A. O. v. T.; Murakami Iha, N. Y.; Templeton, J. L.; Meyer, T. J., *Acc. Chem. Res.* **2009,** *42*, 1954-1965.
79. Kanan, M. W.; Nocera, D. G., *Science* **2008,** *321*, 1072-1075.
80. Lutterman, D. A.; Surendranath, Y.; Nocera, D. G., *J. Am. Chem. Soc.* **2009,** *131*, 3838-3839.
81. Surendranath, Y.; Dincă, M.; Nocera, D. G., *J. Am. Chem. Soc.* **2009,** *131*, 2615-2620.
82. Kanan, M. W.; Surendranath, Y.; Nocera, D. G., *Chem. Soc. Rev.* **2009,** *38*, 109-114.
83. Risch, M.; Khare, V.; Zaharieva, I.; Gerencser, L.; Chernev, P.; Dau, H., *J. Am. Chem. Soc.* **2009,** *131*, 6936-6937.
84. Majumder, S. A.; Khan, S. U. M., *Int. J. Hydrogen Energy* **1994,** *19*, 881-887.
85. Wang, C. M.; Mallouk, T. E., *J. Phys. Chem.* **1990,** *94*, 423-428.
86. Wang, C. M.; Mallouk, T. E., *J. Phys. Chem.* **1990,** *94*, 4276-4280.
87. Cheng, X. F.; Leng, W. H.; Liu, D. P.; Xu, Y. M.; Zhang, J. Q.; Cao, C. N., *J. Phys. Chem. C* **2008,** *112*, 8725-8734.
88. Zhong, D. K.; Sun, J.; Inumaru, H.; Gamelin, D. R., *J. Am. Chem. Soc.* **2009,** *131*, 6086-6087.
89. Zhong, D. K.; Gamelin, D. R., *J. Am. Chem. Soc.* **2010,** *132*, 4202-4207.
90. Steinmiller, E. M. P.; Choi, K.-S., *Proc. Nat. Acad. Sci.* **2009,** *106*, 20633-20636.
91. Linsebigler, A. L.; Lu, G.; Yates, J. T., *Chem. Rev.* **1995,** *95*, 735-758.
92. Ni, M.; Leung, M. K. H.; Leung, D. Y. C.; Sumathy, K., *Renewable Sustainable Energy Rev.* **2006,** *11*, 401-425.

93. O'Regan, B.; Grätzel, M., *Nature* **1991,** *353*, 737-740.
94. Grätzel, M., *J. Photochem. Photobiol., C* **2003,** *4*, 145-153.
95. Youngblood, W. J.; Lee, S.-H. A.; Kobayashi, Y.; Hernandez-Pagan, E. A.; Hoertz, P. G.; Moore, T. A.; Moore, A. L.; Gust, D.; Mallouk, T. E., *J. Am. Chem. Soc.* **2009,** *131*, 926-927.
96. Youngblood, W. J.; Lee, S.-H. A.; Maeda, K.; Mallouk, T. E., *Acc. Chem. Res.* **2009,** *42*, 1966-1973.
97. Mola, J.; Mas-Marza, E.; Sala, X.; Romero, I.; Rodríguez, M.; Viñas, C.; Parella, T.; Llobet, A., *Angew. Chem. Int. Ed.* **2008,** *47*, 5830-5832.
98. Li, G.; Sproviero, E. M.; Snoeberger III, R. C.; Iguchi, N.; Blakemore, J. D.; Crabtree, R. H.; Brudvig, G. W.; Batista, V. S., *Energy Environ. Sci.* **2009,** *2*, 230-238.
99. Brimblecombe, R.; Koo, A.; Dismukes, G. C.; Swiegers, G. F.; Spiccia, L., *J. Am. Chem. Soc.* **2010,** *132*, 2892-2894.
100. Chen, Z.; Concepcion, J. J.; Jurss, J. W.; Meyer, T. J., *J. Am. Chem. Soc.* **2009,** *131*, 15580-15581.
101. Ardo, S.; Meyer, G. J., *Chem. Soc. Rev.* **2009,** *38*, 115-164.

Chapter 3: Solar Water Oxidation by Composite Catalyst/α-Fe_2O_3 Photoanodes

The successful integration of a competent electrocatalyst with a photoanode material is essential in demonstrating the effectiveness of a division-of-labor approach in enhancing photoelectrochemical (PEC) water oxidation. In this chapter, an amorphous cobalt catalyst is conformally electrodeposited onto a prototypical α-Fe_2O_3 photoanode to create a composite catalyst/α-Fe_2O_3 photoanode. α-Fe_2O_3 is a robust, inexpensive, visible light absorbing material that is suitable for tandem solar water splitting, but exhibits poor water oxidation kinetics, leading to high operating potentials. Surface modification with an inexpensive, Earth-abundant cobalt-phosphate water oxidation catalyst (Co-Pi) is expected to decrease the external bias required to drive this reaction. Results from PEC experiments are presented and demonstrate that separating photon absorption, charge separation, and water oxidation catalysis in composite photoanodes is a promising strategy for improving solar hydrogen production. The work in this chapter is reprinted with permission from Zhong, D. K., Sun, J., Inumaru, H., Gamelin, D. R. *J. Am. Chem. Soc.*, **2009**, *131*, 6086-6087.

3.1 Introduction

The photoelectrochemical (PEC) conversion of photon power into chemical fuels is an attractive approach to storing solar energy,[1-6] but it poses many fundamental chemical challenges. Hematite (α-Fe_2O_3) has emerged as a prototype photoanode material for testing strategies to overcome the challenging four-electron oxidation of water, which under basic conditions is described by Equation 3.1.

$$4OH^- \rightarrow O_2 + 4e^- + 2H_2O \qquad \text{(Equation 3.1)}$$

Hematite meets many of the target photoanode requirements: It is inexpensive, oxidatively robust, environmentally benign, and it absorbs visible light (E_g ~ 2.1 eV). Although the α-Fe_2O_3 valence band edge potential is >1 V more negative than required for Equation 3.1 thermodynamically, water oxidation by photogenerated valence-band holes in α-Fe_2O_3 is kinetically inefficient, and additional anodic overpotentials are typically required before significant PEC water splitting is observed. A remaining fundamental limitation of α-Fe_2O_3 is that its conduction band edge potential resides ~200 mV below that required to drive the cathodic half reaction (Equation 3.2).

$$2H_2O + 2e^- \rightarrow H_2 + 2OH^- \qquad \text{(Equation 3.2)}$$

Tandem PEC/photovoltaic (PV) configurations have been envisioned to provide the bias needed to meet these demands.[7-10] Recent advances in controlled growth and doping of α-Fe_2O_3 nanostructures[5-14] have overcome many of the limitations associated with the short hole-diffusion length (~2-4 nm), low electron mobility (~10^{-1} cm^2 V^{-1} s^{-1}), and efficient charge carrier recombination characteristics of bulk α-Fe_2O_3, yielding promising PEC performance. For example, an overall solar-to-hydrogen power conversion efficiency of ~2.1% has been estimated for one set of mesostructured α-Fe_2O_3 photoanodes when powered by a PV device providing

1.4 V in a tandem configuration.[8] Unfortunately, many low-cost PV devices such as dye-sensitized solar cells or organic PVs typically provide <1 V, and two such PVs in series would thus be required to provide the necessary 1.4 V. The development of α-Fe_2O_3 photoanodes that require smaller overpotentials to oxidize water, such that they could be powered by single low-cost PV cells, would thus be attractive for reducing solar hydrogen production costs.

Recently, electrochemical water oxidation with low overpotentials was demonstrated over a range of pH values using an amorphous cobalt/phosphate catalyst ("Co-Pi") electrodeposited onto ITO or FTO electrodes.[15-17] Remaining uncertainties about the catalyst's precise microscopic identity do not diminish its attractiveness for water-splitting PECs. Co-Pi requires only a 0.41 V overpotential at pH 7 to oxidize water with a current density of 1 mA/cm^2,[15] whereas the α-Fe_2O_3 valence band edge potential provides >~1.2 V. Photogenerated holes in α-Fe_2O_3 should thus be amply capable of driving water oxidation by this electrocatalyst. Here we report that composite photoanodes made by electrodeposition of Co-Pi onto mesostructured α-Fe_2O_3 show >350 mV cathodic shifts of the onset potential for PEC water oxidation while retaining substantial photocurrent densities.

3.2 Experimental Details

Following previous reports,[8-10] mesostructured Si-doped α-Fe_2O_3 photoanodes of 400-500 nm thickness were grown on F:SnO_2 (FTO)-coated glass substrates (TEC15, 15 Ω/□ Hartford Glass Co.) by atmospheric pressure chemical vapor deposition (APCVD) using $Fe(CO)_5$ and TEOS as precursors, delivered to an FTO substrate at 470 °C using Ar carrier gas. The precursors, $Fe(CO)_5$ (Aldrich 99.999%) and TEOS (Aldrich 99.999%), were delivered by bubbling Ar gas (Praxair, 5.0 Ultra High Purity) at 11.3 and 19.4 mL/min, respectively, controlled by mass flow controllers. The gas was then mixed with air flowing at 2L/min and directed by a glass tube onto the lower portion of a 50×13×2.3 mm^3 FTO substrate kept at 470°. The Co-Pi catalyst was electrodeposited onto the oxide anodes following the procedures described in ref. 6. The anode was submerged in a buffer solution of 0.1 M potassium phosphate (pH 7) containing 0.5 mM $Co(NO_3)_2$ and a bias of 1.29 V (vs. NHE) was applied for 1hr. For PEC measurements, the anode surface was masked during electrodeposition to yield a catalyst-covered area that matched the irradiated area (ø = 6 mm). Masking was achieved using electrical tape, which was then removed for PEC measurements. Composite Co-Pi/α-Fe_2O_3 anodes for which the mask was not used showed greater dark currents from the Co-Pi catalyst, but were otherwise very similar.

Electronic absorption spectra were measured using a Cary 500 UV/vis/NIR spectrophotometer (Varian). SEM images were collected using a FEI Sirion scanning electron microscope operating at 5 kV.

Electrochemical measurements were performed in a three-electrode configuration using an aqueous hydroxide electrolyte (1 M NaOH, pH 13.6), a Pt counter electrode, and an Ag/AgCl reference electrode. In a typical measurement, a titanium clasp was used to make contact with the upper 25% of the 4 cm long anode, where no α-Fe_2O_3 had been deposited. The bottom ~50% of the anode was submerged in the electrolyte solution in a home-built optical cell. Cyclic voltammetry measurements were performed using a computer-controlled Eco Chemie μAutolab II potentiostat. Potentials are reported *vs* both Ag/AgCl and RHE, the latter obtained using the formula $E_{RHE} = E_{AgCl} + 0.059\ pH\ + 0.1976V$. Photocurrent densities were measured as a function of

applied voltage under simulated AM1.5 solar irradiation (1 sun), achieved using an Oriel 96000 solar simulator integrating a 150 W Xe arc lamp and Oriel 81094 filter, and delivered to the anode via fiber optic. IPCE measurements were performed using a Xe arc lamp with an Oriel Cornerstone 74000 monochromator with slits set to ~10 nm spectral bandwidth at the designated bias voltage provided by the potentiostat. The wavelength was scanned at 1 nm/s. Photon power densities were determined using a calibrated Si photodiode. Dark current measurements probe the entire submerged FTO + α-Fe_2O_3 (or Co-Pi/α-Fe_2O_3) surface, whereas photocurrents represent the response achieved from just the irradiated area normalized to 1 cm^2. This area was circular with a diameter of 6 mm. Typical monochromatic photon power densities in the IPCE measurements were ~0.50W/m^2.

For the data shown in Figure 3.2, the α-Fe_2O_3 photoanode data were collected first, then the Co-Pi catalyst was deposited onto the same α-Fe_2O_3 photoanode, and then the analogous data were collected on the Co-Pi/α-Fe_2O_3 photoanode.

3.3 Results and Discussion

SEM images of a representative α-Fe_2O_3 photoanode are shown in Figure 3.1a,b and reveal a highly structured electrode surface. PEC measurements were then performed in a three-electrode configuration using an aqueous OH^- electrolyte (1 M NaOH, pH 13.6), a Pt counter electrode, and Ag/AgCl as the reference electrode. Photocurrent densities were measured as a function of applied voltage under simulated 1 sun AM1.5 solar irradiation (see Appendix A). As in previous studies, the α-Fe_2O_3 PEC performance was found to depend strongly on surface morphology, Si doping level, and growth temperature, among other parameters.[7-10]

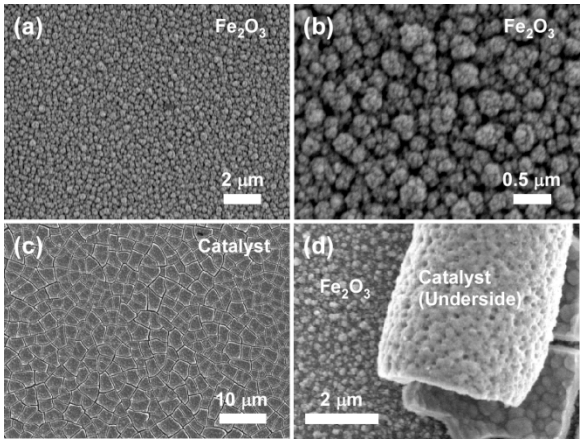

Figure 3.1. SEM Images of α-Fe_2O_3 and Co-Pi/α-Fe_2O_3 Photoanodes
SEM images of mesostructured α-Fe_2O_3 photoanode before **(a,b)** and after **(c,d)** electrodeposition of Co-Pi catalyst. The catalyst layer cracking occurs upon drying for the SEM measurement and in some cases allows inspection of the catalyst underside: Panel (d) shows that the Co-Pi underside topology conforms to the α-Fe_2O_3 mesostructure.

Figure 3.2a shows dark and photocurrent densities for an α-Fe_2O_3 photoanode with backside illumination. Whereas the dark response is negligible up to 1.5 V *vs* RHE, the photoresponse shows a rise and plateau with an onset voltage of ~1 V that typifies α-Fe_2O_3. Figure 3.1c,d show SEM images of a representative α-Fe_2O_3 photoanode following Co-Pi electrodeposition for 1 hr as described in ref. 7. Extensive cracking of the ~200 nm thick catalyst layer occurs upon drying for the SEM measurement. Figure 3.1d shows a portion of the catalyst layer that has curled off of the α-Fe_2O_3 film upon drying, revealing the catalyst underside. This image

shows the inverse mesostructure from the α-Fe_2O_3 anode, demonstrating that the catalyst layer conforms to the topology of the α-Fe_2O_3 surface. A high degree of interfacial contact between the α-Fe_2O_3 and catalyst layers has thus been achieved. Figure 3.2a also shows the dark and photocurrent density responses of the Co-Pi/α-Fe_2O_3 composite photoanode prepared by electrodeposition of the Co-Pi catalyst on the same α-Fe_2O_3 photoanode. The major phenomenological observation is that modification of α-Fe_2O_3 with Co-Pi catalyst reduces the bias voltage required for solar PEC water oxidation by >350 mV, corresponding to a reduction from ~1.2 to <~0.9 V that would be required from the PV in a water splitting PEC/PV tandem cell.

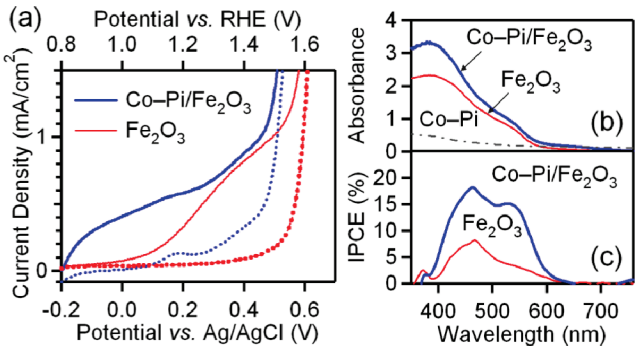

Figure 3.2. PEC and Spectroscopic Measurements of a Co-Pi/α-Fe_2O_3 Photoanode
a) Dark (dashed) and photocurrent (solid) densities for α-Fe_2O_3 (red) and Co-Pi/α-Fe_2O_3 (blue) photoanodes, collected using simulated AM1.5 illumination (1 sun, backside). **b)** Electronic absorption and **c)** IPCE spectra for α-Fe_2O_3 and Co-Pi/α-Fe_2O_3 (at 1.23 and 1 V *vs* RHE, respectively). The absorption spectrum of Co-Pi on FTO without α-Fe_2O_3 is included in (b), but no photocurrent was detected for these anodes.

At 1.4 V (RHE), α-Fe_2O_3 photocurrent densities with front-side illumination are ~2x greater than with backside illumination (see Appendix A), a common observation[8-10] attributable to the greater surface area of the anode front. In the Co-Pi/α-Fe_2O_3 anodes, however, front-side illumination did not greatly enhance the photocurrent, likely because of nonproductive photon absorption by the catalyst layer. Co-Pi absorbs throughout the visible spectral region (Figure 3.2b) but generates no detectable photocurrent, either on α-Fe_2O_3 or directly on FTO. IPCE measurements of the α-Fe_2O_3 (1.23 V *vs* RHE) and Co-Pi/α-Fe_2O_3 (1 V *vs* RHE) photoanodes using backside illumination show essentially identical dispersion (Figure 3.2c), in both cases apparently deriving only from α-Fe_2O_3 excitation. Co-Pi thus behaves strictly as a surface electrocatalyst. The composite photoanode of Figure 3.2c shows IPCE > 15% at 550 nm and 1 V *vs* RHE, conditions where α-Fe_2O_3 alone shows negligible photocurrent (Figure 3.2a). This IPCE maximizes at 450 nm (18%) before decreasing again below ~400 nm because of the decreasing light penetration depth (Figure 3.2b).

Several control experiments were performed to test the possibility that the cathodic photocurrent shift might derive from an unintended side reaction. The possibility of dissolved cobalt acting as redox mediator, or of an unidentified sacrificial reagent contributing to photocurrent, was eliminated by the following observations: (i) Addition of solvated Co^{2+} to the electrolyte had no noticeable effect on current densities (see Appendix A); (ii) Replacement of the PEC electrolyte solution with new stock solution caused no change in photocurrent and did not lead to a photocurrent induction period; (iii) Continuous photocatalysis at 1 V vs RHE for >10 hrs showed no change in performance. We conclude that the cathodic shift in Figure 3.2 reflects the ability to drive Equation 3.1 at much smaller overpotentials using the composite photoanodes than with α-Fe_2O_3 alone.

Most α-Fe_2O_3 PEC cells operating under similar conditions show negligible photocurrent densities below 1 V vs RHE. Modification of the α-Fe_2O_3 surface by adsorption of Co^{2+} from aqueous 10 mM $Co(NO_3)_2$ was previously shown to cause an ~17% increase in current density at 1.23 V vs RHE and an 80 mV cathodic shift of the onset potential. Similarly, growth of RuO_2 onto α-Fe_2O_3 surfaces led to a 120 mV cathodic shift of the onset potential with <80 μA/cm^2 at 1 V vs RHE.[12] Interestingly, α-Fe_2O_3 nanorods have shown greater relative photocurrent densities at low bias than typical mesostructured α-Fe_2O_3 photoanodes, but with photocurrent densities of only ~2 μA/cm^2.[14] We hypothesize that the conformal catalyst deposition facilitates interfacial hole transfer from α-Fe_2O_3 to Co-Pi, allowing photon absorption and redox catalysis to be effectively decoupled while retaining photocurrent densities. Efficient hole transfer from α-Fe_2O_3 to Co-Pi should enhance the electron gradient in the α-Fe_2O_3 mesostructure under irradiation, also contributing to the driving force for electron diffusion to the FTO and reducing deleterious carrier recombination processes. Catalyst electrodeposition onto α-Fe_2O_3 may also passivate surface defects.

3.4. Summary

The experimental results for the Co-Pi/α-Fe_2O_3 composite photoanodes are summarized in the scheme in Figure 3.3. Photoexcitation of α-Fe_2O_3 generates an electron-hole pair. The photogenerated holes are trapped by the Co-Pi catalyst, which excels at water oxidation. Photogenerated electrons migrate to the FTO back contact and pass through the circuit to the Pt counter electrode, where water reduction occurs in the three-electrode configuration. The present results demonstrate that partitioning photoabsorption, charge separation, and redox catalysis in composite photoanodes offer promising opportunities for improving solar water-splitting PECs. A complete microscopic understanding of these composite photoanodes will require a better understanding of the Co-Pi/α-Fe_2O_3 interface and of hole transfer across this interface.

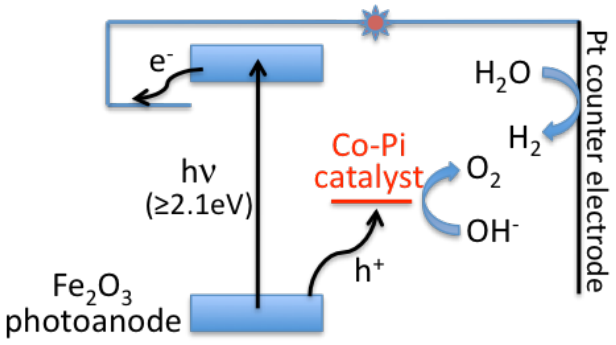

Figure 3.3. Scheme for PEC Water Oxidation with Co-Pi/α-Fe_2O_3

3.5 Notes to Chapter 3

1. Heller, A., *Science* **1984,** *223*, 1141-1148.
2. Grätzel, M., *Nature* **2001,** *414*, 338-344.
3. Lewis, N. S.; Nocera, D. G., *Proc. Nat. Acad. Sci.* **2006,** *103*, 15729-15735.
4. Lewis, N. S., *Science* **2007,** *315*, 798-801.
5. Grimes, C. A.; Varghese, O. K.; Ranjan, S., *Light, Water, Hydrogen*. Springer: New York, 2007.

6. van de Krol, R.; Liang, Y.; Schoonman, J., *J. Mater. Chem.* **2008,** *18*, 2311-2320.
7. Duret, A.; Grätzel, M., *J. Phys. Chem. B* **2005,** *109*, 17184-17191.
8. Cesar, I.; Kay, A.; Gonzalez Martinez, J. A.; Grätzel, M., *J. Am. Chem. Soc.* **2006,** *128*, 4582-4583.
9. Kay, A.; Cesar, I.; Grätzel, M., *J. Am. Chem. Soc.* **2006,** *128*, 15714-15721.
10. Cesar, I.; Sivula, K.; Kay, A.; Zboril, R.; Grätzel, M., *J. Phys. Chem. C* **2009,** *113*, 772-782.
11. Ingler, W. B., Jr.; Khan, S. U. M., *Electrochem. Solid-State Lett.* **2006,** *9*, G144-G146.
12. Majumder, S. A.; Khan, S. U. M., *Int. J. Hydrogen Energy* **1994,** *19*, 881-887.
13. Kleiman-Shwarsctein, A.; Hu, Y.-S.; Forman, A. J.; Stucky, G. D.; McFarland, E. W., *J. Phys. Chem. C* **2008,** *112*, 15900-15907.
14. Lindgren, T.; Wang, H.; Beermann, N.; Vayssieres, L.; Hagfeldt, A.; Lindquist, S.-E., *Sol. Energy Mater.* **2002,** *71*, 231-243.
15. Kanan, M. W.; Nocera, D. G., *Science* **2008,** *321*, 1072-1075.
16. Surendranath, Y.; Dincă, M.; Nocera, D. G., *J. Am. Chem. Soc.* **2009,** *131*, 2615-2620.
17. Lutterman, D. A.; Surendranath, Y.; Nocera, D. G., *J. Am. Chem. Soc.* **2009,** *131*, 3838-3839.

Chapter 4: Photoelectrochemical Water Oxidation by Cobalt Catalyst ("Co-Pi")/α-Fe_2O_3 Composite Photoanodes: Oxygen Evolution and Resolution of a Kinetic Bottleneck

One of the major advantages of the division-of-labor approach to solar water splitting is the flexibility to optimize each component separately. Following the demonstration of enhanced photoelectrochemical (PEC) water oxidation with composite Co-Pi/α-Fe_2O_3 photoanodes, we sought to optimize each individual component for photon conversion and catalysis. In this chapter, the composite photoanodes are optimized for solar water oxidation under front-side illumination in pH 8 electrolytes, the pH of natural seawater. During the course of optimization, a kinetic bottleneck limiting the performance of such photoanodes was identified and shown to be largely overcome by more sparse deposition of Co-Pi onto the α-Fe_2O_3. PEC measurements and sustained O_2 evolution data are presented and demonstrate that integration of this promising water oxidation catalyst with a photon-harvesting substrate can provide a substantial reduction in the external power needed to drive the catalyst's electrochemistry. The work described in this chapter is reprinted with permission from Zhong, D. K., Gamelin, D. R. *J. Am. Chem. Soc.*, **2010**, *132*, 4202-4207.

4.1 Introduction

Photoelectrochemical (PEC) water splitting has been envisioned as a promising strategy for collecting the energy of sunlight and storing it in the form of chemical bonds.[1-5] Water splitting is complicated by its multi-electron nature (Equations 4.1 and 4.2). The more challenging of these two processes, water oxidation (Equation 4.1), requires removal of a total of four electrons and four protons from two water molecules to form one O_2 molecule.

$$2H_2O \rightarrow O_2 + 4H^+ + 4e^- \qquad \text{(Equation 4.1)}$$

$$4H^+ + 4e^- \rightarrow 2H_2 \qquad \text{(Equation 4.2)}$$

Solar PEC water splitting has been explored extensively, but is still hindered by the major challenge of identifying photoelectrode materials that are simultaneously inexpensive, efficient, and stable under reaction conditions.[5-7] Much of this challenge ultimately derives from the fact that materials optimized for photon absorption and charge separation are not generally also optimized for catalysis or stability, and vice versa. For example, in PEC cells, photon absorption and water oxidation are typically performed by the same photoanode material (e.g., α-Fe_2O_3, WO_3, N:TiO_2) that has been optimized globally for PEC performance, balancing the needs for photon absorption and charge separation against the demands of stability and catalytic competence. This compromise usually results in the need for high overpotentials to achieve large current densities, limiting the efficiency of this approach for solar energy conversion.

Solar-powered bulk electrolysis allows separation of the tasks of photon absorption and catalysis, and allows optimization of the photon absorption and water splitting functions independently. This is the strategy

implemented in biology, where water oxidation is catalyzed by the Mn_4O_xCa cluster of photosystem II (PS-II) at low overpotentials,[8,9] with the overpotentials ultimately supplied by solar photons absorbed elsewhere by light-harvesting antennae. Substantial research has been directed at developing several attractive synthetic water oxidation electrocatalysts that can operate at low overpotentials,[10-12] but such electrocatalysts frequently contain expensive metals (Ru, Ir) or require extreme pH conditions. Recently, an amorphous cobalt-phosphate-based material, referred to here as "Co-Pi", was discovered that catalyzes water oxidation at relatively low overpotentials in pH 7 phosphate buffer.[13-15] Co-Pi is fabricated on transparent conducting oxide substrates by a simple electrodeposition method from solutions containing 0.5 mM Co^{2+} and 0.1 M potassium phosphate buffered at pH 7. The active catalyst is believed to have a cubane structure loosely resembling the oxygen evolving complex of PS-II.[16-18] Consisting of earth-abundant elements cobalt, potassium, and phosphorus in a ca. 2:1:1 ratio, Co-Pi meets many of the general criteria for widely distributed electrolysis applications.[18,19] To drive this catalyst, a bias of >~1.51 V vs RHE is needed, and current densities of 1.0 mA/cm^2 are reached at approximately +1.7 V vs RHE in pH 7 phosphate buffer (the sum of the thermodynamic potential for water oxidation and the overpotential required to reach 1.0 mA/cm^2 (+1.23 and ~+0.5 V vs RHE, respectively)).[13] The external power required to drive this electrocatalyst is ultimately envisioned as coming from solar photovoltaics or other renewables.[19,20] If some or all of the need for this external power could be eliminated by directly powering the catalyst using a light-harvesting semiconductor substrate (instead of transparent conducting oxides), this approach to solar energy storage could become even more attractive.

As proof of concept, photoelectrolysis by composite photoanodes prepared by deposition of Co-Pi onto the cheap and abundant photoanode material α-Fe_2O_3 was demonstrated recently.[21] It was found that light can supply some of the energy needed to drive water oxidation by Co-Pi in this integrated composite structure, but operation was only demonstrated under caustic conditions (pH > 13), making this system non-ideal.[20] Sustained solar water oxidation by Co-Pi/α-Fe_2O_3 composite photoanodes at lower pH levels remains to be demonstrated. Additionally, improvement of overall efficiencies could be expected from optimization of these photoanodes for front-side illumination, but this was not demonstrated previously.

Here, we report three major improvements of these composite photoanodes: (*i*) Non-productive photon absorption by the catalyst has been diminished sufficiently to allow front-side illumination, yielding an ~200% enhancement of efficiency at +1.0 V vs RHE relative to the previous report; (*ii*) Sustained operation in buffered salt water at pH 8 has been demonstrated; and (*iii*) Sustained O_2 evolution with a ~500% enhancement over the parent α-Fe_2O_3 photoanodes has been demonstrated at +1.0 V vs RHE. By combining Co-Pi with α-Fe_2O_3 photoanodes, the external bias needed to drive water oxidation by this catalyst at 1 mA/cm^2 has been decreased by more than 0.5 V under 1 sun, AM 1.5 solar irradiation.

4.2 Experimental Details

A. Fabrication of α-Fe_2O_3 photoanodes.

Si doped α-Fe_2O_3 photoanodes were fabricated on fluorine doped tin oxide (FTO) glass (50 x 13 x 2.3 mm TEC 15 Hartford Glass Co.) at 470°C for 5 min by atmospheric pressure chemical vapor deposition (APCVD) following procedures reported previously.[21-23] The α-Fe_2O_3 films investigated here were typically ~400-500 nm thick.

B. Electrodeposition of Co-Pi.

For Co-Pi deposition onto α-Fe_2O_3 photoanodes, electrical tape with an aperture that matched the irradiated area during photoelectrochemical (PEC) experiments (ø = 6 mm diameter) was applied onto the α-Fe_2O_3. Co-Pi was then electrodeposited on the exposed area under the conditions communicated previously.[21] As the working electrode, α-Fe_2O_3 was submerged into a solution of 0.5 mM cobalt nitrate in 0.1 M pH 7 potassium phosphate (KPi) buffer. A Pt mesh was used as the counter electrode and saturated Ag/AgCl was used as the reference electrode. Co-Pi was electrodeposited at +1.1 V vs Ag/AgCl for 15 or 30 min. Typical current densities during deposition were ~20-200 μA/cm^2 (see Appendix B). For electrolysis studies involving Co-Pi on FTO, Co-Pi was electrodeposited for 15 min using the above conditions and a mask of 1 cm x 1 cm.

C. Photoelectrochemical experiments.

Current-voltage characteristics were measured using an Eco Chemie μ-Autolab II potentiostat in a home-built three-electrode optical cell using Ag/AgCl as the reference electrode and a Pt wire as the counter electrode. Contact to the photoanodes was made by a titanium clasp attached to the exposed FTO surface at the top of the anode, while the lower portion containing the sample was submerged in the electrolyte. Measurements were performed in 1 M NaOH(aq) at pH 13.6, 0.1 M KPi buffered at pH 8, and 0.1 M NaCl(aq) buffered at pH 8 with 0.1 M KPi. Potentials are reported vs Ag/AgCl (measured) or RHE (obtained using the relationship $E_{RHE} = E_{Ag/AgCl} + 0.0591*pH + 0.1976$ V). Photocurrent densities were measured under 1 sun, AM 1.5 simulated sunlight using an Oriel 96000 solar simulator equipped with a 150 W Xe arc lamp and an Oriel 81094 filter. The photoanodes were masked to illuminate a circular area of 6 mm diameter. Power dependence measurements were performed using an Ag variable neutral density filter, Thorlabs NDC-50C-2M. Unless otherwise stated, all films were illuminated from the front side of the photoanode. Unless otherwise specified, all experiments were performed at room temperature in air atmosphere.

D. Oxygen detection.

The detection of O_2 was performed using a YSI 5000 dissolved oxygen meter equipped with a YSI 5010 self-stirring Clark-type probe in a three-neck flask with an optical window. Before use, the electrolyte (0.1 M KPi buffered at pH 8) was degassed and purged with argon gas. Measurements were conducted in argon in the same three-electrode configuration described for PEC experiments using the same light source. Again, the photoanodes were masked to illuminate a circular area of 6 mm in diameter. Consecutive measurements were taken at +1.0, 1.1, and 1.23 V vs RHE for two hours at each potential. While the light was off between voltages (~160 seconds), there was no increase and sometimes even a decrease in the O_2 level due to consumption by the Clark electrode.

4.3 Results and Analysis

A. Co-Pi/α-Fe_2O_3 photoanode performance under front-side illumination and mild pH conditions.

We have previously reported the PEC performance of Co-Pi/α-Fe_2O_3 composite photoanodes in 1 M NaOH electrolyte using backside illumination, or illumination through the FTO substrate.[21] Backside illumination was more efficient than front-side illumination because of non-productive absorption of photons by the Co-Pi catalyst layer, but the photocurrent densities obtained with this configuration were relatively low (<1 mA/cm^2). α-Fe_2O_3 prepared by the APCVD method gives ~2x more photocurrent density when illuminated

from the front side,[23] however, so optimization of the composite photoanodes for front-side illumination was an objective of the present study. To reduce photon absorption by the catalyst, Co-Pi deposition times were decreased from the original one-hour duration.

Additionally, the basic electrolyte (pH 13.6) used in our previous study is undesirable for practical applications, and demonstration of Co-Pi water oxidation driven by α-Fe_2O_3 at more neutral pH was also an objective of the present study. A gradual decrease in photocurrent density from α-Fe_2O_3 anodes alone was observed under continuous illumination in 0.1 M KPi electrolyte at pH 7 and +1.3 V vs RHE (see Appendix B). We therefore chose to explore PEC measurements in electrolytes at pH 8, which is around the pH of natural seawater.[24] Two approaches were used to achieve this pH. One involved use of 0.1 M potassium phosphate (KPi), the electrolyte used in most Co-Pi electrolysis experiments,[13,15] buffered to pH 8. The second involved 0.1 M NaCl buffered to pH 8 with 0.1 M KPi.

Figure 4.1 shows current-voltage (J–V) curves collected for Co-Pi/α-Fe_2O_3 composite photoanodes prepared with 30 min deposition of Co-Pi and measured in various electrolytes. Each data set is compared to analogous data collected for the same Fe_2O_3 film measured before Co-Pi deposition. Panel (a) shows the J–V curves collected using 1 M NaOH at pH 13.6 and panel (b) shows data collected using 0.1 M KPi at pH 8. As documented previously,[21] in 1 M NaOH, Co-Pi deposition yields a cathodic shift of >350 mV in the photocurrent onset potential relative to α-Fe_2O_3 (Figure 4.1a). PEC measurements in 0.1 M KPi electrolyte at pH 8 also show similar shifts. With front-side illumination there is only a slight decrease in the photocurrent density at high applied potentials (+1.3-1.6 V) compared to α-Fe_2O_3 alone, attributed to partial photon absorption by the catalyst layer. The data in Figure 4.1 demonstrate that Co-Pi/α-Fe_2O_3 composite photoanodes can operate under reduced pH conditions and with front-side illumination.

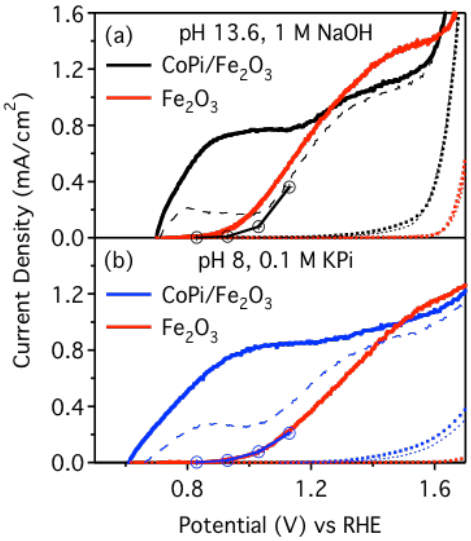

Figure 4.1. *J-V* Curves of Thick Co-Pi/α-Fe_2O_3 Photoanodes in NaOH and KPi
Dark current (dotted) and photocurrent (solid and dashed) densities of α-Fe_2O_3 photoanodes before and after 30 min of Co-Pi deposition, measured in **a)** pH 13.6 NaOH, and **b)** pH 8 KPi at 50 mV/s (thick line) and 10 mV/s (dashed line). The α-Fe_2O_3 data (red curves) were collected at 10 mV/s. The circles denote steady state photocurrent densities after 200 s of continuous illumination under 1 sun, AM 1.5 simulated sunlight.

B. Kinetic bottleneck in Co-Pi/α-Fe_2O_3 composite photoanodes.

In the course of these efforts to optimize the Co-Pi/α-Fe_2O_3 composite photoanodes, it was recognized that improvements in efficiency were often accompanied by increasingly apparent symptoms[25] of kinetic limitations. For example, Figure 4.1 also shows J–V curves of the same Co-Pi/α-Fe_2O_3 composite photoanodes measured at the slower scan rate of 10 mV/s (dashed line). The open circles in Figure 4.1 are the quasi-steady state photocurrent densities measured after 200 s of simulated solar irradiation at each applied potential (*vide infra*). The cathodic shift and photocurrent densities both decrease as the scan rate is slowed, converging on those of the underlying α-Fe_2O_3 at slowest scan rates. Upon increasing the scan rate again, the J–V curves recover their original shape, even after 10+ hours of continuous illumination. Illuminating with chopped light also recovers the photocurrent enhancement. This behavior is largely independent of electrolyte or pH (Figure 4.1), and suggests the existence of a kinetic bottleneck in the performance of these Co-Pi/α-Fe_2O_3 composite photoanodes.

To detail this kinetic bottleneck, its symptoms were explored in various complementary measurements on a single Co-Pi/α-Fe_2O_3 composite photoanode in 0.1 M KPi electrolyte at pH 8. The resulting data are summarized in Figure 4.2. Expanding on Figure 4.1, photocurrents were measured at a greater variety of scan rates to show the evolving characteristics of the J–V curves. With faster scan rates, the first maximum shifts to higher potentials. The inset shows the photocurrent response vs time upon unblocking the light path, measured at +1.1 V vs RHE. A large initial spike in photocurrent upon illumination is followed by multi-exponential decay to a lower steady-state current density with an effective time constant on the order of $\tau \sim 10$ sec, i.e., comparable to the data collection timescale (10s of seconds). At least some of the initial current density in this trace can be attributed to cobalt oxidation, which is an essential step in the water oxidation mechanism.[19] Oxygen detection experiments in 0.1 M KPi at 1 V vs RHE show that this initial high current density is accompanied by a spike in the oxygen evolution rate, however, which then also decreases as the current density decays (see Appendix B). The spike and subsequent current density decay therefore cannot be ascribed solely to an initial charging current for the redox active Co-Pi layer. Figure 4.2b plots the steady-state photocurrent density for a Co-Pi/α-Fe_2O_3 composite photoanode measured as a function of illumination power density between 0 and 1 sun. There is a marked saturation in the photocurrent as the light intensity is increased.

Overall, four major symptoms of this kinetic bottleneck can be identified: (*i*) a scan rate dependence, (*ii*) a kinetic decay in the photocurrent density, (*iii*) photocurrent saturation upon increased illumination, and (*iv*) a sweep-rate-dependent maximum at the beginning of the J–V curve. The sweep-rate dependence of this maximum is a consequence of the superposition of an increasing current density from increasing bias with a current decay of the type illustrated in Figure 4.2(inset).

Parallel measurements were performed for α-Fe_2O_3 photoanodes alone under the same experimental conditions. Under the conditions represented in Figure 4.1, the J–V curves of α-Fe_2O_3 photoanodes did not change significantly with scan rate (data collected at 10 mV/s are plotted in Figure 4.1). In time-dependence measurements, irradiation typically induced a small initial current spike followed by relaxation to a similar steady-state value within a few seconds. Finally, the α-Fe_2O_3 photocurrents increased much more linearly with increasing light intensity under these conditions (Figure 4.2b). These observations suggest that the kinetic

bottleneck is likely associated with the Co-Pi modification, perhaps as an intrinsic limitation of the catalyst under these conditions, or perhaps because of slow interfacial electron transfer.

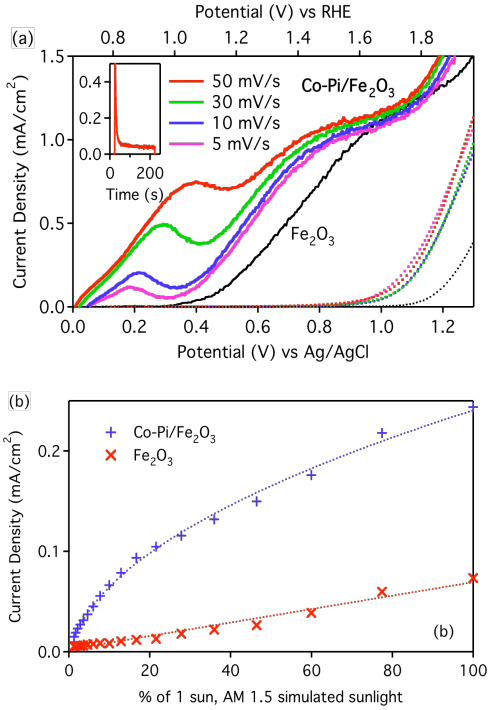

Figure 4.2. Scan Rate and Power Dependence of a Co-Pi/α-Fe_2O_3 Photoanode
a) Dark current (dotted) and photocurrent (solid) densities of an α-Fe_2O_3 photoanode before (thin black) and after 30 min of Co-Pi deposition (thick colored) in 0.1 M KPi electrolyte at pH 8. The α-Fe_2O_3 data (black curves) were collected at 10 mV/s. Inset: Photocurrent density vs time at +1.1 V vs RHE. **b)** Power dependence of photocurrent density for an α-Fe_2O_3 photoanode before (red) and after (blue) Co-Pi deposition, measured at +1.0 V vs RHE.

To test the catalyst alone, Co-Pi was electrodeposited on FTO and electrochemical experiments were conducted in 0.1 M KPi electrolyte buffered to pH 7 with stirring. Figure 4.3 shows the J–V characteristics of Co-Pi at various scan rates, and the current density time dependence under typical electrolysis conditions of +1.1 V vs Ag/AgCl. Like in Figure 4.2, the bulk electrolysis by Co-Pi on FTO also shows a scan rate dependence and a decay in the current density in the region where water oxidation is normally observed, +1.3 V vs NHE, or +1.7 V vs RHE. These observations confirm the hypothesis that the kinetic bottleneck observed in the Co-Pi/α-Fe_2O_3 photoanodes is associated with the Co-Pi catalyst itself rather than with the Co-Pi/α-Fe_2O_3 interface.

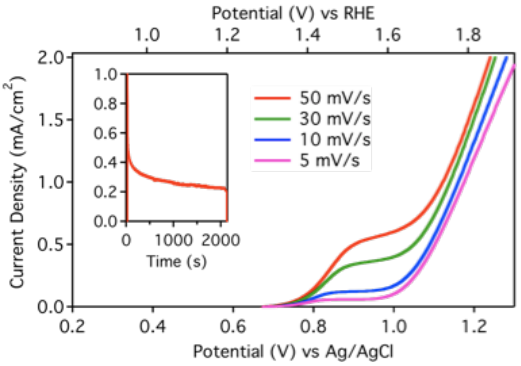

Figure 4.3. Scan Rate Dependence of Co-Pi on FTO
Linear sweep voltammetry of Co-Pi on FTO at various scan rates in pH 7, 0.1 M KPi electrolyte. Inset: Decay of the bulk electrolysis current density over time under these conditions, measured at +1.1 V vs Ag/AgCl (+1.3 V vs NHE).

C. Alleviating the kinetic problem in Co-Pi/α-Fe_2O_3.

If there is a kinetic bottleneck in Co-Pi/α-Fe_2O_3 photoanodes, we hypothesized that even further reduction of the Co-Pi deposition time may remediate the problem. For example, thick layers of Co-Pi may inhibit rapid charge or proton transport from electrolyte through the catalyst, thus restricting current flow and allowing other non-productive recombination pathways to become competitive. To test this possibility, Co-Pi was electrodeposited on α-Fe_2O_3 photoanodes for only 15 min, half the initial deposition time, and a quarter of the time reported previously.[21] Figure 4.4 shows SEM images of the resulting Co-Pi/α-Fe_2O_3 composite photoanode. Unlike the dense coverage of Co-Pi on α-Fe_2O_3 after 1 hr of electrodeposition described previously,[21] 15 min deposition results in only sparse coverage of the α-Fe_2O_3 photoanode by Co-Pi, which now displays ring-like patterns on the surface (Figure 4.4a). These ring patterns are formed from smaller patches of Co-Pi (Figure 4.4b-d). These patches are estimated to be << 100 nm thick, compared to ~200 nm thick film that was deposited during 1 hour deposition,[21] and they show cracking due to drying. The Co-Pi layer conforms to the topology of the α-Fe_2O_3 so well that the microstructure of the α-Fe_2O_3 surface can still even be seen through the catalyst in places. We hypothesize that these patches are somehow associated with scratches or pinholes in the α-Fe_2O_3 that allow current to flow more readily during electrodeposition. Indeed, preliminary energy dispersive X-ray analysis (EDX) experiments demonstrate the existence of a very thin catalyst layer over the entire α-Fe_2O_3 surface, and we thus hypothesize that catalysis is also distributed over the entire surface. Experiments to clarify this issue are underway.

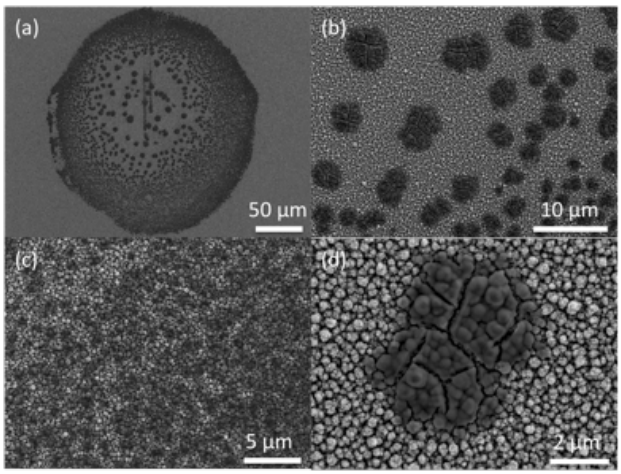

Figure 4.4 Scanning Electron Micrographs of Co-Pi/α-Fe_2O_3 Composite Photoanodes
SEM showing **a)** ring-like deposition of Co-Pi in selective areas of the α-Fe_2O_3 surface, and **b-d)** magnified views of Co-Pi patches within this ring. Panel (d) shows Co-Pi conforming to the topology of the underlying α-Fe_2O_3 mesostructure. The cracks in the Co-Pi result from drying.

PEC measurements were performed on these thinly covered Co-Pi/α-Fe_2O_3 photoanodes and the results are shown in Figure 4.5. Cathodic shifts of ~180 mV are again observed, as are enhanced photocurrents across the entire potential range. Importantly, the J–V curves measured in NaOH electrolytes no longer exhibit the marked scan rate dependence that was observed for the parallel set of photoanodes with greater Co-Pi coverage (Figure 4.1). With a thinner layer of Co-Pi, the enhanced current density is maintained even after 200 sec (Figure 4.5), and the cathodic shift is stable. For PEC measurements conducted in 0.1 M KPi at pH 8, a gradual decay in the photocurrent over time was still evident, and the cathodic shift decreased from ~200 mV to 150 mV after 200 sec of continuous illumination (Figure 4.5b). PEC measurements were also performed in 0.1 M NaCl buffered to pH 8 with KPi. Chloride has been shown previously not to interfere with Co-Pi catalysis at pH 7 in KPi.[14] The resulting J-V curves with NaCl added are essentially indistinguishable from those without NaCl (Figure 4.5b), demonstrating that PEC water oxidation with Co-Pi/α-Fe_2O_3 composite photoanodes can be performed equally well in the presence of chloride.

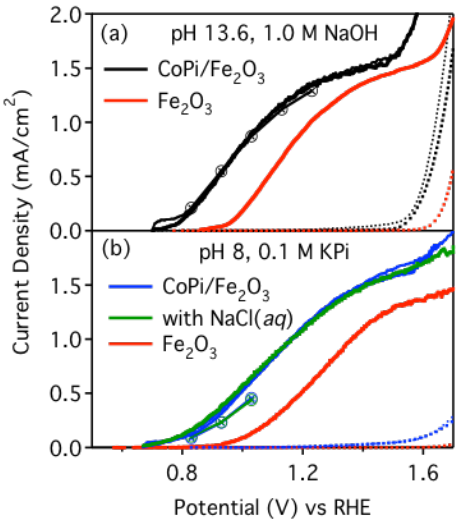

Figure 4.5. *J-V* Curves of Thin Co-Pi/α-Fe_2O_3 Photoanodes in NaOH and KPi
Dark current (dotted) and photocurrent (solid) densities of an α-Fe_2O_3 photoanode before (red) and after 15 min of Co-Pi deposition, measured in **a)** pH 13.6 NaOH, and **b)** pH 8 KPi with (green) and without (blue) 0.1 M NaCl at 50 mV/s (thin line) and 10 mV/s (thick line). The α-Fe_2O_3 data (red curves) were collected at 10 mV/s. The circles denote steady state photocurrent densities after 200 s of continuous illumination under 1 sun, AM 1.5 simulated sunlight.

Figure 4.6 compares the kinetic responses of Co-Pi/α-Fe_2O_3 photoanodes with thicker ((a), 30 min deposition, see Appendix B) and thinner ((b), 15 min deposition, Figure 4.4) Co-Pi coverage. The photocurrent decay curves of panel (a) all show a large initial spike in current density, followed by a multiexponential decrease with $\tau \sim 10$ sec to a small steady-state photocurrent density close to that of the underlying α-Fe_2O_3 photoanode. In contrast, the photoanodes with thinner Co-Pi coverage all show substantially more stable performance. In all cases, the steady-state photocurrent densities in (b) are enhanced relative to those of the parent α-Fe_2O_3 photoanodes (red curves). The result is a sustainable photocurrent density that is enhanced relative to α-Fe_2O_3 by more than an order of magnitude at 0.83 V, where α-Fe_2O_3 alone does not exhibit significant photocurrent (Figure 4.6b). Gains in photocurrent are less substantial at higher applied potentials, likely due to contributions directly from α-Fe_2O_3. Overall, the data in Figures 4.5 and 4.6 demonstrate that reduced Co-Pi deposition onto α-Fe_2O_3 photoanodes circumvents the major kinetic limitations identified above, while still shifting the onset potential of α-Fe_2O_3 by ~180 mV, and simultaneously facilitates front-side illumination for maximum photocurrent densities.

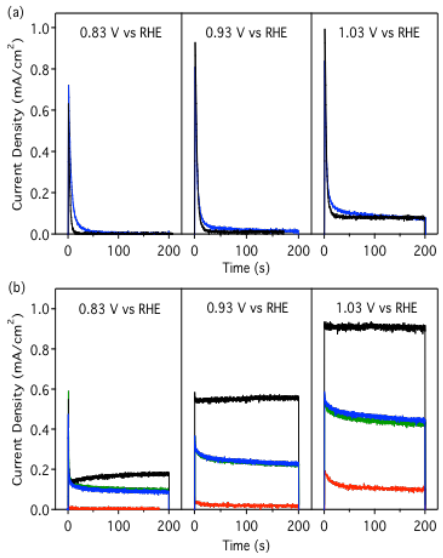

Figure 4.6. Photocurrent Transients of Co-Pi/α-Fe_2O_3 in Various Electrolytes
Photocurrent decay curves measured under 1 sun, AM 1.5 simulated sunlight at various applied potentials for Co-Pi/ α-Fe_2O_3 composite photoanodes in pH 8 KPi (blue), pH 8 buffered salt water (green), and pH 13.6 NaOH (black) electrolytes. **a)** Data collected following 30 min of Co-Pi deposition, and **b)** data collected following 15 min of Co-Pi deposition. Photocurrent decay curves measured for α-Fe_2O_3 in pH 8, 0.1 M KPi electrolyte (red) are included in panel (b) for comparison.

Decreased deposition of Co-Pi onto α-Fe_2O_3 largely overcomes the kinetic limitations described in Figure 4.2, but there is still some evidence of such kinetic effects in KPi electrolyte (Figures 4.5b, 4.6b) that are completely absent in 1 M NaOH. For 1 M NaOH, there is a small initial spike in the photocurrent followed by a small gradual increase to steady state. A similar response has been observed previously in α-Fe_2O_3 at large applied potentials.[26] These observations suggest that the kinetic bottleneck may be related to diffusion of the proton acceptor under these experimental conditions. In the Co-Pi catalytic mechanism proposed in ref. 17, a Co^{3+}-hydroxide intermediate undergoes proton-coupled electron transfer in which the proton is likely removed by the proton-accepting electrolyte. It is conceivable that limited mobility of protons through the amorphous catalyst may contribute to the kinetic bottleneck described by Figures 4.2-4.4, and that OH^- is better able to overcome this limitation. Overall, the data in Figures 4.5 and 4.6 show that this bottleneck is lessened by changing the electrolyte from pH 8 KPi to pH 13.6 NaOH, and is effectively circumvented by reducing the density of catalyst on the α-Fe_2O_3 surface.

D. Oxygen evolution.

In addition to current density measurements, PEC O_2 evolution by the Co-Pi/α-Fe_2O_3 composite photoanodes was also examined. Oxygen evolution was measured at various applied potentials before and after 15 min of Co-Pi electrodeposition onto an α-Fe_2O_3 photoanode. Measurements were performed in 0.1 M KPi electrolyte at pH 8 to allow comparison with electrolysis results collected under similar conditions.[13] Figure 4.7a shows the J–V characteristics of the α-Fe_2O_3 photoanode used for these measurements, before and after Co-Pi deposition, and for both front and backside illumination. Photocurrent densities increased substantially with front-side illumination, particularly at low potentials. Figure 4.7b plots the photocurrent density vs time along with the O_2 concentrations measured simultaneously using the Clark-type electrode.

Sustained photocurrent was observed for the Co-Pi/α-Fe_2O_3 composite photoanode over the course of this ~6 hour experiment. This steady-state photocurrent was enhanced over that of the parent α-Fe_2O_3 film, even after several hours of illumination, and was accompanied by a correspondingly large enhancement in the O_2 evolution rate. The photocurrent density and O_2 evolution enhancement factors (J(Co-Pi/α-Fe_2O_3)/J(α-Fe_2O_3) and {d[O_2]/dt(Co-Pi/α-Fe_2O_3)}/{d[O_2]/dt(α-Fe_2O_3)}, respectively) measured at each applied potential are indicated in Figure 4.7b. The amount of dissolved O_2 detected by the Clark-type electrode was lower than the theoretical maximum for the measured current densities, but this difference is attributable to the adherence of bubbles on the rough surface of the Co-Pi/α-Fe_2O_3 photoanode. Occasional jumps in the photocurrent density were observed for the composite photoanodes and are related to release of these bubbles.

The data in Figure 4.7b show that PEC O_2 evolution by the Co-Pi/α-Fe_2O_3 composite photoanode is enhanced over that of the same α-Fe_2O_3 photoanode without Co-Pi. Despite the gradual decline in photocurrent density for these photoanodes when measured in 0.1 M KPi electrolyte at pH 8 (Figures 4.5, 4.6), after 2 hours of continuous irradiation at +1.0 V vs RHE, ~5 times more oxygen was produced for the Co-Pi modified α-Fe_2O_3 photoanode with no detectable degradation in performance upon re-excitation.

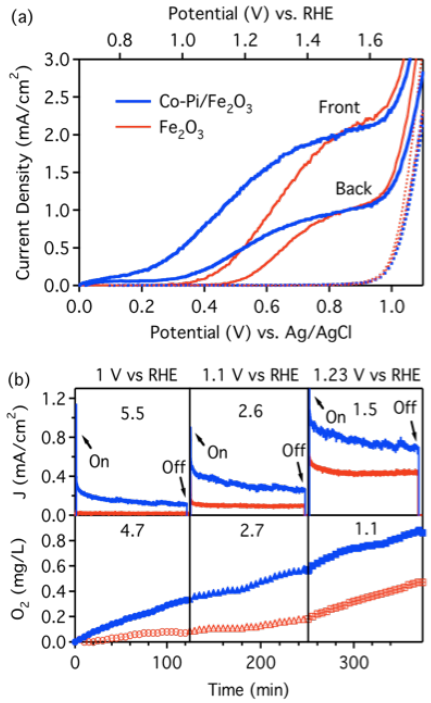

Figure 4.7. PEC and Oxygen Detection Measurements on a Co-Pi/α-Fe_2O_3 Photoanode
a) Dark current (dotted) and photocurrent (solid) densities measured for an α-Fe_2O_3 photoanode before (red) and after (blue) 15 min of Co-Pi deposition. Data collected at 10 mV/s, for both front- and backside illumination. **b)** Photocurrent density and O_2 generation measured for the above photoanodes vs time: Co-Pi/α-Fe_2O_3 (blue) and α-Fe_2O_3 (red). The numbers in (b) indicate the photocurrent and O_2 enhancement factors (see text). Bubbles adhering to and releasing from the photoanode surface cause disruptions in the current density. All PEC data were collected under 1 sun, AM 1.5 simulated solar irradiation.

4.4. Summary

The photoelectrochemical performance of Co-Pi/α-Fe_2O_3 composite photoanodes for water oxidation has been improved by optimization for front-side illumination in pH 8 electrolytes. A kinetic bottleneck was

identified that appears to be related to the Co-Pi catalyst itself under these conditions. This kinetic bottleneck was overcome by more sparse deposition of Co-Pi onto α-Fe_2O_3. Following these improvements, sustained water oxidation by Co-Pi/α-Fe_2O_3 composite photoanodes was demonstrated in both photocurrent and O_2 evolution measurements. Photoelectrochemical water oxidation by the Co-Pi/α-Fe_2O_3 composite photoanodes was enhanced relative to that of α-Fe_2O_3 alone: Under these conditions, a five-fold enhancement in the photocurrent density and water oxidation rate was observed at +1.0 V vs RHE. This enhancement is even more substantial at <1.0 V vs RHE, where α-Fe_2O_3 alone does not exhibit significant photocurrent at all.

It is also interesting to compare these results with those obtained for bulk electrolysis by Co-Pi without a photon-absorbing substrate. By itself, Co-Pi electrolysis current densities reach ~1.2 mA/cm^2 at an applied bias of +1.29 V vs NHE (pH 7),[13] or ~+1.7 V vs RHE. In conjunction with an inexpensive and robust photoanode such as α-Fe_2O_3 under 1 sun, AM 1.5 illumination, the applied bias necessary to achieve the same current density can be reduced by over 0.5 V in buffered salt water at pH 8, the average pH of sea water.[24] The results described here thus demonstrate that sustained O_2 evolution in mild salt water conditions can be achieved with significantly reduced external power demands relative to Co-Pi alone, albeit in the low current density regime, by integrating this catalyst with a light-harvesting semiconductor substrate. The overall process, in which photogenerated holes in α-Fe_2O_3 are converted to oxidizing equivalents in Co-Pi, yielding O_2 evolution well below the Co-Pi bulk electrolysis threshold potential, is summarized schematically in Figure 4.8. Further improvement of the performance of these composite photoanodes can be anticipated, for example, by variation of the Co-Pi deposition conditions to optimize photocurrent densities at extremely low bias. More generally, these results emphasize that composite photoanode strategies offer promising prospects for sustainable, affordable, and distributed solar fuel technologies, and warrant efforts to extend this strategy to include other catalysts such as IrO_2,[27,28] Mn-oxo complexes,[29,30] or $[Ru(L)_2(OH_2)]^{2+}$ complexes,[31] that can be powered in part or entirely by light-harvesting electrodes.

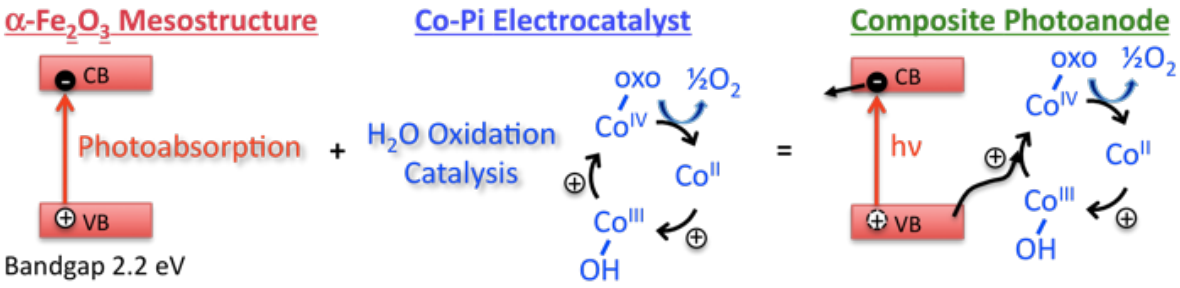

Figure 4.8. Scheme of O_2 Evolution with Co-Pi/α-Fe_2O_3 Composite Photoanodes

4.5 Notes to Chapter 4

1. Heller, A., *Science* **1984,** *223*, 1141-1148.
2. Grätzel, M., *Nature* **2001,** *414*, 338-344.
3. Lewis, N. S.; Nocera, D. G., *Proc. Nat. Acad. Sci.* **2006,** *103*, 15729-15735.
4. Lewis, N. S., *Science* **2007,** *315*, 798-801.
5. Grimes, C. A.; Varghese, O. K.; Ranjan, S., *Light, Water, Hydrogen*. Springer: New York, 2007.

6. Woodhouse, M.; Parkinson, B. A., *Chem. Mater.* **2008,** *20*, 2495-2502.
7. Kudo, A.; Miseki, Y., *Chem. Soc. Rev.* **2009,** *38*, 253-278.
8. McEvoy, J. P.; Brudvig, G. W., *Chem. Rev.* **2006,** *106*, 4455-4483.
9. Barber, J.; Murray, J. W., *Coord. Chem. Rev.* **2008,** *252*, 233-243.
10. Tseng, H.-W.; Zong, R.; Muckerman, J. T.; Thummel, R., *Inorg. Chem.* **2008,** *47*, 11763-11773.
11. McDaniel, N. D.; Coughlin, F. J.; Tinker, L. L.; Bernhard, S. J., *J. Am. Chem. Soc.* **2008,** *130*, 210-217.
12. Romero, I.; Rodríguez, M.; Sens, C.; Mola, J.; Kollipara, M. R.; Francàs, L.; Mas-Marza, E.; Escriche, L.; Llobet, A., *Inorg. Chem.* **2008,** *47*, 1824-1834.
13. Kanan, M. W.; Nocera, D. G., *Science* **2008,** *321*, 1072-1075.
14. Surendranath, Y.; Dincă, M.; Nocera, D. G., *J. Am. Chem. Soc.* **2009,** *131*, 2615-2620.
15. Lutterman, D. A.; Surendranath, Y.; Nocera, D. G., *J. Am. Chem. Soc.* **2009,** *131*, 3838-3839.
16. Risch, M.; Khare, V.; Zaharieva, I.; Gerencser, L.; Chernev, P.; Dau, H., *J. Am. Chem. Soc.* **2009,** *131*, 6936-6937.
17. Kanan, M. W.; Surendranath, Y.; Nocera, D. G., *Chem. Soc. Rev.* **2009,** *38*, 109-114.
18. Nocera, D. G., *Inorg. Chem.* **2009,** *48*, 10001-10017.
19. Nocera, D. G., *ChemSusChem* **2009,** *2*, 387-390.
20. Turner, J., *Nature Mater.* **2008,** *7*, 770-771.
21. Zhong, D. K.; Sun, J.; Inumaru, H.; Gamelin, D. R., *J. Am. Chem. Soc.* **2009,** *131*, 6086-6087.
22. Kay, A.; Cesar, I.; Grätzel, M., *J. Am. Chem. Soc.* **2006,** *128*, 15714-15721.
23. Cesar, I.; Sivula, K.; Kay, A.; Zboril, R.; Grätzel, M., *J. Phys. Chem. C* **2009,** *113*, 772-782.
24. Doney, S. C., *Sci. Am.* **2006,** *294*, 58-65.
25. Licht, S., *Encyclopedia of Electrochemistry: Semiconductor Electrodes and Photoelectrochemistry*. Wiley-VCH: Weinheim, 2002.
26. Eggleston, C. M.; Shankle, A. J. A.; Moyer, A. J.; Cesar, I.; Grätzel, M., *Aquat. Sci.* **2009,** *71*, 151-159.
27. Youngblood, W. J.; Lee, S.-H. A.; Maeda, K.; Mallouk, T. E., *Acc. Chem. Res.* **2009,** *42*, 1966-1973.
28. Nakagawa, T.; Bjorge, N. S.; Murray, R. W., *J. Am. Chem. Soc.* **2009,** *131*, 15578-15589.
29. Li, G.; Sproviero, E. M.; McNamara, W. R.; Snoeberger, R. C., III; Crabtree, R. H.; Brudvig, G. W.; Batista, V. S., *J. Phys. Chem. B* **2010,** *114*, 14214-14222.
30. Dismukes, G. C.; Brimblecombe, R.; Gelton, G. A. N.; Pryadun, R. S.; Sheats, J. E.; Spiccia, L.; Swiegers, G. F., *Acc. Chem. Res.* **2009,** *42*, 1935-1943.
31. Chen, Z.; Concepcion, J. J.; Jurss, J. W.; Meyer, T. J., *J. Am. Chem. Soc.* **2009,** *131*, 15580-15581.

Chapter 5: Photo-Assisted Electrodeposition of Cobalt-Phosphate (Co-Pi) Catalyst on Hematite Photoanodes for Solar Water Oxidation

Optimal integration of a surface electrocatalyst onto a mesostructured semiconductor photoanode requires an effective and reliable method of applying catalysts onto photoanode surfaces. As shown in Chapter 4, electrodeposition of cobalt-phosphate (Co-Pi) onto high surface area α-Fe_2O_3 photoanodes results in a non-uniform distribution of catalyst that may lead to catalytically inactive areas. Because semiconductor photoanode surfaces are often mesoporous and highly structured, scratches or pinholes in the film can lead to patches of catalyst depositing where current flows more readily during electrodeposition. In this chapter, a photo-assisted electrodeposition approach is used to deposit Co-Pi onto recently improved dendritic mesostructures of α-Fe_2O_3. This approach is compared to electrodeposition of Co-Pi, and Co^{2+} wet impregnation. By allowing deposition only where visible light generates oxidizing equivalents, photo-assisted electrodeposition provides a more uniform distribution of Co-Pi onto α-Fe_2O_3 than obtained by electrodeposition. This approach of fabricating catalyst-modified metal-oxide photoelectrodes may be attractive for optimization in conjunction with tandem or hydrid photoelectrochemical cells. The α-Fe_2O_3 photoanodes in this study were fabricated by Maurin Cornuz and Kevin Sivula in the Grätzel lab. All other experiments were conducted by the author. The work in this chapter is reproduced by permission of The Royal Society of Chemistry (RSC) from Zhong, D. K., Cornuz, M., Sivula, K., Grätzel, M., Gamelin, D. R. *Energy Environ. Sci*, **2011**, *4*, 1759-1764 (http://pubs.rsc.org/en/content/articlelanding/2011/ee/c1ee01034d). The general method of photo-assisted electrodeposition is patented in Gamelin, D. R., Zhong, D. K. Composite Photoanodes. *PCT Int. App*. PCT/US2011/027603, filed 03/08/2011.

5.1 Introduction

The maturation of photoelectrochemical (PEC) water splitting as a viable solar fuels technology has been hindered by the need to identify photoelectrode materials that are simultaneously efficient at solar energy conversion, stable under reaction conditions, and inexpensive.[1-4] Whereas high solar-to-hydrogen conversion efficiencies of 12.4% have been demonstrated using epitaxial pnictide-semiconductor multilayer devices,[2] these efficiencies are not sustainable even on the one-day timescale because of rapid electrode decomposition. Metal oxides have been widely studied as chemically robust alternatives, beginning with the seminal report by Honda and Fujishima[5] involving TiO_2, but have been limited by various factors including low carrier mobilities, low absorption coefficients, or poor catalytic proficiencies.[6-11] Hematite (α-Fe_2O_3) has emerged as a prototype photoanode for PEC water oxidation because of its balance of visible light absorption (bandgap of 2.1 eV), chemical stability, low cost, and large positive valence band edge potential.[12-16] Low mobilities (10^{-2}-10^{-1} cm^2 V^{-1} s^{-1})[17] and short hole diffusion lengths (2-4 nm or 20 nm)[18,19] have generally led to low PEC water oxidation efficiencies in bulk α-Fe_2O_3, but doping and nanostructuring have been used to sidestep these shortcomings, by increasing carrier density, decreasing the distance minority carriers have to travel to reach the reactive surface, and increasing semiconductor-electrolyte interfaces.[3,9] Doping with silicon has been suggested to increase photocurrent densities by several orders of magnitude in mesostructure α-Fe_2O_3 films.[12,20,21] Nanowires and

nanotubes of α-Fe_2O_3 have also shown increased photocurrent densities relative to bulk, although such structures have so far been limited to absolute one-sun current densities on the order of μA/cm^2.[14,22-24] Higher photocurrent densities (several mA/cm^2) have been achieved with porous films prepared from colloid solutions[25,26] and with silicon-doped dendritic mesostructures of α-Fe_2O_3 grown by atmospheric pressure chemical vapor deposition (APCVD).[27,28] Although doping and morphological control has proved invaluable for achieving such high current densities, slow water oxidation kinetics still necessitate large applied potentials to drive this challenging four-electron multi-nuclear redox chemistry.

Interfacing such mesostructured metal-oxide photoanodes with competent water oxidation catalysts offers one approach to improving their performance.[29] Similar to Nature's photosynthesis, the separation of photon absorption, charge separation, and water oxidation tasks in composite photoelectrodes allows components performing each task to be optimized independently and thereby enables a greater flexibility in the selection of component materials. In one recent illustration, electrodeposition of the well-known cobalt-phosphate water oxidation catalyst (Co-Pi)[30-32] onto dendritic α-Fe_2O_3 photoanodes was shown to decrease the onset potential for solar water oxidation by over two hundred millivolts.[33,34]

PEC measurements suggests that the Co-Pi functions as a surface water oxidation electrocatalyst on α-Fe_2O_3.[33,34] When light excites α-Fe_2O_3 and photogenerated electron-hole pairs separate, the resulting holes can undergo either electron-hole recombination or water oxidation at the surface. For α-Fe_2O_3 alone poor water oxidation kinetics can make the probability of surface recombination quite high, especially at low overpotentials. The application of a Co-Pi surface electrocatalyst capable of facile water oxidation may decrease the probability of recombination. At higher applied potentials PEC enhancement with Co-Pi is less significant as water oxidation by α-Fe_2O_3 becomes less kinetically inhibited and the likelihood of electron-hole recombination is reduced.

Electrodeposition of Co-Pi forms an adequate junction between the catalyst and semiconductor for interfacial charge transfer, and the resulting Co-Pi/α-Fe_2O_3 composite photoanodes are stable under photolysis conditions. A kinetic bottleneck was observed with thick layers of Co-Pi that hindered the steady-state turnover of the composite photoanodes, especially at low applied potentials.[34] This kinetic limitation was remediated by reducing the Co-Pi coverage, but at the expense of overpotential. With short electrodeposition times, however, Co-Pi was found to deposit preferentially at pinholes, scratches, or other imperfections in the α-Fe_2O_3 film, where more current can flow from the underlying conductive FTO substrate. This inhomogeneity affects the performance of Co-Pi/α-Fe_2O_3 photoanodes by creating areas where the catalyst layer is too thick (kinetic bottleneck), and it influences the reproducibility of the Co-Pi deposition itself. Ultimately, a stable and efficient water oxidation photoanode is desired, and methods to apply a uniform thin catalyst layer onto highly mesostructured metal-oxide photoanodes, such as α-Fe_2O_3 are therefore needed.

Recently, Steinmiller and Choi demonstrated that irradiation of ZnO nanorods on a conductive FTO substrate in the presence of Co-Pi precursors allowed selective deposition of Co-Pi onto just the ZnO nanorods, without deposition onto the more conductive FTO substrate.[35] Using UV light at a wavelength absorbed only by the ZnO, photogenerated valence-band holes in ZnO can oxidize Co^{2+} in the deposition solution to form Co-Pi. The photogenerated conduction-band electrons reduce water to hydrogen. Nodules of Co-Pi were observed covering the ZnO surfaces. Although ZnO itself is impractical for PEC because of its UV energy gap (3.4 eV),

the demonstration of Co-Pi deposition via photoexcitation is encouraging because such deposition provides a simple and flexible method for driving selective self-assembly of the targeted interface. We hypothesized that under the right conditions a similar approach might allow uniform thin layers of Co-Pi to be deposited onto mesostructured α-Fe_2O_3 photoanodes, avoiding formation of islands and nodules entirely, and that such uniform deposition would translate to improved Co-Pi/α-Fe_2O_3 PEC performance.

Here, we describe photo-assisted electrodeposition of Co-Pi onto mesostructured α-Fe_2O_3 photoanodes, and present a comparison between this approach, electrodeposition of Co-Pi, and Co^{2+} adsorption. These three approaches are summarized in Figure 5.1. Among these, photo-assisted electrodeposition of Co-Pi is found to yield superior PEC performance by all metrics, including absolute onset potential, cathodic shift of the onset potential, and maximum current density. In combination with recently improved dendritic α-Fe_2O_3 photoanodes,[36] the photo-assisted electrodeposition of Co-Pi yields arguably the best overall α-Fe_2O_3 photoanodes for PEC solar water splitting reported to date, with stable current densities of 1.0 mA/cm^2 at 1.0 V and 2.8 mA/cm^2 at 1.23 V vs RHE measured under standard 1 sun, AM 1.5 illumination conditions at pH 13.6.

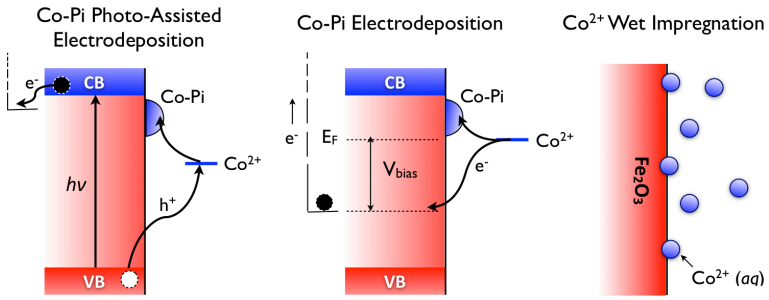

Figure 5.1. Scheme of Co-Pi PEC Deposition, Electrodeposition, and Co^{2+} Wet Impregnation

5.2 Experimental Section

Mesostructured α-Fe_2O_3 photoanodes were fabricated on FTO glass by an APCVD method reported previously.[36] Masks with apertures of 6 mm in diameter were applied to define the active surface areas. Co-Pi was electrodeposited onto α-Fe_2O_3 photoanodes by modification of published procedures.[30,32-34] A three-electrode cell was used with α-Fe_2O_3 as the working electrode, Ag/AgCl as the reference electrode, and Pt mesh as the counter electrode. 0.9 V vs Ag/AgCl was applied in a solution of 0.5 mM cobalt nitrate in 0.1 M potassium phosphate buffer at pH 7. The amount of Co-Pi deposited was controlled by the deposition time, which ranged between 200-500s. Current densities were typically ~2-10 μA/cm^2 during deposition.

Photo-assisted electrodepostion of Co-Pi onto mesostructured α-Fe_2O_3 was performed from the same electrolyte composition used for electrodeposition, 0.5 mM cobalt nitrate in 0.1 M potassium phosphate buffer at pH 7, but with 1 sun AM 1.5 simulated sunlight illumination. Because conduction-band electrons in α-Fe_2O_3 do not have sufficient potential to reduce water, an external bias (~0.1–0.4 V) was applied. The amount of Co-Pi was again controlled by the deposition time, which ranged between 500-750 s. Current densities were typically ~2-5 μA/cm^2 during deposition.

Following a previously reported procedure,[27] Co^{2+} adsorption onto mesostructured α-Fe_2O_3 photoanodes was achieved by dipping the photoanode in a solution of 0.1 M cobalt nitrate for 5 minutes. The

amount of Co^{2+} adsorbed was optimized by repetition of this dipping process. Typically, PEC enhancement reached its maximum after about three cycles. Subsequent cycles resulted in either no change or a decrease in the PEC performance.

PEC measurements were conducted in 1M NaOH (pH 13.6) using a three-electrode configuration, with the photoanode as the working electrode, Ag/AgCl as the reference electrode, and Pt as the counter electrode. Photocurrent densities were measured with front-side illumination under 1 sun AM 1.5 simulated sunlight using an Oriel 96000 solar simulator equipped with a 150 W Xenon arc lamp and an Oriel AM 1.5 filter. Potentials vs. RHE are calculated using the Nernst equation $E_{RHE} = E_{Ag/AgCl} + 0.0591(pH) + 0.1976$ V. Very similar α-Fe_2O_3 photoanodes were used for all PEC measurements. The amount of catalyst applied was optimized to give the largest sustainable cathodic shift and overall current density by controlling the amount of catalyst loading, either by adjusting the time of deposition for Co-Pi or the number of cobalt dipping cycles for Co^{2+} adsorption. Cathodic shifts were calculated as the average voltage shifts in the window where current densities range from 0.5-1.5 mA/cm^2. For uniformity, reported photocurrent increases with catalyst deposition refer specifically to the difference in photocurrent at 1.1 V vs RHE. Photocurrent onset potentials were calculated by extrapolation to zero current from the linear portion of the J-V curve where current densities range from 0.5-1.5 mA/cm^2.

Scanning electron microscopy (SEM) and energy dispersive X-ray (EDX) analyses were performed using a FEI Sirion SEM equipped with an energy dispersive spectrometer. No conductive coating was deposited onto samples for these measurements.

5.3 Results & Discussion

SEM images of a representative mesostructured α-Fe_2O_3 photoanode are shown in Figure 5.2a,b. The photoanode possesses the dendritic features typical of α-Fe_2O_3 grown by APCVD.[27] All catalyst-modified photoanodes show similar dendritic features but the images are slightly blurred (Figure 5.2c-h), suggesting that the catalysts make the surfaces more insulating and hence more susceptible to charging effects from the electron beam. All photoanode surfaces appear uniform except for the one involving electrodeposited Co-Pi (Figure 5.2c,d), which shows patches of Co-Pi. On the other films, the catalyst itself is not resolved by the SEM measurement, but it can be detected by EDX (Figure 5.3a). EDX measurements on large and small areas of the films from Figure 5.2e-h yield similar results, indicating uniform cobalt coverage on these length scales (Figure 5.3). Mapping cobalt over large areas also shows uniform distribution (see Appendix C).

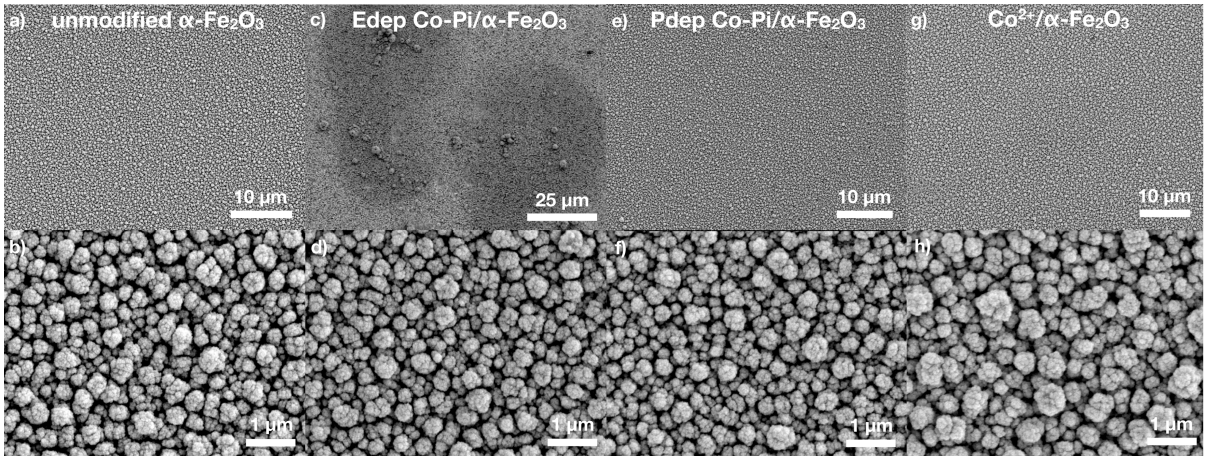

Figure 5.2 SEM Images of α-Fe_2O_3 and Cobalt-Catalyst Modified α-Fe_2O_3 Photoanodes
Wide- and narrow-angle SEM images of **(a,b)** an unmodified α-Fe_2O_3 mesostructured photoanode, and similar α-Fe_2O_3 photoanodes following **(c,d)** Co-Pi electrodeposition, **(e,f)** photo-assisted electrodeposition of Co-Pi, and **(g,h)** Co^{2+} adsorption. Panel (c) shows islands of Co-Pi, which form over defects in the α-Fe_2O_3 film.

The amount of catalyst on α-Fe_2O_3 photoanodes that yields the largest sustainable PEC enhancement can be roughly estimated using the EDX results. Although the low percentage of cobalt and the proximity of the Co (K) peak to the Fe (K) peak complicate quantitative analysis, cobalt is clearly seen in Figure 5.3. As expected for surface deposition, increasing the probe depth by increasing the electron acceleration voltage from 10 to 15 keV results in a substantial decrease in the relative cobalt peak intensity. Approximating the probe depth of a 10 keV electron beam to be ~ 200 nm[37] the assumption of a uniform flat surface would yield a Co-Pi thickness of ~30 nm, but this value represents an upper limit because of the very high surface roughness of the α-Fe_2O_3 mesostructure (roughness ~ 20).[27] The active Co-Pi cluster is now believed to possess seven cobalt ions, with a volume of ~700 $Å^3$,[32,38] from which an upper limit of 34 clusters thickness is obtained. In all likelihood, the actual thickness is substantially smaller. For example, it is interesting to note that the amount of cobalt detected by EDX is about the same for optimized Co-Pi/α-Fe_2O_3 as for Co^{2+}-impregnated α-Fe_2O_3 (Figure 5.3b). Co^{2+} adsorption has previously been suggested to yield only monolayer coverage,[27] implying closer to one monolayer of Co-Pi cluster as well. Overall, these results clearly indicate that Co-Pi/α-Fe_2O_3 composite photoelectrodes optimized for steady-state photocurrents possess far thinner Co-Pi layers than the analogous Co-Pi-coated electrodes used in electrocatalysis.[30] This difference relates to the kinetic bottleneck described previously, which likely reflects the important role of surface electron-hole recombination under PEC conditions.[34]

a)

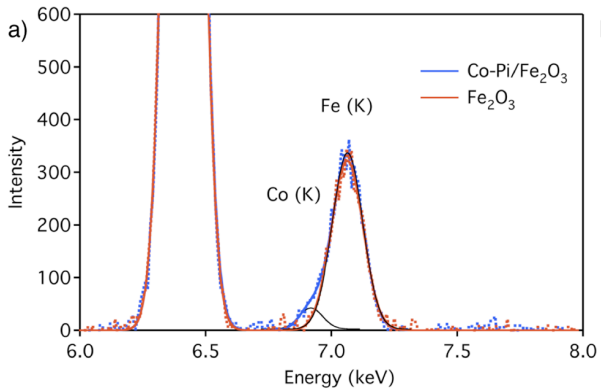

b)

Material	Probe area	Fe (%)	Co (%)
α-Fe_2O_3	1700 μm^2	38.11	-
Photodeposited Co-Pi/α-Fe_2O_3	430 μm^2	33.35	1.00
Photodeposited Co-Pi/α-Fe_2O_3	0.25 μm^2 (single nodule)	35.52	1.06
Electrodeposited Co-Pi/α-Fe_2O_3	430 μm^2	33.71	1.23
Co^{2+} adsorbed/α-Fe_2O_3	1700 μm^2	34.02	0.94

Figure 5.3. EDX of α-Fe_2O_3 and Co-Pi/α-Fe_2O_3
a) EDX spectra of α-Fe_2O_3 (red dotted) and Co-Pi/α-Fe_2O_3 (blue dotted) photoanodes measured using a probe beam of 10 keV. The solid colored lines show calculated gaussian fits. The solid black curves show the individual gaussians representing cobalt and iron intensities in the Co-Pi/α-Fe_2O_3 photoelectrode. **b)** Table of EDX results for iron and cobalt. An SEM image of the single nodule used for EDX analysis is shown in Appendix C.

Figure 5.4 compares current-voltage (J-V) characteristics of representative Co-Pi/α-Fe_2O_3 and Co^{2+}-modified α-Fe_2O_3 photoelectrodes. All photoelectrodes have been optimized to give the largest steady-state cathodic shift and PEC enhancement compared to their parent α-Fe_2O_3 photoanodes. Photo-assisted electrodeposition of Co-Pi onto α-Fe_2O_3 (Figure 5.4a) yields the greatest cathodic shift of the onset potential for PEC water oxidation, ~170 mV. Similar results were described previously for electrodeposition of Co-Pi onto α-Fe_2O_3 following optimization.[34] The best electrodeposited Co-Pi/α-Fe_2O_3 photoanode in this set showed a ~100 mV cathodic shift (Figure 5.4b), and the best Co^{2+}-impregnated α-Fe_2O_3 photoanode showed an ~80 mV shift.

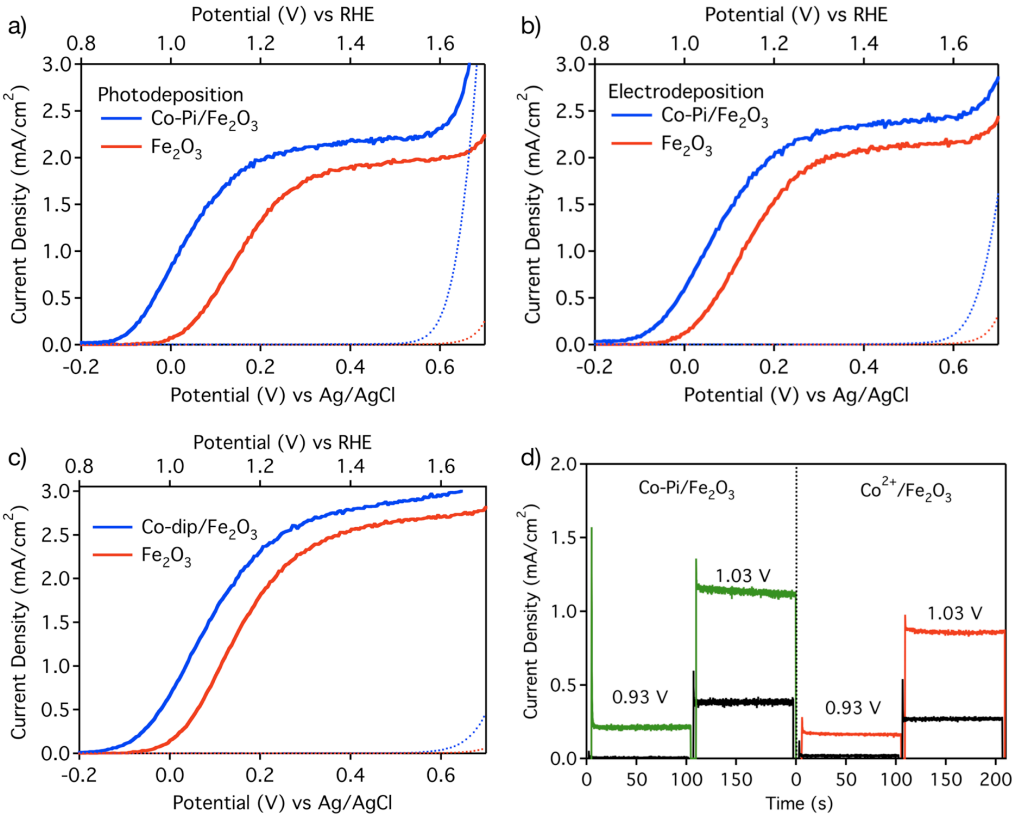

Figure 5.4. PEC Measurements on Various Cobalt Catalyst/α-Fe_2O_3 Photoanodes
Dark-current (dotted) and photocurrent (solid) densities of **a)** a Co-Pi/α-Fe_2O_3 electrode prepared by photo-assisted electrodeposition, **b)** a Co-Pi/α-Fe_2O_3 electrode prepared by electrodeposition, and **c)** a Co^{2+}/α-Fe_2O_3 electrode prepared by surface adsorption (all in blue), compared to the parent α-Fe_2O_3 photoanodes (all in red). **d)** Transient photocurrent densities measured for Co-Pi/α-Fe_2O_3 (green) and Co^{2+}/α-Fe_2O_3 (red) photoanodes at the indicated voltages, compared to the parent α-Fe_2O_3 photoanodes (black).

Figure 5.4d plots photocurrent densities vs time for representative Co-Pi-modified and Co^{2+}-impregnated α-Fe_2O_3 photoanodes, compared to their parent α-Fe_2O_3 photoanodes, at two voltages. The primary qualitative difference between the two occurs immediately after exposure to light. As described previously,[34] the Co-Pi/α-Fe_2O_3 photoanode exhibits a large initial peak within the first second of irradiation at low potentials (0.93 V), whereas the Co^{2+}-impregnated and bare α-Fe_2O_3 films show only small peaks in this time window. This behavior in the Co-Pi/α-Fe_2O_3 photoanode is attributed to oxidation of the catalyst itself, which is required to activate it for water oxidation.[31,38] Beyond this difference, the current densities for each of these films are stable and reproducible after multiple J-V scans and under illumination for over 72 hours (see Appendix C), even after weeks of storage at room temperature in air.

Interesting variations in performance are observed from film to film, much of which derives from variations in the underlying α-Fe_2O_3 photoanode performance. Such differences are illustrated in Figure 5.5, which shows the photocurrent responses of two quite different composite photoanodes in comparison with those of their parent α-Fe_2O_3 photoanodes. The photoanode in Figure 5.5a shows large, stable photocurrent densities at high bias, whereas the one in Figure 5.5b excels at low bias. These differences are due to a small variation in the deposition temperature.[28] These data also emphasize that Co-Pi surface deposition has a similar effect on each parent α-Fe_2O_3 photoanode, despite their absolute performance differences. Both films show comparable

cathodic shifts of their photocurrent onset potentials and small enhancements of their maximum photocurrent densities upon deposition of Co-Pi.

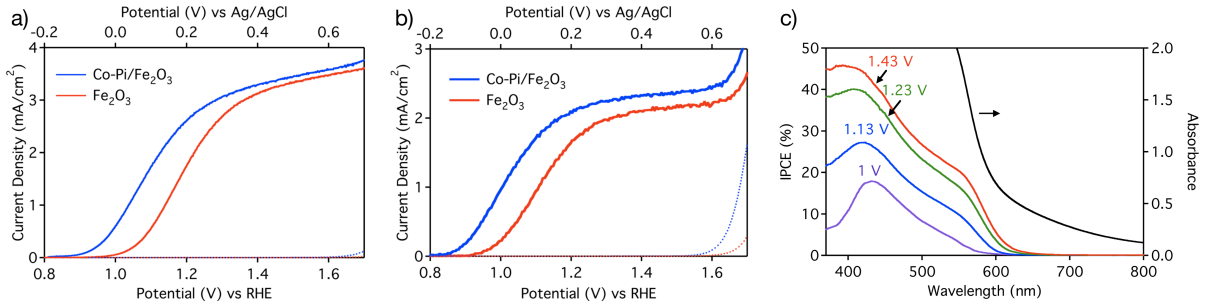

Figure 5.5. PEC and IPCE Data on the Best Co-Pi/α-Fe_2O_3 Photoanodes
a,b) Dark-current (dotted) and photocurrent (solid) densities of Co-Pi/α-Fe_2O_3 photoanodes prepared by photo-assisted electrodeposition (blue) and of the parent α-Fe_2O_3 photoanodes (red) illustrating the effect of Co-Pi on two α-Fe_2O_3 photoanodes with qualitatively different responses. **c)** Incident photon-to-current conversion efficiencies (IPCEs, colored) and absorption spectrum (black) of a Co-Pi/α-Fe_2O_3 photoanode prepared by photo-assisted electrodeposition.

Incident-photon-to-current conversion efficiency (IPCE) measurements on a Co-Pi/α-Fe_2O_3 photoanode prepared by photo-assisted electrodeposition (Figure 5.5c) show a value of 40% at 400 nm and 1.23 V vs RHE, with large visible-light conversion efficiencies even at lower bias. The photocurrent response spectrum of the Co-Pi/α-Fe_2O_3 photoanode exhibits the same features as α-Fe_2O_3, indicating the primary photoresponse is from the α-Fe_2O_3 mesostructure and not in the Co-Pi itself. We note the particularly strong response from the indirect bandgap feature at ~550 nm relative to many other α-Fe_2O_3 PEC cells.[12-15,19,20] The prominence of this band here is attributed to the very high surface areas of these dendritic α-Fe_2O_3 photoanodes, which allow hole harvesting even following excitation of such a localized transition, and to the role of Co-Pi in facilitating productive use of those holes for water oxidation. In addition, we note that the integration of the IPCE data with the standard solar spectral distribution gives predicted solar photocurrents in agreement with the measured values, verifying the light source and confirming the solar photocurrent magnitudes reported (see Appendix C).

To put the above comparisons on a more quantitative footing, Figure 5.6 summarizes the PEC results obtained from the investigation of a total of 12 catalyst-modified photoanodes, with particular care given to ensuring that they all involved very similar parent α-Fe_2O_3 photoanodes as their starting points. The maximum cathodic shift (top panel), maximum photocurrent density increase (middle panel), and absolute photocurrent onset potentials (bottom panel) of the best photoanodes in each category are plotted as a bar graph. The average performance in each category is indicated by a horizontal line in the top two graphs and by an empty bar in the bottom graph. Plotting one metric vs another confirms the linear relationship between cathodic shift and reduced photocurrent onset potential (see Appendix C). Similarly, greater absolute photocurrent densities are strongly correlated with larger increases in photocurrent density upon Co-Pi deposition (see Appendix C). From these data, we conclude that photo-assisted electrodeposition of Co-Pi onto α-Fe_2O_3 photoanodes yields both a lower onset potential and a greater increase in photocurrent density than either Co-Pi electrodeposition or Co^{2+} surface adsorption.

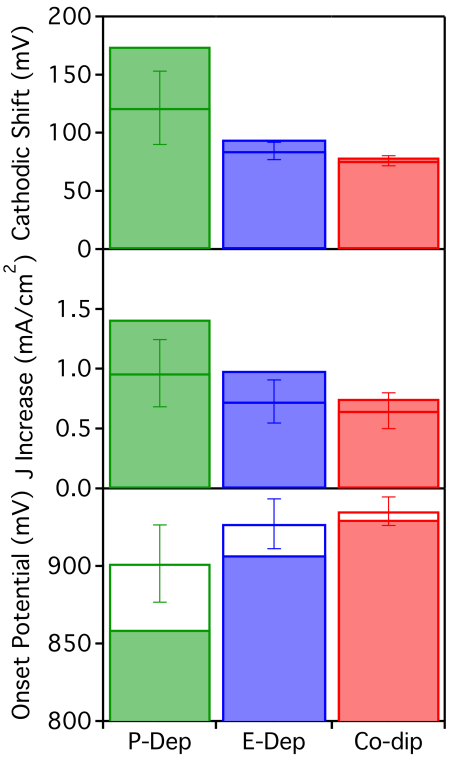

Figure 5.6. Comparison of Various Cobalt-Based Catalysts on α-Fe_2O_3
The best (filled bars) and average (empty line) cathodic shifts, photocurrent density increases, and onset potentials for Co-Pi/α-Fe_2O_3 photoanodes prepared by photo-assisted electrodeposition (P-Dep) and electrodeposition (E-Dep) of Co-Pi, and for Co^{2+}/α-Fe_2O_3 photoanodes prepared by surface adsorption of Co^{2+} (Co-dip). Standard deviations are shown with error bars. Photo-assisted electrodeposition of Co-Pi outperforms the other methods by all metrics.

Beyond variations in the α-Fe_2O_3 substrates themselves, the range of PEC results obtained following Co-Pi deposition is broader than that following Co^{2+} impregnation. Co^{2+} adsorption onto mesostructured α-Fe_2O_3 is relatively straightforward, with maximum PEC water oxidation enhancements peaking after about three adsorption cycles. The maximum cathodic shift is consistently between 70 and 80 mV, essentially identical to what has been reported previously.[27] In contrast, Co-Pi deposition involves more experimental variables and the results show greater variation from sample to sample. Overall, however, these data clearly reveal the superiority of photo-assisted electrodeposition over simple electrodeposition for the preparation of Co-Pi/α-Fe_2O_3 composite photoanodes. They also illustrate the improvements in α-Fe_2O_3 PEC performance obtained using Co-Pi rather than surface-adsorbed Co^{2+} as the electrocatalyst.

In addition to their ease of preparation, Earth-abundant composition, and highly stable photocurrent densities, the absolute performances of Co-Pi/α-Fe_2O_3 photoanodes are comparable with those of IrO_2/α-Fe_2O_3 photoanodes prepared by attachment of nanocrystals of the well-known water oxidation catalyst, IrO_2, onto similar α-Fe_2O_3 photoanodes.[36] Compared to the Co-Pi/α-Fe_2O_3 photoanode in Figure 5.5a, the best IrO_2/α-Fe_2O_3 photoanode showed a 50 mV greater cathodic shift, a 60 mV lower onset potential, and a ~13% larger photocurrent density at 1.23 V vs RHE. An important difference between Co-Pi/α-Fe_2O_3 and IrO_2/α-Fe_2O_3 photoanodes, however, is that the photocurrent responses of the IrO_2/α-Fe_2O_3 photoanodes appear to

diminish on short (200 s) timescales because of detachment of the IrO_2 particles from the α-Fe_2O_3 surface.[36] The Co-Pi/α-Fe_2O_3 composite photoanodes show no similar instability (see Appendix C).

Despite the reduced onset potential, a positive voltage must still be applied in order to drive PEC water oxidation using α-Fe_2O_3. Ideally, this voltage would be supplied by a photovoltaic (PV) device in a tandem configuration. For the photoanode in Figure 5.5a, the increase in photocurrent density from 2.1 to 2.8 mA/cm^2 at 1.23 V (the thermodynamic potential for electrolysis) following Co-Pi deposition corresponds to a 33% improvement and yields a solar to hydrogen conversion efficiency of η_{sth} = 3.4%, based on the Gibbs free energy of the reaction and assuming a faradaic efficiency of unity.[1] At 1.43 V, the photocurrent density of 3.3 mA/cm^2 corresponds to η_{sth} = 4.1%. Unfortunately, most low cost PV devices such as DSSCs provide less than 1.0 V at open circuit, and multiple PV devices connected in series would thus be required to achieve the above efficiencies.[39] To minimize cost, PEC photocurrent densities at low applied potentials should be optimized, and the cathodic shifts provided by Co-Pi modification are therefore of interest. The Co-Pi/α-Fe_2O_3 photoanode of Figure 5.5b shows a relatively high photocurrent density of 1.0 mA/cm^2 at 1.0 V vs RHE, which constitutes a 500% improvement over α-Fe_2O_3 alone at the same voltage (0.2 mA/cm^2).

5.4 Summary

Photo-assisted electrodeposition of Co-Pi onto mesostructured α-Fe_2O_3 yields better performing photoanodes than either electrodeposition of Co-Pi or simple Co^{2+} wet impregnation. A stable ~170 mV cathodic shift was observed with photodeposition of Co-Pi, while the electrodeposition of Co-Pi gave cathodic shifts of ~100 mV, and Co^{2+} impregnation gave ~80 mV cathodic shifts. Photo-assisted electrodeposition provides a more uniform distribution of Co-Pi on α-Fe_2O_3 than obtained by electrodeposition by allowing deposition only where visible light generates oxidizing equivalents. Optimization of the photo-assisted electrodeposition conditions allowed elimination of all nodules and islands to yield thin uniform films of Co-Pi over the entire photoanode surface. The resulting catalyst-modified metal-oxide photoelectrodes are attractive for solar water oxidation in tandem or hybrid PEC cells.

5.5 Notes to Chapter 5

1. Grimes, C. A.; Varghese, O. K.; Ranjan, S., *Light, Water, Hydrogen*. Springer: New York, 2007.
2. Khaselev, O.; Turner, J. A., *Science* **1998,** *280*, 425-427.
3. Navarro Yerga, R. M.; Álvarez Galván, M. C.; del Valle, F.; Villoria de la Mano, J. A.; Fierro, J. L. G., *ChemSusChem* **2007,** *2*, 471-485.
4. Kudo, A.; Miseki, Y., *Chem. Soc. Rev.* **2009,** *38*, 253-278.
5. Fujishima, A.; Honda, K., *Nature* **1972,** *238*, 37-8.
6. Alexander, B. D.; Kulesza, P. J.; Rutkowska, I.; Solarska, R.; Augustynski, J., *J. Mater. Chem.* **2008,** *18*, 2298-2303.
7. Rajeshwar, K., *J. Appl. Electrochem.* **2007,** *37*, 765-787.
8. Osterloh, F. E., *Chem. Mater.* **2008,** *20*, 35-54.
9. van de Krol, R.; Liang, Y.; Schoonman, J., *J. Mater. Chem.* **2008,** *18*, 2311-2320.
10. Woodhouse, M.; Parkinson, B. A., *Chem. Mater.* **2008,** *20*, 2495-2502.

11. Aroutiounian, V. M.; Arakelyan, V. M.; Shahnazaryan, G. E., *Sol. Energy* **2005,** *78*, 581-592.
12. Shinar, R.; Kennedy, J. H., *Sol. Energy Mater.* **1982,** *6*, 323-35.
13. Majumder, S. A.; Khan, S. U. M., *Int. J. Hydrogen Energy* **1994,** *19*, 881-887.
14. Lindgren, T.; Wang, H.; Beermann, N.; Vayssieres, L.; Hagfeldt, A.; Lindquist, S.-E., *Sol. Energy Mater.* **2002,** *71*, 231-243.
15. Duret, A.; Grätzel, M., *J. Phys. Chem. B* **2005,** *109*, 17184-17191.
16. Wang, H.; Deutsch, T.; Turner, J. A., *J. Electrochem. Soc.* **2008,** *155*, F91-F96.
17. Gardner, R. F. G.; Sweett, F.; Tanner, D. W., *J. Phys. Chem. Solids* **1963,** *24*, 1183-1186.
18. Kennedy, J. H.; Frese, K. W., Jr., *J. Electrochem. Soc.* **1978,** *125*, 709-14.
19. Dare-Edwards, M. P.; Goodenough, J. B.; Hamnett, A.; Trevellick, P. R., *J. Chem. Soc., Faraday Trans.* **1983,** *79*, 2027-2041.
20. Kennedy, J. H.; Shinar, R.; Ziegler, J. P., *J. Electrochem. Soc.* **1980,** *127*, 2307-9.
21. Cesar, I.; Kay, A.; Gonzalez Martinez, J. A.; Grätzel, M., *J. Am. Chem. Soc.* **2006,** *128*, 4582-4583.
22. Bjoerksten, U.; Moser, J.; Grätzel, M., *Chem. Mater.* **1994,** *6*, 858-863.
23. Beermann, N.; Vayssieres, L.; Lindquist, S.-E.; Hagfeldt, A., *J. Electrochem. Soc.* **2000,** *147*, 2456-2461.
24. Mohapatra, S. K.; John, S. E.; Banerjee, S.; Misra, M., *Chem. Mater.* **2009,** *21*, 3048-3055.
25. Sivula, K.; Zboril, R.; Le Formal, F.; Robert, R.; Weidenkaff, A.; Tucek, J.; Frydrych, J.; Grätzel, M., *J. Am. Chem. Soc.* **2010,** *132*, 7436-7444.
26. Brillet, J.; Grätzel, M.; Sivula, K., *Nano Lett.* **2010,** *10*, 4155-4160.
27. Kay, A.; Cesar, I.; Grätzel, M., *J. Am. Chem. Soc.* **2006,** *128*, 15714-15721.
28. Cesar, I.; Sivula, K.; Kay, A.; Zboril, R.; Grätzel, M., *J. Phys. Chem. C* **2009,** *113*, 772-782.
29. Sun, J.; Zhong, D. K.; Gamelin, D. R., *Energy Environ. Sci.* **2010,** *3*, 1252-1261.
30. Kanan, M. W.; Nocera, D. G., *Science* **2008,** *321*, 1072-1075.
31. Kanan, M. W.; Surendranath, Y.; Nocera, D. G., *Chem. Soc. Rev.* **2009,** *38*, 109-114.
32. Kanan, M. W.; Yano, J.; Surendranath, Y.; Dincă, M.; Yachandra, V. K.; Nocera, D. G., *J. Am. Chem. Soc.* **2010,** *132*, 13692-13701.
33. Zhong, D. K.; Sun, J.; Inumaru, H.; Gamelin, D. R., *J. Am. Chem. Soc.* **2009,** *131*, 6086-6087.
34. Zhong, D. K.; Gamelin, D. R., *J. Am. Chem. Soc.* **2010,** *132*, 4202-4207.
35. Steinmiller, E. M. P.; Choi, K.-S., *Proc. Nat. Acad. Sci.* **2009,** *106*, 20633-20636.
36. Tilley, S. D.; Cornuz, M.; Sivula, K.; Grätzel, M., *Angew. Chem. Int. Ed.* **2010,** *49*, 6405-6408.
37. Goldstein, J.; Newbury, D. E.; Joy, D. C.; Lyman, C. E.; Echlin, P.; Lifshin, E.; Sawyer, L.; Michael, J. R., *Scanning Electron Microscopy and X-Ray Microanalysis*. 3rd ed.; Springer: New York, 2003.
38. Surendranath, Y.; Kanan, M. W.; Nocera, D. G., *J. Am. Chem. Soc.* **2010,** *132*, 16501-16509.
39. Brillet, J.; Cornuz, M.; Le Formal, F.; Yum, J.-H.; Grätzel, M.; Sivula, K., *J. Mater. Res.* **2010,** *25*, 17-24.

Chapter 6: Near-Complete Suppression of Surface Recombination in Solar Photoelectrolysis by "Co-Pi" Catalyst-Modified W:$BiVO_4$

Unassisted tandem solar water splitting with two photoelectrodes requires that current flow between the two cells be matched at a particular operating voltage. For a Co-Pi/α-Fe_2O_3 photoanode, to operate at 1 mA/cm^2 in a tandem configuration, its partner cell must provide 1 mA/cm^2 at the same potential. Unfortunately, the onset potential for water oxidation with Co-Pi/α-Fe_2O_3 composite photoanodes is still too high for most low cost photoelectrochemical (PEC) or photovoltaic (PV) cells. It is unclear whether this is a limitation of Co-Pi or α-Fe_2O_3. Employing a semiconductor material with lower onset potentials, but still absorbs visible light, such as $BiVO_4$, may result in even lower operating potentials and provide insight into the catalyst/semiconductor relationship in general. In this chapter, we investigate the influence of an earth-abundant water oxidation electrocatalyst, Co-Pi, on solar water oxidation by W:$BiVO_4$. Peroxide as a hole scavenger is used to probe the surface electron-hole (e-h) recombination efficiency before and after Co-Pi surface modification. The results obtained for W:$BiVO_4$ are then compared with those reported for Co-Pi/α-Fe_2O_3 photoanodes. The work presented in this chapter is reprinted with permission from Zhong, D. K., Choi, S., Gamelin, D. R. *J. Am. Chem. Soc.*, **2011**, *133*, 18370-18377. Copyright 2011 American Chemical Society.

6.1 Introduction

Photoelectrochemical (PEC) water splitting is a promising strategy for the capture and storage of the Earth's abundant solar energy influx.[1-5] The greatest challenge in this chemistry is the water oxidation reaction, which is a multi-step, four-electron, four-proton process. Because of kinetic barriers, large overpotentials are typically required to drive this reaction electrochemically. In PEC water splitting, additional overpotentials are needed to also overcome competing electron-hole recombination processes, at the expense of solar-energy-conversion efficiency.[2-5] In both experiments, these needs can be addressed in part by introduction of surface electrocatalysts, which improve water-oxidation kinetics and thereby improve energy conversion efficiencies. To a large extent, successful integration of water-oxidation catalysts with PEC photoanodes has been limited to Pt or RuO_2.[5]

Any potential PEC technology must balance efficiency against cost and scalability considerations. For this reason, much research has been focused on the development of oxides as photoelectrode materials.[2-8] Oxides are frequently inexpensive, stable, easily prepared on a large scale, and robust under PEC operating conditions. Successful development of even moderately efficient oxide PEC cells for solar water splitting would be a major advance toward the goal of large-scale, distributable solar hydrogen generation.

Among candidate oxides, $BiVO_4$ (bismuth yellow) has attracted broad attention recently as an inexpensive and robust semiconductor for potential application as a water-oxidation photocatalyst.[9-23] $BiVO_4$ exists in three polymorphs, with the monoclinic scheelite structure being the most reactive for water oxidation.[10,17] With its direct band gap of ~2.4-2.5 eV at room temperature, scheelite $BiVO_4$ can use visible light to drive water oxidation. Photoelectrochemical (PEC) measurements using polycrystalline photoanodes show that $BiVO_4$ has a relatively low onset potential for water oxidation (~0.5 V vs RHE) and can achieve

photocurrent densities of a few mA/cm^2 with visible-light excitation.[11] Doping,[12,15,18] along with surface catalyst modification,[19,20,24] may improve the overall PEC water-oxidation efficiencies of $BiVO_4$ photoanodes. For example, several studies have demonstrated improvement of $BiVO_4$ PEC performance by tungsten doping.[15,18,22] According to DFT calculations, tungsten is an n-type dopant in $BiVO_4$, substituting for V^{5+} as W^{6+} (+ e^-_{CB}).[23] Mott-Schottky plots confirm that tungsten doping increases the majority carrier density in $BiVO_4$.[15,18]

In the present study, we evaluate the effects of interfacing W:$BiVO_4$ photoanodes with cobalt-phosphate ("Co-Pi"), a simple but effective earth-abundant water-oxidation electrocatalyst.[25-27] Although many surface catalysts have already been explored with $BiVO_4$ and related photoanodes,[22] Co-Pi offers the attractive advantages of being easily integrated with complex surface topologies, in addition to being regenerative under PEC conditions. Co-Pi has previously been shown to improve PEC water oxidation by various photoelectrodes including α-Fe_2O_3,[28-31] ZnO,[32] WO_3,[33] Si/Co,[34] and Si/ITO.[34,35] While the present work was in progress, encouraging data were reported showing phenomenologically that Co-Pi also markedly improves the PEC performance of W:$BiVO_4$,[22] although analysis of this observation was not the focus of that study. In all cases, Co-Pi deposition onto the photoanode surface yielded large cathodic shifts of the onset potentials for water oxidation. The thickness of the Co-Pi layer was shown to play an important role in photoanode performance, with increased Co-Pi thicknesses reducing overpotentials but also impairing the ability to sustain high current densities.[29] This trend has been attributed to competition between productive water oxidation and unproductive surface electron-hole recombination,[29,30] highlighting a key contrast between electrochemical and PEC water oxidation. In electrochemical water oxidation with Co-Pi, thicker catalyst layers improve overall electrolysis current densities.[27] In PEC water oxidation with Co-Pi, thick catalyst layers reduce the ability of productive water oxidation to compete with non-productive surface electron-hole recombination.[29,30] To circumvent this kinetic bottleneck, a photo-assisted electrodeposition method was developed to deposit thin (<30 nm), uniform, and conformal Co-Pi layers onto mesostructured photoelectrode surfaces.[30]

Here, we report that photo-assisted electrodeposition of Co-Pi onto W:$BiVO_4$ photoanodes results in a remarkable ~440 mV cathodic shift in the onset potential for sustained water oxidation, significantly larger than the cathodic shifts observed with other oxide photoanodes.[28-30,32,33] PEC water oxidation by the resulting Co-Pi/ W:$BiVO_4$ composite photoelectrodes is shown to be as facile as PEC hydrogen peroxide oxidation by the parent photoelectrode (W:$BiVO_4$), indicating extremely effective hole capture and conversion to O_2 at the Co-Pi/ W:$BiVO_4$ interface. Analysis shows nearly complete elimination of surface electron-hole recombination at all potentials following Co-Pi deposition, leading to nearly quantitative surface hole capture and onset potentials as low as 310 mV vs RHE. These results highlight the critical importance of suppressing surface electron-hole recombination in order to achieve efficient PEC solar water oxidation, and demonstrate the effective suppression of such losses in an attractive and widely investigated oxide photocatalyst, $BiVO_4$, using the simple, earth-abundant electrocatalyst, Co-Pi.

6.2 Experimental Section

$BiVO_4$ photoanodes were fabricated by modification of literature metal-organic decomposition (MOD) methods.[11,16] Equimolar amounts of bismuth nitrate hexahydrate (0.173 g) and vanadyl acetylacetonate (0.095 g) were added to a 5 mL solution of 1:8.25 acetic acid and acetylacetone. The dark green solution was

then sonicated for 15 min. For W:$BiVO_4$ photoanodes, 7 atomic % tungstic acid was added to the solution and the vanadium concentration was decreased to 93%. The final solution was spin coated onto an FTO substrate (TEC 15, Hartford Glass Co.) at 1000 rpm for 30 s and annealed at 500 °C for 10 min for each of several coats. Altogether, 16 coats were applied, with a 2-hour annealing time after 8 coats. The final films were annealed for 8 hrs at 500 °C.

PEC measurements were performed in a three-electrode PEC cell with the photoanode as the working electrode, Ag/AgCl as the reference electrode, and a Pt wire mesh as the counter electrode. A Gamry Series G 300 potentiostat was used for all measurements. Unless otherwise stated, all PEC measurements were conducted under 1 sun AM 1.5 simulated sunlight with an Oriel 96000 solar simulator integrating a 150 W xenon arc lamp and Oriel 81094 filter. The photoanodes were masked with a 6 mm aperture to maintain the same area for dark and light measurements. Experiments were performed in 0.1 M potassium phosphate (KPi) buffered to pH 8, unless otherwise stated. Potentials are reported as measured vs Ag/AgCl and as calculated vs RHE using the Nernstian relation $E_{RHE} = E_{Ag/AgCl} + 0.0591pH + 0.1976$ V. Transient photocurrent density measurements were performed under constant applied potential for 35 s with a 30 s light pulse turned on after 2 s. IPCE measurements were collected with a 250 W tungsten light source directed through an Oriel Cornerstone 74000 monochromator blazed at 350 nm. Light intensity was measured with a calibrated silicon detector with a maximum light output of ~6 mW/cm^2 at 540 nm. We have previously demonstrated[30] that integration of IPCE data from this system with the standard solar spectral distribution predicts solar photocurrents that agree well with the values measured under one-sun AM1.5 irradiation, verifying the light source and confirming the solar photocurrent magnitudes reported.

Co-Pi was applied onto W:$BiVO_4$ photoanodes by the photo-assisted electrodeposition method described previously.[30] Co-Pi was deposited for 3-5 min at ~0.2-0.4 V vs RHE, with typical photocurrent densities of ~1-4 μA/cm^2 during deposition. Oxygen detection was performed in a three-neck flask with an optical window by an Ocean Optics NeoFox fluorescence measurement system equipped with a temperature sensor and FOXY-AR-WW oxygen probe. The instrument was calibrated by a two-point calibration in air and under argon. The total oxygen evolved was calculated from the amount of oxygen measured in the headspace using the ideal gas law and the amount of oxygen dissolved in the electrolyte using Henry's Law. The volume of the liquid and headspace were measured to be 97.5 mL and 82.5 mL, respectively. Prior to the measurement the electrolyte, 0.1 M pH 8 KPi, was degassed and purged with argon. Measurements were conducted in argon in the same three-electrode configuration described for PEC experiments. The photoanode was not masked for the O_2 measurements, making the illumination power density approximate (~ one sun).

Scanning electron microscopy (SEM) and energy dispersive X-ray (EDX) analyses were conducted using an FEI Sirion SEM equipped with an energy dispersive spectrometer at an accelerative voltage of 5 keV for images and 10 keV for EDX measurements. X-ray diffraction (XRD) patterns were collected using a Bruker F8 Focus XRD and calibrated using a NIST standard reference corundum alumina disc as an external standard and FTO as an internal standard.

6.3 Results

A. General aspects of the $BiVO_4$ and W:$BiVO_4$ photoanodes.

Figure 6.1 shows SEM images of representative $BiVO_4$ and W:$BiVO_4$ photoanodes used for the PEC measurements described in the present study. The $BiVO_4$ photoanodes are polycrystalline with primary features having dimensions of ~100-200 nm. The structures seen in Figure 6.1a are similar to those reported for $BiVO_4$ made by the same technique previously.[11] Tungsten incorporation does not substantially alter the film morphology (Figure 6.1b), although slightly smaller feature sizes are observed. EDX mapping of bismuth, vanadium, and tungsten show uniform distribution of these elements throughout the W:$BiVO_4$ films (see Appendix D). The thicknesses of these films were both estimated from cross-sectional SEM to be ~300 nm.

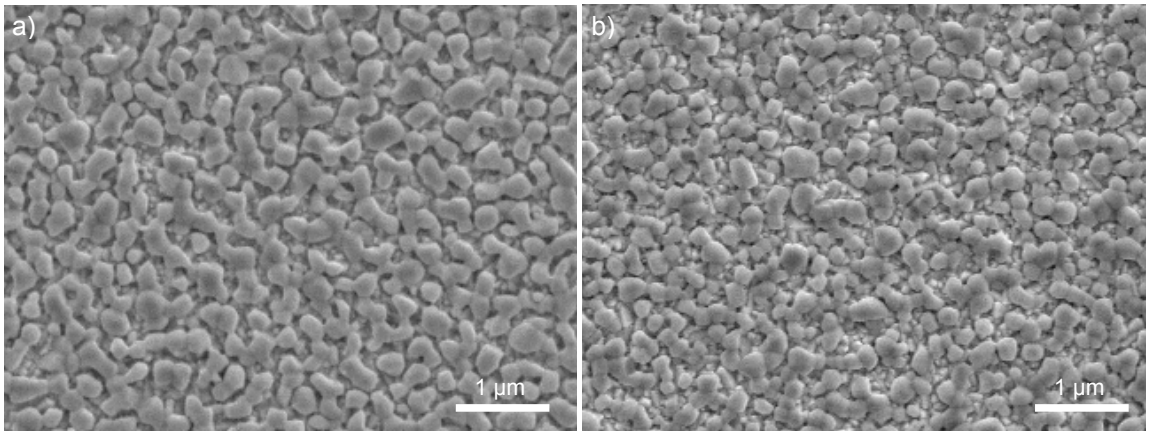

Figure 6.1. SEM Images of $BiVO_4$ and W:$BiVO_4$ Photoanodes
Top-view SEM images of representative (a) $BiVO_4$ and (b) W:$BiVO_4$ photoanodes. Both films were estimated from cross-sectional SEM to be ~300 nm.

Figure 6.2 shows XRD patterns of representative $BiVO_4$ and W:$BiVO_4$ photoanodes, along with the JCPDS diffraction peaks of FTO, $BiVO_4$, and WO_3. The diffraction pattern of these $BiVO_4$ photoanodes agrees well with expectations for monoclinic scheelite.[10,36,37] Upon tungsten incorporation, small monoclinic WO_3 peaks were also observed, indicating that at least some of the tungsten has segregated out of the $BiVO_4$ lattice. Tungsten also appears to be doped into $BiVO_4$ based on the observed shifts[37] of the diffraction peaks (see Appendix D). Tungsten (W^{6+}) likely substitutes for V^{5+},[15,23] causing lattice deformation.[36,37] To our knowledge, Vegard's law for W-doping of $BiVO_4$ has not been thoroughly documented, so the percentage W^{6+} incorporated within the $BiVO_4$ is unknown. Tungsten doping does not introduce any noticeable new electronic transitions (Figure 6.3a). Absorption features from phase-segregated WO_3 are also not evident, presumably because of the small amount present. The spectra in Figure 6.3 show an absorption edge at ~500 nm, consistent with the ~2.4-2.5 eV direct band gap of $BiVO_4$. The relatively small band gap of this oxide has been attributed to an upward dispersion of the valence band maximum resulting from O(2p)-Bi(6s) hybridization, and hybridization between V(3d), O(2p), and Bi(6p) orbitals also lowering the conduction band minimum.[38,39]

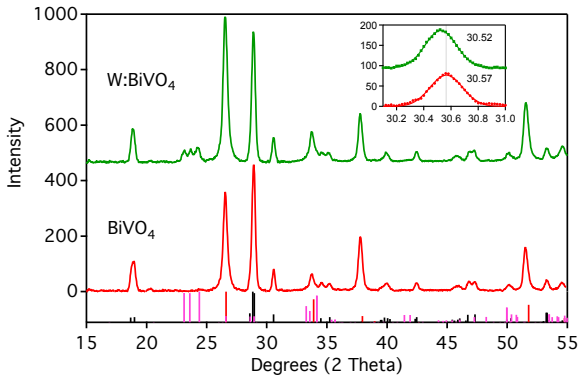

Figure 6.2. XRD of $BiVO_4$ and W:$BiVO_4$
XRD data from representative $BiVO_4$ (red) and W:$BiVO_4$ (green) photoanodes. The vertical lines indicate JCPDS diffraction peaks of FTO (black), monoclinic scheelite $BiVO_4$ (red), and WO_3 (pink). The inset shows the shift in the 040 diffraction peak of scheelite $BiVO_4$ observed upon introduction of tungsten, using FTO as the internal standard.

Figure 6.3b shows current density–voltage (*J-V*) curves measured for the same $BiVO_4$ and W:$BiVO_4$ photoanodes under front- and back-side illumination in 0.1 M $NaHCO_3$ electrolyte. $BiVO_4$ reportedly performs best in this electrolyte because of the catalytic role of carbonate ions.[16] The specific role is unclear, although it has been proposed that the mechanism may involve carbonate radicals or peroxocarbonates. For our $BiVO_4$ photoanodes, photocurrent densities achieved with back-side illumination are greater than those achieved with front-side illumination, indicating that hole diffusion is more facile than electron diffusion in these $BiVO_4$ films. Upon tungsten incorporation, the difference between photocurrents obtained with front- and back-side illumination decreases substantially, suggesting that electron mobility is improved by tungsten doping, consistent with W^{6+} (+ e^-_{CB}) incorporation. Similarly, under front-side illumination, the IPCE of $BiVO_4$ drops rapidly at wavelengths below ~460 nm (Figure 6.3a), whereas the same film under back-side illumination shows its IPCE maximum at ~430 nm. Conversely, front-side illumination of W:$BiVO_4$ yields more photocurrent than back-side illumination and has its maximum at shorter wavelengths. These trends are again manifestations of the improved electron mobility of $BiVO_4$ following tungsten doping.

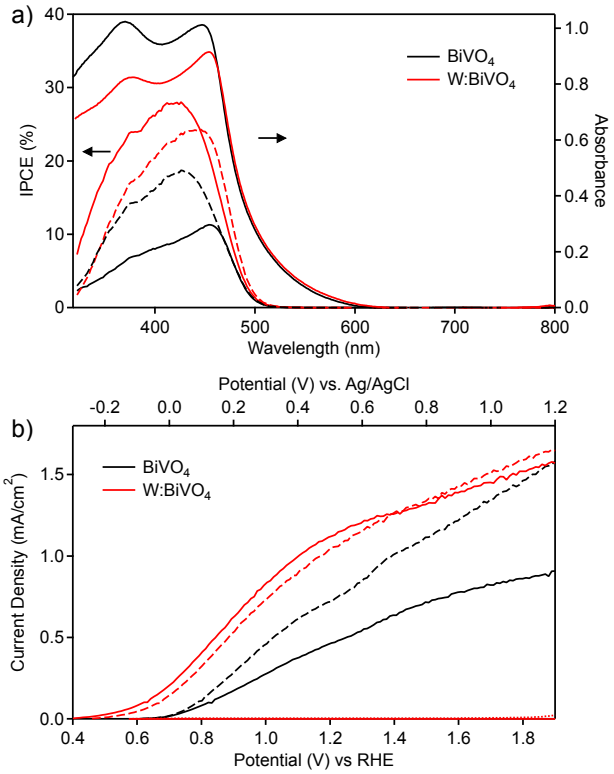

Figure 6.3. IPCE and *J-V* Curves of $BiVO_4$ and W:$BiVO_4$
a) Absorption spectra, photocurrent action (IPCE) spectra measured at 1.23 V vs RHE, and **b)** current density–voltage (*J-V*) curves measured for representative $BiVO_4$ (black) and W:$BiVO_4$ (red) photoanodes under one-sun AM1.5 front-side illumination (solid), back-side illumination (dashed), and in the dark (dotted), measured in 0.1 M $NaHCO_3$ electrolyte at pH 8.5 for ease of comparison to the data in ref. 16. $BiVO_4$ photoanodes reportedly perform best in this electrolyte because of the catalytic role of carbonate ions.[16] The tail in the absorption spectra below 500 nm comes from scattering.

The above results are consistent with those reported previously for $BiVO_4$ and W:$BiVO_4$ photoanodes,[11,15,18,37] and hence the conclusions drawn from investigation of these photoanodes are expected to be generally applicable to other $BiVO_4$-based photoanodes.

B. Co-Pi deposition and water oxidation.

We next examined modification of the W:$BiVO_4$ surfaces with the amorphous electrocatalyst Co-Pi, which excels at water oxidation. We have previously reported that photo-assisted electrodeposition of Co-Pi onto α-Fe_2O_3 photoanodes yields superior PEC performance than Co-Pi electrodeposition or Co^{2+} surface impregnation.[30] In contrast with electrolysis, PEC water oxidation appears to be quite sensitive to the Co-Pi film thickness, slowing considerably at thicknesses exceeding only a few tens of nanometers.[29] Electrodeposition of Co-Pi onto α-Fe_2O_3 photoanodes yielded islands where pinholes exposed the more conductive TCO substrate, but photo-assisted electrodeposition yielded uniform thin layers of Co-Pi, deposited only where light generated oxidizing equivalents, and this procedure was shown to translate into better PEC performance.[30] For these reasons, Co-Pi was deposited onto W:$BiVO_4$ by photo-assisted electrodeposition in the present study. Similar to the behavior of α-Fe_2O_3,[29] deposition of excess Co-Pi onto $BiVO_4$ leads to a decrease in sustainable PEC water oxidation rates for both front- and back-side illumination, so all measurements reported here were performed with front-side illumination following optimization of the Co-Pi thickness for PEC current density. Despite the

reported enhanced performance of $BiVO_4$ in bicarbonate electrolyte, due to its poor buffering ability and potentially non-innocent role, PEC experiments were conducted in 0.1 M KPi electrolyte buffered to pH 8.

Figure 6.4 summarizes PEC results obtained from a representative W:$BiVO_4$ photoanode. Figure 6.4a shows *J-V* curves collected using a W:$BiVO_4$ photoanode before and after Co-Pi deposition. Co-Pi deposition yields a remarkable ~440 mV cathodic shift in the onset potential for water oxidation relative to the parent W:$BiVO_4$ photoanode. As a result, the Co-Pi/W:$BiVO_4$ photoanode exhibits an onset potential of only ~310 mV vs RHE. This onset potential is ~550 mV lower than that obtained with the best Co-Pi/α-Fe_2O_3 photoanodes (~860 mV).[30] Very similar results are obtained using $BiVO_4$ except that the overall photocurrent densities are smaller (see Appendix D). The maximum photocurrent densities of these Co-Pi/W:$BiVO_4$ photoanodes are not as large as those achieved with Co-Pi/α-Fe_2O_3 photoanodes, but because of the very low onset potentials, the overall thermodynamic solar-to-hydrogen conversion efficiencies of the single-junction PEC cells based on Co-Pi/W:$BiVO_4$ are greater (*vide infra*).

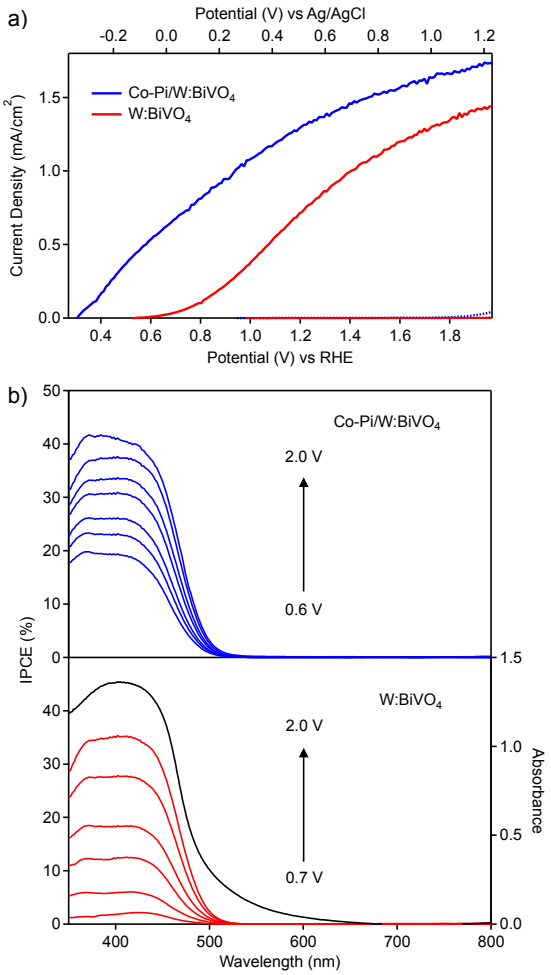

Figure 6.4. PEC and IPCE Measurements of a Co-Pi/W:$BiVO_4$ Photoanode
a) Current density–voltage (*J-V*) curves measured for a W:$BiVO_4$ photoanode before (red) and after (blue) photo-assisted electrodeposition of Co-Pi under front-side illumination (solid line) and in the dark (dotted line). Experiments were performed with 1 sun, AM 1.5 simulated solar irradiation in 0.1 M KPi buffer at pH 8 at a scan rate of 10 mV/s. **b)** Absorption (black) and photocurrent action spectra of the same W:$BiVO_4$ photoanode before (red) and after (blue) Co-Pi deposition. Photocurrent action spectra were collect at applied potentials of 0.6, 0.7, 0.8, 1.0, 1.2, 1.6, and 2.0 V vs RHE.

Photocurrent action spectra (Figure 6.4b) mirror the substantial improvements seen in Figure 6.4a after Co-Pi modification, especially at low applied potentials. Co-Pi itself does not contribute any additional features to the photocurrent action spectra of the composite Co-Pi/W:$BiVO_4$ photoanodes. Instead, increased IPCE values are observed across the entire W:$BiVO_4$ response curve. Co-Pi yields an IPCE maximum of ~20% at 0.6 V vs RHE (λ = 370 nm), where essentially no photocurrent was observed using W:$BiVO_4$ alone, and of ~33% at 1.23 V vs RHE. These data confirm the function of Co-Pi as a surface electrocatalyst that improves conversion of photo-generated holes into productive redox equivalents, without directly contributing to light harvesting or causing significant occlusion of the underlying photoanode.

Oxygen detection experiments confirm that this enhanced photocurrent is associated with O_2 evolution. Figure 6.5 plots O_2 generation vs time in a PEC experiment performed while irradiating a Co-Pi/W:$BiVO_4$ photoanode with one-sun simulated AM1.5 light at 1 V vs RHE in 0.1 M KPi buffered at pH 8. At this bias, the parent W:$BiVO_4$ photoanode shows only one third the PEC current density of the Co-Pi/W:$BiVO_4$ photoanode.

Following an initial spike when irradiation begins, attributable in part to cobalt oxidation, the photocurrent was very stable throughout the course of the experiment. The small nonlinearities in the O_2 evolution data result from formation, accumulation, and release of oxygen bubbles at the photoanode surface. Overall, the data show an average O_2 evolution rate of ~2.4×10^{-9} mol/sec·cm^2 with one-sun illumination. The solid pink curve plots the O_2 concentration predicted from the photocurrent assuming 100% faradaic efficiency. The excellent agreement between this line and the experimental O_2 evolution data confirms that the photocurrent densities measured for this Co-Pi/W:$BiVO_4$ photoanode are associated with water oxidation, and hence that Co-Pi substantially improves the solar water oxidation efficiency of W:$BiVO_4$.

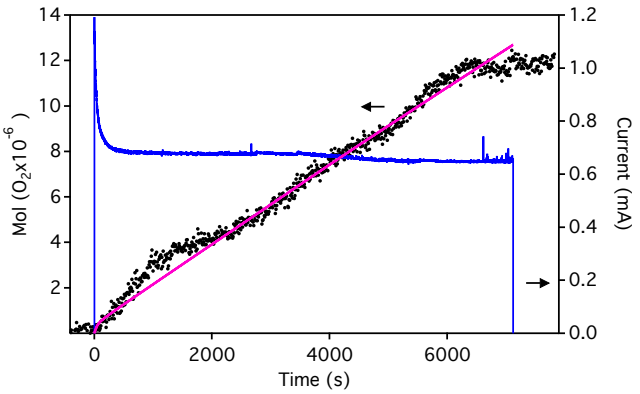

Figure 6.5. Oxygen Detection of a Co-Pi/W:$BiVO_4$ Photoanode
Total O_2 produced (black dots) from approximately one-sun AM1.5 illumination of a Co-Pi/W:$BiVO_4$ photoanode poised at 1 V vs RHE in 0.1 M KPi buffered at pH 8. The pink curve shows the O_2 evolution calculated from the measured photocurrent (blue curve) assuming 100% faradaic efficiency.

C. Comparison with H_2O_2 oxidation.

The remarkable reduction in onset potential for PEC water oxidation by W:$BiVO_4$ photoanodes following Co-Pi deposition implies facile water oxidation under these experimental conditions. To assess the effectiveness of this catalyst, an easily oxidized surrogate substrate was sought that would reveal the ultimate performance limit for these photoanodes in the absence of surface electron-hole recombination. Various sacrificial reductants such as quinol[40] and Na_2SO_3[18] have been used for this purpose previously. Recently, PEC H_2O_2 oxidation was shown to provide a useful metric for assessing the performance limits of α-Fe_2O_3 photoanodes.[41] With a structure similar to H_2O, oxidation kinetics at least 10 times faster than H_2O, and a low reduction potential of 0.68 V compared to 1.23 V for H_2O, H_2O_2 is a suitable surrogate for H_2O, and we therefore examined PEC H_2O_2 oxidation by W:$BiVO_4$ photoanodes.

Figure 6.6 presents *J-V* curves and photocurrent transients measured for a W:$BiVO_4$ photoanode with and without H_2O_2, and compares these data to parallel results collected during PEC water oxidation by the same photoanode following Co-Pi deposition, all in 0.1 M KPi buffer at pH 8. The onset potential for PEC water oxidation by the W:$BiVO_4$ photoanode is ~740 mV (Figure 6.6a). Spikes followed by slow decay are observed in the photocurrent transients at low potentials. These effects diminish with increasing applied potential, where the photocurrent responses become more square (Figure 6.6b,c). Together, these observations indicate the presence of surface recombination processes in which initial hole accumulation at the photoanode/electrolyte interface is followed by some degree of electron-hole recombination before steady-state photocurrents are

reached. Recombination is most prevalent at low applied potentials, leading to little or no steady-state photocurrent. Adding 0.1 M H_2O_2 to the electrolyte suppresses these spikes, indicating suppressed surface recombination, and the onset potential shifts cathodically down to 290 mV. The square transient photocurrent responses seen in Fig. 4b are consistent with the conclusion that all holes reaching the photoanode surface are successfully captured by H_2O_2. The PEC data collected with H_2O_2 as the surrogate substrate thus illustrate the limiting behavior that can be expected from these W:$BiVO_4$ photoanodes in the absence of surface recombination losses.

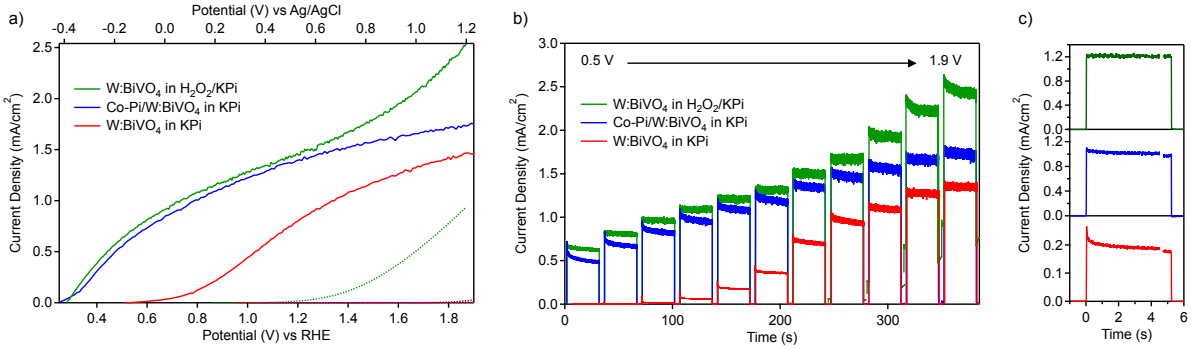

Figure 6.6. PEC Measurements of W:$BiVO_4$ Photoanodes in H_2O_2
a) *J-V* curves measured for a W:$BiVO_4$ photoanode in 0.1 M KPi buffer (pH 8) under one-sun AM1.5 front-side illumination (solid) and in the dark (dotted). The red curve describes PEC water oxidation by the W:$BiVO_4$ photoanode, and the green curve describes the PEC behavior after addition of 0.1 M H_2O_2 to the electrolyte solution. The blue curve describes PEC water oxidation by the W:$BiVO_4$ photoanode after Co-Pi deposition. **b)** Photocurrent transients associated with the curves in panel (a) as a function of increasing applied potentials (0.5, 0.6, 0.7, 0.8, 0.9, 1.0, 1.2, 1.4, 1.6, 1.8, and 1.9 V vs RHE). **c)** Expanded view of the photocurrent transients measured at 0.9 V vs RHE, showing the first 4.5 s and the last 0.5 s of the 30 s pulse.

Figure 6.6 also plots results from PEC measurements performed after Co-Pi deposition onto W:$BiVO_4$, again collected in 0.1 M KPi at pH 8. The *J-V* curve of the Co-Pi/W:$BiVO_4$ composite photoanode performing H_2O oxidation very closely resembles that of the W:$BiVO_4$ photoanode performing H_2O_2 oxidation. Very similar photocurrent densities are achieved for the two at all potentials below 1.5 V vs RHE, and their divergence above 1.5 V vs RHE simply results from the large dark current for H_2O_2 oxidation at those potentials (Figure 6.6a, dotted). Like the curves obtained with H_2O_2 oxidation, the photocurrent transients observed from PEC water oxidation with the Co-Pi/W:$BiVO_4$ photoanode show nearly square profiles with only small initial peaks, most likely from cobalt oxidation. These results demonstrate that Co-Pi is highly effective at promoting water oxidation by W:$BiVO_4$ photoanodes, almost completely suppressing losses due to surface electron-hole recombination. Evidently, Co-Pi provides a facile route by which photogenerated holes in W:$BiVO_4$ can be captured and used in the productive four-electron oxidation of water. The similarity of the PEC responses for H_2O_2 oxidation with W:$BiVO_4$ and H_2O oxidation with Co-Pi/W:$BiVO_4$ further suggests that Co-Pi does not alter the characteristics of the photoanode/electrolyte interface, for example by influencing charge separation within the space charge layer of the W:$BiVO_4$ electrode. Overall, these results show that Co-Pi makes W:$BiVO_4$ photoanodes as reactive toward H_2O as they are toward H_2O_2, a remarkable transformation.

6.4 Analysis and Discussion

The productive and non-productive kinetic processes relevant to PEC water oxidation by W:$BiVO_4$ and Co-Pi/W:$BiVO_4$ photoanodes are summarized in Figure 6.7. Here, J_{abs} is the photocurrent density that would result from an absorbed photon conversion efficiency (APCE) of 100%, *i.e.*, the photon absorption rate. Upon light absorption, part of J_{abs} is lost to bulk recombination, giving a charge-separation current density of $J_{sep} = J_{abs} - J_{br}$, where J_{br} describes bulk recombination, such that the quantum efficiency for migration of photogenerated holes to the semiconductor/electrolyte interface without being annihilated via bulk recombination is $\varphi_{sep} = J_{sep}/J_{abs}$. For simplicity, we include recombination in the depletion region within J_{br}. This current density may then be reduced by surface recombination losses (J_{sr}) or be successfully converted to substrate oxidation (J_{ox}) such that the quantum efficiency for substrate oxidation by a surface hole is $\varphi_{ox} = J_{ox}/J_{sep} = 1 - J_{sr}/J_{sep}$. When faradaic, the surviving electrons are collected at the back contact with the same rate as holes are converted to substrate oxidation, namely with the observed PEC photocurrent density (J_{PEC}). The photocurrent density arising from PEC water oxidation is thus described by Equation 6.1.

$$J_{PEC} = J_{abs}\phi_{sep}\phi_{ox} \qquad \text{(Equation 6.1)}$$

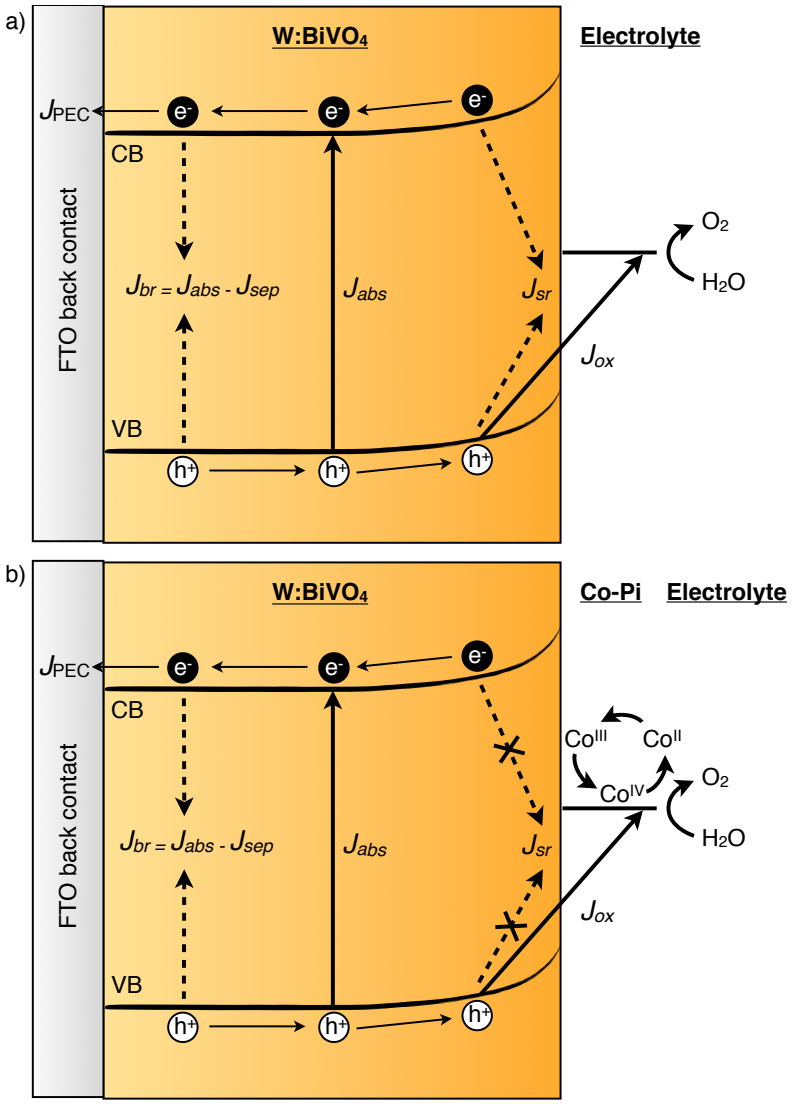

Figure 6.7. Energy Diagram of PEC Water Oxidation by W:$BiVO_4$ with and without Co-Pi
Energy diagram showing the kinetic processes active in the **a)** W:$BiVO_4$ and **b)** Co-Pi/W:$BiVO_4$ PEC photoanodes. Electron-hole pairs are generated with a current density associated with photon absorption (J_{abs}) and can recombine non-productively with current densities associated with radiative or nonradiative bulk (J_{br}) and surface (J_{sr}) recombination. Electron collection at the back contact (J_{PEC}) and hole transfer to the oxidizable substrate (J_{ox}) are productive processes contributing to PEC device efficiency.

The surface and bulk recombination processes in these W:$BiVO_4$ PEC cells can be assessed quantitatively by analysis of the data in Figure 6.6 using Equation 6.1.[41] In the limit of rapid and facile substrate oxidation, such as with H_2O_2, surface recombination is completely suppressed and $\varphi_{ox} = 1$. The photocurrent density in this limit is then $J_{PEC} \equiv J^{H2O2} = J_{abs} \times \varphi_{sep}$. When probing H_2O oxidation with the same photoanode, $\varphi_{ox} < 1$ and can be calculated from the ratio J^{H2O}/J^{H2O2}. Similarly, φ_{sep} can be calculated from J^{H2O2}/J_{abs}. Here, $J_{abs} \sim 5.26$ mA/cm^2 is estimated from the absorption spectrum of the W:$BiVO_4$ photoanode used in Figure 6.6.

Figure 6.8 plots φ_{sep} and φ_{ox} determined in this way for W:$BiVO_4$ and Co-Pi/W:$BiVO_4$ photoanodes performing PEC water oxidation at various applied potentials. Before Co-Pi modification, φ_{ox} of the W:$BiVO_4$ photoanode is very low at potentials below 1.0 V vs RHE, but it increases to ~0.75 at 1.5 V vs RHE. After Co-Pi

modification, φ_{ox} approaches unity throughout the entire potential range (φ_{ox} = 0.8-1.0). Meanwhile, φ_{sep} increases gradually from ~0.1 to 0.3 over this potential range.

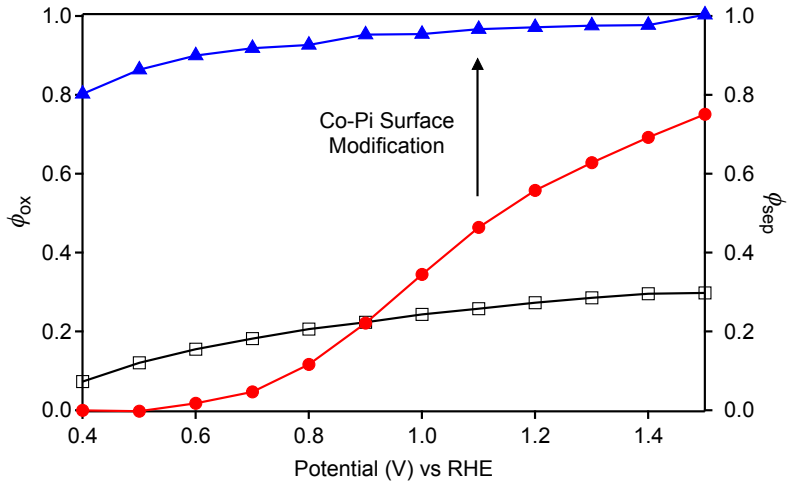

Figure 6.8. Water Oxidation and Charge Separation Efficiencies of W:BiVO$_4$
Substrate oxidation efficiencies (φ_{ox}) determined from the data in Figure 6.6 for Co-Pi/W:BiVO$_4$ (blue triangles) and W:BiVO$_4$ (red circles) photoanodes under PEC water oxidation conditions. The hollow squares plot the charge separation yields (φ_{sep}, applicable to both electrodes) at various potentials.

This analysis confirms the conclusion drawn above that Co-Pi almost completely suppresses surface recombination losses in W:BiVO$_4$ photoanodes. For bare W:BiVO$_4$ (Figure 6.7a), surface recombination (J_{sr}) is a major loss pathway and results in poor water oxidation (J_{ox}) and consequently poor PEC photocurrent densities, especially at low applied potentials. After Co-Pi modification, J_{ox} increases dramatically relative to J_{sr} such that φ_{ox} approaches unity (Figure 6.7b). Evidently, photo-generated holes that migrate to the W:BiVO$_4$ surfaces are captured by the Co-Pi electrocatalyst with near 100% quantum efficiency, where they also oxidize water with near 100% quantum efficiency. Overall, water oxidation becomes much more facile, making the desired catalysis kinetically competitive with non-productive surface electron-hole recombination processes. It is not known whether this improvement stems from an absolute increase in J_{ox}, an absolute decrease in J_{sr}, or both.

Using φ_{sep} determined in the above analysis, the effective hole diffusion lengths (L_p) of W:BiVO$_4$ photoanodes can be estimated from the Gärtner model[42] using Equation 6.2, where α is the absorption coefficient, and W is the effective depletion layer width.[4,40,42]

$$\phi_{sep} = 1 - \frac{e^{-\alpha W}}{1 + \alpha L_p} \qquad \text{(Equation 6.2)}$$

An absorption coefficient (α) of ~40,000 cm^{-1} at λ = 420 nm is estimated from the experimental absorption spectrum and a dielectric constant of $\varepsilon_r \sim 68$ has been determined.[43,44] W at large bias (1.5 V) can be estimated from the Mott-Schottky analyses of various BiVO$_4$ and W:BiVO$_4$ photoanodes reported previously (see Appendix D for details).[11,15,18] Experimentally, BiVO$_4$ and W:BiVO$_4$ donor densities (N_d) from 10^{18} to 10^{21} cm^{-3}

have been reported.[11,15,18] To ensure a reasonably general estimate of L_p, an even larger range (N_d ~ 10^{18}-10^{23} cm^{-3}) was considered, but W is not strongly influenced by N_d at large bias. Using the above parameters, Equation 6.2 yields a conservative general estimate of L_p ~ 100-200 nm (see Appendix D). Although ~10-100 times larger than that of α-Fe_2O_3, L_p in W:$BiVO_4$ is comparable to the absorption length (~250 nm at 420 nm) and hence still too small to not hinder performance, as illustrated by Figure 6.8.

Importantly, this analysis allows the conclusion that PEC water oxidation by Co-Pi/W:$BiVO_4$ photoanodes is no longer limited by surface recombination effects, as was the case with W:$BiVO_4$ alone, but it is now limited solely by bulk-like charge recombination processes (Figure 6.8). The latter could potentially be improved by use of thinner films (at the expense of J_{abs}), materials with higher structural quality and hence fewer bulk defects (*e.g.*, epitaxial films), reduced dimensionality to accelerate charge collection (*e.g.*, nanowires or mesostructures),[17,45-48] or via refined impurity doping. As proof of concept, the thicknesses of the W:$BiVO_4$ photoanodes described here (~300 nm) were optimized to give the highest photocurrent densities, but W:$BiVO_4$ films that were half as thick still gave ~80% of the same photocurrent density, suggesting significantly less bulk recombination in the thinner films.

Interestingly, the effect of Co-Pi surface modification is more substantial on W:$BiVO_4$ than observed previously on α-Fe_2O_3 photoanodes.[29,30] Surface recombination is a major loss mechanism in α-Fe_2O_3 photoanodes,[40,49] and in its absence (*e.g.*, using H_2O_2), photocurrent onset potentials of ~0.5 V vs RHE have been achieved.[41] Surface catalysts including Co^{2+},[50] Co-Pi,[28-30] and IrO_2[51] all improve hole capture and conversion to water oxidation by mesostructured α-Fe_2O_3 photoanodes, but none has shown onset potentials below ~0.8 V vs RHE. Even with excellent surface catalysts, surface electron-hole recombination is thus still kinetically competitive in α-Fe_2O_3. Possible causes of this inefficiency include (*i*) incomplete surface coverage by the catalyst, perhaps due to the high porosity and surface roughness of the dendritic photoanodes, (*ii*) slow hole transfer from the surface to the catalyst, perhaps arising from the presence of deep hole traps,[40] or (*iii*) fast surface electron-hole recombination.[40,49] The latter two factors are most probable, and together they conspire to make surface electron-hole recombination in α-Fe_2O_3 photoanodes problematic even in the presence of effective surface electrocatalysts. In contrast, the data and analysis presented in Figures 6.6 and 6.8 indicate that surface electron-hole recombination has been largely eliminated in Co-Pi/W:$BiVO_4$ photoanodes.

Although characterized by an intense direct-gap absorption in the visible, the performance of $BiVO_4$ as a photoanode is limited by its inability to absorb more of the solar spectrum. From its 2.4-2.5 eV band gap, the maximum theoretical photocurrent density achievable from $BiVO_4$ under 1 sun AM 1.5 sunlight is J_{abs} ~ 6.5 mA/cm^2. α-Fe_2O_3 (~2.1 eV) can reach roughly twice this theoretical maximum (J_{abs} ~ 12.5 mA/cm^2) under the same conditions, but its large bulk electron-hole recombination rates and short hole diffusion lengths limit φ_{sep} to ~0.25,[40,41] well below the values observed here for W:$BiVO_4$. Light harvesting by $BiVO_4$ could conceivably be improved through alloying, or this limitation could be circumvented by its integration with other materials in layered structures.[52]

Finally, we address the overall solar-to-hydrogen conversion efficiencies of PEC cells involving these Co-Pi/W:$BiVO_4$ composite photoanodes. Using the photocurrent from 1 sun, AM 1.5 simulated solar irradiation (100 mW/cm^2), overall solar-to-hydrogen (STH) conversion efficiencies of the single-junction PEC process can be calculated from the Gibbs free energy of the reaction using Equation 3, which accounts for the

thermodynamic losses associated with application of an external anodic bias and assumes 100% faradaic efficiency.

$$\eta_{STH}(\%) = I(\mathrm{mA/cm^2}) \times (1.23\mathrm{V} - V_{app}) \qquad \text{(Equation 6.3)}$$

The maximum efficiency obtained from these Co-Pi/W:$BiVO_4$ composite photoanodes after accounting for external bias is 0.40% at 0.72 V vs RHE. This value is almost twice that of the best Co-Pi/α-Fe_2O_3 photoanodes reported previously (0.23%).[30] These numbers refer to the experimental solar power conversion efficiencies of these specific single-junction photoanodes. However, it is envisioned that PEC solar water splitting will not be implemented using single-junction devices with external bias, but instead the necessary anodic bias will be supplied by a second photoelectrode or PV device configured in a tandem geometry,[3,6,53,54] thereby improving η_{STH}. In this configuration, V_{app} is effectively zero and Equation 3 becomes $\eta_{STH}(\%) = I(\mathrm{mA/cm^2})*1.23\mathrm{V}$. Although both φ_{sep} and φ_{ox} are greater in W:$BiVO_4$ than in α-Fe_2O_3, Co-Pi/α-Fe_2O_3 photoanodes in this configuration provide larger solar-to-hydrogen conversion efficiencies (~4.1%) than Co-Pi/W:$BiVO_4$ photoanodes (1.7%), when calculated from photocurrents measured at 1.43 V vs RHE. This difference comes from the different light-harvesting abilities (J_{abs}) of the two materials. Practically, however, it is difficult to achieve the 1.43 V needed for this device structure without using two additional PV or PEC cells connected in series,[54] which raises costs. Co-Pi/W:$BiVO_4$ excels in the voltage range typically accessible from low-cost PEC or PV cells (< 1.0 V), making it well suited for a simple tandem configuration.

6.5 Conclusion

Modification of W:$BiVO_4$ photoanode surfaces with the electrocatalyst Co-Pi has yielded a ~440 mV cathodic shift in the onset potential for PEC water oxidation. PEC experiments with H_2O_2 as a surrogate substrate have revealed that Co-Pi addition almost completely eliminates losses due to surface electron-hole recombination. The nearly quantitative substrate oxidation efficiencies (φ_{ox}) achieved with Co-Pi-modified W:$BiVO_4$ imply that photo-generated holes migrate to the W:$BiVO_4$ surfaces and are evidently captured by the Co-Pi electrocatalyst with nearly quantum efficiency, where they also oxidize water with nearly quantum efficiency. With Co-Pi, water oxidation becomes much more facile, making the desired catalysis out-compete unproductive surface electron-hole recombination.

The low absolute onset potential of ~310 mV vs RHE achieved at pH 8 with Co-Pi/W:$BiVO_4$ is promising for solar water splitting in low-cost tandem PEC cells. The results presented here demonstrate that Co-Pi largely eliminates a major performance limitation of W:$BiVO_4$ photoanodes by making J_{sr} kinetically uncompetitive with J_{ox}, even at the low applied potentials accessible from low-cost single-junction PEC or PV cells in a tandem device configuration. The primary performance limitation of the Co-Pi/W:$BiVO_4$ photoanodes is now their insufficient photon harvesting (J_{abs}), and efforts should be focused on developing this and related materials to improve this aspect.

6.6 Notes on Chapter 6

1. Fujishima, A.; Honda, K., *Nature* **1972,** *238*, 37-8.
2. Bard, A. J.; Fox, M. A., *Acc. Chem. Res.* **1995,** *28*, 141-145.
3. Grätzel, M., *Nature* **2001,** *414*, 338-344.
4. Grimes, C. A.; Varghese, O. K.; Ranjan, S., *Light, Water, Hydrogen*. Springer: New York, 2007.
5. Walter, M. G.; Warren, E. L.; McKone, J. R.; Boettcher, S. W.; Mi, Q.; Santori, E. A.; Lewis, N. S., *Chem. Rev.* **2010,** *110*, 6446-6473.
6. Alexander, B. D.; Kulesza, P. J.; Rutkowska, I.; Solarska, R.; Augustynski, J., *J. Mater. Chem.* **2008,** *18*, 2298-2303.
7. van de Krol, R.; Liang, Y.; Schoonman, J., *J. Mater. Chem.* **2008,** *18*, 2311-2320.
8. Scaife, D. E., *Sol. Energy* **1980,** *25*, 41-54.
9. Kudo, A.; Ueda, K.; Kato, H.; Mikami, I., *Catal. Lett.* **1998,** *53*, 229-230.
10. Tokunaga, S.; Kato, H.; Kudo, A., *Chem. Mater.* **2001,** *13*, 4624-4628.
11. Sayama, K.; Nomura, A.; Arai, T.; Sugita, T.; Abe, R.; Yanagida, S.; Oi, T.; Iwasaki, Y.; Abe, Y.; Sugihara, H., *J. Phys. Chem. B* **2006,** *110*, 11352-11360.
12. Yao, W.; Iwai, H.; Ye, J., *Dalton Trans.* **2008**, 1426-1430.
13. Luo, W.; Wang, Z.; Wan, L.; Li, Z.; Yu, T.; Zou, Z., *J. Phys. D: Appl. Phys.* **2010,** *43*, 405402.
14. Ng, Y. H.; Iwase, A.; Kudo, A.; Amal, R., *J. Phys. Chem. Lett.* **2010,** *1*, 2607-2612.
15. Li, M.; Zhao, L.; Guo, L., *Int. J. Hydrogen Energy* **2010,** *35*, 7127-7133.
16. Sayama, K.; Wang, N.; Miseki, Y.; Kusama, H.; Onozawa-Komatsuzaki, N.; Sugihara, H., *Chem. Lett.* **2010,** *39*, 17-19.
17. Su, J.; Guo, L.; Yoriya, S.; Grimes, C. A., *Cryst. Growth Des.* **2010,** *10*, 856-861.
18. Ye, H.; Lee, J.; Jang, J. S.; Bard, A. J., *J. Phys. Chem.* **2010,** *114*, 13322-13328.
19. Chatchai, P.; Kishioka, S.-y.; Murakami, Y.; Nosaka, A. Y.; Nosaka, Y., *Electrochim. Acta* **2010,** *55*, 592-596.
20. Berglund, S. P.; Flaherty, D. W.; Hahn, N. T.; Bard, A. J.; Mullins, C. B., *J. Phys. Chem. C* **2011,** *115*, 3794-3802.
21. Hong, S. J.; Lee, S.; Jang, J. S.; Lee, J. S., *Energy Environ. Sci.* **2011,** *4*, 1781-1787.
22. Ye, H.; Park, H. S.; Bard, A. J., *J. Phys. Chem. C* **2011,** *115*, 12464-12470.
23. Yin, W.-J.; Wei, S.-H.; Al-Jassim, M. M.; Turner, J.; Yan, Y., *Phys. Rev. B* **2011,** *83*, 155102.
24. Sun, J.; Zhong, D. K.; Gamelin, D. R., *Energy Environ. Sci.* **2010,** *3*, 1252-1261.
25. Kanan, M. W.; Nocera, D. G., *Science* **2008,** *321*, 1072-1075.
26. Lutterman, D. A.; Surendranath, Y.; Nocera, D. G., *J. Am. Chem. Soc.* **2009,** *131*, 3838-3839.
27. Surendranath, Y.; Kanan, M. W.; Nocera, D. G., *J. Am. Chem. Soc.* **2010,** *132*, 16501-16509.
28. Zhong, D. K.; Sun, J.; Inumaru, H.; Gamelin, D. R., *J. Am. Chem. Soc.* **2009,** *131*, 6086-6087.
29. Zhong, D. K.; Gamelin, D. R., *J. Am. Chem. Soc.* **2010,** *132*, 4202-4207.
30. Zhong, D. K.; Cornuz, M.; Sivula, K.; Grätzel, M.; Gamelin, D. R., *Energy Environ. Sci.* **2011,** *4*, 1759-1764.

31. Barroso, M.; Cowan, A. J.; Pendlebury, S. R.; Grätzel, M.; Klug, D. R.; Durrant, J. R., *J. Am. Chem. Soc.* **2011,** *133*, 14858-14871.
32. Steinmiller, E. M. P.; Choi, K.-S., *Proc. Nat. Acad. Sci.* **2009,** *106*, 20633-20636.
33. Seabold, J. A.; Choi, K.-S., *Chem. Mater.* **2011,** *23*, 1105-1112.
34. Young, E. R.; Costi, R.; Paydavosi, S.; Nocera, D. G.; Bulovic, V., *Energy Environ. Sci.* **2011,** *4*, 2058-2061.
35. Pijpers, J. J. H.; Winkler, M. T.; Surendranath, Y.; Buonassisi, T.; Nocera, D. G., *Proc. Natl. Acad. Sci. U. S. A.* **2011,** *108*, 10056-10061.
36. Sleight, A. W.; Aykan, K.; Rogers, D. B., *J. Solid State Chem.* **1975,** *13*, 231-236.
37. Park, H. S.; Kweon, K. E.; Ye, H.; Paek, E.; Hwang, G. S.; Bard, A. J., *J. Phys. Chem. C* **2011,** *115*, 17870-17879.
38. Payne, D. J.; Robinson, M. D. M.; Egdell, R. G.; Walsh, A.; McNulty, J.; Smith, K. E.; Piper, L. F. J., *Appl. Phys. Lett.* **2011,** *98*, 212110.
39. Walsh, A.; Yan, Y.; Huda, M. N.; Al-Jassim, M. M.; Wei, S.-H., *Chem. Mater.* **2009,** *21*, 547-551.
40. Dare-Edwards, M. P.; Goodenough, J. B.; Hamnett, A.; Trevellick, P. R., *J. Chem. Soc., Faraday Trans.* **1983,** *79*, 2027-2041.
41. Dotan, H.; Sivula, K.; Grätzel, M.; Rothschild, A.; Warren, S., *Energy Environ. Sci.* **2011,** *4*, 958-964.
42. Gärtner, W. W., *Phys. Rev.* **1959,** *116*, 84-87.
43. Valent, M.; Suvorov, D., *J. Am. Ceram. Soc.* **2000,** *83*, 2721-2729.
44. Wee, S.-H.; Kim, D.-W.; Yoo, S.-I., *J. Am. Ceram. Soc.* **2004,** *87*, 871-874.
45. Hagedorn, K.; Forgacs, C.; Collins, S.; Maldonado, S., *J. Phys. Chem. C* **2011,** *114*, 12010-12017.
46. Liu, R.; Lin, Y.; Chou, L.-Y.; Sheehan, S. W.; He, W.; Zhang, F.; Hou, H. J. M.; Wang, D., *Angew. Chem. Int. Ed.* **2011,** *50*, 499-502.
47. Lin, Y.; Zhou, S.; Sheehan, S. W.; Wang, D., *J. Am. Chem. Soc.* **2011,** *133*, 2398-2401.
48. Ling, Y.; Wang, G.; Wheeler, D. A.; Zhang, J. Z.; Li, Y., *Nano Lett.* **2011,** *11*, 2119-2125.
49. Klahr, B. M.; Martinson, A. B. F.; Hamann, T. W., *Langmuir* **2011,** *27*, 461-468.
50. Kay, A.; Cesar, I.; Grätzel, M., *J. Am. Chem. Soc.* **2006,** *128*, 15714-15721.
51. Tilley, S. D.; Cornuz, M.; Sivula, K.; Grätzel, M., *Angew. Chem. Int. Ed.* **2010,** *49*, 6405-6408.
52. Sivula, K.; Le Formal, F.; Grätzel, M., *Chem. Mater.* **2009,** *21*, 2862-2867.
53. Arakawa, H.; Shiraishi, C.; Tatemoto, M.; Kishida, H.; Usui, D.; Suma, A.; Takamisawa, A.; Yamaguchi, T., *Proc. SPIE* **2007,** *6650*, 665003.
54. Brillet, J.; Cornuz, M.; Le Formal, F.; Yum, J.-H.; Grätzel, M.; Sivula, K., *J. Mater. Res.* **2010,** *25*, 17-24.

Chapter 7: Understanding the Cobalt-Catalyst/Semiconductor Interface: Conclusions and Outlook

7.1 The Catalyst/Semiconductor Relationship

In previous chapters we have shown that surface modification of semiconductor photoanodes with a cobalt-phosphate water oxidation electrocatalyst (Co-Pi) enhances their photoelectrochemical (PEC) performance. A cathodic shift of the *J-V* curve and more square-like photocurrent vs. time response were observed after Co-Pi modification.[1-4] The photocurrent enhancement is derived solely from excitation of the semiconductor itself, and not from Co-Pi, and is directly correlated with enhanced oxygen formation.[1,2] From these results it is clear that Co-Pi leads to a reduction in the overpotential for PEC water oxidation when applied onto various oxide photoanodes. Following the success with α-Fe_2O_3, similar results were also observed with Co-Pi modification on ZnO,[5] WO_3,[6] $BiVO_4$,[4,7] and Si.[8,9] Most likely Co-Pi acts as a surface electrocatalyst in the composite material. Upon light excitation, photogenerated holes from the semiconductor migrate to the Co-Pi catalyst where water oxidation proceeds at lower overpotentials relative to the bare semiconductor. Although this scenario is most likely responsible for the PEC enhancement with Co-Pi, to date, there is no direct evidence verifying that Co-Pi behaves as a surface electrocatalyst in the composite assembly. Aside from a catalytic role, Co-Pi may reduce surface recombination due to interfacial effects, or passivate traps on the semiconductor surface, resulting in enhanced PEC performance. There have been many reports on the effects of applying Co-Pi on photoanodes but few focus on understanding the interaction between the semiconductor and Co-Pi.

Recently, Durrant and coworkers published transient absorption studies on Co-Pi/α-Fe_2O_3 photoanodes to address the role of Co-Pi in enhancing the photocatalytic activity of α-Fe_2O_3 towards water oxidation.[10] They observed that the transient absorption features of Co-Pi/α-Fe_2O_3 photoanodes without an external bias resemble those of bare α-Fe_2O_3 with an external bias. Analysis of the data reveal that the lifetime of photogenerated holes on α-Fe_2O_3 is increased by three orders of magnitude (μs to ms) with Co-Pi.[10] Since the hole resides on α-Fe_2O_3, Co-Pi does not actively participate in water oxidation within the composite Co-Pi/α-Fe_2O_3 photoanode. Instead, water oxidation still occurs on the α-Fe_2O_3 surface and Co-Pi simply reduces e-h recombination in α-Fe_2O_3 to be competitive with slow water oxidation kinetics. One possible explanation for this behavior is the formation of a Schottky-type heterojunction between Co-Pi and α-Fe_2O_3, leading to increased band-bending that facilitates e-h separation near the photoanode surface.

The results from those transient absorption studies are surprising and suggest that enhancement effects of Co-Pi on the surface of α-Fe_2O_3 are due solely to interfacial effects and do not require hole transfer to Co-Pi. However, the conclusions are contingent upon the interpretation of the transient absorption data and it is unclear whether the 900 nm feature used in the analysis is due solely to photogenerated holes in α-Fe_2O_3. In the same publication,[10] a bleach is also observed in the transient absorption data that correlates to a loss in Co^{III} species. Mechanistic studies, involving electrochemistry,[11,12] XANES,[13,14] and EPR,[15] on Co-Pi show that water oxidation occurs through a self-healing process involving a cycle of multiple cobalt oxidation states. The mechanism is shown in Figure 7.1. Under an anodic bias, Co^{III} in Co-Pi is oxidized to Co^{IV}, forming Co-μ-oxo groups that eventually release O_2 and reduce cobalt to Co^{II}.[12] The Co^{II} is labile, but under oxidizing conditions

the catalyst reverts back to Co^{III} as Co-Pi.[11] If α-Fe_2O_3 excitation results in a loss of Co^{III} species, then hole transfer to Co-Pi and water oxidation through the Co^{IV} intermediate is conceivable.

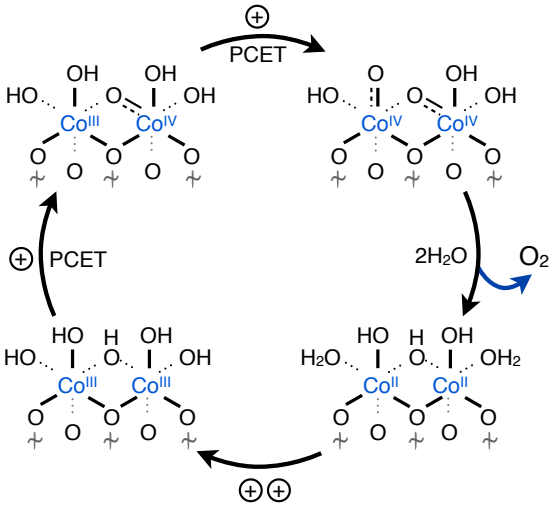

Figure 7.1. Scheme for Mechanism of Water Oxidation by Co-Pi

PEC studies on Co-Pi/semiconductor photoanodes consistently support the idea that Co-Pi behaves as a water oxidation catalyst within the composite construct. The prefeature prior to the catalytic wave observed in bulk electrolysis by Co-Pi is also observed in composite Co-Pi/semiconductor photoanodes.[2] This prefeature is associated with the oxidation of Co^{II} to Co^{III}, and partially Co^{IV} in Co-Pi,[12,16] indicating that water oxidation by Co-Pi under PEC and electrochemical conditions may be similar. Although Durrant and coworkers present evidence of an alternative mechanism, the absence of an applied bias and bleach of a Co^{III} signal suggests that a catalytic role of the Co-Pi layer cannot be ruled out under normal operating conditions. Moreover, if PEC enhancement by Co-Pi is indeed due to interfacial effects, such as formation of a heterojunction causing increased band-bending, a Mott-Schotty analysis that probes band potentials would be sensitive to this change. Mott-Schottky plots of Co-Pi/ZnO photoanodes compared to ZnO show that Co-Pi does not alter the flatband potential of ZnO.[5]

With contradictory reports on the role of Co-Pi in enhancing PEC water oxidation on semiconductor photoanodes, it is still unknown how the electrocatalyst behaves when integrated with a semiconductor. Possible roles Co-Pi may play in PEC enhancement include: *i*) promoting water oxidation by providing a more kinetically favorable pathway, *ii*) passivating surface traps to reduce recombination at the semiconductor surface, *iii*) increasing e-h separation by increasing band-bending, and *iv*) a combination of the above factors. Identifying which of the above scenarios are relevant will not be straightforward and will likely involve a combination of in situ PEC and spectroscopic studies.

In this chapter, I will try to elucidate the role of Co-Pi by analyzing the kinetic bottleneck observed in Co-Pi/semiconductor photoanodes, PEC results with various composite photoanodes, impedance spectroscopies, photoconductive microscopies, and PEC kinetic studies of catalyst-modified α-Fe_2O_3 photoanodes. Since functionalizing semiconductor surfaces with water oxidation electrocatalysts has been

demonstrated to be an effective method for increasing water oxidation efficiency, a better understanding of the catalyst/semiconductor interface and hole transfer across this interface is necessary for continued development of PEC cells based on this motif.

7.2 Origin of the Kinetic Bottleneck

In Chapter 4 a kinetic bottleneck associated with thick layers of Co-Pi deposited onto α-Fe_2O_3 was identified and was subsequently remediated by applying thin layers of catalyst through short-term electrodeposition and photo-assisted electrodeposition.[2,3] This kinetic bottleneck was also observed with TiO_2, ZnO, and $BiVO_4$ photoanodes in our lab. In all of these cases, when the catalyst layer becomes too thick, the steady state photocurrent density converges to that of the underlying semiconductor. The kinetic bottleneck occurs with both front and backside illumination of the composite photoanode, confirming that the decreased photocurrent is not simply from increased light absorption from the catalyst under frontside illumination.

Although the kinetic bottleneck was successfully circumvented by decreasing the amount of catalyst deposited, its origin has not been thoroughly investigated. If photogenerated holes in a Co-Pi/semiconductor photoanode do not transfer to the Co-Pi for catalytic water oxidation, but instead tunnel through the Co-Pi layer, then a PEC dependence on Co-Pi thickness might be expected. However, this does not appear to be the case. When the catalyst layer becomes too thick, one would expect photogenerated holes to recombine and annihilate the photocurrent, instead of converging to that of the underlying semiconductor.

Since surface modification with Co-Pi introduces a kinetic bottleneck that is not present in the semiconductor alone, an investigation into the properties of Co-Pi was initiated. In bulk electrolysis with Co-Pi on FTO, the water oxidation activity increases with the amount of Co-Pi electrodeposited due to the water permeable nature of Co-Pi. However, a slight loss of activity is observed as the amount of catalyst increases, shown previously in Chapter 4 and in Figure 7.2 below. Figure 7.2 shows the steady state current obtained from water electrolysis by Co-Pi as a function of the amount of catalyst deposited. It can be seen that the current dependence is not linear, but begins to saturate as the Co-Pi thickness increases, indicating that the catalyst is less efficient with increasing thickness. Indeed, the turnover frequency of Co-Pi has been reported to decrease with increasing Co-Pi deposition as well.[12]

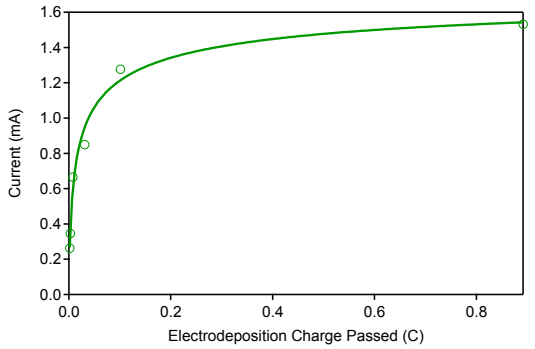

Figure 7.2. Dependence of the Water Oxidation Current with Co-Pi Thickness
Current from bulk electrolysis using Co-Pi films of varying thickness at 1.1 V vs Ag/AgCl, or 1.3 V vs NHE in 0.1 M KPi at pH 7. The charge passed during electrodeposition from a 0.5 mM Co^{2+} solution in 0.1 M KPi at 1.1 V vs NHE is directly proportional to the amount of Co-Pi deposited.

Despite inefficiencies with increasing Co-Pi thickness, however, appreciable water oxidation is still observed under electrolysis conditions even with catalyst layers that are several μm in thickness.[16,17] In contrast, in PEC water oxidation, the optimal Co-Pi thickness in Co-Pi/α-Fe_2O_3 photoanodes is only several tens of nanometers.[3] This stark difference is also observed in dark and light electrochemical experiments with composite photoanodes. Figure 7.3a shows the *J-V* curve of an α-Fe_2O_3 photoanode before (red curve) and after Co-Pi photo-assisted electrodeposition (blue curve). The other *J-V* curves are measured after partial dissolution of Co-Pi over hours in water under open circuit conditions (thin blue to bold black to thin green curves). Figure 7.3b follows the PEC and electrochemical water oxidation activity over the course of Co-Pi dissolution. The results show that whenever too much Co-Pi is deposited onto the photoanode, PEC performance can be improved by slowly redissolving the Co-Pi in water. At a certain point, too much Co-Pi is removed and PEC performance decreases again. While the PEC performance maximizes at a particular Co-Pi amount, the dark current does not show the same drop in steady state current density as Co-Pi thickness increases. Instead, the current density continues to increase with increasing Co-Pi deposition, similar to what is generally observed with Co-Pi under bulk electrolysis conditions. This result confirms that the kinetic bottleneck is a property of PEC cells and may be associated with photoexcitation.

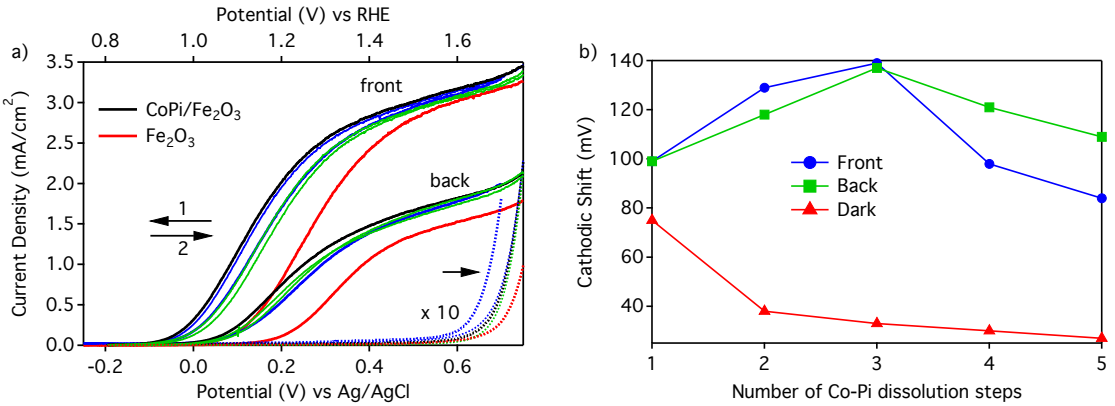

Figure 7.3. Dependence of Co-Pi/α-Fe_2O_3 Performance on the Co-Pi Thickness
a) *J-V* curves measured for an α-Fe_2O_3 photoanode before (red) and immediately after (blue) photo-assisted electrodeposition of Co-Pi. Additional curves were measured for various durations of Co-Pi dissolution (thin blue to bold black to green) in the dark (dotted) and under 1 sun, AM 1.5 simulated solar irradiation (solid). Measurements were made in 1 M NaOH at a scan rate of 10 mV/s. **b)** Cathodic shifts measured for the composite photoanode in panel (a) over the course of Co-Pi dissolution in the dark (red), under front-side illumination (blue), and under backside (green) illumination.

Surface electron-hole recombination represents a major loss channel in PEC cells that is not present in electrochemical cells. Our studies suggest that the kinetic bottleneck observed with thick Co-Pi coverage is a result of increased surface e-h recombination relative to water oxidation. Increasing the Co-Pi thickness thus makes surface e-h recombination kinetics more competitive with water oxidation kinetics. Because the catalyst itself is not changing and is permeable to water molecules, this result suggests that the bottleneck ultimately derives from hole diffusion through the Co-Pi film. When holes diffuse, more photoexcitation events are needed to accumulate four oxidizing equivalents in any one active site, and this leads to a greater probability for electron-hole recombination.

7.3 Other Composite Catalyst/Semiconductor Photoanodes

In Chapter 6, the electrocatalyst Co-Pi was applied onto W:$BiVO_4$ semiconductor photoanodes that exhibit significantly lower onset potentials for water oxidation than α-Fe_2O_3.[4] Using peroxide as a surface hole scavenger, PEC experiments revealed that Co-Pi modification almost completely eliminates surface e-h recombination losses in W:$BiVO_4$ by making water oxidation much more competitive. These experiments allowed us to examine the differences between W:$BiVO_4$ and α-Fe_2O_3 photoanodes and their effects on the PEC performance of the resulting composite photoanodes. The more substantial PEC enhancement with Co-Pi on W:$BiVO_4$ compared to α-Fe_2O_3 suggests differences in their recombination kinetics, since their band potentials are similar (see Figure 1.2). From PEC analysis, the performance of Co-Pi/α-Fe_2O_3 photoanodes is most likely limited by a combination of slow hole transfer kinetics to the catalyst, perhaps from deep hole traps, and fast e-h recombination at the α-Fe_2O_3 surface.[4]

The ability of Co-Pi to integrate with a variety of semiconductor materials makes the catalyst quite versatile. Aside from α-Fe_2O_3 and $BiVO_4$, Co-Pi can also be applied onto ZnO and TiO_2, although ZnO was unstable under water oxidizing conditions. TiO_2 nanowire photoanodes were fabricated from hydrothermal synthesis on FTO. An SEM image of the c-axis oriented rutile nanowires is presented in Figure 7.4a. Figure 7.4b shows the *J-V* curves of TiO_2 nanowire photoanodes before and after Co-Pi photo-assisted electrodeposition. A cathodic shift of ~190 mV was observed and was optimized for Co-Pi thickness. Altogether, from PEC results of various Co-Pi/semiconductor photoanodes one can infer that *i*) the reduced onset potential for water oxidation with Co-Pi is a result of the Co-Pi catalyst and not specific to the semiconductor, *ii*) the onset potentials for water oxidation are largely limited by the properties of the underlying semiconductor in the composite photoanodes, and *iii*) the kinetic bottleneck associated with thick Co-Pi layers under photoexcitation conditions affects all Co-Pi/semiconductor photoanodes.

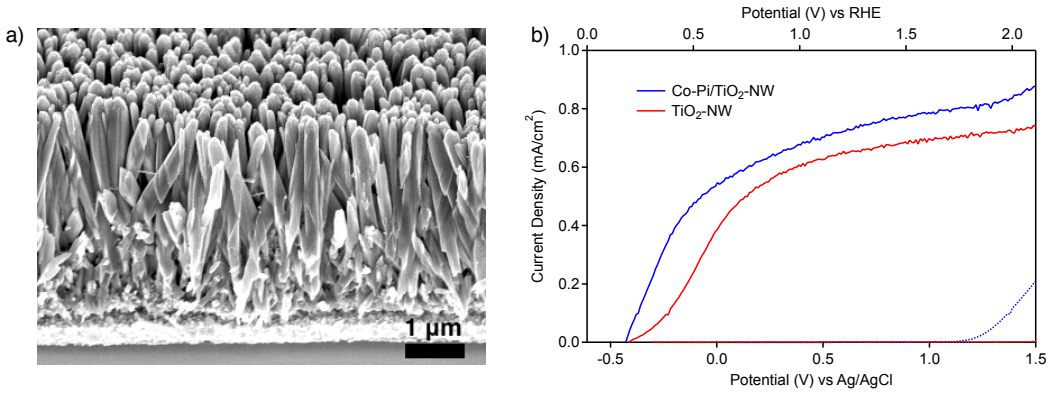

Figure 7.4. SEM and *J-V* Curves of a TiO_2 Nanowire Photoanode and Co-Pi-modified TiO_2 Photoanode
a) SEM image of a representative rutile TiO_2 nanowire photoanode at a 45° angle. **b)** *J-V* curves of a TiO_2 nanowire photoanode before (red) and after Co-Pi photo-assisted electrodeposition (blue) measured in 0.1 M KPi pH 7 buffer at a scan rate of 50 mV/s. The dotted and solid curves were recorded in the dark and under 1 sun, AM 1.5 simulated sunlight, respectively.

A comparison between Co-Pi and other cobalt or transition metal catalysts in the same composite framework may provide further insight into the role of Co-Pi in PEC water oxidation. Cobalt-methyl phosphonate (Co-MePi) is part of the same family of cobalt catalysts as Co-Pi, but is electrodeposited from a

methyl phosphonate buffer solution.[17] Figure 7.5 illustrates the *J-V* curves of a Co-MePi/α-Fe_2O_3 photoanode compared to the parent α-Fe_2O_3 photoanode under 1 sun, AM 1.5 simulated sunlight. The PEC behavior after the addition of Co-MePi is comparable to those after Co-Pi modification, with a cathodic shift of ~100 mV. When excess catalyst is added, the steady state PEC performance also degrades, same as with the Co-Pi/α-Fe_2O_3 photoanodes, due to a kinetic bottleneck associated with thick catalyst coating. Another cobalt-based electrocatalyst also gives similar PEC results when integrated with α-Fe_2O_3. A cobalt oxide catalyst, referred to here as "CoO_x," is formed by electrodeposition from an aqueous solution of Co^{2+}, such as cobalt nitrate, cobalt acetate, or cobalt sulfate.[18] X-ray diffraction experiments show that CoO_x does not match the typical diffraction patterns of known cobalt oxides, CoO, Co_2O_3, or Co_3O_4.[18] Figure 7.6 shows the *J-V* characteristics of a composite CoO_x/α-Fe_2O_3 photoanode compared to the unmodified α-Fe_2O_3 photoanode after electrodeposition from an aqueous solution of cobalt nitrate. A ~100 mV cathodic shift of the onset potential for water oxidation is observed after CoO_x deposition. The above results demonstrate that the effects of Co-based oxygen evolving catalysts on α-Fe_2O_3 are generally similar and that cobalt may play a vital role in the PEC enhancement. Simple adsorption of cobalt ions onto the α-Fe_2O_3 surface have also been shown to lead to a catalytic effect with an 80 mV cathodic shift in the onset potential for water oxidation.[3,19]

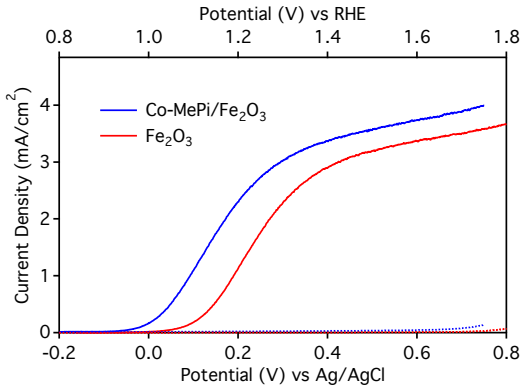

Figure 7.5. *J-V* Curves of a Co-MePi/α-Fe_2O_3 Composite Photoanode
Current density-voltage curves of an α-Fe_2O_3 photoanode before (red) and after (blue) Co-MePi photo-assisted electrodeposition, under 1 sun, AM 1.5 simulated solar irradiation (solid) and in the dark (dotted) in 1 M NaOH, pH 13.6 at 10 mV/s. Co-MePi was deposited onto α-Fe_2O_3 from a solution of 1 mM Co^{2+} in 0.1M pH 8.0 Na-MePi at 0.04 V vs Ag/AgCl for a total of 0.43 mC/cm^2.

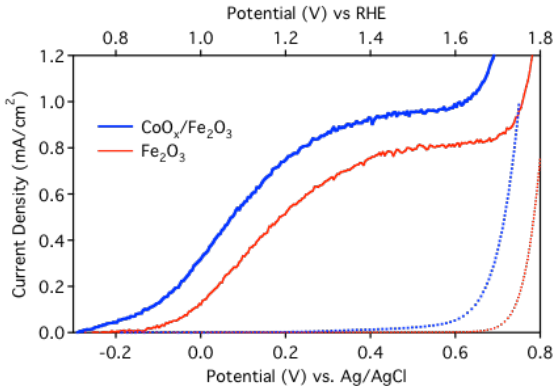

Figure 7.6. *J-V* Curves of a CoO_x/α-Fe_2O_3 Composite Photoanode
Dark current (dotted) and photocurrent (solid) densities measured for an α-Fe_2O_3 photoanode before (red) and after (blue) CoO_x photo-assisted electrodeposition. Data was collected at 10 mV/s with frontside illumination under 1 sun AM 1.5 simulated sunlight. CoO_x was deposited for 15 min at 50μA/cm^2 and ~1.1-1.3 V vs Ag/AgCl.

To test the role of surface phosphates in the PEC enhancement of α-Fe_2O_3, an iron phosphate (Fe-Pi) compound was electrodeposited onto α-Fe_2O_3 photoanodes in a similar manner as electrodeposition of Co-Pi. Cyclic voltammetry of a Fe-Pi film on FTO is shown in Figure 7.7a. The low current densities are on par with bare FTO and reveal that Fe-Pi does not exhibit catalytic behavior towards water oxidation, although redox features likely associated with iron oxidation and reduction are observed. SEM and EDX analysis show that a compound containing Fe and P was indeed electrodeposited onto the substrate with a Fe:P ratio of 2.4, similar to the Co:P ratio of Co-Pi.[16,17] The Fe-Pi compound was then electrodeposited onto an α-Fe_2O_3 photoanode and the *J-V* curves of the resulting photoanode are plotted in Figure 7.7b. After Fe-Pi addition, the PEC performance was reduced overall with an *anodic* shift of ~110 mV. This reduction in the photocurrent indicates that the surface of the photoanode is now less active towards water oxidation, consistent with the deposition of a poor water oxidation catalyst.

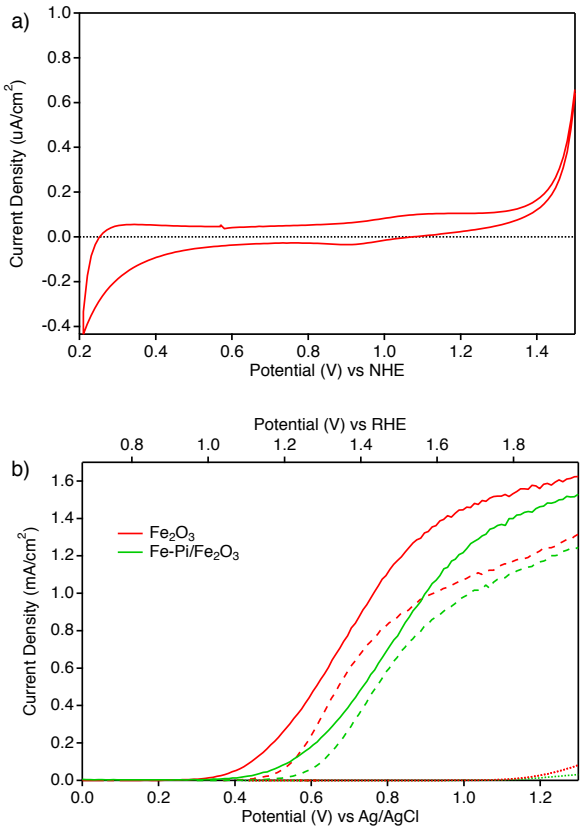

Figure 7.7. CV of Fe-Pi and *J-V* Curves of Fe-Pi/α-Fe_2O_3 and the Parent α-Fe_2O_3 Photoanode
a) Cyclic voltammogram of iron-phosphate ("Fe-Pi") on FTO in 0.1 M KPi pH 7 buffer at a scan rate of 20 mV/s. The Fe-Pi film was electrodeposited from a solution of 10 mM Fe^{2+} in 0.1 M KPi (pH ~4) for 2 hr at 1.61 V vs NHE and 0.2-0.5 μA/cm^2. **b)** *J-V* Curves of an α-Fe_2O_3 photoanode before (red) and after (green) Fe-Pi electrodeposition measured in the dark (dotted) and under 1 sun, AM 1.5 simulated solar irradiation (solid) in 0.1 M KPi pH 8 buffer at 20 mV/s. Fe-Pi was electrodeposited for 280 s at 1.61 V vs NHE and 10-20 μA/cm^2.

PEC experiments with Co-Pi and other Co-based water oxidation catalysts applied onto a variety of oxide semiconductor photoanodes verify that the properties observed with Co-Pi/α-Fe_2O_3 are universal. Addition of the Co-Pi water oxidation electrocatalyst onto α-Fe_2O_3, ZnO, TiO_2, and $BiVO_4$ photoanodes results in a decreased onset potential for water oxidation regardless of the semiconductor morphology or photocurrent onset. In conjunction, similar results were obtained with other cobalt-containing electrocatalysts, suggesting that cobalt may play a vital role in the PEC enhancement consistent with the proposed mechanism for water oxidation. Addition of a noncatalytic "Fe-Pi" layer onto α-Fe_2O_3 confirms that surface modification with phosphate ions is not responsible for the cathodic shift in α-Fe_2O_3. These results highlight the importance of using a water oxidation electrocatalyst in order to effectively separate photon absorption, charge separation, and water oxidation catalysis and support the role of Co-Pi as a water oxidation surface electrocatalyst on α-Fe_2O_3.

7.4 Impedance Spectroscopy and Mott-Schottky Analyses

There is a possibility that Co-Pi deposited onto semiconductor photoanodes leads to a cathodic shift in the PEC onset potential because of increased band bending or formation of a heterojunction as described by Durrant and coworkers.[10] Mott-Schottky plots from impedance spectroscopy have routinely been used to probe the flatband potentials of semiconductors.[20-22] The basic principles of Mott-Schottky analyses are described in

Chapter 1. The flatband potential, achieved by elimination of band-bending in a semiconductor with an applied potential, is determined from the x-intercept of a Mott-Schottky plot that expresses $1/C^2$ vs V. If Co-Pi alters the flatband potential at the photoanode surface then that change will be reflected in the Mott-Schottky plots. Mott-Schottky plots of ZnO before and after Co-Pi photodeposition have shown no changes in flatband potentials, suggesting no changes in band bending.[5]

It is important to use thin catalyst layers when probing band-bending behavior in catalyst/ semiconductor composite electrodes. Impedance measurements are strongly dependent on the semiconductor/ electrolyte interface especially as the depletion layer width approaches zero near the flatband potential. When a thick layer of catalyst is deposited between the semiconductor and electrolyte, the impedance cannot be described by the simple band-bending model discussed in Chapter 1. Additionally, as the amount of Co-Pi increases, cobalt reduction dominates the current density near the flatband potential and convolutes the measurement. Mott-Schottky plots of a ~2 μm thick Co-Pi coated WO_3 electrode showed Fermi-level pinning followed by an additional flatband feature not present in bare WO_3.[6] These features also coincide with cathodic current densities in the composite photoelectrode arising from the reduction of cobalt ions in Co-Pi. Therefore, it is crucial to deposit thin, uniform catalyst layers, such as by photo-assisted electrodeposition onto semiconductor photoanodes for reliable Mott-Schottky plots.

Impedance measurements of Co-Pi/α-Fe_2O_3 and α-Fe_2O_3 photoanodes in a three-electrode configuration were obtained for Mott-Schottky analysis. Figure 7.8 shows complex impedance data represented in Nyquist plots for an α-Fe_2O_3 photoanode before and after Co-Pi deposition measured at 0.8 V and 1.25 V vs RHE. In general, complex impedance is composed of an imaginary part (Z_i) formed by the capacitance of the sample, and a real part (Z_r) formed by the resistance. A Nyquist plot of Z_i vs. Z_r results in a semicircle, where each point on the curve is measured at a different frequency and each curve is associated with a particular applied potential. From the Nyquist plots in Figure 7.8, Co-Pi addition to α-Fe_2O_3 causes a smaller semicircle, indicating the charge-transfer resistance from the electrode to water oxidation is diminished with Co-Pi modification. Nyquist plots of Co-Pi on $BiVO_4$ also show similar results.[23]

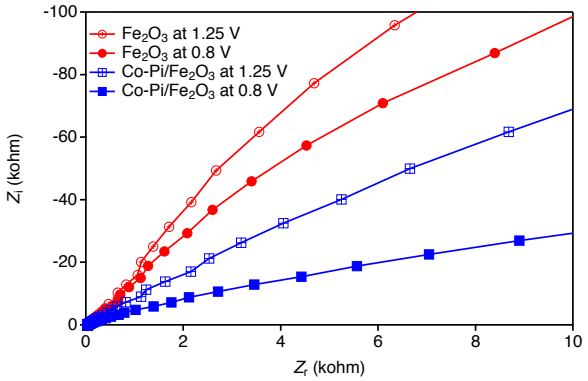

Figure 7.8. Nyquist Plots of Co-Pi/α-Fe_2O_3 and Unmodified α-Fe_2O_3 Photoanodes
Nyquist plots from dark complex impedance measurements of a Co-Pi/α-Fe_2O_3 composite and the parent α-Fe_2O_3 photoanodes at 0.8 V and 1.25 V vs RHE in 1 M NaOH electrolyte. The Co-Pi catalyst was applied by photo-assisted electrodeposition[3] at 0.1 V vs Ag/AgCl and 3.8 μA/cm^2 for 90 s. Only large frequencies are shown at the beginning of the semicircles.

For a more quantitative analysis, the Nyquist plots were fit to an equivalent circuit shown in Figure 7.9, representing the electrochemical cell with the series resistance (R_S), the electrode resistance (R_{SC}), and electrode capacitance (C_{SC}). The resulting electrode resistance (R_{SC}) and capacitance (C_{SC}) parameters from the fit are given in Figure 7.9. Overall, Co-Pi deposition onto the α-Fe_2O_3 photoanode causes an order of magnitude decrease in the electrode charge transfer resistance at each applied potential. This result indicates that hole transfer resulting in water oxidation is more facile following Co-Pi deposition, in agreement with the cathodic shifts observed with Co-Pi/α-Fe_2O_3 photoanodes. However, the nature of this decrease is unclear and a Mott-Schottky analysis is needed to distinguish between catalytic and interfacial effects.

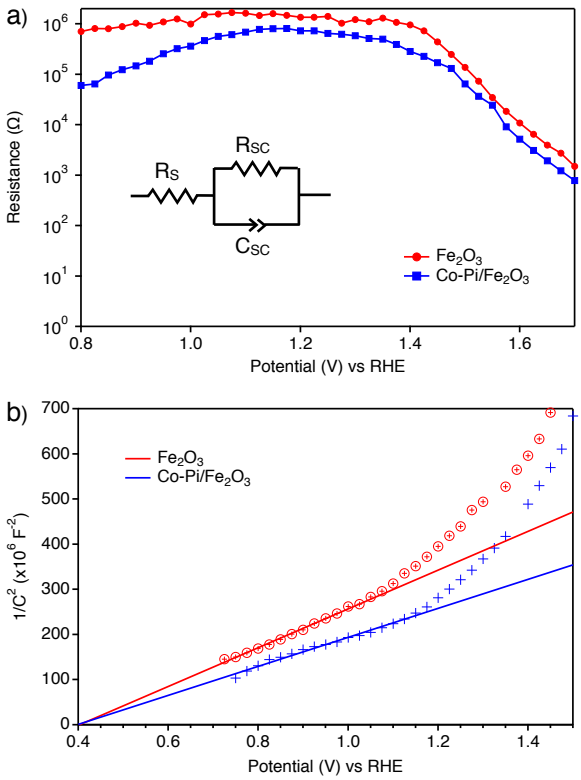

Figure 7.9. Resistance and Mott-Schottky Plot of Co-Pi/α-Fe_2O_3 and α-Fe_2O_3
a) Charge transfer resistance (R_{SC}) obtained from fitting Nyquist curves measured using Co-Pi/α-Fe_2O_3 and α-Fe_2O_3 photoanodes in Figure 7.8 to the equivalent circuit depicted in the inset and **b)** Mott-Schottky plot for the Co-Pi/α-Fe_2O_3 and α-Fe_2O_3 photoanodes in Figure 7.8.

Figure 7.9b plots the capacitance of the composite Co-Pi/α-Fe_2O_3 and parent α-Fe_2O_3 photoanode in Mott-Schottky form. The slope of the Mott-Schottky plot can be used to obtain the donor density, but in this case, a quantitative comparison between the two photoanodes cannot be made because the surface area may differ after Co-Pi deposition. Nonetheless, for the bare α-Fe_2O_3 photoanode, taking the dielectric constant to be 80 and an approximate surface roughness of 20,[24] a donor density of 2.2×10^{21} cm^{-3} was calculated. This value is similar to that obtained for other silicon doped α-Fe_2O_3 photoanodes grown by APCVD.[24,25] Due to the high donor density, the flatband potential can be directly estimated from the x-intercept of Figure 7.9b. A linear extrapolation to zero from the data at low applied potentials is used to determine the flatband potential. Mott-Schottky plots of α-Fe_2O_3 before and after Co-Pi modification both intersect the x-axis at ~0.4 V vs RHE

indicating the flatband potential is the same for both films. Subtracting *kT/e* from the x-intercept leads to a flatband potential of 0.38 V for α-Fe_2O_3 and 0.37 V for the composite Co-Pi/α-Fe_2O_3 photoanode, consistent with the values typically obtained for bare α-Fe_2O_3.[24,25]

The observation of a significant cathodic shift in PEC onset potential without any corresponding shift in the flatband potential of α-Fe_2O_3 argues against improved PEC performance originating primarily from band-bending effects, although the possibility of a Schottky-type heterojunction[10] between α-Fe_2O_3 and Co-Pi cannot be exclusively eliminated. There remain two other mechanisms by which Co-Pi can increase PEC water oxidation by α-Fe_2O_3. Co-Pi can passivate surface traps, thereby reducing surface e-h recombination, or it can provide a more facile catalytic route towards water oxidation. Surface trap passivation cannot be resolved with Mott-Schottky analysis as similar Mott-Schottky results were also obtained on α-Fe_2O_3 photoanodes with an Al_2O_3 surface passivating layer.[26] To distinguish between surface and catalytic effects, studies of charge separation and the kinetics of water oxidation were initiated with photoconductive microscopies and electrochemical kinetics.

7.5 Photoconductive Microscopy on Cobalt Catalyst/α-Fe_2O_3 Photoanodes

Co-Pi may passivate surface defects or function solely as a superior water oxidation catalyst in place of α-Fe_2O_3. To date, studies on photoelectrode surfaces have concentrated on macroscopic techniques that provide an average, rather than a local survey of its properties. However, the PEC performance of Co-Pi/α-Fe_2O_3 composite photoanodes is sensitive to catalyst thicknesses that can vary substantially on the microscopic level.[2] Thus, microscopic measurement techniques can be an invaluable tool for understanding interfacial charge transfer in these composite assemblies, and how and under what conditions catalyst/semiconductor interfaces give the most favorable PEC enhancement.

Recently, conductive and photoconductive atomic force microscopies (cAFM and pcAFM) have been used to correlate surface conductivities and carrier mobilities to local device performances in semiconducting polymers for organic PVs.[27-29] These types of studies in collaboration with the Ginger lab allowed us to probe charge generation, collection, and trapping on α-Fe_2O_3 as a function of catalyst coating with 10-100 nm resolution. Natural variations in catalyst deposition allowed probing of empty, thick, and thin catalyst covered areas from electrodeposition as well as photo-assisted electrodeposition. In this study all AFM and cAFM experiments were conducted on dry photoanodes with and without laser excitation using a setup described previously.[28]

Figure 7.10a shows an AFM image of a Co-Pi/α-Fe_2O_3 electrode after electrodeposition of Co-Pi. An island of Co-Pi is shown in the lower right corner, in agreement with SEM images of the composite photoanode. The corresponding conductive and photoconductive AFM properties of the same electrode are shown in panels b and c, respectively. Very little dark and light current is collected through the Co-Pi layer, while away from Co-Pi, a substantial dark and photocurrent response is observed. These results show that Co-Pi is highly insulating. Modification of the electrode surface does not result in greater current flow in the pcAFM experiment, suggesting that the primary role of Co-Pi is to facilitate catalysis, not charge separation. Samples with thin layers of Co-Pi or CoO_x after photo-assisted electrodeposition did not reveal much difference between the composite catalyst/α-Fe_2O_3 and bare α-Fe_2O_3 electrode.

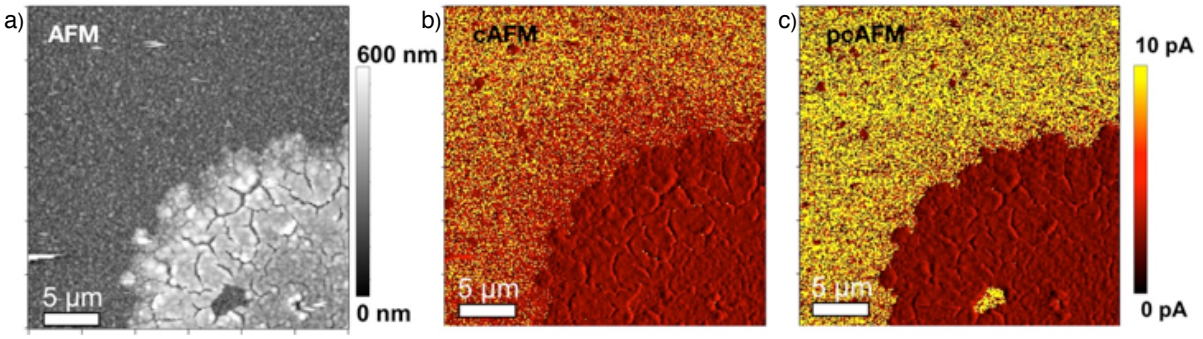

Figure 7.10. AFM, cAFM, and pcAFM Images of a Co-Pi/α-Fe_2O_3 Composite Photoanode
Images from **a)** AFM, **b)** conductive AFM with +5 V, and **c)** photoconductive AFM with +5 V under 405 nm laser irradiation for a Co-Pi/α-Fe_2O_3 composite photoanode under ambient conditions. The circular feature at the bottom right corner of each panel is an island of Co-Pi on the α-Fe_2O_3 photoanode. Co-Pi is highly insulating in the dark and under 10^7 W/m^2 of 405 nm laser irradiation.

Since surface modification with a cobalt electrocatalyst does not increase charge collection, the PEC enhancement in catalyst/α-Fe_2O_3 photoanodes cannot be attributed to increased charge separation by passivation of surface traps or increased band bending with catalyst addition. This result supports the conclusion that the role of Co-Pi is to act as a surface water oxidation electrocatalyst, improving the kinetics of water oxidation to make them more competitive with surface e-h recombination. Future cAFM and pcAFM experiments mimicking PEC operating conditions immersed in electrolyte would provide further insight into the role of Co-Pi. These experiments, however, are complicated by the use of a conductive AFM tip in a highly conductive electrolyte and may require fabrication of a specialized AFM tip.

7.6 Photoelectrochemical Kinetics Analyses

In the division-of-labor scheme for water oxidation by Co-Pi/α-Fe_2O_3 photoanodes, photogenerated holes on the α-Fe_2O_3 surface transfer to the Co-Pi electrocatalyst where water oxidation chemistry occurs at lower overpotentials than α-Fe_2O_3 alone. If water oxidation proceeds through the Co-Pi catalyst, then presumably the mechanism for water oxidation would follow that of Co-Pi and not α-Fe_2O_3. The kinetics and mechanism of bulk electrolysis by Co-Pi have been extensively studied through electrochemical experiments,[11,12] isotopic labeling,[11,12] and EPR spectroscopy.[15] From these studies, the mechanism depicted in Figure 7.1 has been proposed.

Electrochemical experiments to examine the kinetics of water oxidation by Co-Pi involved the interpretation of Tafel and pH dependence results from bulk electrolysis.[12] These experiments were conducted in a current-potential regime where the reaction is purely activation controlled without electron or mass transport limitations. The Tafel equation, based on the Butler-Volmer equation, relates current and potential by Equation 7.1 for anodic reactions, where i is the current density, i_0 is the exchange current density, α is the transfer coefficient dependent on the reaction mechanism, η is the thermodynamic overpotential, F is Faraday's constant, R is the ideal gas constant, and T is temperature.[30,31]

$$i = i_0 e^{\alpha \eta F / RT} \qquad \text{Equation 7.1}$$

In a more general logarithmic form, the Tafel equation simplifies to $\eta = a + b \log i$, where a and b are constants. A plot of η as a function of log(*i*) would give a curve with slope $b = 2.3RT/\alpha F$, related to the reactivity of the electrode. The Tafel plot linear dependence is only valid at moderate overpotentials where mass transport limitations can be neglected.[31] A Tafel plot of Co-Pi has a slope near 59 mV/decade, characteristic of an O_2 evolution mechanism involving a reversible one-electron transfer step, such as the oxidation of Co^{III} to Co^{IV}, prior to a rate limiting step. A series of pH dependence measurements also reveal a Nernstian or first order dependence on pH. This result indicates an inverse first order dependence on proton activity, consistent with a PCET transformation prior to a rate limiting step.

The Tafel slope and pH dependence of PEC water oxidation by α-Fe_2O_3 are likely substantially different than those of Co-Pi. In the case that Co-Pi acts as a surface water oxidation catalyst in the composite photoanode, then the water oxidation kinetics of an α-Fe_2O_3 photoanode will change to be consistent with those of the Co-Pi mechanism upon Co-Pi deposition. Figure 7.11 shows the *J-V* curves, Tafel plots, and pH dependence curves of an α-Fe_2O_3 photoanode before and after Co-Pi deposition measured in 0.1 M KPi. The Tafel plot measured prior to Co-Pi deposition is linear with a slope near 120 mV/decade, in good agreement with previous measurements of α-Fe_2O_3.[32,33] Although the semiconductor/electrolyte interface is considerably more complex than the simple metal electrode model used for the Butler-Volmer equation, Tafel plots for α-Fe_2O_3 photoanodes are linear at low photocurrents.[33] A Tafel slope of 120 mV/decade is consistent with an α value of 0.5 and has been observed for metal oxide materials such as PtO_2,[30,34] MnO_2,[30] and α-Fe_2O_3.[32,33]

Next, Co-Pi was photo-assisted electrodeposited onto the α-Fe_2O_3 photoanode. To ensure complete coverage the catalyst was deposited slowly under low current density (~2 μA/cm^2) for a relatively long period of time (30 min). Figure 7.11a shows a cathodic shift of ~100 mV after Co-Pi deposition, similar to the shifts observed previously for Co-Pi/α-Fe_2O_3 photoanodes. The Tafel slope after Co-Pi modification was reduced to 65 mV/decade, indicative of a reduced kinetic barrier to water oxidation. Along with a change in the Tafel slope, the pH dependence of PEC water oxidation, shown in Figure 7.11c, also changed from -76 mV/pH for the bare α-Fe_2O_3 photoanode to -55 mV/pH after Co-Pi surface modification. These results reveal a first-order dependence on pH, where $\log(i)/pH \approx 1$. The Tafel slope, pH dependence, and reaction order are close to the 59 mV/decade, -59 mV/pH, and 1 value measured for water electrolysis by Co-Pi[12] and strongly support the role of Co-Pi as a catalyst for water oxidation in the Co-Pi/α-Fe_2O_3 composite photoanode.

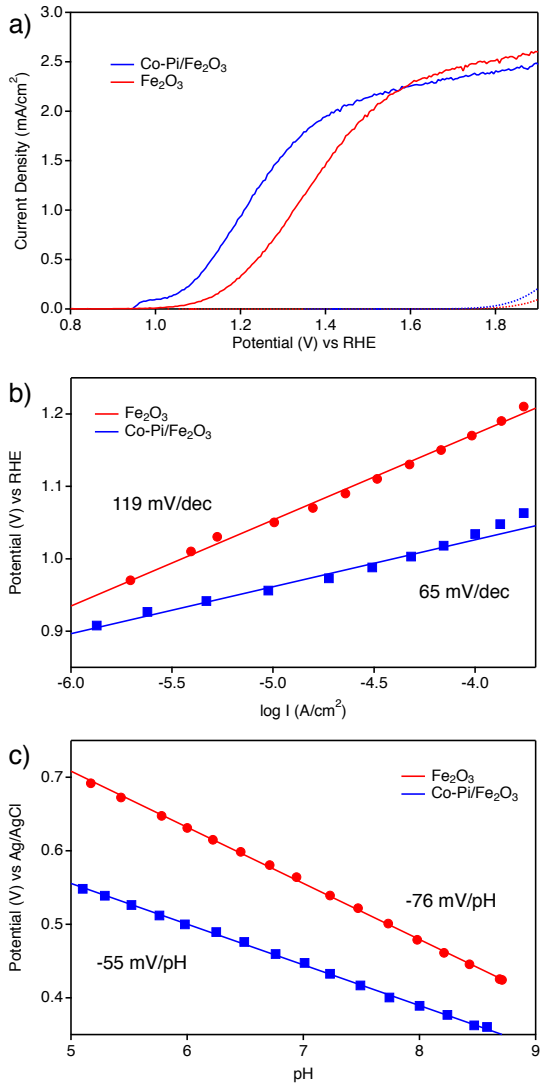

Figure 7.11. PEC Kinetic Measurements on Co-Pi/α-Fe_2O_3
a) *J-V* curves of a α-Fe_2O_3 photoanode before and after Co-Pi photo-assisted electrodeposition measured in 0.1 M pH 8 KPi in the dark and under 1 sun AM 1.5 simulated solar irradiation at a scan rate of 10 mV/s. **b)** Tafel plot of the photoanodes in panel a obtained from steady state photocurrent densities after 120 s of applied potential in 0.1 M pH 8 KPi. **c)** pH dependence plot of the same photoanodes showing the applied potential necessary to maintain a constant current density of 30 μA/cm^3 under steady-state conditions after 120 s.

It is important to note that kinetic measurements with semiconductor photoelectrodes are more complicated than the simple model described by the Tafel equation, and mechanistic information about water oxidation may be complicated by the electrical properties of the photoelectrode. For *npp*$^+$Si | ITO | Co-Pi electrodes, for example, a Tafel slope of 110 mV/decade was obtained, larger than the 59 mV/decade observed for Co-Pi, attributed to the hindered conduction of holes across a 50 nm ITO coating.[8] Nonetheless, a decrease in the Tafel slope suggests reduced overpotentials for the PEC water oxidation reaction. Such a large hindrance is not expected for pristine α-Fe_2O_3 photoanodes. To verify that the change in the Tafel slope and pH dependence with Co-Pi/α-Fe_2O_3 is related to the Co-Pi water oxidation mechanism, an analogous set of experiments was conducted with "Ni-B_i", a nickel-borate water oxidation catalyst[35] with different kinetic properties than Co-Pi.

Ni-B_i is a thin film water oxidation electrocatalyst deposited from a dilute solution of Ni^{2+} in borate buffer at pH 9.2.[35] It exhibits long-term stability in water and operates at moderate overpotentials with activity similar to that of NiO(OH) under alkaline conditions.[35] Ni-B_i exhibits a Tafel slope of ~59mV/decade, within the range typical of nickel oxides. The pH dependence of Ni^{II}/Ni^{III} reveals a slope of -90mV/pH, corresponding to a $2e^-$-$3H^+$ mechanism,[35] in contrast to the $1e^-$-$1H^+$ PCET of Co-Pi oxidation.[12]

To observe the effects of Ni-B_i on α-Fe_2O_3, Ni-B_i was loaded onto an α-Fe_2O_3 photoanode by photo-assisted electrodeposition from the same electrolyte composition[35] used for electrodeposition. The composite Ni-B_i/α-Fe_2O_3 photoanode was conditioned for 10+ hours under 1 sun AM 1.5 simulated sunlight at 1.3 V in order to achieve full catalytic activity. Conditioning was also required for the bare Ni-B_i electrode in order to obtain reproducible electrokinetic behavior, possibly due to slow formation of the active catalyst.[35] Conditioning substantially increases the cathodic shift obtained after Ni-Bi deposition onto α-Fe_2O_3. Figure 7.12a shows the *J-V* curves of the post-conditioned Ni-B_i/α-Fe_2O_3 composite photoanode compared to the parent α-Fe_2O_3 photoanode measured under 1 sun AM 1.5 illumination and in the dark. A cathodic shift in the PEC onset potential of ~150 mV was obtained with the addition of the Ni-B_i electrocatalyst.

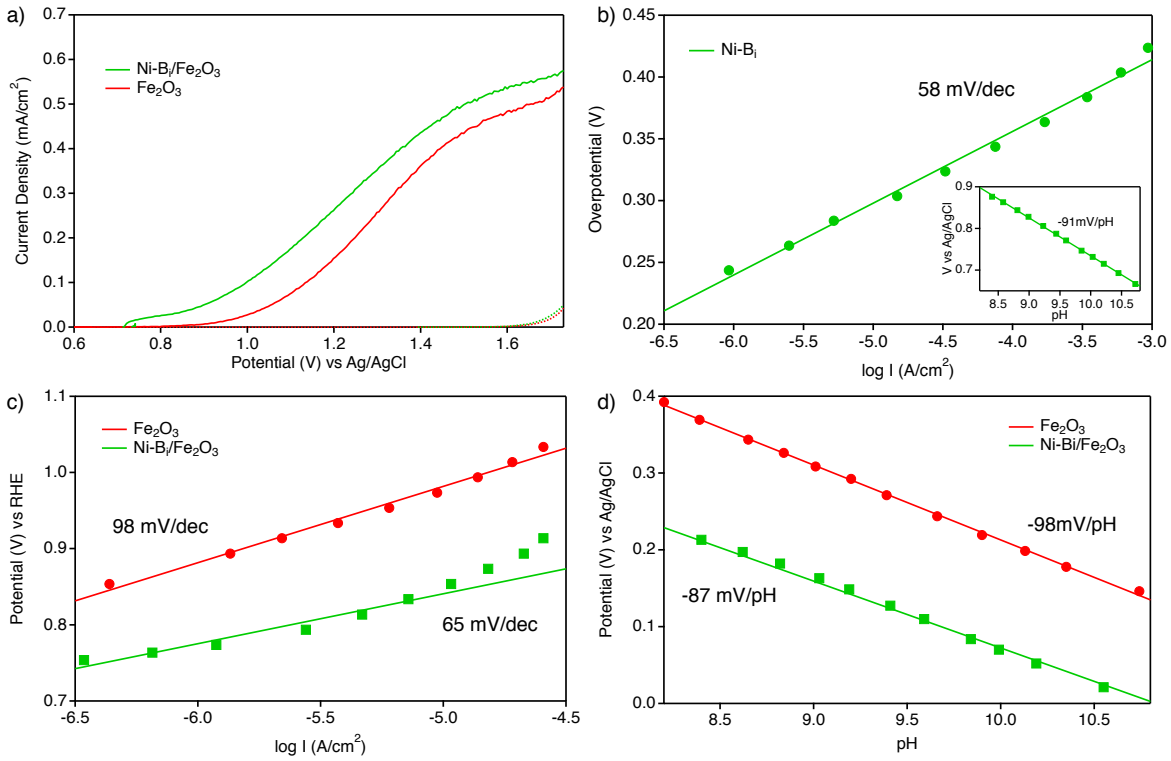

Figure 7.12. Electrochemical Kinetics on Ni-B_i and Ni-B_i/α-Fe_2O_3 Composite Electrodes
a) *J-V* curves of the an α-Fe_2O_3 photoanode before and after Ni-B_i photo-assisted electrodeposition in the dark (dotted) and under 1 sun AM 1.5 simulated sunlight measured in 0.2 M pH 9.2 KBi at 10 mV/s. **b)** Tafel plot and pH dependence (inset) of water electrolysis by Ni-B_i on FTO in 0.2 M KBi buffer at pH 9.2. The steady-state current density was obtained after 120 s of applied potential for each point. **c)** Tafel plot of the photoanodes in panel b obtained from steady state photocurrent densities after 120 s of applied potential in 0.1 M pH 9.2 KBi. **d)** pH dependence plots of the photoanodes in panel a showing the applied potential necessary to maintain a constant current density of 30 μA/cm^2 under steady-state conditions after 120 s.

Figure 7.12b shows the Tafel slope and pH dependence (inset) of Ni-B_i deposited on FTO according to literature procedures[35] from a solution of nickel nitrate in 0.1 M KB_i. The Tafel plot and pH dependence was obtained after conditioning the Ni-B_i electrode for 10+ hours under operating conditions, as required for bare Ni-B_i.[35] Figure 7.12b shows a Tafel slope of 58 mV/decade consistent with the reported ~59 mV/decade for Ni-B_i.[35] This Tafel slope may not be unique for Ni-Bi because of the conditioning process. The pH dependence in the inset was obtained by the same galvanostatic pH titration method[12] used for Co-Pi water oxidation and matches the -90mV/pH slope reported for nickel oxidation. This pH dependence suggests that nickel oxidation may be a critical step in the water oxidation mechanism by Ni-B_i.

To probe the photoelectrochemical kinetics of Ni-B_i on α-Fe_2O_3, analogous Tafel and pH dependence plots of the bare and Ni-B_i-modified α-Fe_2O_3 photoanode were collected, shown in Figure 7.12c and d, respectively. After Ni-B_i surface modification the Tafel slope of α-Fe_2O_3 decreased from 98 mV/decade to 65 mV/decade, near the 59 mV/decade slope characteristic of Ni-B_i electrodes, following the same conditioning procedure as closely as possible. As for the pH dependence in Figure 7.12d, the unmodified α-Fe_2O_3 photoanode shows a slope of -98 mV/pH. After Ni-B_i modification the slope decreased to -87 mV/pH, consistent with the -90 mV/pH slope obtained from water electrolysis by Ni-B_i. These results demonstrate that the kinetics of PEC water oxidation have changed to more closely resemble electrolysis by the electrocatalyst after Ni-B_i surface modification of α-Fe_2O_3.

Both the Co-Pi and Ni-B_i catalyst modified α-Fe_2O_3 photoanodes exhibit a decrease in the Tafel slope and pH dependence after the catalyst was applied onto the semiconductor. In both cases, after catalyst application the electrochemical kinetics changed to mimic those of the catalyst in the resulting composite photoanodes. For the Co-Pi/α-Fe_2O_3 film, the Tafel slope, pH dependence, and reaction order were near 59 mV/decade, -59 mV/pH, and 1, respectively, and for the Ni-B_i/α-Fe_2O_3 film they were near 59 mV/decade, -90 mV/pH, and 1.5, respectively. Although it is difficult to prove the exact mechanism of water oxidation in the catalyst/semiconductor photoanodes, these results strongly suggest that PEC water oxidation is *catalyzed* by the Co-Pi or Ni-B_i electrocatalyst in the composite structure.

7.7 Conclusions and Outlook

This work has demonstrated that modifying the surface of α-Fe_2O_3 and $BiVO_4$ photoanodes with a Co-Pi water oxidation catalyst results in a decrease in the onset potential for PEC water oxidation, along with an increase in the amount of oxygen produced at the same external bias compared to the unmodified semiconductor.[1-4] The enhanced photoactivity is due to effective separation of the tasks of photon absorption, charge separation, and water oxidation catalysis in the composite photoanodes. Photons are absorbed by the semiconductor, and the resulting photogenerated holes are transferred to the surface electrocatalyst whereby it oxidizes water more efficiently than the underlaying semiconductor.[36] The role of Co-Pi as a surface electrocatalyst is reasonably supported by various PEC and oxygen detection experiments.

In the process of optimizing parameters in the composite photoanodes for efficient PEC water oxidation, a kinetic bottleneck associated with thick Co-Pi layers was discovered on a variety of semiconductor materials.[2] This kinetic bottleneck appears to be a consequence of photo-electrolysis and not dark electrolysis in these composite photoanodes, and may result from reentrant competitiveness of surface electron-hole

recombination in photoanodes with thick Co-Pi layers. When holes diffuse through thick Co-Pi layers, more photoexcitation events are needed to accumulate four oxidizing equivalents in any one active site, and this leads to a greater probability for electron-hole recombination. In addition, the fact that the kinetic bottleneck is observed only in the photoexcitation process is an indication that photogenerated holes transfer to, instead of bypassing, the Co-Pi catalyst.

To circumvent the kinetic bottleneck, a thin layer of Co-Pi can be deposited onto semiconductor surfaces via a new method called photo-assisted electrodeposition.[3] In photo-assisted electrodeposition, Co-Pi deposits where light generates oxidizing equivalents that oxidize cobalt to form Co-Pi directly on the semiconductor surface. The advantage of this deposition technique is that the catalyst can be deposited onto a variety of semiconductor morphologies, such as nanowires and mesostructured surfaces, without depositing onto the underlying conductive substrate. The result is a thin uniform catalyst layer that maximizes PEC performance.

While surface modification of α-Fe_2O_3 by Co-Pi reduces the onset potential for water oxidation by over one hundred millivolts, the operating potentials of Co-Pi/α-Fe_2O_3 photoanodes are still quite high, with a current density of 1 mA/cm^2 at 1 V. Most low cost PEC/PV cells exhibit open circuit voltages of less than 1 V where photocurrent is zero. Hence, very little current flow occurs at >0.8 V, and powering Co-Pi/α-Fe_2O_3 at such low current densities is impractical.

Co-Pi was then applied onto W:$BiVO_4$,[4] a semiconductor that exhibits visible light absorption with a band gap of 2.4-2.5 eV, but has much lower onset potentials for water oxidation compared to α-Fe_2O_3. The resulting Co-Pi/W:$BiVO_4$ composite photoanodes showed a substantial 440 mV cathodic shift in the onset potential for water oxidation, resulting in an absolute onset potential of 310 mV vs RHE, 550 mV lower than what has been observed with Co-Pi/α-Fe_2O_3. Quantitative PEC experiments with a peroxide surrogate substrate revealed that surface e-h recombination is almost completely suppressed when Co-Pi is deposited onto W:$BiVO_4$. Compared to α-Fe_2O_3, W:$BiVO_4$ has slower surface e-h recombination rates and a ~10 times longer hole diffusion length, resulting in lower onset potentials due to PEC water oxidation becoming more competitive with e-h recombination. The results imply that photo-generated holes on the W:$BiVO_4$ surface are captured by Co-Pi with near 100% quantum efficiency, where they also oxidize water with near 100% quantum efficiency. By completely eliminating surface e-h recombination with Co-Pi, the low applied potentials required for solar water splitting are now accessible from low-cost single-junction PEC or PV cells in a tandem device configuration. The primary performance limitation of the Co-Pi/W:$BiVO_4$ photoanodes is now their high bulk recombination rate and insufficient photon harvesting ability.

The successful integration of inexpensive, Earth-abundant water oxidation electrocatalysts with light-harvesting semiconductor photoanodes has drawn considerable attention to composite catalyst/semiconductor photoelectrodes for addressing the challenges of solar water splitting through the separation of tasks. This approach has shown that water splitting can be achieved at significantly lower onset potentials, reducing the demand for external power and manufacturing costs for solar hydrogen production. Yet, for such a remarkable system, exactly how it works at the microscopic level is not entirely understood.

PEC characteristics, impedance spectroscopy, photoconductive microscopies, and PEC kinetic experiments were analyzed to understand the role of Co-Pi in enhancing the photocatalytic activity of α-Fe_2O_3

towards water oxidation. The above experiments combined present compelling evidence that the enhanced PEC performance in catalyst/semiconductor composite photoanodes directly results from the efficient separation of photon absorption, charge separation, and water oxidation catalysis. By interfacing a competent water oxidation catalyst with a semiconductor chromophore, the water oxidation reaction becomes more competitive with surface e-h recombination and higher solar-to-hydrogen conversion efficiencies are achieved at lower applied potentials. Future experiments that can verify the existence of the Co^{4+} intermediate or where O_2 is formed in the composite photoanodes, perhaps through photo-induced EPR, Raman, or transient absorption spectroscopies and oxygen evolution with ^{18}O-enriched Co-Pi layers, would provide more insight into the roles of Co-Pi and related catalysts in composite photoanodes.

7.8 Notes to Chapter 7

1. Zhong, D. K.; Sun, J.; Inumaru, H.; Gamelin, D. R., *J. Am. Chem. Soc.* **2009,** *131*, 6086-6087.
2. Zhong, D. K.; Gamelin, D. R., *J. Am. Chem. Soc.* **2010,** *132*, 4202-4207.
3. Zhong, D. K.; Cornuz, M.; Sivula, K.; Grätzel, M.; Gamelin, D. R., *Energy Environ. Sci.* **2011,** *4*, 1759-1764.
4. Zhong, D. K.; Choi, S.; Gamelin, D. R., *J. Am. Chem. Soc.* **2011,** *133*, 18370-18377.
5. Steinmiller, E. M. P.; Choi, K.-S., *Proc. Nat. Acad. Sci.* **2009,** *106*, 20633-20636.
6. Seabold, J. A.; Choi, K.-S., *Chem. Mater.* **2011,** *23*, 1105-1112.
7. Ye, H.; Park, H. S.; Bard, A. J., *J. Phys. Chem. C* **2011,** *115*, 12464-12470.
8. Pijpers, J. J. H.; Winkler, M. T.; Surendranath, Y.; Buonassisi, T.; Nocera, D. G., *Proc. Natl. Acad. Sci. U. S. A.* **2011,** *108*, 10056-10061.
9. Young, E. R.; Costi, R.; Paydavosi, S.; Nocera, D. G.; Bulovic, V., *Energy Environ. Sci.* **2011,** *4*, 2058-2061.
10. Barroso, M.; Cowan, A. J.; Pendlebury, S. R.; Grätzel, M.; Klug, D. R.; Durrant, J. R., *J. Am. Chem. Soc.* **2011,** *133*, 14858-14871.
11. Lutterman, D. A.; Surendranath, Y.; Nocera, D. G., *J. Am. Chem. Soc.* **2009,** *131*, 3838-3839.
12. Surendranath, Y.; Kanan, M. W.; Nocera, D. G., *J. Am. Chem. Soc.* **2010,** *132*, 16501-16509.
13. Risch, M.; Khare, V.; Zaharieva, I.; Gerencser, L.; Chernev, P.; Dau, H., *J. Am. Chem. Soc.* **2009,** *131*, 6936-6937.
14. Kanan, M. W.; Yano, J.; Surendranath, Y.; Dincă, M.; Yachandra, V. K.; Nocera, D. G., *J. Am. Chem. Soc.* **2010,** *132*, 13692-13701.
15. McAlpin, J. G.; Surendranath, Y.; Dincă, M.; Stich, T. A.; Stoian, S. A.; Casey, W. H.; Nocera, D. G.; Britt, R. D., *J. Am. Chem. Soc.* **2010,** *132*, 6882-6883.
16. Kanan, M. W.; Nocera, D. G., *Science* **2008,** *321*, 1072-1075.
17. Surendranath, Y.; Dincă, M.; Nocera, D. G., *J. Am. Chem. Soc.* **2009,** *131*, 2615-2620.
18. Suzuki, O.; Takahasi, M.; Rukunaga, T.; Kuboyama, J. Novel cobalt oxide and an electrode having the cobalt oxide coating. 3,399,966, September 3, 1968.
19. Kay, A.; Cesar, I.; Grätzel, M., *J. Am. Chem. Soc.* **2006,** *128*, 15714-15721.
20. Grimes, C. A.; Varghese, O. K.; Ranjan, S., *Light, Water, Hydrogen*. Springer: New York, 2007.

21. Licht, S., *Encyclopedia of Electrochemistry: Semiconductor Electrodes and Photoelectrochemistry*. Wiley-VCH: Weinheim, 2002.
22. Grätzel, M., *Nature* **2001,** *414*, 338-344.
23. Jeon, T. H.; Choi, W.; Park, H., *PCCP* **2011,** *13*, 21392-21401.
24. Cesar, I.; Sivula, K.; Kay, A.; Zboril, R.; Grätzel, M., *J. Phys. Chem. C* **2009,** *113*, 772-782.
25. Saremi-Yarahmadi, S.; Wijayantha, K. G. U.; Tahir, A. A.; Vaidhyanathan, B., *J. Phys. Chem. C* **2009,** *113*, 4768-4778.
26. Le Formal, F.; Tétreault, N.; Cornuz, M.; Moehl, T.; Grätzel, M., *Chem. Sci.* **2011,** *2*, 737-743.
27. Pingree, L. S. C.; MacLeod, B. A.; Ginger, D. S., *J. Phys. Chem. C* **2008,** *112*, 7922-7927.
28. Pingree, L. S. C.; Reid, O. G.; Ginger, D. S., *Nano Lett.* **2009,** *9*, 2946-2952.
29. Reid, O. G.; Munechika, K.; Ginger, D. S., *Nano Lett.* **2008,** *8*, 1602-1609.
30. O'Sullivan, E. J. M.; Calvo, E. J., Reactions at Metal Oxide Electrodes. In *Comprehensive Chemical Kinetics*, Compton, R. G., Ed. Elsevier Publishing Co.: Amsterdam, 1987; Vol. 27, pp 247-360.
31. Gileadi, E., *Electrode Kinetics for Chemists, Chemical Engineers, and Materials Scientists*. Wiley-VCH: New York, 1993.
32. Sivula, K.; Le Formal, F.; Grätzel, M., *Chem. Mater.* **2009,** *21*, 2862-2867.
33. Carver, C.; Ulissi, Z.; Ong, C. K.; Dennison, S.; Hellgardt, K.; Kelsall, G. H., *ECS Trans.* **2010,** *28*, 103-117.
34. Trasatti, S., Transition Metal Oxides: Versatile Materials for Electrocatalysis. In *Electrochemistry of Novel Materials*, Lipkowski, J.; Ross, P. N., Eds. VCH Publishers: New York, 1994; pp 207-296.
35. Dincă, M.; Surendranath, Y.; Nocera, D. G., *Proc. Natl. Acad. Sci. U. S. A.* **2010,** *107*, 10337-10341.
36. Sun, J.; Zhong, D. K.; Gamelin, D. R., *Energy Environ. Sci.* **2010,** *3*, 1252-1261.

Bibliography

1. Alexander, B. D.; Kulesza, P. J.; Rutkowska, I.; Solarska, R.; Augustynski, J., J. *Mater. Chem. 2***008,** 1*8,* 2298-2303.
2. Arakawa, H.; Shiraishi, C.; Tatemoto, M.; Kishida, H.; Usui, D.; Suma, A.; Takamisawa, A.; Yamaguchi, T., P*roc. SPIE 2***007,** 6*650,* 665003.
3. Ardo, S.; Meyer, G. J., C*hem. Soc. Rev. 2***009,** 3*8,* 115-164.
4. Aroutiounian, V. M.; Arakelyan, V. M.; Shahnazaryan, G. E., S*ol. Energy 2***005,** 7*8,* 581-592.
5. Bak, T.; Nowotny, J.; Rekas, M.; Sorrell, C. C., I*nt. J. Hydrogen Energy 2***002,** 2*7,* 991-1022.
6. Barber, J.; Murray, J. W., Coord. Chem. Rev. 2008, 252, 233-243.
7. Bard, A. J.; Fox, M. A., A*cc. Chem. Res. 1***995,** 2*8,* 141-145.
8. Barroso, M.; Cowan, A. J.; Pendlebury, S. R.; Grätzel, M.; Klug, D. R.; Durrant, J. R., J. *Am. Chem. Soc. 2***011,** 1*33,* 14858-14871.
9. Beermann, N.; Vayssieres, L.; Lindquist, S.-E.; Hagfeldt, A., J. *Electrochem. Soc. 2***000,** 1*47,* 2456-2461.
10. Berglund, S. P.; Flaherty, D. W.; Hahn, N. T.; Bard, A. J.; Mullins, C. B., J. *Phys. Chem. C 2***011,** 1*15,* 3794-3802.
11. Bjoerksten, U.; Moser, J.; Grätzel, M., C*hem. Mater. 1***994,** 6*,* 858-863.
12. Boettcher, S. W.; Spurgeon, J. M.; Putnam, M. C.; Warren, E. L.; Turner-Evans, D. B.; Kelzenberg, M. D.; Maiolo, J. R.; Atwater, H. A.; Lewis, N. S., S*cience 2***010,** 3*27,* 185-187.
13. Bolton, J. R.; Strickler, S. J.; Connolly, J. S., N*ature 1***985,** 3*16,* 495-500.
14. Brillet, J.; Cornuz, M.; Le Formal, F.; Yum, J.-H.; Grätzel, M.; Sivula, K., J. *Mater. Res. 2***010,** 2*5,* 17-24.
15. Brillet, J.; Grätzel, M.; Sivula, K., N*ano Lett. 2***010,** 1*0,* 4155-4160.
16. Brimblecombe, R.; Dismukes, G. C.; Swiegers, G. F.; Spiccia, L., D*alton Trans. 2***009,** 9374-9384.
17. Brimblecombe, R.; Koo, A.; Dismukes, G. C.; Swiegers, G. F.; Spiccia, L., J. *Am. Chem. Soc. 2***010,** 1*32,* 2892-2894.
18. Burdinski, D.; Wieghardt, K.; Steenken, S., J. *Am. Chem. Soc 1***999,** 1*21,* 10781-10787.
19. Butler, M. A., J. *Appl. Phys. 1***977,** 4*8,* 1914-1920.
20. Carver, C.; Ulissi, Z.; Ong, C. K.; Dennison, S.; Hellgardt, K.; Kelsall, G. H., E*CS Trans. 2***010,** 2*8,* 103-117.
21. Cesar, I.; Kay, A.; Gonzalez Martinez, J. A.; Grätzel, M., J. *Am. Chem. Soc. 2***006,** 1*28,* 4582-4583.
22. Cesar, I.; Sivula, K.; Kay, A.; Zboril, R.; Grätzel, M., J. *Phys. Chem. C 2***009,** 1*13,* 772-782.
23. Chapin, D. M.; Fuller, C. S.; Pearson, G. L., J. *Appl. Phys. 1***954,** 2*6,* 676-677.
24. Chatchai, P.; Kishioka, S.-y.; Murakami, Y.; Nosaka, A. Y.; Nosaka, Y., E*lectrochim. Acta 2***010,** 5*5,* 592-596.
25. Chen, Z.; Concepcion, J. J.; Jurss, J. W.; Meyer, T. J., J. *Am. Chem. Soc. 2***009,** 1*31,* 15580-15581.
26. Cheng, X. F.; Leng, W. H.; Liu, D. P.; Xu, Y. M.; Zhang, J. Q.; Cao, C. N., J. *Phys. Chem. C 2***008,** 1*12,* 8725-8734.

27. Chirilă, A.; Buecheler, S.; Pianezzi, F.; Bloesch, P.; Christina Gretener, C.; Uhl, A. R.; Fella, C.; Kranz, L.; Perrenoud, J.; Seyrling, S.; Verma, R.; Nishiwaki, S.; Romanyuk, Y. E.; Bilger, G.; Tiwari, A. N., N*at. Mater.* **2011,** 1*0,* 857-861.
28. Concepcion, J. J.; Jurss, J. W.; Brennaman, M. K.; Hoertz, P. G.; Patrocinio, A. O. v. T.; Murakami Iha, N. Y.; Templeton, J. L.; Meyer, T. J., A*cc. Chem. Res.* **2009,** 4*2,* 1954-1965.
29. Dare-Edwards, M. P.; Goodenough, J. B.; Hamnett, A.; Trevellick, P. R., J. *Chem. Soc., Faraday Trans. 1* **983,** 7*9,* 2027-2041.
30. Dincă, M.; Surendranath, Y.; Nocera, D. G., P*roc. Natl. Acad. Sci. U. S. A.* **2010,** 1*07,* 10337-10341.
31. Dismukes, G. C.; Brimblecombe, R.; Gelton, G. A. N.; Pryadun, R. S.; Sheats, J. E.; Spiccia, L.; Swiegers, G. F., A*cc. Chem. Res.* **2009,** 4*2,* 1935-1943.
32. Doney, S. C., S*ci. Am.* **2006,** 2*94,* 58-65.
33. Dotan, H.; Sivula, K.; Grätzel, M.; Rothschild, A.; Warren, S., E*nergy Environ. Sci.* **2011,** 4*,* 958-964.
34. Duret, A.; Grätzel, M., J. *Phys. Chem. B* **2005,** 1*09,* 17184-17191.
35. Eggleston, C. M.; Shankle, A. J. A.; Moyer, A. J.; Cesar, I.; Grätzel, M., A*quat. Sci.* **2009,** 7*1,* 151-159.
36. Frank, A. J.; Honda, K., J. *Photochem.* **1985,** 2*9,* 195-204.
37. Frank, A. J.; Honda, K., J. *Phys. Chem.* **1982,** 8*6,* 1933-1935.
38. Fujishima, A.; Honda, K., N*ature* **1972,** 2*38,* 37-8.
39. Gardner, R. F. G.; Sweett, F.; Tanner, D. W., J. *Phys. Chem. Solids* **1963,** 2*4,* 1183-1186.
40. Gärtner, W. W., P*hys. Rev.* **1959,** 1*16,* 84-87.
41. Geletii, Y. V.; Huang, Z.; Hou, Y.; Musaev, D. G.; Lian, T.; Hill, C. L., J. *Am. Chem. Soc.* **2009,** 1*31,* 7522-7523.
42. Gerischer, H., J. *Electrochem. Soc.* **1966,** 1*13,* 1174-1182.
43. Gerischer, H.; Mindt, W., E*lectrochim. Acta* **1968,** 1*3,* 1329-1341.
44. Gileadi, E., E*lectrode Kinetics for Chemists, Chemical Engineers, and Materials Scientists*. Wiley-VCH: New York, 1993.
45. Glasscock, J. A.; Barnes, P. R. F.; Plumb, I. C.; Savvides, N., J. *Phys. Chem. C* **2007,** 1*11,* 16477-16488.
46. Goldstein, J.; Newbury, D. E.; Joy, D. C.; Lyman, C. E.; Echlin, P.; Lifshin, E.; Sawyer, L.; Michael, J. R., S*canning Electron Microscopy and X-Ray Microanalysis*. 3rd ed.; Springer: New York, 2003.
47. Grätzel, M., J. *Photochem. Photobiol., C* **2003,** 4*,* 145-153.
48. Grätzel, M., N*ature* **2001,** 4*14,* 338-344.
49. Gray, H. B., N*at. Chem.* **2009,** 1*,* 7-7.
50. Grimes, C. A.; Varghese, O. K.; Ranjan, S., L*ight, Water, Hydrogen.* Springer: New York, 2007.
51. Hagedorn, K.; Forgacs, C.; Collins, S.; Maldonado, S., J. *Phys. Chem. C* **2011,** 1*14,* 12010-12017.
52. Han, H.; Frei, H., J. *Phys. Chem. C* **2008,** 1*12,* 16156-16159.
53. Hardee, K. L.; Bard, A. J., J. *Electrochem. Soc.* **1976,** 1*23,* 1024-1026.
54. Harriman, A.; Pickering, I. J.; Thomas, J. M.; Christensen, P. A., J. *Chem. Soc., Faraday Trans. 1* **1988,** 8*4,* 2795 - 2806.
55. Heller, A., S*cience* **1984,** 2*23,* 1141-1148.

56. Hoffert, M. I.; Caldeira, K.; Benford, G.; Criswell, D. R.; Green, C.; Herzog, H.; Jain, A. K.; Kheshgi, H. S.; Lackner, K. S.; Lewis, J. S.; Lightfoot, H. D.; Manheimer, W.; Mankins, J. C.; Mauel, M. E.; Perkins, L. J.; Schlesinger, M. E.; Volk, T.; Wigley, T. M. L., S*cience 2***002,** 2*98,* 981-987.
57. Hoffmann, M. R.; Martin, S. T.; Choi, W.; Bahnemann, D. W., C*hem. Rev. 1***995,** 9*5,* 69-96.
58. Hong, S. J.; Lee, S.; Jang, J. S.; Lee, J. S., E*nergy Environ. Sci. 2***011,** 4*,* 1781-1787.
59. Hu, Y.-S.; Kleiman-Shwarsctein, A.; Forman, A. J.; Hazen, D.; Park, J.-N.; McFarland, E. W., C*hem. Mater. 2***008,** 2*0,* 3803-3805.
60. Hu, Y.-S.; Kleiman-Shwarsctein, A.; Stucky, G. D.; McFarland, E. W., C*hem. Comm. 2***009,** 2652-2654.
61. Huang, P.; Magnuson, A.; Lomoth, R.; Abrahamsson, M.; Tamm, M.; Sun, L.; van Rotterdam, B.; Park, J.; Hammarström, L.; Åkermark, B.; Styring, S., J. *Inorg. Biochem. 2***002,** 9*1,* 159-172.
62. Ingler, W. B., Jr.; Khan, S. U. M., E*lectrochem. Solid-State Lett. 2***006,** 9*,* G144-G146.
63. Inoue, Y., E*nergy Environ. Sci. 2***009,** 2*,* 364-386.
64. Internation Energy Outlook 2010. U. S. Department of Energy: Energy Information Administration: Washington, DC, 2010; Vol. DOE/EIA-0484.
65. Iordanova, N.; Dupuis, M.; Rosso, K. M., J. *Chem. Phys. 2***005,** 1*22,* 144305-10.
66. Jeon, T. H.; Choi, W.; Park, H., P*CCP 2***011,** 1*3,* 21392-21401.
67. Jorand Sartoretti, C.; Ulmann, M.; Alexander, B. D.; Augustynski, J.; Weidenkaff, A., C*hem. Phys. Lett. 2***003,** 3*76,* 194-200.
68. Kanan, M. W.; Nocera, D. G., S*cience 2***008,** 3*21,* 1072-1075.
69. Kanan, M. W.; Surendranath, Y.; Nocera, D. G., C*hem. Soc. Rev. 2***009,** 3*8,* 109-114.
70. Kanan, M. W.; Yano, J.; Surendranath, Y.; Dincă, M.; Yachandra, V. K.; Nocera, D. G., J. *Am. Chem. Soc. 2***010,** 1*32,* 13692-13701.
71. Kaneko, M.; Yao, G.-J.; Kira, A., C*hem. Commun. 1***989,** 1338-1939.
72. Kato, H.; Kudo, A., J. *Phys. Chem. B 2***002,** 1*06,* 5029-5034.
73. Kato, H.; Kudo, A., J. *Phys. Chem. B. 2***001,** 1*05,* 4285-4292.
74. Kay, A.; Cesar, I.; Grätzel, M., J. *Am. Chem. Soc. 2***006,** 1*28,* 15714-15721.
75. Kazmerski, L. Best Research Cell Efficiencies. http://www.nrel.gov/ncpv/images/efficiency_chart.jpg (accessed 10/26/2011).
76. Kennedy, J. H.; Frese, K. W., Jr., J. *Electrochem. Soc. 1***978,** 1*25,* 709-14.
77. Kennedy, J. H.; Shinar, R.; Ziegler, J. P., J. *Electrochem. Soc. 1***980,** 1*27,* 2307-9.
78. Khan, S. U. M.; Akikusa, J., J. *Phys. Chem. B 1***999,** 1*03,* 7184-7189.
79. Khaselev, O.; Turner, J. A., S*cience 1***998,** 2*80,* 425-427.
80. Kim, H. G.; Hwang, D. W.; Kim, J.; Kim, Y. G.; Lee, J. S., C*hem. Commun. 1***999,** 1*2,* 1077-1078.
81. Klahr, B. M.; Martinson, A. B. F.; Hamann, T. W., L*angmuir 2***011,** 2*7,* 461-468.
82. Kleiman-Shwarsctein, A.; Hu, Y.-S.; Forman, A. J.; Stucky, G. D.; McFarland, E. W., J. *Phys. Chem. C 2***008,** 1*12,* 15900-15907.
83. Kudo, A.; Miseki, Y., C*hem. Soc. Rev. 2***009,** 3*8,* 253-278.
84. Kudo, A.; Ueda, K.; Kato, H.; Mikami, I., C*atal. Lett. 1***998,** 5*3,* 229-230.
85. LaTempa, T. J.; Feng, X.; Paulose, M.; Grimes, C. A., J. *Phys. Chem. C 2***009,** 1*13,* 16293-16298.

86. Le Formal, F.; Tétreault, N.; Cornuz, M.; Moehl, T.; Grätzel, M., C*hem. Sci. 2***011,** 2*,* 737-743.
87. Lewis, N. S., A*cc. Chem. Res. 1***990,** 2*3,* 176-183.
88. Lewis, N. S., M*RS Bulletin 2***007,** 3*2,* 808-820.
89. Lewis, N. S., S*cience 2***007,** 3*15,* 798-801.
90. Lewis, N. S.; Nocera, D. G., P*roc. Nat. Acad. Sci. 2***006,** 1*03,* 15729-15735.
91. Li, G.; Sproviero, E. M.; McNamara, W. R.; Snoeberger, R. C., III; Crabtree, R. H.; Brudvig, G. W.; Batista, V. S., J. *Phys. Chem. B 2***010,** 1*14,* 14214-14222.
92. Li, G.; Sproviero, E. M.; Snoeberger III, R. C.; Iguchi, N.; Blakemore, J. D.; Crabtree, R. H.; Brudvig, G. W.; Batista, V. S., E*nergy Environ. Sci. 2***009,** 2*,* 230-238.
93. Li, M.; Zhao, L.; Guo, L., I*nt. J. Hydrogen Energy 2***010,** 3*5,* 7127-7133.
94. Licht, S., E*ncyclopedia of Electrochemistry: Semiconductor Electrodes and Photoelectrochemistry.* Wiley-VCH: Weinheim, 2002.
95. Lin, Y.; Zhou, S.; Sheehan, S. W.; Wang, D., J. *Am. Chem. Soc. 2***011,** 1*33,* 2398-2401.
96. Lindgren, T.; Wang, H.; Beermann, N.; Vayssieres, L.; Hagfeldt, A.; Lindquist, S.-E., S*ol. Energy Mater. 2***002,** 7*1,* 231-243.
97. Ling, Y.; Wang, G.; Wheeler, D. A.; Zhang, J. Z.; Li, Y., N*ano Lett. 2***011,** 1*1,* 2119-2125.
98. Linsebigler, A. L.; Lu, G.; Yates, J. T., C*hem. Rev. 1***995,** 9*5,* 735-758.
99. Liu, R.; Lin, Y.; Chou, L.-Y.; Sheehan, S. W.; He, W.; Zhang, F.; Hou, H. J. M.; Wang, D., A*ngew. Chem. Int. Ed. 2***011,** 5*0,* 499-502.
100. Liu, W. K.; Salley, G. M.; Gamelin, D. R., J. Phys. Chem. B 2005, 109, 14486-14495.
101. Lomoth, R.; Magnuson, A.; Sjödin, M.; Huang, P.; Styring, S.; Hammarström, L., P*hotosynth. Res. 2***005,** 8*7,* 25-40.
102. Luo, W.; Wang, Z.; Wan, L.; Li, Z.; Yu, T.; Zou, Z., J. *Phys. D: Appl. Phys. 2***010,** 4*3,* 405402.
103. Lutterman, D. A.; Surendranath, Y.; Nocera, D. G., J. *Am. Chem. Soc. 2***009,** 1*31,* 3838-3839.
104. Maeda, K.; Domen, K., C*hem. Mater. 2***010,** 2*2,* 612-623.
105. Maeda, K.; Domen, K., J. *Phys. Chem. C 2***007,** 1*11,* 7851-7861.
106. Maeda, K.; Higashi, M.; Lu, D.; Abe, R.; Domen, K., J. *Am. Chem. Soc. 2***010,** 1*32,* 5858-5868.
107. Maeda, K.; Teramura, K.; Takata, T.; Hara, M.; Saito, N.; Toda, K.; Inoue, Y.; Kobayashi, H.; Domen, K., J. *Phys. Chem. B 2***005,** 1*09,* 20504-20510.
108. Magnuson, A.; Anderlund, O. J.; Lindblad, P.; Lomoth, R.; Polivka, T.; Ott, S.; Stensjö, K.; Styring, S.; Sundström, V.; Hammarström, L., A*cc. Chem. Res. 2***009,** 4*2,* 1899-1909.
109. Majumder, S. A.; Khan, S. U. M., I*nt. J. Hydrogen Energy 1***994,** 1*9,* 881-887.
110. McAlpin, J. G.; Surendranath, Y.; Dincă, M.; Stich, T. A.; Stoian, S. A.; Casey, W. H.; Nocera, D. G.; Britt, R. D., J. *Am. Chem. Soc. 2***010,** 1*32,* 6882-6883.
111. McDaniel, N. D.; Coughlin, F. J.; Tinker, L. L.; Bernhard, S. J., J. *Am. Chem. Soc. 2***008,** 1*30,* 210-217.
112. McEvoy, J. P.; Brudvig, G. W., C*hem. Rev. 2***006,** 1*06,* 4455-4483.
113. McEvoy, J. P.; Gascon, J. A.; Batista, V. S.; Brudvig, G. W., P*hotochem. Photobiol. Sci. 2***005,** 4*,* 940-949.
114. Mills, A., Chem. Soc. Rev. 1989, 18, 285-316.
115. Mohapatra, S. K.; John, S. E.; Banerjee, S.; Misra, M., C*hem. Mater. 2***009,** 2*1,* 3048-3055.

116. Mola, J.; Mas-Marza, E.; Sala, X.; Romero, I.; Rodríguez, M.; Viñas, C.; Parella, T.; Llobet, A., A*ngew. Chem. Int. Ed. 2***008,** 4*7,* 5830-5832.

117. Nakagawa, T.; Bjorge, N. S.; Murray, R. W., J. *Am. Chem. Soc. 2***009,** 1*31,* 15578-15589.

118. Navarro Yerga, R. M.; Álvarez Galván, M. C.; del Valle, F.; Villoria de la Mano, J. A.; Fierro, J. L. G., C*hemSusChem 2***007,** 2*,* 471-485.

119. Navarro, R. M.; Alvarez-Galvan, M. C.; Villoria de la Mano, J. A.; Al-Zahranib, S. M.; Fierroa, J. L. G., E*nergy Environ. Sci. 2***010,** 3*,* 1865-1882.

120. Ng, Y. H.; Iwase, A.; Kudo, A.; Amal, R., J. *Phys. Chem. Lett. 2***010,** 1*,* 2607-2612.

121. Ni, M.; Leung, M. K. H.; Leung, D. Y. C.; Sumathy, K., R*enewable Sustainable Energy Rev. 2***006,** 1*1,* 401-425.

122. Nocera, D. G., C*hemSusChem 2***009,** 2*,* 387-390.

123. Nocera, D. G., I*norg. Chem. 2***009,** 4*8,* 10001-10017.

124. Nozik, A. J., A*nnu. Rev. Phys. Chem. 1***978,** 2*9,* 189-222.

125. Nozik, A.; Memming, R., J. *Phys. Chem. 1***996,** 1*00,* 13061-13078.

126. O'Regan, B.; Grätzel, M., *Nature* **1991,** *353*, 737-740.

127. O'Sullivan, E. J. M.; Calvo, E. J., Reactions at Metal Oxide Electrodes. In *Comprehensive Chemical Kinetics*, Compton, R. G., Ed. Elsevier Publishing Co.: Amsterdam, 1987; Vol. 27, pp 247-360.

128. Osterloh, F. E., *Chem. Mater.* **2008,** *20*, 35-54.

129. Park, H. S.; Kweon, K. E.; Ye, H.; Paek, E.; Hwang, G. S.; Bard, A. J., *J. Phys. Chem. C* **2011,** *115*, 17870-17879.

130. Payne, D. J.; Robinson, M. D. M.; Egdell, R. G.; Walsh, A.; McNulty, J.; Smith, K. E.; Piper, L. F. J., *Appl. Phys. Lett.* **2011,** *98*, 212110.

131. Pijpers, J. J. H.; Winkler, M. T.; Surendranath, Y.; Buonassisi, T.; Nocera, D. G., *Proc. Natl. Acad. Sci. U. S. A.* **2011,** *108*, 10056-10061.

132. Pingree, L. S. C.; MacLeod, B. A.; Ginger, D. S., *J. Phys. Chem. C* **2008,** *112*, 7922-7927.

133. Pingree, L. S. C.; Reid, O. G.; Ginger, D. S., *Nano Lett.* **2009,** *9*, 2946-2952.

134. Rajeshwar, K., *J. Appl. Electrochem.* **2007,** *37*, 765-787.

135. Rangaraju, R. R.; Panday, A.; Raja, K. S.; Misra, M., *J. Phys. D: Appl. Phys.* **2009,** *42*, 135303.

136. Reid, O. G.; Munechika, K.; Ginger, D. S., *Nano Lett.* **2008,** *8*, 1602-1609.

137. Risch, M.; Khare, V.; Zaharieva, I.; Gerencser, L.; Chernev, P.; Dau, H., *J. Am. Chem. Soc.* **2009,** *131*, 6936-6937.

138. Romero, I.; Rodríguez, M.; Sens, C.; Mola, J.; Kollipara, M. R.; Francàs, L.; Mas-Marza, E.; Escriche, L.; Llobet, A., *Inorg. Chem.* **2008,** *47*, 1824-1834.

139. Rupprecht, J.; Hankamer, B.; Mussgnug, J. H.; Ananyev, G.; Dismukes, G. C.; Kruse, O., *Appl. Microbiol. Biotechnol.* **2006,** *72*, 422-449.

140. Ruttinger, W.; Dismukes, G. C., *Chem. Rev.* **1997,** *97*, 1-24.

141. Sala, X.; Romero, I.; Rodríguez, M.; Escriche, L.; Llobet, A., *Angew. Chem. Int. Ed.* **2009,** *48*, 2842-2852.

142. Saremi-Yarahmadi, S.; Wijayantha, K. G. U.; Tahir, A. A.; Vaidhyanathan, B., *J. Phys. Chem. C* **2009,** *113*, 4768-4778.

143. Sartoretti, C. J.; Alexander, B. D.; Solarska, R.; Rutkowska, I. A.; Augustynski, J.; Cerny, R., *J. Phys. Chem. B* **2005,** *109*, 13685-13692.
144. Sartoretti, C. J.; Ulmann, M.; Alexander, B. D.; Augustynski, J.; Weidenkaff, A., *Chem. Phys. Lett.* **2003,** *376*, 194-200.
145. Satsangi, V. R.; Kumari, S.; Singh, A. P.; Shrivastav, R.; Dass, S., *Int. J. Hydrogen Energy* **2008,** *33*, 312-318.
146. Sayama, K.; Nomura, A.; Arai, T.; Sugita, T.; Abe, R.; Yanagida, S.; Oi, T.; Iwasaki, Y.; Abe, Y.; Sugihara, H., *J. Phys. Chem. B* **2006,** *110*, 11352-11360.
147. Sayama, K.; Wang, N.; Miseki, Y.; Kusama, H.; Onozawa-Komatsuzaki, N.; Sugihara, H., *Chem. Lett.* **2010,** *39*, 17-19.
148. Scaife, D. E., *Sol. Energy* **1980,** *25*, 41-54.
149. Seabold, J. A.; Choi, K.-S., *Chem. Mater.* **2011,** *23*, 1105-1112.
150. Shinar, R.; Kennedy, J. H., *Sol. Energy Mater.* **1982,** *6*, 323-35.
151. Shockley, W.; Queisser, H. J., *J. Appl. Phys.* **1961,** *32*, 510-519.
152. Sivula, K.; Le Formal, F.; Grätzel, M., *Chem. Mater.* **2009,** *21*, 2862-2867.
153. Sivula, K.; Le Formal, F.; Grätzel, M., *ChemSusChem* **2011,** *4*, 432-449.
154. Sivula, K.; Zboril, R.; Le Formal, F.; Robert, R.; Weidenkaff, A.; Tucek, J.; Frydrych, J.; Grätzel, M., *J. Am. Chem. Soc.* **2010,** *132*, 7436-7444.
155. Sleight, A. W.; Aykan, K.; Rogers, D. B., *J. Solid State Chem.* **1975,** *13*, 231-236.
156. Solar Spectra. http://rredc.nrel.gov/solar/spectra/ (accessed 10/16/11).
157. Souza, F. L.; Lopes, K. P.; Nascente, P. A. P.; Leite, E. R., *Sol. Energy Mater. Sol. Cells* **2009,** *93*, 362-368.
158. Spray, R. L.; Choi, K.-S., *Chem. Mater.* **2009,** *21*, 3701-3709.
159. Spurgeon, J. M.; Atwater, H. A.; Lewis, N. S., *J. Phys. Chem. C* **2008,** *112*, 6186-6193.
160. Steinmiller, E. M. P.; Choi, K.-S., *Proc. Nat. Acad. Sci.* **2009,** *106*, 20633-20636.
161. Su, J.; Guo, L.; Yoriya, S.; Grimes, C. A., *Cryst. Growth Des.* **2010,** *10*, 856-861.
162. Suleymanov, A. S., *Int. J. Hydrogen Energy* **1991,** *16*, 741-743.
163. Sun, J.; Zhong, D. K.; Gamelin, D. R., *Energy Environ. Sci.* **2010,** *3*, 1252-1261.
164. Sun, L.; Hammarström, L.; Akermark, B.; Styring, S., *Chem. Soc. Rev.* **2001,** *30*, 36-49.
165. Surendranath, Y.; Dincă, M.; Nocera, D. G., *J. Am. Chem. Soc.* **2009,** *131*, 2615-2620.
166. Surendranath, Y.; Kanan, M. W.; Nocera, D. G., *J. Am. Chem. Soc.* **2010,** *132*, 16501-16509.
167. Suzuki, O.; Takahasi, M.; Rukunaga, T.; Kuboyama, J. Novel cobalt oxide and an electrode having the cobalt oxide coating. 3,399,966, September 3, 1968.
168. Tahir, A. A.; Wijayantha, K. G. U.; Saremi-Yarahmadi, S.; Mazhar, M.; McKee, V., *Chem. Mater.* **2009,** *21*, 3763-3772.
169. Tilley, S. D.; Cornuz, M.; Sivula, K.; Grätzel, M., *Angew. Chem. Int. Ed.* **2010,** *49*, 6405-6408.
170. Tokunaga, S.; Kato, H.; Kudo, A., *Chem. Mater.* **2001,** *13*, 4624-4628.
171. Trasatti, S., Transition Metal Oxides: Versatile Materials for Electrocatalysis. In *Electrochemistry of Novel Materials*, Lipkowski, J.; Ross, P. N., Eds. VCH Publishers: New York, 1994; pp 207-296.
172. Tseng, H.-W.; Zong, R.; Muckerman, J. T.; Thummel, R., *Inorg. Chem.* **2008,** *47*, 11763-11773.

173. Turner, J., *Nature Mater.* **2008,** *7*, 770-771.
174. Valent, M.; Suvorov, D., *J. Am. Ceram. Soc.* **2000,** *83*, 2721-2729.
175. van de Krol, R.; Liang, Y.; Schoonman, J., *J. Mater. Chem.* **2008,** *18*, 2311-2320.
176. Walsh, A.; Yan, Y.; Huda, M. N.; Al-Jassim, M. M.; Wei, S.-H., *Chem. Mater.* **2009,** *21*, 547-551.
177. Walter, M. G.; Warren, E. L.; McKone, J. R.; Boettcher, S. W.; Mi, Q.; Santori, E. A.; Lewis, N. S., *Chem. Rev.* **2010,** *110*, 6446-6473.
178. Wang, C. M.; Mallouk, T. E., *J. Phys. Chem.* **1990,** *94*, 423-428.
179. Wang, H.; Deutsch, T.; Turner, J. A., *J. Electrochem. Soc.* **2008,** *155*, F91-F96.
180. Weare, W. W.; Pushkar, Y.; Yachandra, V. K.; Frei, H., *J. Am. Chem. Soc* **2008,** *130*, 11355-11363.
181. Wee, S.-H.; Kim, D.-W.; Yoo, S.-I., *J. Am. Ceram. Soc.* **2004,** *87*, 871-874.
182. Woodhouse, M.; Parkinson, B. A., *Chem. Mater.* **2008,** *20*, 2495-2502.
183. Yachandra, V. K.; Sauer, K.; Klein, M. P., *Chem. Rev.* **1996,** *96*, 2927-2950.
184. Yagi, M.; Kaneko, M., *Chem. Rev.* **2001,** *101*, 21-35.
185. Yan, X.; Liu, G.; Wang, L.; Wang, Y.; Zhu, X.; Zou, J.; Lu, G. Q., *J. Mater. Res.* **2010,** *25*, 182-188.
186. Yano, J.; Kern, J.; Sauer, K.; Latimer, M. J.; Pushkar, Y.; Biesiadka, J.; Loll, B.; Saenger, W.; Messinger, J.; Zouni, A.; Yachandra, V. K., *Science* **2006,** *314*, 821-825.
187. Yao, W.; Iwai, H.; Ye, J., *Dalton Trans.* **2008**, 1426-1430.
188. Ye, H.; Lee, J.; Jang, J. S.; Bard, A. J., *J. Phys. Chem.* **2010,** *114*, 13322-13328.
189. Ye, H.; Park, H. S.; Bard, A. J., *J. Phys. Chem. C* **2011,** *115*, 12464-12470.
190. Yeh, L.-S. R.; Hackerman, N., *J. Electrochem. Soc.* **1977,** *124*, 833-836.
191. Yin, W.-J.; Wei, S.-H.; Al-Jassim, M. M.; Turner, J.; Yan, Y., *Phys. Rev. B* **2011,** *83*, 155102.
192. Young, E. R.; Costi, R.; Paydavosi, S.; Nocera, D. G.; Bulovic, V., *Energy Environ. Sci.* **2011,** *4*, 2058-2061.
193. Youngblood, W. J.; Lee, S.-H. A.; Kobayashi, Y.; Hernandez-Pagan, E. A.; Hoertz, P. G.; Moore, T. A.; Moore, A. L.; Gust, D.; Mallouk, T. E., *J. Am. Chem. Soc.* **2009,** *131*, 926-927.
194. Youngblood, W. J.; Lee, S.-H. A.; Maeda, K.; Mallouk, T. E., *Acc. Chem. Res.* **2009,** *42*, 1966-1973.
195. Zhong, D. K.; Choi, S.; Gamelin, D. R., *J. Am. Chem. Soc.* **2011,** *133*, 18370-18377.
196. Zhong, D. K.; Cornuz, M.; Sivula, K.; Grätzel, M.; Gamelin, D. R., *Energy Environ. Sci.* **2011,** *4*, 1759-1764.
197. Zhong, D. K.; Gamelin, D. R., *J. Am. Chem. Soc.* **2010,** *132*, 4202-4207.
198. Zhong, D. K.; Sun, J.; Inumaru, H.; Gamelin, D. R., *J. Am. Chem. Soc.* **2009,** *131*, 6086-6087.
199. Zou, Z.; Arakawa, H., *J. Photochem. Photobiol., A* **2003,** *158*, 145-162.
200. Zou, Z.; Ye, J.; Sayama, K.; Arakawa, H., *Nature* **2001,** *414*, 625-627.

Appendix A. Supplementary Information for Chapter 3

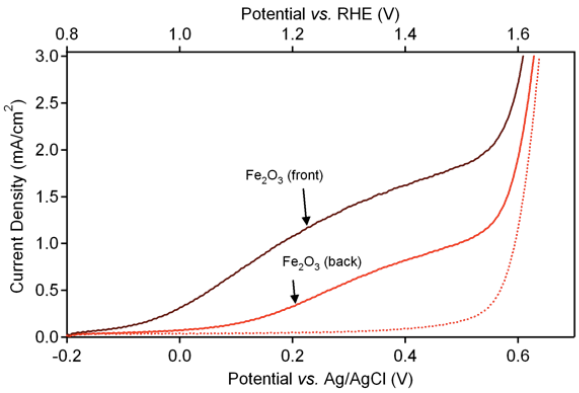

Figure A.1. PEC Water Oxidation with Front and Backside Illumination of α-Fe_2O_3
Dark (dashed) and photocurrent (solid) densities for mesoscopic α-Fe_2O_3 photoanodes used in the study in Chapter 3 under backside (red) and frontside (black) illumination, collected using simulated AM1.5 sunlight (1 sun). Scan rate 50 mV/s.

To test for the possibility that the cathodic photocurrent shift comes from the action of solvated cobalt as a redox mediator, a set of control experiments involving deliberate addition of solvated Co^{2+} was performed by adding $Co(OH)_4^{2-}$ to the 1M NaOH electrolyte of the PEC cell. $Co(OH)_4^{2-}$ was prepared by dissolving cobalt nitrate in a 50 wt% concentrated NaOH aqueous solution to make a ~0.005M $Co(OH)_4^{2-}$ solution, which was then added to distilled water to reach pH ~13.

The final solution was added dropwise to the electrolyte of the PEC cell under operating conditions, where its influence on dark and photocurrent densities of various photoanodes could be monitored. Although sparingly soluble at pH 13.6, the precipitation of solid $Co(OH)_2$ from the electrolyte solution is likely slow, as indicated by observation of the characteristic $Co(OH)_4^{2-}$ $^4T_1(P)$ ligand field band in the absorption spectrum of the pH ~ 13 stock solution even ~30 min after preparation (Figure S2), which is roughly three times longer than required to collect the PEC data. Although solvated $Co(OH)_4^{2-}$ was difficult to detect spectroscopically in the PEC cell at very low concentrations, its presence was readily detected electrochemically by an increase in dark current for both FTO and α-Fe_2O_3-modified FTO anodes. When $Co(OH)_4^{2-}$ was added to the PEC cell during α-Fe_2O_3 film measurement, an increase in dark current was observed but no significant change in photocurrent resulted, arguing against interpretation of the cathodic shift described in the manuscript as arising from participation of a soluble Co^{2+} redox mediator. Independent control experiments in which I-V scans of unmodified FTO anodes were measured before and after repeated photocurrent measurements on Co-Pi/α-Fe_2O_3 composite photoanodes without replacing the electrolyte also failed to detect any solvated Co^{2+}, again arguing against interpretation of the cathodic photocurrent shift described in the manuscript as arising from participation of a soluble Co^{2+} redox mediator.

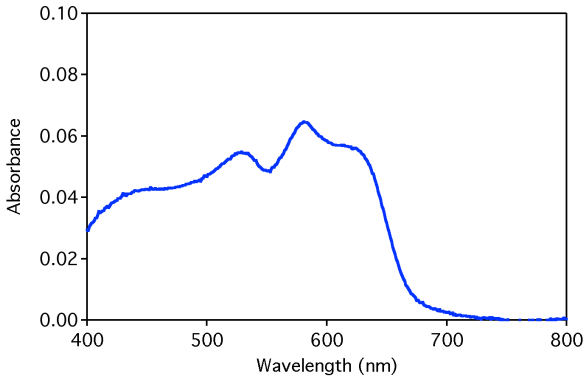

Figure A.2. $Co(OH)_4^{2-}$ Spectrum at pH ~13
Absorption spectrum of $Co(OH)_4^{2-}$ at pH ~13 measured ~30 min after preparation of the solution.

Appendix B. Supplementary Information for Chapter 4

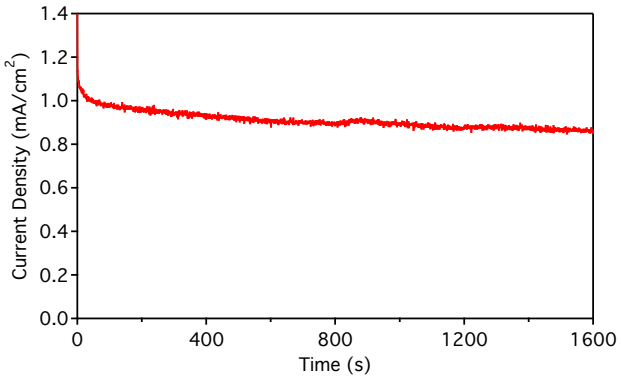

Figure B.1. α-Fe_2O_3 Photoanode in pH 7 KPi
Photocurrent decay of α-Fe_2O_3 photoanode measured in pH 7, 0.1 M KPi buffer at +1.3 V vs RHE, 1 sun AM 1.5.

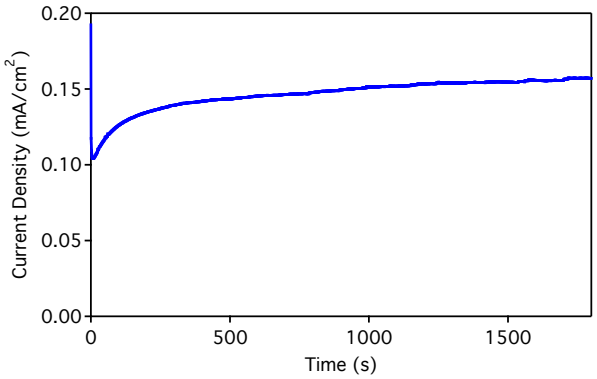

Figure B.2. Electrodeposition of Co-Pi on α-Fe_2O_3 for 30 Min
Co-Pi electrodeposition on α-Fe_2O_3 photoanode in pH 7, 0.1 M KPi buffer at +1.1 V vs Ag/AgCl for 30 min.

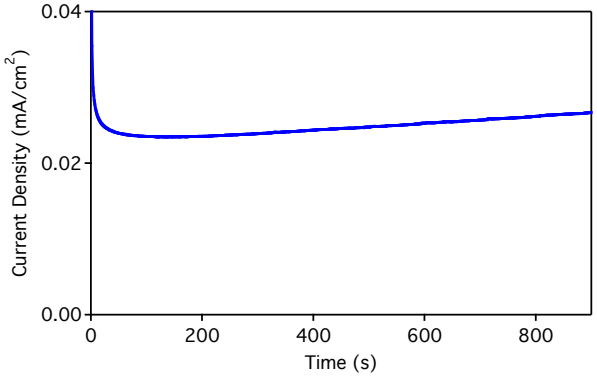

Figure B.3. Electrodeposition of Co-Pi on α-Fe_2O_3 for 15 Min
Co-Pi electrodeposition on α-Fe_2O_3 photoanode in pH 7, 0.1 M KPi buffer at +1.1 V vs Ag/AgCl for 15 min.

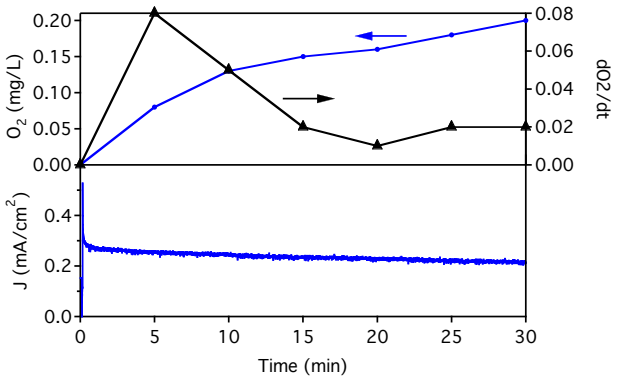

Figure B.4. Initial Oxygen Detection for Co-Pi/α-Fe_2O_3
O_2 generation and photocurrent density over time measured for a Co-Pi/α-Fe_2O_3 composite photoanode at +1.0 V vs RHE in 0.1 M KPi at pH 8. Co-Pi was electrodeposited on α-Fe_2O_3 for 30 min. The top panel shows an initial spike in the rate of O_2 evolution before relaxation to a steady state rate.

Appendix C. Supplementary Information for Chapter 5

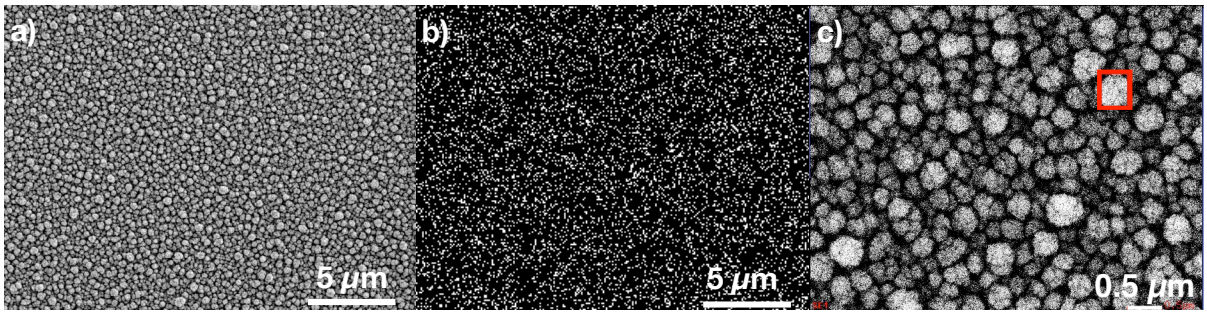

Figure C.1. SEM and EDX Data on Co-Pi/α-Fe_2O_3
a) SEM image of a Co-Pi/α-Fe_2O_3 photoanode prepared by photo-assisted electrodeposition of Co-Pi. **b)** Map of the Co(K) signal intensity in the area depicted in panel (a). **c)** The single nodule (of a Co-Pi/α-Fe_2O_3 film prepared by photo-assisted electrodeposition) used in the EDX analysis of Figure 5.2b. The nodule is marked with a red box.

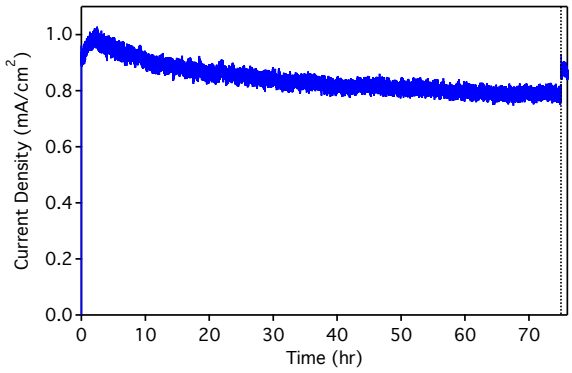

Figure C.2. Stability of Co-Pi/α-Fe_2O_3 Under PEC Conditions
Time dependence of the photocurrent density of a Co-Pi/α-Fe2O3 photoanode prepared by photo-assisted electrodeposition, measured at 1.0 V vs RHE in 1 M NaOH under continuous 1 sun, AM 1.5 simulated solar irradiation. The electrolyte was not stirred. The electrolyte was replaced after 75 hrs (dashed line), resulting in recovery of photocurrent density.

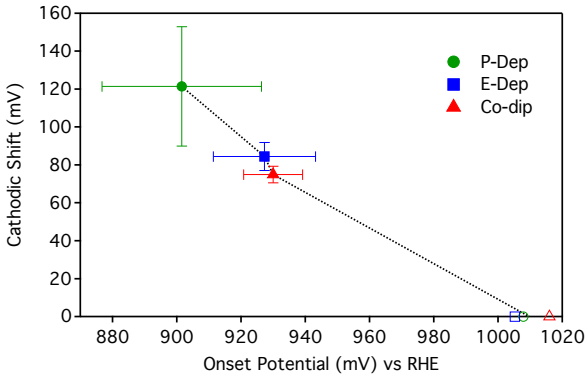

Figure C.3. Cathodic Shift with Onset Potential of Co-Pi/α-Fe_2O_3 and Co^{2+}/α-Fe_2O_3 Photoanodes
Average cathodic shifts plotted vs average onset potentials for Co-Pi/α-Fe_2O_3 photoanodes prepared by photo-assisted electrodeposition (P-Dep) and electrodeposition (E-Dep) of Co-Pi, and for Co^{2+}/α-Fe_2O_3 photoanodes prepared by surface adsorption of Co^{2+} (Co-dip) for the 12 films of Figure 5.5. Error bars indicate standard deviations. The open symbols represent the parent α-Fe_2O_3 photoanodes. These data show a strong correlation between the two performance metrics, with photo-assisted electrodeposition of Co-Pi leading to the lowest onset potentials and the greatest cathodic shifts.

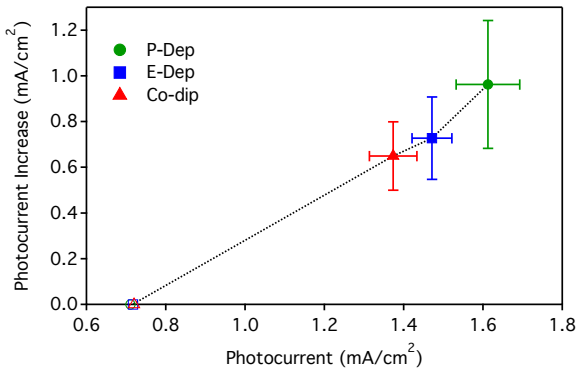

Figure C.4. Photocurrent Increase of Co-Pi/α-Fe_2O_3 and Co^{2+}/α-Fe_2O_3 Photoanodes
Average photocurrent density increase vs photocurrent at 1.1 V vs RHE (one-sun) for the 12 films of Figure 5.5. Photo-assisted electrodeposition of Co-Pi yields the largest photocurrent density increases and the highest absolute photocurrent densities. Error bars indicate standard deviations. The open symbols represent the parent α-Fe_2O_3 photoanodes.

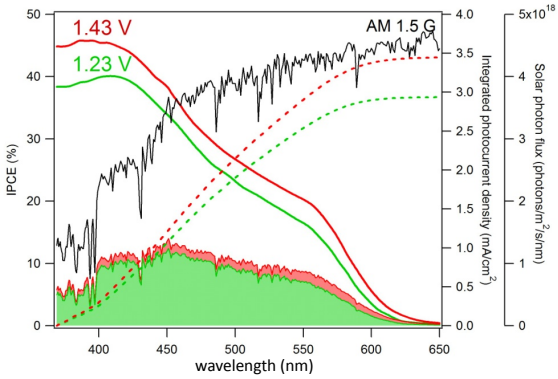

Figure C.5. Integration of IPCE Spectra of Co-Pi/α-Fe_2O_3
The IPCE (solid colored curves) at 1.23 and 1.43 V vs RHE of a Co-Pi/α-Fe_2O_3 photoanode prepared by photo-assisted electrodeposition are shown with the solar photon flux (AM 1.5G, 100 mW/cm^2) as a function of wavelength. Multiplication of the IPCE and the solar photon flux give the shaded areas, which are integrated with respect to the wavelength to give the predicted solar photocurrents (broken colored curves) of 2.9 and 3.4 mA/cm^2 at 1.23 and 1.43 V vs RHE, respectively.

Appendix D. Supplementary Information for Chapter 6

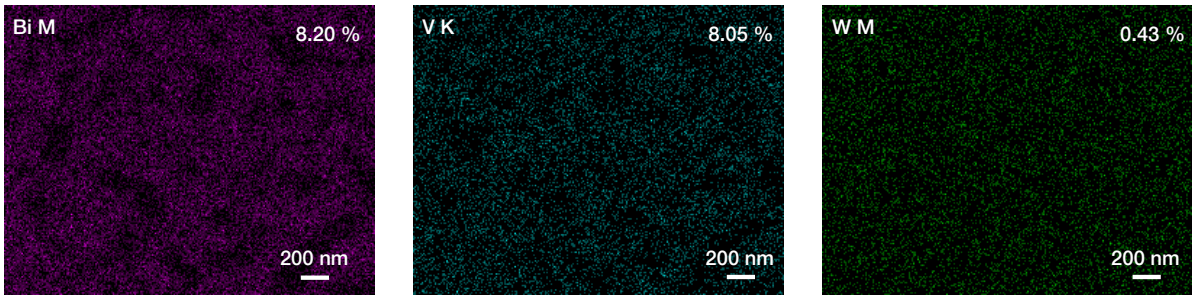

Figure D.1. EDX of a W:$BiVO_4$ Photoanode
Energy dispersive X-ray analysis (EDX) maps of a W:$BiVO_4$ photoanode probing the Bi(M), V(K), and W(M) transition at 10 keV. The atomic percentages of each element are given in the upper right hand corner.

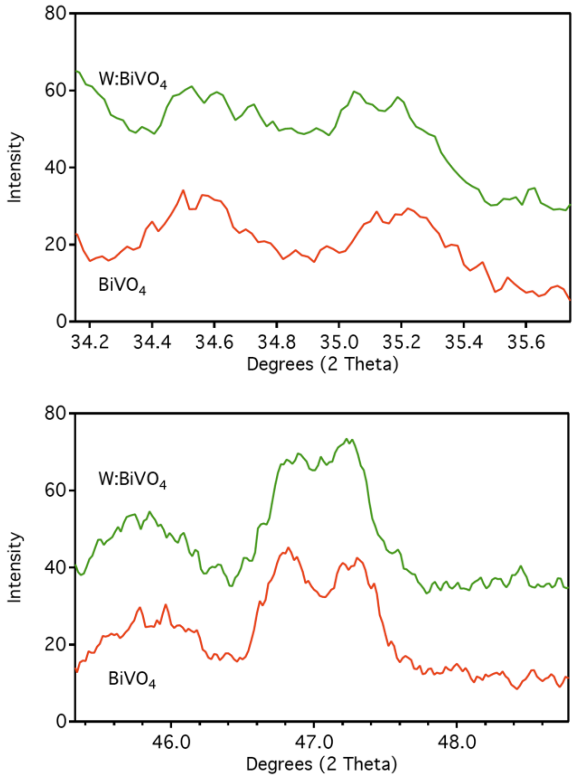

Figure D.2. XRD Shifts from Tungsten Doping $BiVO_4$
Expansion of the XRD data from Figure 6.2. **Top)** The (200) and (002) peaks of monoclinic scheelite BiVO4 at 34.5˚ and 35.2˚ shift toward one another upon addition of W to the synthesis. **Bottom)** The (240) and (042) peaks of $BiVO_4$ at 46.7˚ and 47.3˚ shift toward one another upon addition of W to the synthesis. Similar shifts have been reported previously to arise from W doping in $BiVO_4$.[1]

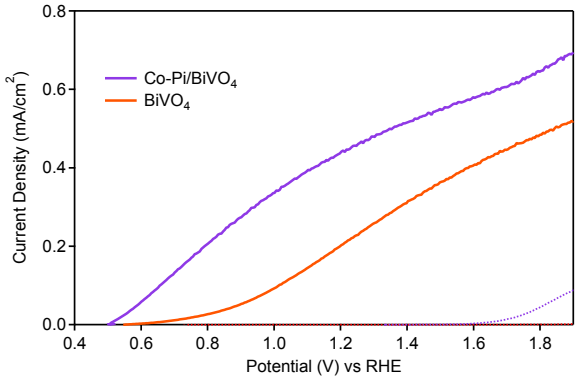

Figure D.3. *J-V* Curves of Co-Pi/$BiVO_4$
Current density-voltage (*J-V*) curves for a $BiVO_4$ photoanode before (red) and after Co-Pi surface modification (blue) under 1 sun AM 1.5 simulated solar irradiation (solid) and in the dark (dotted) in pH 9 sodium borate buffer. Note: the experimental conditions used for these measurements were slightly different from those used in the Chapter 6, including use of a different buffer (sodium borate vs potassium phosphate). This photoanode has not been optimized, but the similar cathodic shift in onset potential upon addition of Co-Pi as described for W:$BiVO_4$ photoanodes indicates that this shift independent of W^{6+} doping or WO_3 segregation.

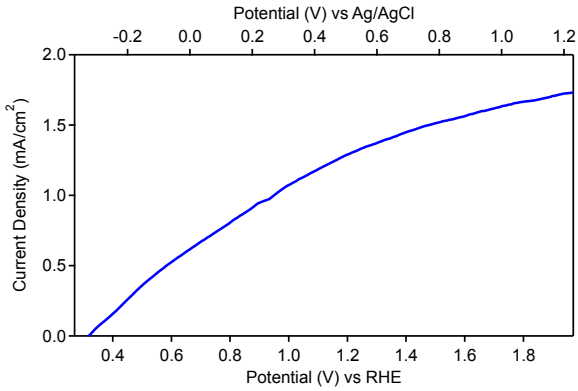

Figure D.4. *J-V* Curve of the Co-Pi/W:$BiVO_4$ Photoanode Used for O_2 Detection
Current density–voltage (*J-V*) curve for the Co-Pi/W:$BiVO_4$ photoanode used for the O_2 evolution measurements shown in Figure 6.5 of the Chapter 6, measured under 1 sun illumination. Note that the O_2 illumination power in Figure 6.5 is approximate because the film was unmasked to increase net O_2 evolution, whereas this *J-V* measurement was performed with a mask to define the illuminated area. In the former, the photon power density additionally possesses a gaussian profile rather than the top-hat profile of the measurements on masked films. Nevertheless, the average O_2 evolution rate of ~2.4×10^{-9} mol/sec·cm^2 at 1.0 V vs RHE estimated from Figure 6.5 is consistent with a current density of 0.93 mA/cm^2, close to the 1.08 mA/cm^2 in the *J-V* curve here. The measured O_2 evolution rate at steady state thus matches that anticipated from this *J-V* curve reasonably well given the different experimental conditions.

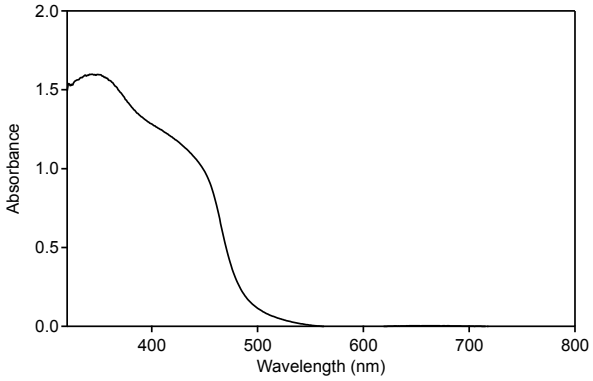

Figure D.5. Absorption Spectrum of W:$BiVO_4$
Absorption spectrum of the W:$BiVO_4$ photoanode used in Figure 6.6 in Chapter 6.

Estimation of the hole diffusion length in W:$BiVO_4$:

A hole diffusion length of L_p ~ 100 - 200 nm is estimated in the manuscript text. This range was estimated from Equation 6.2 of Chapter 6 using φ_{sep} from Figure 6.8 and depletion widths (W) derived from literature data. Specific values of W were determined from Equation D.1, where ε_0 is the permittivity of free space, ε_r is the dielectric constant (ε_r ~ 68 from refs. 2,3), and q is the elementary charge.

$$W = \left(\frac{2\varepsilon_0 \varepsilon_r (V - V_F)}{qN_d} \right)^{1/2} \qquad \text{(Equation D.1)}$$

Literature values of the flatband potentials (V_F) and donor densities (N_d) for a variety of $BiVO_4$ and W:$BiVO_4$ photoanodes, as determined from Mott-Schottky plots, are provided in Table D.1. From these values and Equation D.1, the depletion widths W in Table D.1 were calculated. The corresponding hole diffusion lengths (L_p) were then calculated for each sample using Equation 6.2 of Chapter 6, assuming the value of φ_{sep} determined for the W:$BiVO_4$ photoanodes of the present study, and are also summarized in Table D.1. All literature values of V_F are within 50mV of one another, and all values of L fall within the range 90-160 nm, despite differences of 10^4 in N_d. Our estimated range of L ~ 100-200 nm summarizes these calculations (with fewer significant digits).

Table D.1. Mott-Schottky parameters, depletion widths, and estimated hole diffusion lengths.

Source	Material	V_F (V vs RHE)	N_d (cm^{-1})	W at 1.5V	L_p (nm)
ref. 4	W:$BiVO_4$	0.04	2.5×10^{20}	6.6×10^{-7}	130
ref. 5	W:$BiVO_4$	0.03	8.4×10^{18}	3.6×10^{-6}	90
ref. 6	$BiVO_4$	-0.01	1.6×10^{21}	2.7×10^{-7}	140
hypothetical example	W:$BiVO_4$	0.02	1.0×10^{23}	3.4×10^{-8}	160

References:

1. Park, H. S.; Kweon, K. E.; Ye, H.; Paek, E.; Hwang, G. S.; Bard, A. J., *J. Phys. Chem. C* **2011,** *115*, 17870.

2. Valent, M.; Suvorov, D., *J. Am. Ceram. Soc.* **2000,** *83*, 2721.
3. Wee, S.-H.; Kim, D.-W.; Yoo, S.-I., *J. Am. Ceram. Soc.* **2004,** *87*, 871.
4. Ye, H.; Lee, J.; Jang, J. S.; Bard, A. J., *J. Phys. Chem. C* **2010,** *114*, 13322.
5. Li, M.; Zhao, L.; Guo, L., *Int. J. Hydrogen Energy* **2010,** *35*, 7127.
6. Sayama, K.; Nomura, A.; Arai, T.; Sugita, T.; Abe, R.; Yanagida, S.; Oi, T.; Iwasaki, Y.; Abe, Y.; Sugihara, H., *J. Phys. Chem. B* **2006,** *110*, 11352.

Vita

Diane K. Zhong was born in Canton, China in 1984. In 1986, she moved with her family to Brooklyn, NY, where she grew up. In 2006, she earned a Bachelor of Arts degree *magna cum laude* from Barnard College in New York, NY. Afterwards, she joined the research lab of Professor Daniel R. Gamelin in 2007 at the University of Washington, where she earned a Doctor of Philosophy in Chemistry in 2012.